VTT SYMPOSIUM 264

Baltica VIII

Life Management and Maintenance for Power Plants
Vol. 1

VTT SYMPOSIUM 264

Keywords: thermal power plant, nuclear plant, boiler, turbine, condition, life, fuel, maintenance, inspection, monitoring, risk, reliability, material, damage, corrosion, fatigue, creep, degradation

Baltica VIII

Life Management and Maintenance for Power Plants

Vol. 1

Helsinki–Stockholm–Helsinki
18–20 May, 2010

Edited by Pertti Auerkari & Juha Veivo

Organised by

VTT

ISBN 978-951-38-7591-6 (soft back ed.)
ISSN 0357–9387 (soft back ed.)

ISBN 978-951-38-7592-3 (URL: http://www.vtt.fi/publications/index.jsp)
ISSN 1455–0873 (URL: http://www.vtt.fi/publications/index.jsp)

Copyright © VTT 2010

JULKAISIJA – UTGIVARE – PUBLISHER

VTT, Vuorimiehentie 5, PL 1000, 02044 VTT
puh. vaihde 020 722 111, faksi 020 722 4374

VTT, Bergsmansvägen 5, PB 1000, 02044 VTT
tel. växel 020 722 111, fax 020 722 4374

VTT Technical Research Centre of Finland
Vuorimiehentie 5, P.O. Box 1000, FI-02044 VTT, Finland
phone internat. +358 20 722 111, fax + 358 20 722 4374

Cover: TVO/Korpi-Hallila

Edita Prima Oy, Helsinki 2010

Preface

The Baltica Conferences have since 1988 witnessed a continuous change in the environment for the technology and business of power plants. Apart from the shift towards large actors and more unified practices, also grids and businesses are increasingly connected by the developments in the political landscape, technology, and the ability of people to contact each other anywhere. Meanwhile, some aspects may simply come around: the first Baltica Conference took place two years after Chernobyl, and new nuclear seems to be rising again. One driver of change is global warming, easy or not it is to remember after a hard winter in Europe and a decade of steady world mean temperature.

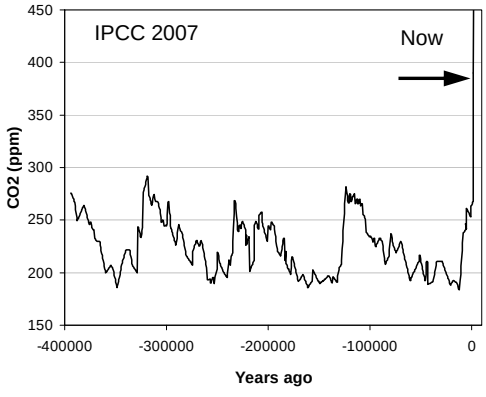

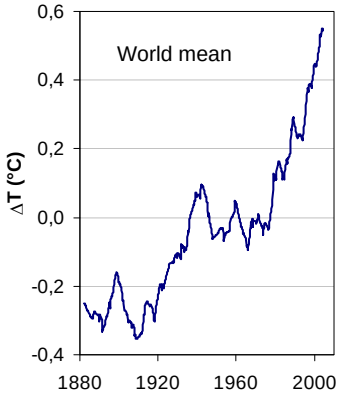

To start an ice age – something not everybody want – requires in air less than 300 ppm CO_2. Hydro, wind, other renewables and nuclear can push, but the world is not easily or quickly weaned from coal, oil and gas, or taught to apply carbon capture. The current level is 390 ppm CO_2 and rising, and the countermeasures provide a background for BALTICA VIII.

The editors wish to thank all authors, referees, organisers and the Board of the Conference for their invaluable help in preparing for the event and the proceedings. Financial and other contributions by the supporting and sponsoring organisations are also gratefully acknowledged.

Espoo, 18 May 2010

Pertti Auerkari & Juha Veivo

Editors

Contents

Approaches for lifetime management of nuclear power plants

Martti Vilpas
Radiation and Nuclear Safety Authority of Finland (STUK)
Nuclear Reactor Regulation
Helsinki, Finland

Abstract

The presentation gives a general view to lifetime management issues of operating nuclear power plants. Principles for safety assessment are described in brieffrom the regulatory point of view. The factors important to lifetime management and its evaluation through periodic safety review process are presented with some experiences.

1. Introduction

The majority of today's 436 nuclear power plants (NPP) in the world have been built in the 70's and 80's and their operating years are thus approaching and in some cases exceeding 30–40 years. This is the case also in Finland where the commercial age of four operating plants is now 28–33 years (Table 1). Ageing of the NPP fleet sets increasing requirements to assure safety and reliability of the plants by proper operation, adequate control as well as sufficient lifetime management actions. Lifetime management consists of a number of measures that ensure safe and reliable operation of a NPP until its final removal from service. Lifetime management is thus an effective tool to quantify the safety status of an operating NPP. It also supports the process of operating licence renewal which is periodically required for each plant.

This presentation reviews in brief the principles for safety assessment and lifetime management from regulatory point of view. One important tool in evaluation of the safety of an operating NPP is periodic safety review (PSR), the principles, realisation and feedback of which are addressed.

Table 1. Summary on Finnish NPP's [1].

NPP unit	Power (MWe)	Start of commercial operation	Operation years in 2010	Cumulative efficiency at the end of 2009 (%)
Loviisa 1	510/488	1977	33	86.4
Loviisa 2	510/488	1981	29	88.9
Olkiluoto 1	890/860	1979	31	92.2
Olkiluoto 2	890/860	1982	28	93.3
Olkiluoto 3	1 600			

2. Principles for safety assessment

In Finland, Nuclear Energy Act (1987) requires that the operating licence shall be granted for a fixed period of time. The length of the time period is not given in the Nuclear Energy Act. When considering the length particular attention shall be paid to ensuring safety and the estimated duration of operations. STUK's Regulatory Guide YVL 1.1 [2] states that if the operating licence is granted for a longer period than 10 years, STUK requires a Periodic Safety Review (PSR) to be performed at least every 10 years. The guide sets the basic requirements for the PSR and also requires adoption of IAEA's requirements for PSR implementation [3]. This means that the operating licence period is not necessarily 10 years at the Finnish NPP's but the periodic safety review is required at least by 10 year intervals.

Continuous safety improvement of NPP's is thus a necessity during the whole operating period. This can be derived e.g. from the Nuclear Energy Act, Section 7 a, prescribing that *"The safety of nuclear energy use shall be maintained at as high a level as practically possible. For the further development of safety, measures shall be implemented that can be considered justified considering operating experience and safety research and advances in science and technology."* These actions are further detailed and timely updated in STUK's regulatory guides that take into account e.g. new international requirements,

national and international experiences and new safety research results. STUK also makes a separate decision on how a new or revised YVL guide applies to the operating NPP's. These so called implementation decisions are used as references in the PSR process.

3. Lifetime management of NPP

Lifetime management of a NPP is a comprehensive set of continuous improvement measures that ensure safe and reliable operation of a NPP from design until its final removal from service. In this context it is not necessarily appropriate to speak about "lifetime extension" of a NPP when taking effectively care of "lifetime management". Lifetime management suits better to continuous and proactive control of NPP's reliability and safety which are reviewed during operation as well as in the periodic safety reviews. In principle NPP's also have a "design lifetime", meaning a minimum lifetime guaranteed by the vendor in the main contract (e.g. 60 years for Olkiluoto unit 3). In Finland the design lifetime is, however, not a regulatory limit and not mentioned in the operating licences. First of all it is important that adequate safety level is demonstrated periodically and much earlier than when approaching the expired "design lifetime".

General principles of lifetime management are related to maintaining the safety and reliability of the NPP operation. This is linked to the need for:

- Minimising thermal and mechanical loading transients (shut down, start up, power changes) with gentle operation.
- Avoiding the effects from chemical impurities causing corrosion of the primary and other equipment
- Providing regular and efficient maintenance and modifications
- Monitoring the condition and reliability of equipment by means of periodical testing and inspections
- Repairing or replacing on time all deteriorating or unreliable equipment that are important for safety or reliable operation
- Keeping record and analysing equipment performance

Lifetime management also must consider the possibilities for upgraded safety requirements and how to follow the principle of continuous safety improvement. Lifetime management also includes maintenance of skills, knowledge and tools

of the operating organisation. This involves continuous training of personnel, improvements of operational procedures when seen appropriate, keeping plant documentation updated and consistent with the actual plant situation, and ensuring availability of adequate knowledge on the key design features of the main equipment.

A similar approach of lifetime management practice is prescribed also in the WENRA (Western European Nuclear Regulators' Association) harmonisation principles where it is called ageing management [5]. It is thus expectable that the regulators committed to the harmonisation of WENRA work will benefit from common requirement basis for lifetime management. Ageing management is instructed also in IAEA Safety Guide NS-G-2.12 [4]. Also presently ongoing YVL guide renewal process includes a separate guide preparation for national requirements on ageing management.

4. Periodic safety review

Periodic Safety Review (PSR) of NPP's was developed in the 1990's. PSR is a comprehensive safety review that complements the ongoing safety assessment programmes by the owner and the day-to-day safety oversight by regulators. PSR is organised by the owner/operator but its contents need to be agreed with the regulatory body in advance. The regulatory body also makes its own assessment of the PSR results.

All national nuclear regulatory organisations in Europe have committed to require a PSR for their nuclear power plants. This commitment is part of the process driven by WENRA for harmonisation of safety for operating power reactors in Europe. The frequency of the PSRs is not specified in the WENRA documents, but 10 year interval is the generally adopted standard period.

The basic aim of PSR is to determine the safety status of a NPP in comparison with current safety standards and practices. It also reviews the adequacy of arrangements for maintaining plant safety until the next PSR or the end of plant lifetime. PSR also determines the safety improvements needed to resolve new safety issues.

PSRs enable the following issues to be addressed in a systematic way:

- Plants are subject to physical ageing – how do the gradual changes over an extended time period affect safety in a cumulative way?
- Review of safety documentation that has not been adequate or has not been updated properly during operation

- NPP has been built to fulfill older safety standards; comparison to current safety standards will be made
- Improved inspection and analytical techniques have become available
- External conditions for NPP have changed, e.g. more competitive markets, reduced availability of technical support services and suppliers for spare parts
- Impact of changes in management practices to the safety culture.

PSR is an important process to provide also the regulator with confidence that the plant is safe and is likely to remain in safe mode until the next review (being also subject to the outcome of day-to-day regulatory oversight). PSR provides also the NPP licencee with improved confidence to produce electricity: the regulator is not likely to require major additional expenditure on safety enhancements until the next PSR – unless new risks will be identified from future operating experience.

It is also becoming increasingly necessary to publicly justify that NPP's are acceptably safe. This particularly applies to the local population living in the vicinity of a NPP, national population and governments, the international community as well as the financial institutions. PSR is a useful tool also for these purposes.

PSR may be a part of the licence renewal process or a review of its own. Many countries have a practice to issue an operating licence for a limited time, typically for 10 years. In these circumstances it has been found practicable to require a PSR as a condition to licence renewal. Documentation required for this process, explicitly indicated in the national legislation, may, however, include similar elements as PSR documentation given in the IAEA safety standards [3]. It is therefore advisable to coordinate the PSR activity with other national legislation and avoid overlapping with excessive writing work.

According to the IAEA transmitted information on PSR experience, 50–150 person years can be allocated on PSR only. These figures do not include work needed for plant specific PSA and renewed deterministic safety analyses. The need for resources is, however, very much dependent from the context of PSR: a large part of preparatory work can be done outside PSR, significantly reducing the resources dedicated directly to PSR. The PSR contains so called safety factors as follows [3]:

- Plant
  - Plant design
  - Actual condition of systems, structures and components
  - Equipment qualification
  - Ageing
- Safety analysis
  - Deterministic safety analysis
  - Probalistic safety analysis
  - Hazard analysis
- Performance and feedback of experience
  - Safety performance
  - Use of experience from other plants and research findings
- Management
  - Organization and administration
  - Procedures
  - The human factor
  - Emergency planning
- Environment
  - Radiological impact on the environment.

Finally a global safety assessment is derived from the above factors. This gives an overall assessment of the NPP safety, with results obtained from the individual safety factors, including agreed corrective actions and/or safety improvements.

The PSR typically proceeds as described in Figure 1. As a starting point there are arrangements between the operating organisation and regulator on the scope and set of requirements for the specific PSR. After the review procedure there follows an overall approval of an integrated management programme of the corrective actions.

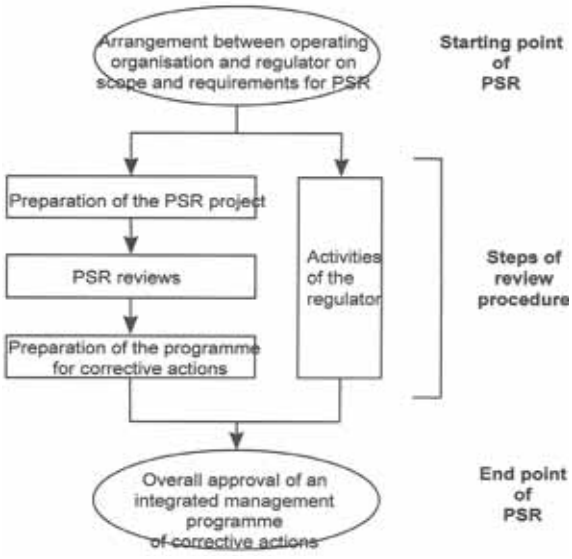

Figure 1. Flowchart of the PSR process [3].

The implementation of a PSR has been noticed to bring about a number of benefits that can be classified as follows:

- Common benefits, PSR:
  - results in safer and more reliable NPP and gives greater confidence in the safety of future operation
  - is an unique opportunity for the new generation of experts to get a deep and comprehensive view on NPP design bases and safety issues.
- Operator's benefits, PSR:
  - ensures updating / upgrading of plant documentation
  - provides technical and legal basis for safety improvements, continued long-term operation, possibly a license renewal
  - gives more reliable input for plant life time management, including support to investment decisions
  - identifies possible life limiting factors.
- Regulator's benefits, PSR:
  - is a reliable instrument for verifying present safety and providing assurance for future (10 years) safety.

According to experience from the Finnish NPP's, it seems evident that PSRs at 10 years intervals are effective measures to assess plant safety. In this context it should be also noted that the plants are subjected to day-to-day regulatory oversight and control during operation. It is also required that the plants shall have a continuous ageing management programme to indicate plant condition during operation and when approaching the end of the operating licence period. When considering renewal of operating licence, it is important to update all safety related analyses and ageing management plans for the new plant age.

5. Summary

The presentation provides a general view to lifetime management issues of operating nuclear power plants. The principles for safety assessment are briefly reviewed from the regulatory point of view. The features and role of the periodic safety review (PSR) process are described with objectives and realisation. Some experiences from PSR's are also addressed in brief.

Acknowledgement

The author is grateful to Prof. Jukka Laaksonen, Mrs. Kirsi Alm-Lytz and Mr. Petri Vuorio from STUK for technical information and co-operation.

References

1. Ydinenergia ja Suomi (Nuclear Energy and Finland). Suomen Atomiteknillinen Seura, 2010. 28 p.

2. YVL 1.1. Ydinlaitosten turvallisuuden valvonta. (Regulatory control of safety at nuclear facilities), 10.2.2006. 20 p.

3. IAEA Safety Guide NS-G-2.10. Periodic Safety Review of Nuclear Power Plants, 2003.

4. IAEA Safety Guide NS-G-2.12. Ageing Management for Nuclear Power Plants, 2009.

5. WENRA Reactor Safety Reference levels. Western European Nuclear Regulator's Association. Reactor Harmonization Working Group, January 2008.

Key performance indicators in plant asset management: hype, burden or real help?

Alexandar Jovanovic and Jörg M. Bareiß*
Steinbeis Advanced Risk Technologies, Stuttgart, Germany
*EnBW, Stuttgart, Germany

Abstract

The paper tackles the increasing role and use of indicators (e.g. the key performance indicators, KPIs) in asset management in power and process plants, in particular for risk and safety management (safety performance indicators, SPIs), inspection, maintenance, emerging risks analysis and aging management. The two main aspects of the use of indicators are monitoring of performance (e.g. of a single unit) and benchmarking (e.g. among different units).

The basis for the considerations presented in the paper are several international projects in the field, showing that the main issue in the field is not and cannot be just the introduction of new indicators as such. They deal with the principles of establishing indicators, establishing generally accepted indicators (goal "globally accepted" indicators), creating of "repositories" of indicators in industry and respective tools. The repository/tool developed in the EU project iNTeg-Risk is presented in more detail.

The main proposed criteria for successful introduction are the acceptance, transparency and clear added value, e.g. when the indicators help in finding solutions for the issues where the conventional analysis, e.g. the one based on engineering models and analysis is too expensive, complex or simply unavailable.

Three practical cases are briefly shown in the paper: one for the improved asset management in a refinery, one for the identification of indicators helping to deal with emerging risks (how to identify them and how to assess risks of a new technology) and one for the implementation of a complex aging management program for industrial plants.

1. Introduction

Generally speaking, the Key Performance Indicators (KPIs) are metrics used to quantify objectives to reflect strategic performance of an organization, unit, plant or system. In the last two decades they have been permanently gaining importance, because they often provide the only practicable and/or suitable way to "measure things difficult to measure". So for instance, KPIs are frequently used to "value" difficult to measure activities such as the benefits of leadership development, engagement, service and satisfaction. KPIs are typically tied to an organization's strategy (as exemplified through techniques such as the Balanced Scorecard). They help an organization to measure progress towards their organizational goals, especially toward difficult to quantify knowledge-based processes and, thus, become a key part of a measurable objective (e.g. safety levels – Figure 1).

The indicators can be defined formally (e.g. [1] as "measured characteristics or a set of characteristics of a phenomenon, according to a given formula, which assess the evolution" (with a note saying "Indicators are related to objectives").

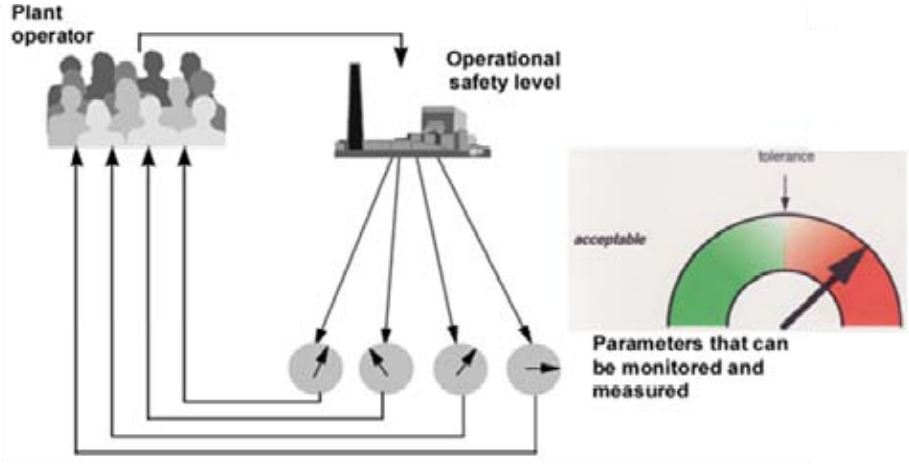

Figure 1. Industrial plants as source of industrial risks.

In the area of power plant maintenance, the trend of increased use of KPIs has resulted in, e.g., European standard [1] providing Maintenance KPIs to support (company/plant) management in achieving maintenance excellence and utilize technical assets in a competitive manner. Newer EU standardization documents

such as CWA 15740 [2] or [3], preceding research results (e.g. [5] and [6]), national standards and recommended practices (e.g. [7], [8], [9] and [10]) or industrial guidelines (e.g. [11], [12] and [13]) include also the inspection and maintenance relevant KPIs involving risk aspects. On the application level KPIs are directly included also in the respective software tools (e.g. such as [14] and/or [15]).

The majority of these indicators apply to all industrial and supporting facilities (buildings, infrastructure, transport, distribution, networks, etc), but in this paper primarily those used in or relevant for Plant Asset Management will be considered more in detail, with a wish to check if they real help or just hype/burden.

As in other areas of application of KPIs, also the KPIs in plant asset management are used to:

a) measure the status
b) compare (internal and external benchmarks)
c) discover indicators, diagnose and analyze strengths, weaknesses and risks
d) identify objectives and define targets to be reached
e) plan improvement actions
f) continuously monitor performance and/or measure changes over time.

Benchmarking and monitoring (items b and f, above) are those of particular interest in big companies, which typically, is the case of power plant owners. Identification of indicators, diagnosis and analysis strengths, weaknesses and risks (item c above) is of particular interest for the new technologies, e.g. where historical data are not (yet) available and as such the KPIs are one of the key elements in the R&D projects dealing with risks of new technologies, such as, e.g., iNTeg-Risk ("Early Recognition, Monitoring, and Integrated Management of Emerging, New Technology related Risks") project [16].

In iNTeg-Risk project KPIs are one of the cornerstones of the work on establishing the consolidated EU response to the risks related to the development and use of new technologies, such as nanotechnologies, carbon-capture sequestration, use of unmanned devices in industry, etc. For the 17 selected technologies, chosen as a target for the project, a common concept (framework) will be developed and tested by a group of over 80 leading European partners and KPIs will play a pivoting role in this process.

2. KPIs and SPIs; Lagging and leading indicators

If/when KPIs are tackling the safety issues and major hazards they are often labelled as “safety performance indicators” (SPIs, see e.g. [17], [18], [19] or [20]). In that sense, SPIs can be considered as a subset of KPIs, and are treated so in this paper. In practice, the two terms are sometimes used as synonyms, probably due to the fact that that all KPIs and SPIs share a common idea: manage the process and prevent adverse events by monitoring indicators, in case of SPIs, prevent hazards, as shown in Figure 2. Both KPIs and SPIs are essentially used to help find answers to the questions like:

a) Diagnosis: What can go wrong?

b) Analysis: What kind of protection is in place, can one do in order to prevent it?

c) Monitoring: How can one be sure that the plants, people processes operate as intended?

d) Mitigation, improvement, evergreening: How can one improve the operation of plants based on and using the indicators? How do multiple plants/systems compare to each other?

In the concept of indicators the terms “lagging” and “leading” have been well established, and they mean:

Leading: Indicators from active monitoring, requiring a routine systematic checks that key actions or activities are undertaken as intended; measures of process or inputs essential to deliver the desired (safety) outcome.

Lagging: Indicators from reactive monitoring requiring the reporting and investigation of specific incidents and events to discover weaknesses, the incidents or events do not have to result in major damage or injury or major problem (e.g. loss of containment), providing that they represent a failure of a significant control system which guards against or limits the consequences of a major incident; lagging indicators show when the desired safety outcome has not been achieved.

Up to this point virtually all systems of indicators agree and provide, for own particular area of application, a significant amount of very useful information and hints about

a) principles of defining indicators
b) building hierarchies of indicators
c) examples or even example sets applicable in different cases.

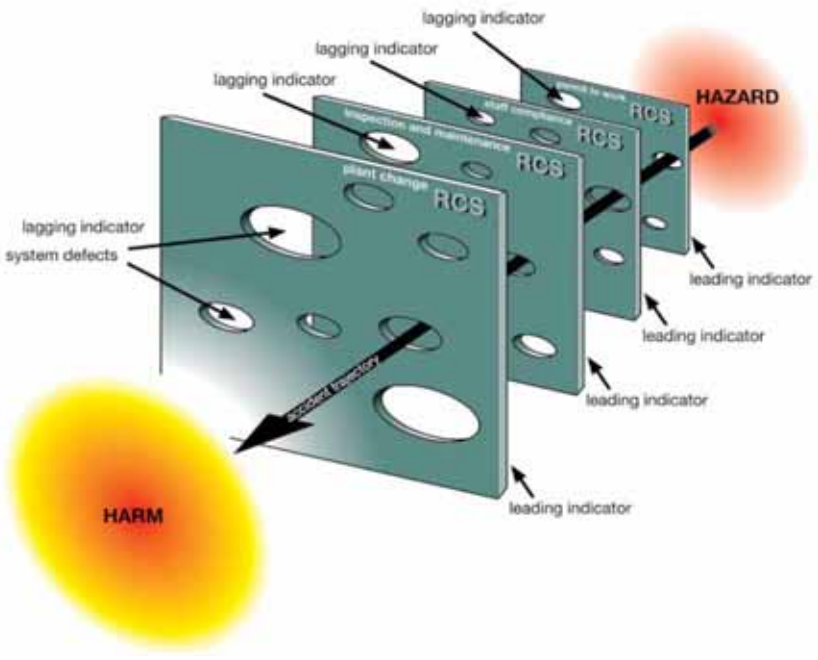

Figure 2. Preventing unwanted/adverse event by looking at leading and lagging indicators – as from [19], original figure from Managing the Risks of Organizational Accidents James Reason 1997 Ashgate Publishing Limited.

a) the indicators dealing with safety performance (SPIs) need a large degree of acceptance and agreement/consensus among many stakeholders, and in their quintessence represent the "common denominator" of the requirements of many parties; it is a natural tendency that the number of these indicators is kept low and their changes often subdue to a complex agreement process;

b) the indicators dealing with production performance (KPIs) within a company often need just the company management decision – their number and definition grow or shrink according to the short-term needs of the company.

The above situation is schematically depicted in Figure 3.

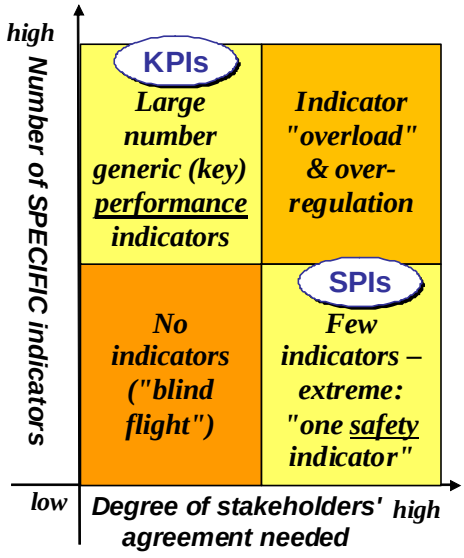

Figure 3. Measuring performance vs. measuring safety.

In fact, large number of indicators used for performance monitoring and benchmarking (KPIs in Figure 3) in other than safety areas, is a natural consequence of the diversity of industrial plants and operating conditions. Hence, in this area, the main criteria for developing indicators are

a) Transparency (it must be cleared what is measured and how)

b) Comparability (it should be possible to compare plants/systems/processes despite their diversity) and

c) Economy of use (introducing KPIs should result in savings and performance improvement).

On the contrary, for SPIs,

a) Acceptance (by possibly many stakeholders)

b) Possibility to implement same indicators in possibly many different types of plants, and

c) Elimination of possible ambiguities in definition, use and interpretation are essential (Figure 4).

In terms of real industrial use it means that the need for finding consensus about the definition, use and interpretation of indicators is reduced to a relatively small number of indicators – e.g. to 5-20 “core indicators” in most of the systems of

indicators referenced here. Number of general KPIs is nowadays well beyond 100 in most of the systems (Figure 5). Thus, the distinguishing between what is needed to monitor safe operation (SPIs) and what is needed to monitor efficient operation of a plant, process or parts thereof is very much simplified.

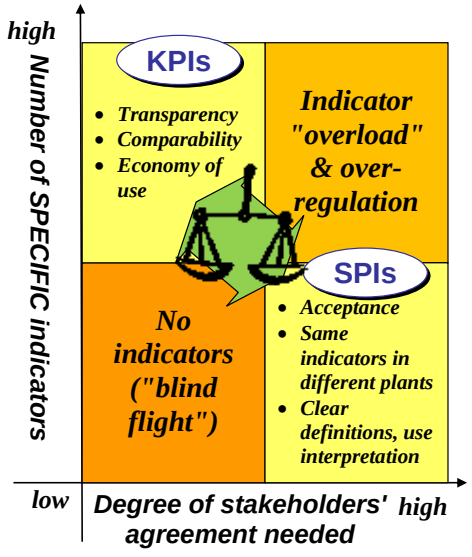

Figure 4. Essential characteristics of general (key) performance indicators vs. safety performance indicators.

As an example of "core indicators" one could take, e.g., the set of indicators proposed by Cefic (see http://www.cefic.org/Files/Publications/rapport_annuel2008.pdf), showing that the "core" is reduced to unintended releases of substances or energy to be reported to top management if (as a part of the so-called LoPC reporting – loss of primary containment):

a) a lost time incident of >1 day was suffered, or
b) a fire or explosion with direct cost > € 20,000 occurred, or
c) if the releases exceed the following thresholds[1]:
- GHS toxicity category 1 + 2 (or T+, T)[2] [3]: 5 kg
- Any other hazardous substance: 100 kg
- All other substances: 2 000 kg.

[1] Lower thresholds already defined might apply and stay in place
[2] As long as GHS categories are not available
[3] Use classification readily available with material safety data sheets

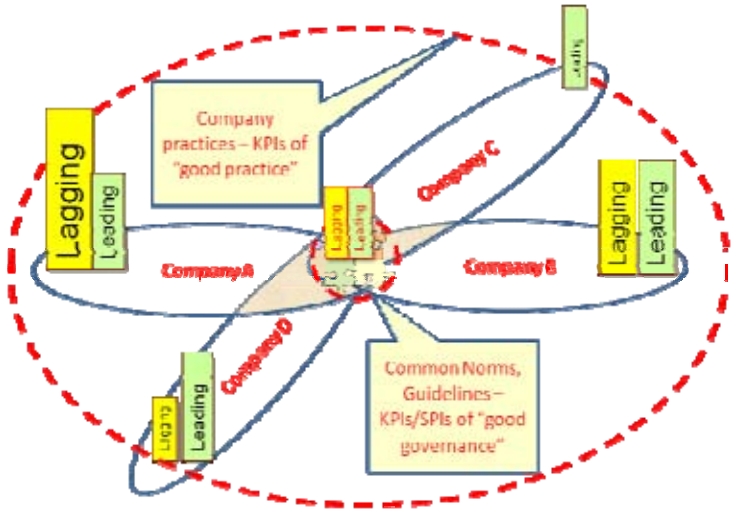

Figure 5. Essential characteristics of general (key) performance indicators vs. safety performance indicators.

A broader list of (17) indicators in the same system includes the following indicators:

Safety and occupational health

1. Number of fatalities (for employees and contractors)
2. Lost time injury frequency rate (for employees and contractors)

Environmental protection, including climate change

3. Hazardous waste for disposal
4. Non-hazardous waste for disposal
5. Sulphur dioxide
6. Nitrogen oxides
7. Volatile organic compounds
8. Carbon dioxide
9. Nitrous oxide
10. Hydrofluorocarbons
11. Chemical oxygen demand
12. Phosphorus compounds
13. Nitrogen compounds

Use of resources

14. Use of energy, specific

15. Energy consumption
16. Water consumption

Transport

17. Transport incidents.

In other words the SPIs are just the “top of the pyramid (of indicators)” shown in Figure 6.

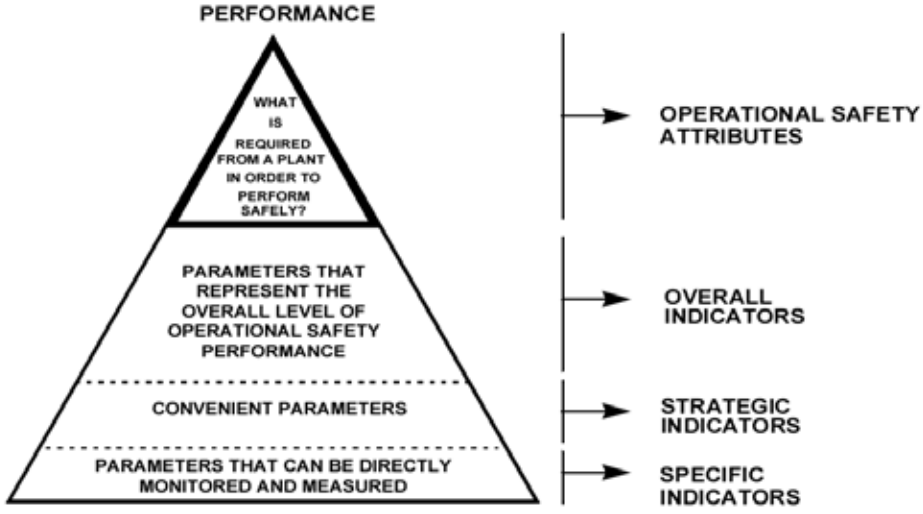

Figure 6. The “pyramid of indicators” – the basis of the pyramid reflects also the number of indicators available/used.

3. Technical solution

The solution proposed by here looks for a good balance between the two groups of indicators shown (Figures 4 and 5). It follows the principle that the set of indicators needed to help reaching goals set in chapter 2 (diagnosis, analysis, monitoring, benchmarking...) is always a matter of consensus and prior agreement, no matter if such an agreement is made at the level of a company or a the level of an industrial association or at the state level. Hence, in today's situation where many large companies operate globally or at least internationally, one should be able to “measure” the performance of a plant according to different metrics.

As proposed in [21], in order to achieve the above goal, one should:

Step 1. Collect and manage the indicators she/he wants to use

Step 2. Select those applicable for given conditions (e.g. given type of a plant in a given country)

Step 3. Create a "check-list" based on the indicators above – e.g. as a basis for monitoring or benchmarking

Step 4. Apply the above the list and

Step 5. Show/represent the results conveniently.

In the case of the system proposed here (e.g. in the software system proposed by Steinbeis Advanced Risk technologies, Germany), the above has lead creation of a large database serving as a basis for the KPI web-based system enabling analyses described below. The system currently (spring 2010) contains nearly 2,000 indicators collected from different sources. A subset of them, selected/filtered according to different criteria can be used to create the "check-lists" which can then be used as described in the examples below (steps 2 to 4, step 1 is done by creating the web system).

The concepts of the integrated solution and its use in iNTeg-Risk project [16] are presented in Figure 7.

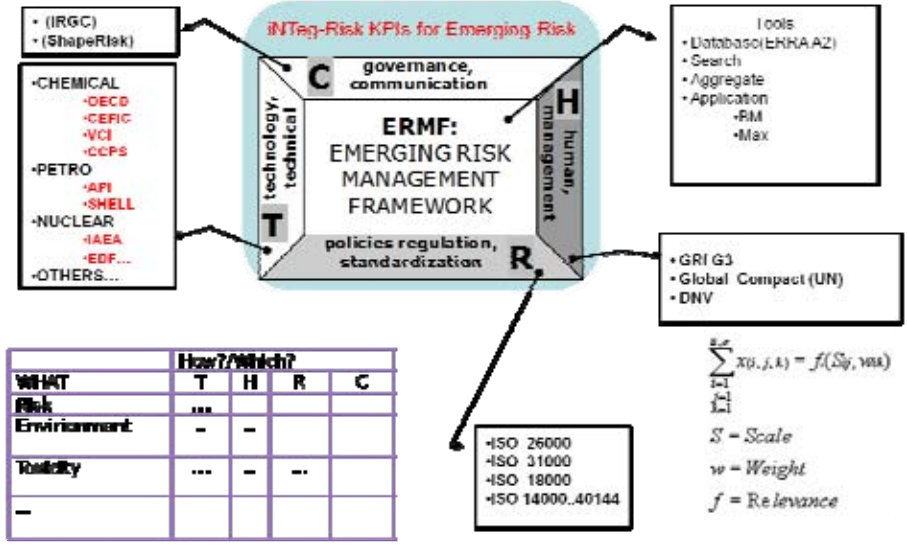

Figure 7. Use of the KPI database in iNTeg-Risk project.

4. Application results

4.1 Benchmarking and performance monitoring of refinery plants

In this application the set of API indicators [8] was preselected and the corresponding check-list created and applied. The included over 100 indicators covering following main topics:

1. Leadership and Administration
2. Process Safety Information
3. Process Hazard Analysis
4. Management of Change
5. Operating Procedures
6. Safe Work Practice
7. Training
8. Mechanical Integrity
9. Pre-Sartup Safety Review
10. Emergency Response
11. Incident Investigation
12. Contractors
13. Assessment

An example of more detailed indicators looked at in single chapters is shown below:

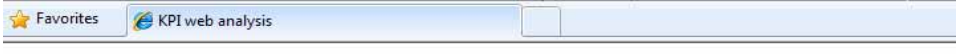

Leadership and Administration

IndicatorFormula	Max	plant1	plant2	plant3	plant4
Does the organization at the corporate or local level have a general policy statement reflecting management's commitment to Process Safety Management, and emphasizing safety and loss control issues?	10	7	8	4	3
Is the policy contained in manuals?	2	2	1	2	1
Is the policy posted in various locations?	2	2	2	2	2
Is the policy included as a part of all rule booklets?	2	1	2	2	2
Is the policy referred to in all major training programs?	2	2	1	2	1
Is the policy used in other ways? (Describe)	2	2	2	2	2
Are responsibilities for process safety and health issues clearly defined in every manager's job description?	10	8	7	4	6
Are annual objectives in the area of process safety and health issues established for all management personnel, and are they then included as an important consideration in their regular annual appraisals?	15	14	3	8	7
What percentage of the total management team has participated in a formal training course or outside conference or seminar on Process Safety Management over the last	10	4	6	8	9

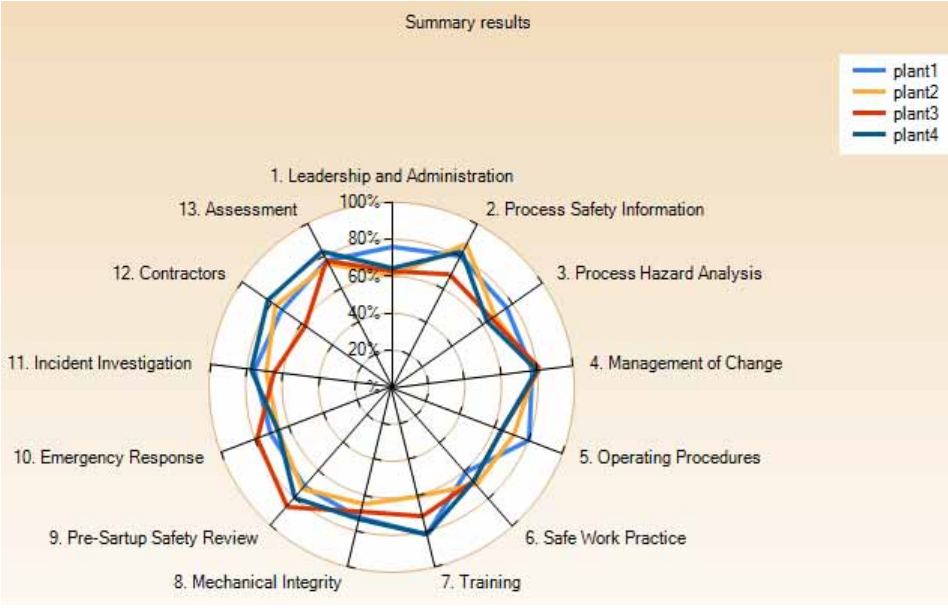

Figure 8. Application of the concept in a benchmarking exercise for 4 refinery plants.

4.2 Assessing (emerging) risks of new technologies

In iNTeg-Risk project [22] the concept has been widely applied to a range of applications (so called ERRAs, see [23]) including:

ERRAS Group A

new materials, technologies and products (e.g. nano, H_2, CO_2, advanced engineering materials, renewable energies, underground storage)n

ERRAS Group B

new production processes and management (e.g. unmanned aerial surveillance, outsourcing, resilient IT safety systems)

ERRAS Group C

complex industrial systems and networks (e.g. integrated HSSE, on-line risk monitoring, use of bio-inspired models, virtual plants/reality), and new global/EU/local **emerging risk policies** (e.g. EU safety legislation for SMEs and non-EU European countries, regional interaction nature-technology (NaTech).

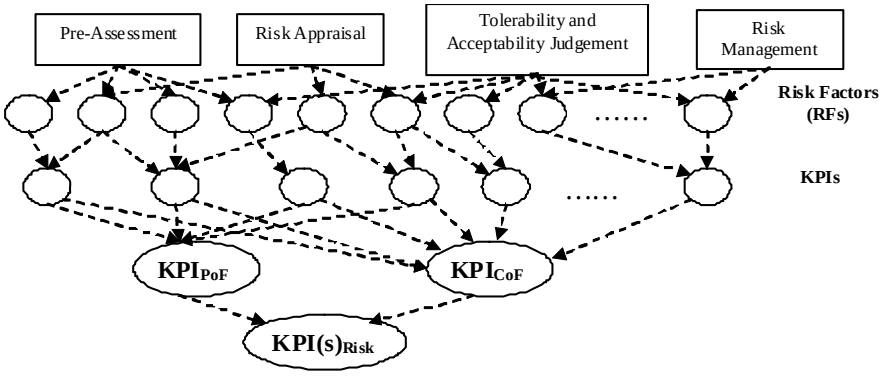

Figure 9. The hierarchy of KPIS used in iNTeg-Risk projects for assessing risks.

Setting up a hierarchy of application specific KPIs (Figure 9) it was possible to create a system for comparison of risks in different types of new technology related applications being considered in the project (Figure 10), PoF and CoF representing likelihood of occurrence and impact of a risk scenario, respectively).

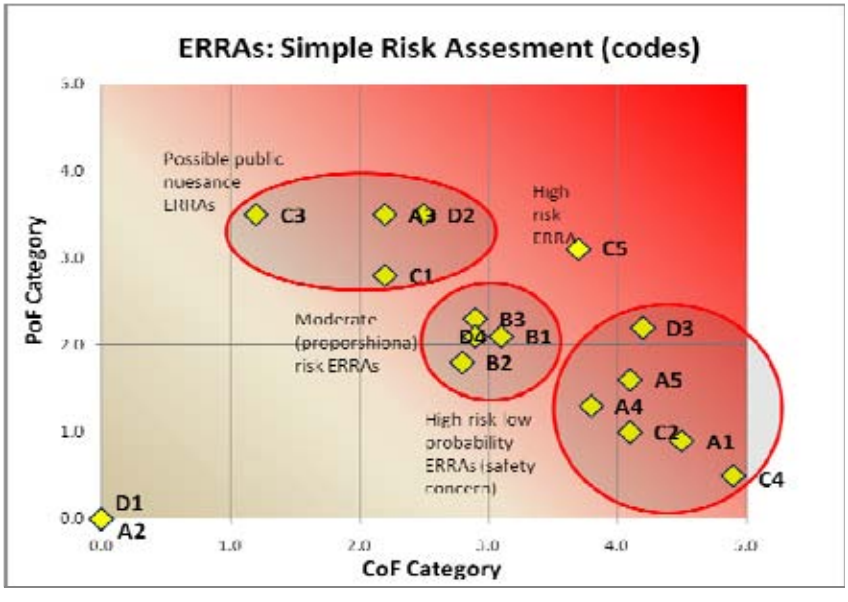

Figure 10. Applications considered in iNTeg-Risk: Thanks to KPIs the risks can be compared and clustered.

4.3 Optimizing aging management programs for large industrial plants

In 2009 a large national program on management of aging of large industrial plants has been launched by the French Ministry of Ecology, Energy, Sustainable Development and Land Use Planning (MEEDDAT) [24] with a goal to study and manage aging in industrial facilities and mitigate major risks. As part of this action plan, a list of recommendations partly present in regulatory texts, standards and professional guidelines, partly yet to be developed, is used as a basis for analysis and comparison of practices in French and EU industry. The plan contains 38 measures grouped into six categories, namely:

- General activities related to modernization of safety management systems in order to improve considerations related to the problem of aging of plants and components
- Civil engineering
- Storage tanks
- Transportation pipelines
- Vessels and piping (pipelines inside the industrial site)
- Safety instruments.

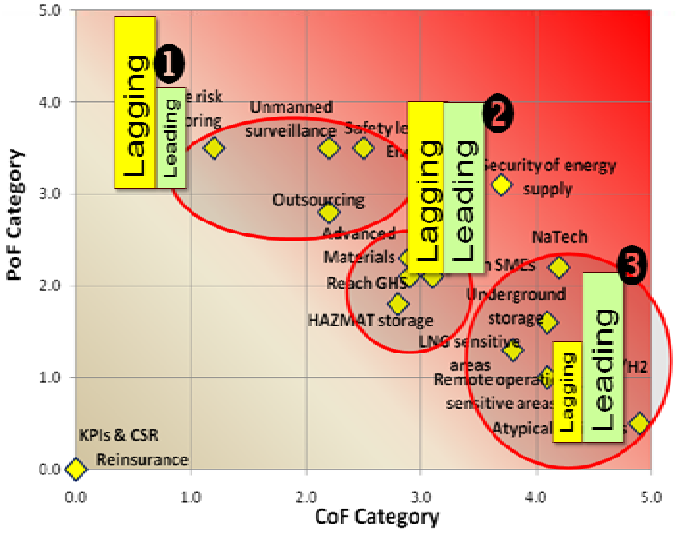

Figure 11. Use of different types of KPIs in iNTeg-Risk applications (the 3 clusters of KPIs are explained in Figure 10).

Current version of the plan [24]does not provide provisions related to comparison of the results of the measures related to the application of the program, but it will be proposed as the next step in May 2010 [25]. The proposal will be to measure the success of implementation of the plan by means of a set of indicators developed on the basis of those proposed for maintenance in [1], defining 3 main groups of indicators, namely

1. economic indicators
2. technical indicators and
3. organizational indicators,

divided in 3 hierarchical levels, the indicators from Levels 2 and Level 3 helping to define those of Level 1 (Figure 12).

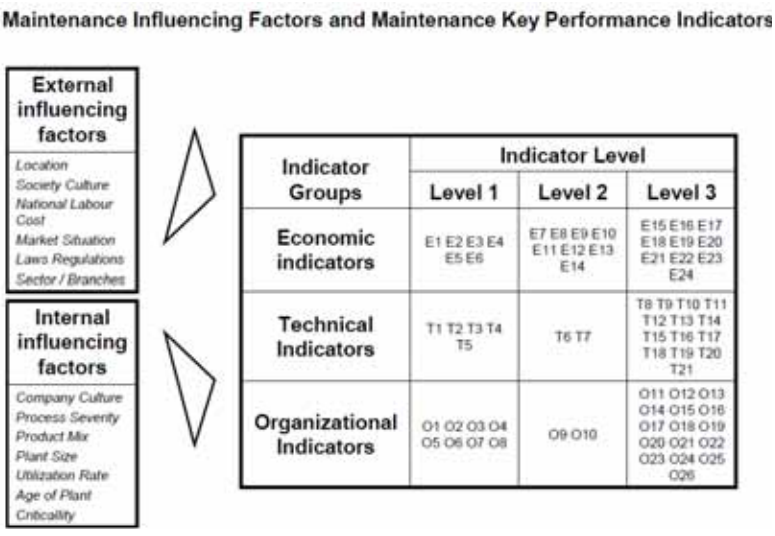

Figure 12. Hierarchical organization of KPIs in [1].

The extension of the set will cover primarily aging specific issues, primarily technical ones.

5. Conclusions: Open issues

The consent about the general and practical usefulness of key performance indicators is often challenged by the factors like

a. lack of internationally recognized and accepted references and de facto standards,

b. lack of consistency between higher-level indicators (e.g. those dealing with corporate responsibility or business continuity) and safety related ones,

c. differences, incompatibilities and, often, respective exclusion of similar indicators used in different branches of industry (e.g. chemical industry vs. nuclear industry vs. IT), or even single industrial applications within the same branch – particular difficulties are present in the area of "new technologies" (e.g. nano, H_2, CO_2, renewables, …),

d. gap between the (widely agreed) theoretical concept, on one side, and practical application related publicly available agreed "examples of good practice", on the other side,

e. "high profile" of the performance indicators related activities, often considered to be privilege of big and rich stakeholders only, in a way a luxury which an SME (small/medium enterprise), for instance, cannot afford.

Efforts of organizations and bodies like OECD, Cefic or HSE have largely improved the situation in terms of guidelines and anchoring of basic references, but a lot remains to be done. One of the areas would certainly be the area of education: inclusion of the KPIs/SPIs related issues into the respective, risk/safety related academic and professional education is still to be done.

References

1. BS EN 15341:2007 Maintenance – Maintenance key performance indicators. BSi, UK 2007.

2. CWA 15740:2008 "Risk-Based Inspection and Maintenance Procedures for European Industry", CEN EU 20008.

3. BSi PAS 55 – the British Standards Institution's (BSI) Publicly Available Specification for the optimized management of physical assets. BSi, UK 2008. http://pas55.net/.

4. RIMAP. European R&D project RIMAP "Risk-Based Inspection and Maintenance Procedures for European Industry". Project Number GIRD-CT-2001-03008, EU 2002.

5. Jovanovic, A. Risk-based inspection and maintenance in power and process plants in Europe. Nuclear Engineering and Design, 2003. Vol. 226, pp. 165–182.

6. Jovanovic, A. Overview of RIMAP project and its deliverables in the area of power plants. International Journal of Pressure Vessels and Piping, 2004. Vol. 81, pp. 815-824.

7. ANSI/API (2000). RP 580 – Risk-Based Inspection, American Petroleum Institute API, USA 2002; www.api.org/publications/.

8. API (2000). API 581 – Base Resource Document – Risk Based Inspection, American Petroleum Institute API, USA 2000, www.api.org/Publications/.

9. ASME (2003). ASME CRTD – Vol. 41, "Risk-based Methods for Equipment Life Management: An Application Handbook", ISBN 0791835073, ASME International, New York USA 2003; www.asme.org/Publications/.

10. Wintle, J. B. et al. Best practice for risk based Inspection as a part of plant integrity management. Health and Safety Executive HSE Books CRR 363/2001, HSE, UK 2001; www.hsebooks.com/Books/, ISBN 0717620905.

11. EEMUA. Risk Based Inspection - Guide to Effective Use of the RBI process. Engineering Equipment and Materials Users Association EEMUA, UK, 2006. Publication 206. www.eemua.co.uk/publications.htm#cat ; ISBN 0-85931-150-3.

12. VGB-R506 Condition Monitoring – Guideline Condition Monitoring and Inspection of Components of Steam Boiler Installations and Water or Steam Bearing High-pressure Pipes. VGB, Essen, Germany 2008.

13. Bareiß, J. M. Methoden der Zustandsüberwachung - Ergebnisse aus der praktischen Anwendung an Komponenten von Dampfkesselanlage und FD-/HZÜ-Rohrleitungen. VGB-Workshop Entwurf VGB-Richtlinie 506, April 2008.

14. iRiS. iRiS-Power – integrated RISK MANAGEMENT SYSTEM for Power plants. Steinbeis Advanced Risk Technologies, Stuttgart, 2009.

15. iRiS. iRiS-Petro – integrated RISK MANAGEMENT SYSTEM for Petrochemical plants. Steinbeis Advanced Risk Technologies, Stuttgart, 2008.

16. iNTeg-Risk. iNTeg-Risk – Early Recognition, Monitoring and Integrated Management of Emerging. New Technology Related Risks (2008-2013). EEU FP7 project No. CP-IP 213345-2, EU 2008, www.integrisk.eu-vri.eu.

17. OECD. Guidance on Developing Safety Performance Indicators related to Chemical Accident Prevention, Preparedness and Response; Guidance for Public Authorities and Communities, Public, Environment Directorate, OECD Environment, Health and Safety Publications Series on Chemical Accidents No. 18. Organisation for Economic Cooperation and Development, Paris 2008.

18. OECD. Guidance on Developing Safety Performance Indicators related to Chemical Accident Prevention, Preparedness and Response; Guidance for Industry, Public, Environment Directorate, OECD Environment, Health and Safety Publications Series on Chemical Accidents No. 19. Organisation for Economic Cooperation and Development, Paris 2008.

19. HSE. Developing process safety indicators – A step-by-step guide for chemical and major hazard industries. HSE, UK, 2006. http://www.hse.gov.uk/pubns/priced/hsg254.pdf. ISBN 978-0-7176-6180-0.

20. CCPS. Process Safety - Leading and Lagging Metrics: You Don't Improve What You Don't Measure, CCPS, USA, 2008. http://www.aiche.org/uploadedFiles/CCPS/Resources/KnowledgeBase/%20CCPSR11Readers.pdf.

21. Jovanovic, A. Practical steps towards sustainable use of safety performance indicators in the EU industry (keynote lecture). ESREL Conference 2008, Valencia, Spain.

22. Jovanovic, A. Conference Book of the 1st iNTeg-Risk Conference. Stuttgart , June 2009, EU-VRi, Germany.

23. iNTeg-Risk. FP7 Project iNTeg-Risk Early Recognition, Monitoring and Integrated Management of Emerging, New Technology Related Risks, Annex I (DoW) to Grant agreement no. CP-IP 213345-2, 2008.

24. MEEDDAT. Plan de modernisation des installations industrielles: Prévenir les risques liés au vieillissement, dossier, Ministère de L'Écologie, de l'Énergie, du Développement durable et de la Mer en charge des Technologies vertes et des Négociations sur le climat, France, 2010.

25. ETPIS. ETPIS Technical Workshop "New challenges in Structural Safety in the context of the EU 2020 Strategy and EU Grand Challenges", Paris, May 31, 2010.

Statistical methods and materials characterisation

Kim R. W. Wallin, Academy Professor
VTT Technical Research Centre of Finland
Espoo, Finland

Abstract

Statistics is a wide mathematical area, which covers a myriad of analysis and estimation options, some of which suit special cases better than others. A comprehensive coverage of the whole area of statistics would be an enormous effort and would also be outside the capabilities of this author. Therefore, this does not intend to be a textbook on statistical methods available for general data analysis and decision making. Instead it will highlight a certain special statistical case applicable to mechanical materials characterization. The methods presented here do not in any way rule out other statistical methods by which to analyze mechanical property material data.

1. Introduction

A metallic material is not a continuum. It contains imperfections constituted by dislocation pile-ups, grains, precipitates and inclusions. For a macroscopically homogeneous material, these imperfections are approximately randomly distributed in the material, making the material microscopically inhomogeneous, but macroscopically homogeneous. However, often there is an additional variation in the material (weld beads, heat affected zones, texture, etc.) and then the material is more or less also macroscopically inhomogeneous. All the different microstructural features may affect the mechanical properties by causing scatter. The macroscopical inhomogeneity can often be accounted for by careful specimen sampling, but the microscopical inhomogeneity leads to fracture mechanism

specific scatter. In order to be able to assess the materials properties properly, knowledge of the nature of the scatter combined with some statistical methods are required, by which both the scatter due to microscopic inhomogeneity as well as those due to macroscopic inhomogeneity can be estimated.

Different tests will respond to the microscopic inhomogeneity differently. As a rule, the more local the event controlling the parameter is, the larger the scatter will be. In a normal tensile test, the whole specimen is loaded rather evenly and a large material volume is involved in the deformation process. This causes', the scatter in tensile properties generally to be small for macroscopically homogenous materials. In the case of e.g. fracture toughness, the situation is different. The material volume involved in the fracture process is much smaller than in a tensile test and in an extreme case, the fracture may be controlled by a single material imperfection in front of the macroscopic crack. This leads to a very pronounced micromechanism related scatter.

Any test result, belongs to one of three distributions, shown graphically in Figure 1. These probability distributions are f(x), P(x) and S(x). The first distribution f(x) is the probability density function. The second distribution P(x) = ∫f(x) is the cumulative probability distribution function and the third distribution S(x) = 1-P(x) is the survival probability distribution function.

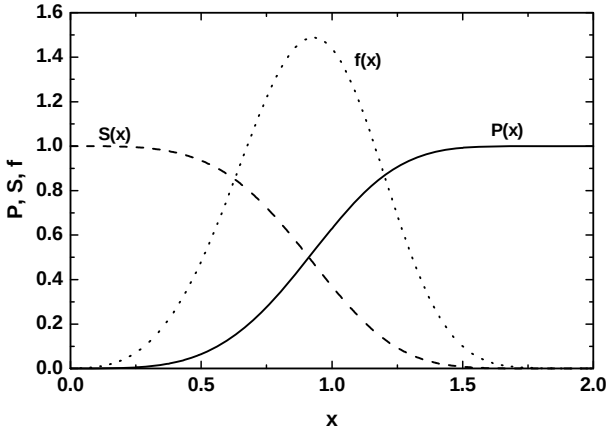

Figure 1. Graphical representation of the probability density function f(x), the cumulative probability distribution function P(x) and the survival probability distribution function S(x).

Material testing contains often some size related criterions for parameter validity. Any value exceeding the validity limit is usually disregarded from

further analysis. This leads to a censored data set. The problem is shown graphically in Figure 2, where an assumed probability density function is plotted. If all specimens produce valid results, the data describes the distribution function correctly and the result is the true cumulative probability distribution. If, however, part of the specimens yield invalid results, and the information from the invalid results is not included in the data base, the result will be an incomplete distribution, which will underestimate the true scatter, as shown in Figure 2. If also the lower tail of the probability density function is censored due to some validity requirement the apparent scatter is even less. This is shown in Figure 3. Any statistical analysis of incomplete distributions is erroneous, unless the information of the censored data is accounted for statistically. It is thus imperative to analyse censored data sets correctly. One such method will be presented here. The method is related to rank probability analysis and is applicable for data corresponding to a single variable (like constant temperature). The result is independent of assumed probability distribution form.

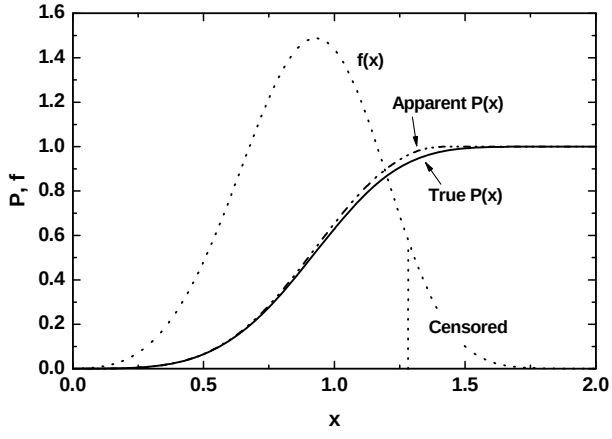

Figure 2. Example of effect of upper tail censoring on resulting apparent cumulative probability distribution if censoring is ignored in analysis.

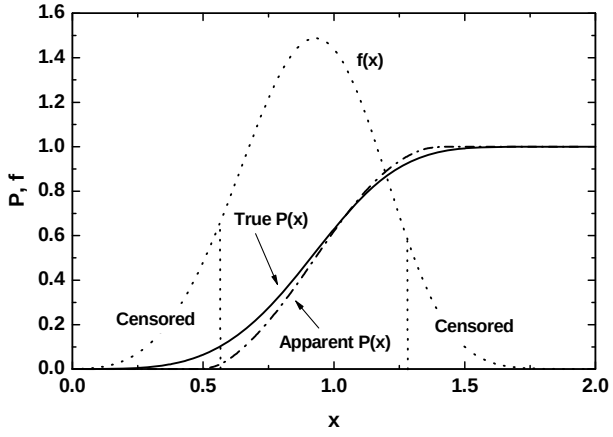

Figure 3. Example of effect of combined upper and lower tail censoring on resulting apparent cumulative probability distribution if censoring is ignored in analysis.

2. Some distribution functions

As mentioned before, different fracture micromechanisms are connected to different inherent statistical behaviour. The parameters describing different micromechanisms have specific distribution functions and require case specific evaluation procedures. Cleavage fracture initiation fracture toughness should not be assessed by the same statistical method as ductile tearing or creep.

The most well known statistical distribution is probably the normal distribution. This distribution is defined by only two parameters, the mean ($\bar{x}$) and the standard deviation (σ). An example of the normal distribution is given in Figure 4. It is a non-skewed distribution in that it shows a symmetrical scatter around the mean. The normal distribution has no asymptotic values, so that both positive and negative values are possible. In the case of mechanical properties, negative values are physically not possible, since a negative value would indicate instantaneous failure of a non-stressed structure. Thus, from a physical point of view, the normal distribution is not descriptive of the scatter in material properties. However, the macroscopic material variation and some measuring uncertainties related to the fracture toughness test itself can often be treated as being normally distributed.

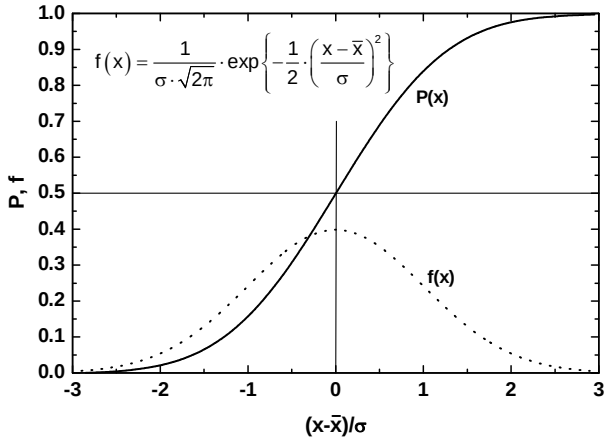

Figure 4. The normal distribution.

Mechanical properties are generally better described by probability distributions that have an asymptotic lower bound. Such distributions are e.g. the log-normal distribution, the Weibull distribution and other exponential distributions. All these distributions have in common that they contain a lower limit. Their scatter can be expressed in percentage, proportional to the mean value. The limit value is for the log-normal distribution generally zero, but the distribution can be modified to include also a minimum value larger than zero. The Weibull distribution is to its form quite similar to the log-normal distribution. It can also have a minimum value equal to zero or higher and it has the same number of parameters as the log-normal distribution (three parameters in the case of a limiting value larger than zero). However, the Weibull distribution is somewhat less flexible than the log-normal distribution. The Weibull distribution is theoretically a good distribution to describe events that are described by weakest link statistic. Thus, contrary to the log-normal distribution, there is a theoretical background of the distribution, relating it to a physical mechanism.

Usually test data sets correspond at any single condition to less than 30 results. Thus the sets represent small samples from a statistical view point. Small samples cannot describe the actual distribution accurately. One can state that, if the sample size is less than 30, no attempts to fit a specific distribution to the data should be made. Even if a good description of the data is obtained, the distribution can still be much in error. For small sample data sets, the only estimate with any accuracy is the estimate of the mean and to a lesser extent the standard deviation. This means that the test data normally cannot be used to

select the proper probability distribution. The distribution should be decided based on the physical nature of the fracture event, not what a small data set indicates. The above also means that the use of Bayesian statistics to analyze fracture toughness data is not very productive.

The focus of the following treatment is on simple statistical estimation methods suited for small data sets.

3. Rank probability estimation [1]

A popular way of analyzing intermediate size data sets visually is by rank probability statistics. Since all test results represent individual random probabilities, they follow the rules of order statistics.

When test results are ordered by rank based on e.g. toughness, they can be designated rank probabilities, which describe the cumulative probability distribution. The rank probability estimates are not real measured values, but estimates of the cumulative probability based on order statistics. Each data point corresponds to a certain cumulative failure probability with a certain confidence. This can be expressed in a mathematical form based on the binomial. The equation for the probability distribution of individual rank probability estimates can be expressed in the form of Equation (1).

$$P_{conf} = 1 - \sum_{j=1}^{i} \frac{n!}{(j-1)! \cdot (n-j+1)!} \cdot P_{rank}^{j-1} \cdot (1 - P_{rank})^{n-j+1} \quad (1)$$

P_{conf} is the probability that the rank estimate corresponds to the cumulative probability P_{rank}, n is the number of points and i is the rank number. Equation (1) can be used to calculate e.g. rank confidence estimates. The estimation requires the solving of P_{rank} for a specific P_{conf} and this makes the estimation somewhat cumbersome. An example of the rank probability estimate based on Equation (1) is presented in Figure 5 for a data set consisting of 10 values. The estimates corresponding to 5%, 50% and 95% confidence levels are plotted. The figure shows well the degree of uncertainty in the rank probability for small data sets. Due to the slight inconvenience in using Equation (1), people usually prefer to use simple approximations of the median (P_{conf} = 0.5) or the mean rank probability estimate. The most accurate analytical simple median rank estimate has the form given in Equation (2).

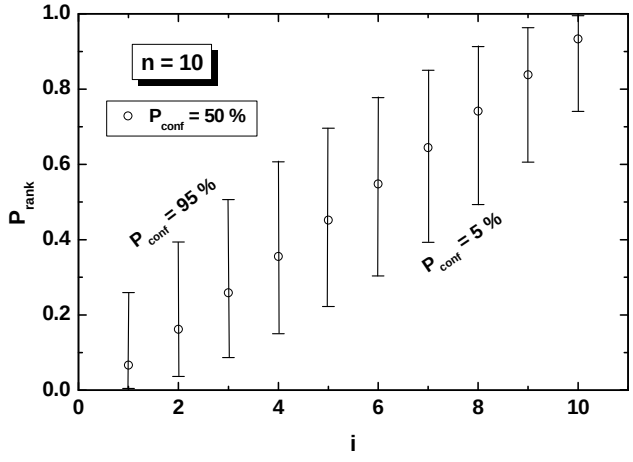

Figure 5. Example of rank probability estimates based on Equation (1).

$$P_{rank} = \frac{i - 0.3}{n + 0.4} \tag{2}$$

The median rank corresponds to P_{conf} = 0.5 in Equation (1) and therefore it is well suited to describe the median estimate combined with confidence bands. Other rank probability estimates like the one for the mean do not correspond to a specific constant P_{conf} value.

3.1 Censored rank probability

Equation (2) can only be used, as such, for data sets were all results correspond to failure. It can also be used with data sets where all values above a certain value has been censored e.g. due to non-failure or exceeding the measuring capacity limit, but in this case the data set size, n, must refer to the total data set including the censored data.

If the data set contains non-censored failure results at higher values than the lowest censored value, a method of random censoring (often called the suspended items concept) is needed. In this case the order number, i, in the rank estimation do not remain an integer. The increment in the order number, Δi_j, after censoring has the form of Equation (3a). This increment is used on all failures following a censored value until another censored value is reached. Then a new increment is calculated. This rank probability estimate for censored data sets refers only to the median rank estimate and it should not be used with other expressions.

$$\Delta i_j = \frac{(n+1) - i_{j-1}}{n+2-j} \tag{3a}$$

Instead of estimating the increment, the censoring expression can also be expressed directly in the form of the effective order number in the form of Equation (3b). The censoring parameter δ_j is zero for censored data and one for non-censored data. Even though Equation (3b) is used on all values, only the non-censored values may be used in the resulting analysis.

$$i_j = \frac{(n+1-j)\cdot i_{j-1} + (n+1)\cdot \delta_j}{n+1-j+\delta_j} \tag{3b}$$

An example of the use of Equations (3a and b) is given in Figure 6. It shows an exemplary data set containing 20 random numbers ordered by rank. Thus all results in this column are “valid”. The second data set shows the data after application of a random censoring criterion so that part of the data has now been censored. If the probability in the sensoring set was less than the probability in the first set, the probability in the second set was taken and the data was denoted as “censored”. The combined data was ordered by rank and Equation (3a) was used to calculate the value $i+\Delta i$, which was then used to estimate the median rank probability estimate referring to Equation (2). Before being affected by censoring, both estimates are of course identical. After censoring takes effect, the estimates deviate, but the deviation is only the effect of the uncertainty related to the rank probability itself. The trend in both data sets remains the same. Equation (3b) results in an identical estimate as Equation (3a) so it is up to the user to decide the preferred form. It is important to note that Equations (3a) and (3b) should only be used together with Equation (2), not other simplified rank probability estimates.

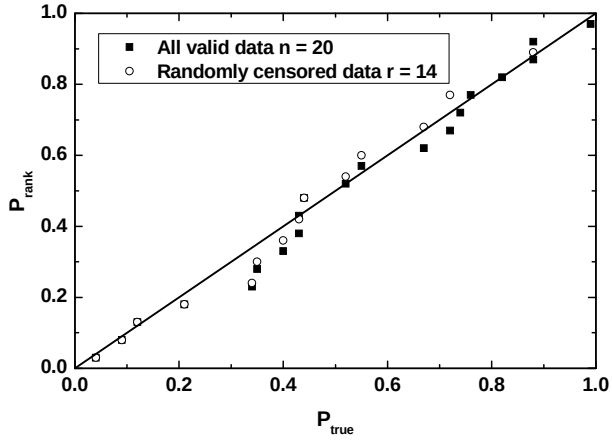

Figure 6. Comparison of rank probability estimates for all valid data and censored data.

3.2 Confidence bounds on rank probability

One disadvantage of the theoretical expression for confidence bounds, based on binomial theory, is that it can be applied only to specific data points not allowing for extrapolation to other probabilities outside the data point values. This reduces the applicability of the theoretical expression for graphic presentations. In order to achieve a good graphic presentation one must use some analytical approximations of the rank probabilities that can be extrapolated outside the data points. The analytical approximation equation for the median rank estimate provides a continuous presentation, but it does not provide any information about the confidence limits of the probability estimate. These limits have to be obtained from other expressions. Based on a numerical analysis of the theoretical rank estimate, an approximate analytical expression, for the 90% confidence limits, has been developed. The 90% confidence bounds, corresponding to lower 5% and upper 95% confidence limits, for the rank estimate can be obtained by solving the following set of equations for $P_{0.05\text{-}0.95}$ (Equations 4–7). It is important to note that only uncensored data affects the accuracy of the estimate. Thus, for censored data sets, n should be replaced by the number of uncensored data, denoted here as r.

$$\sqrt{\frac{n}{2}} \cdot \left(P_{0.5} - P_{0.05-0.95} \right) = \pm A \cdot \sqrt{P_e - P_e^2} \tag{4}$$

$$P_e = P_{0.5} - \sqrt{\frac{1}{2}} \cdot \left(P_{0.5} - P_{0.05-0.95} \right) \tag{5}$$

$$\text{For } P_e \le 0.5\text{: For } P_e \le 0.5\text{:} \quad A = \min \begin{vmatrix} 1.162 - 0.342 / n \\ 0.82 + P_e \cdot \ln(n) \end{vmatrix} \tag{6}$$

$$\text{For } P_e > 0.5\text{: For } P_e > 0.5\text{:} \quad A = \min \begin{vmatrix} 1.162 - 0.342 / n \\ 0.82 + (1 - P_e) \cdot \ln(n) \end{vmatrix} \tag{7}$$

In the analytical expression the positive sign corresponds to the upper 0.95 reliability level and the negative sign corresponds to the lower 0.05 probability level. The set of equations can be expressed either in the form of a second or a fourth order equation, depending on the value of P_e. In the cases where a fourth order equation is obtained, iteration of the value for $P_{0.05\text{-}0.95}$ is recommended. The result of the second order equation can be used as seed for the iteration, thus making the required number of iteration repetitions quite small.

Rank order statistics is a powerful of visualizing data as long as the confidence bounds are included in the figure. The confidence bounds reveal the uncertainty of the data set with respect to the probability distribution itself. One should remember that any distribution falling inside the rank probability confidence bounds is a possible candidate for the real distribution. The rank probability confidence bounds can thus be used to determine confidence limits to the parameters used to describe the probability distribution. They may also prevent people from making too lengthy conclusions about the significance of their data set.

3.3 Distribution comparison

The use of the rank ordering for a direct distribution comparison is very simple. If for two test cases (size, geometry, etc.) an equal amount of all valid test results exist, the comparison is as simple as shown in Figure 7. The results are ordered by rank and data values for matching ranks are compared directly. If the two cases contain an unequal number of results, or censored values, Equations (2) and (3) must be used to give the rank probabilities. Since this will lead to non-matching rank probabilities for the two cases, the smaller data set should be taken as basis and, by using interpolation, estimate a matching value from the larger data set. A suitable simple linear interpolation can be performed with Equation (8), where K_M is the matching toughness corresponding to rank

probability P_M for the smaller data set. K_L is the closest lower toughness value corresponding to rank probability P_L for the larger data set and K_H is the closest higher toughness corresponding to P_H.

$$K_M = K_L + \frac{(P_M - P_L)\cdot(K_H - K_L)}{P_H - P_L} \tag{8}$$

Virtual replication offers an attractive option to the interpolation procedure, for cases which contain only non-censored data. Virtual replication is explained through the following example. Figure 8 shows a rank probability description of two random data sets, one containing 15 probability (P_n=15) values and one containing 20 values (P_n=20).

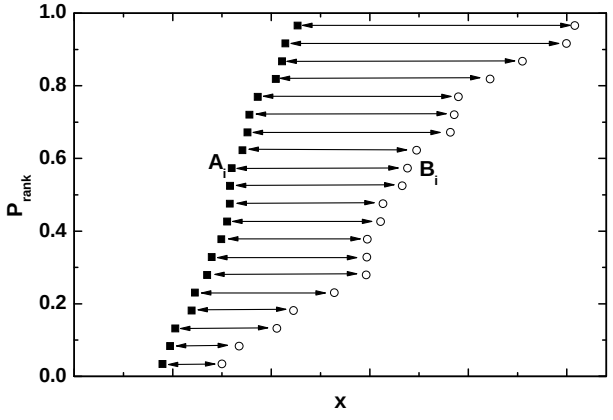

Figure 7. Schematic presentation of the principle of comparing data corresponding to equivalent rank probability.

Two distribution comparisons were performed on the data sets. First, Equation 8 was used to estimate the interpolated values of the P_n = 20 data that correspond to specific P_n = 15 values. Second, a virtual replication of the data sets was performed. The P_n = 15 data was replicated 4 times to produce 60 data and the P_n = 20 data was replicated 3 times to do the same.

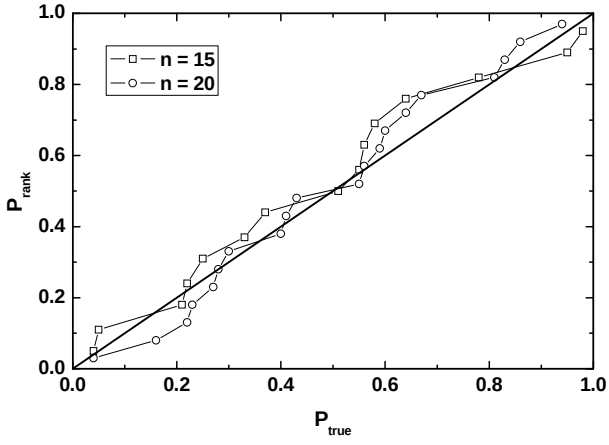

Figure 8. Two exemplary random data sets of different size.

Now, with both sets containing 60 data, a direct comparison can be made. The results of using both methods are shown in Figure 9. As seen from the figure, both methods result in very similar distribution comparisons.

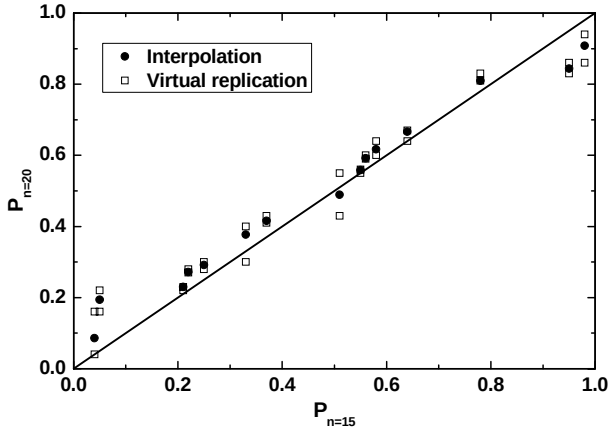

Figure 9. Comparison of distribution comparisons for different size data sets using interpolation or virtual replication.

The confidence of the comparison is not directly related to the scatter in the data, but is defined by the number of non-censored data in the smaller data set. For a good accuracy, at least 30 non-censored values for each data set are desired. Smaller data sets can be used, but their information will be more of a qualitative nature.

The strength of the distribution comparison is that it enables a quantitative comparison of two data sets, without having to do any assumptions regarding the underlying statistics of the individual distribution.

Acknowledgements

This work is part of the authors Academy Professorship and is funded by the Academy of Finland decision 117700.

References

[1] Wallin, K. Statistical Methods. In: I. Milne, R. O. Ritchie and B. Karihaloo (Eds.) Comprehensive Structural Integrity. Elsevier: Oxford, 2007, Vol. 10, pp. 137–157.

Development of materials for nuclear power plants

Hannu Hänninen
Aalto University School of Science and Technology,
Department of Engineering Design and Production, Engineering Materials
Espoo, Finland

Abstract

Concerns to material failures of nuclear power plant components have been changing during the years. Corrosion related failures of stainless steel components have been the major concern, especially pipe cracking due to weld sensitization has caused outages and repairs in BWRs. IGSCC of locally cold-worked stainless steel components without sensitization is an emerging problem in aging plants. The major issue concerning failures of stainless steel components has also been environment-assisted cracking (IGSCC and IASCC) of reactor core internal components, where handling of highly active stainless steel materials in repairs is causing also a major concern. In PWRs the long-time concern has been the steam generator tube corrosion damage both on the primary and secondary side as well as the irradiation embrittlement of the reactor pressure vessel steel and its weldments. The new big issue is the Ni-alloy weld metal cracking in reactor pressure vessel safe-end welds and in reactor head and bottom penetrations. Many of these failure modes are time-dependent and, thus, are expected to become more prevalent when the plants are aging.

1. Introduction

In nuclear reactors a very broad range of materials are used and in addition to materials scientists and engineers people active in diverse disciplines such as solid state physics, chemistry, metallurgy, mechanical engineering, electrical

engineering and electronics, polymer science and engineering, civil engineering etc. are also involved in various materials science questions. The basic material of the commercial nuclear reactors is uranium oxide (UO_2) pellets which have been irradiated in reactors in millions and they have performed well. The first reactors used fuel claddings and other structural parts of the fuel elements (guide tubes and grids) made of stainless steel. Very quickly the Zr-alloys, because of their low thermal neutron capture cross section and good corrosion properties in high temperature water, became commonly used for fuel cladding and structural components of the fuel elements. The structural materials of the nuclear reactors are mainly low alloy (pressure vessels and piping) and stainless (piping, reactor internals, pumps and valves etc.) steels and Ni-alloys (steam generators, bolts/pins, dissimilar welds). Selection of the structural materials is based on the functional requirements (T, p, water chemistry etc.), design codes and standards and technological aspects such as manufacturing experience and capability. Other important criteria are lifetime, inspectability, repairability and cost of material and the processing. Various aspects of materials selection are implemented in the requirements of the nuclear codes, which therefore play a key role in materials selection. These codes and standards on which the design, construction and plant operation are based include detailed materials and quality requirements, which have become more stringent during the increase of experience. Conventional codes, regulations and standards are used for materials and component design of the non-nuclear part of the nuclear reactor system. For the nuclear part of the system, additional requirements are imposed with respect to the safety-related importance of the component. The requirements of reliability of materials and components are highest in the pressurized reactor coolant system, including the first isolation valve. Second safety/quality class covers all components that are connected with the primary coolant, e.g., steam generator. The lower safety class components are typically separated by barriers, such as heat exchangers or valves, from the higher safety class systems.

In the following the materials science questions related to the structural materials of the nuclear reactors are examined. Especially, the main materials degradation modes during the operation are examined and the proposed mitigation methods are summarized.

2. Codes, standards and quality assurance

Engineers involved in materials science and technology in the nuclear industry are especially familiar with the features how the material aspects are covered by the codes, standards and good industrial practices. The American Society of Mechanical Engineers (ASME) has published the Boiler and Pressure Vessel Code with various technical sections. The application of the ASME code with rules for the construction of nuclear components (Section III) and with rules for in-service inspection (Section XI) are mandatory for nuclear power plant components. Many countries have also their own codes, such as KTA Safety Standards in Germany, RCC-M in France, MITI Notification 501 in Japan etc., which include detailed requirements on selection of materials, fabrication planning, testing procedures, repair and documentation for various product forms and on in-service inspection (ISI).

Technical capability and experience in combination with quality control during the fabrication and the ease of inspection and maintenance during operation contribute to a successful result. High-level quality assurance (QA) is required in all phases of the construction and operation of the nuclear power plant to assure the structural integrity for full operation lifetime and to minimize the repair or replacement of components. For the fabrication of components of a large modern PWR unit more than 10^6 quality requirements exist, for which material quality controls such as the chemical analysis, tensile tests, impact tests, hardness and metallographic examinations have to be performed. Requirements related to material toughness values or critical flaw size are directly related to the safety assessment of the components. Therefore, tests have to be performed by qualified personnel using qualified procedures and facilities. Also a full documented traceability of materials, processes and procedures is necessary for the survaillance by independent inspectors. The quality assurance requirements for nuclear power plants have been defined in all countries and the structural material aspects are covered mainly in the implementation of the QA program.

For the structural integrity assessment in the design phase, during fabrication and during in-service inspection and maintenance/repair actions especially the non-destructive examination (NDE) of the weldments is important, which requires the cooperation of the welding engineers, metallurgists and NDE inspectors. The common NDE techniques used are liquid penetrant, magnetic particle, radiography, ultrasonic and eddy current techniques, which have specific sensitivity with respect to the defect size and type but also to the type of material and its

microstructure. At present there is a general trend toward fully automated testing and evaluation by data acquisition and processing techniques. Also the major issue at the moment is the qualification of the NDE inspections.

3. Materials for water-cooled reactors

The selection and the behavior of the structural materials in the core and the near-core region must be considered based on the thermal neutron spectrum and the water chemistry of the coolant. The basic principles of operation are similar for all light water reactors LWR (Pressurized Water Reactor, PWR, and Boiling Water Reactor, BWR), but the materials selection and design details of the various manufacturers differ. These differences have resulted in varying numbers of material failures during the operation of the plants in different countries. Also the lifetime of the nuclear power plants is becoming an issue of increasing importance as the existing plants age. The extension of officially specified service life (typically 40 years) requires new legal regulations and extensive research programs for plant life extension (PLEX) are required especially on materials degradation by irradiation embrittlement and various aging mechanisms as well as corrosion. Fatigue and stress corrosion cracking (SCC) are the key issues in PLEX and critical flaw sizes and the use of fracture mechanics are important for the re-evaluation after detection of flaws in the structures by NDE during ISI.

3.1 Reactor pressure vessel

A reactor pressure vessel is constructed from materials that will provide an adequate margin of protection against failure by either brittle fracture, ductile tearing or sub-critical crack growth, assuming that aging (e.g., irradiation embrittlement) during service does not reduce the fracture prevention margin below an acceptable level. Major degradation mechanisms during service of PWR pressure vessels are irradiation embrittlement and low cycle fatigue. The failure modes in these cases may be brittle fracture caused by pressurized thermal shock (PTS) or ductile tearing leading to a leakage. In the case of BWR pressure vessels the possible degradation mechanisms are low and high cycle fatigue, SCC and irradiation embrittlement, the possible failure mode being ductile tearing leading to a leakage. Possible sites of degradation are in PWR pressure vessels the beltline weld region, nozzles (inlet/outlet, control rod drive

mechanism (CRDM) and instrumentation penetrations), safe-end welds and flange closure studs. In BWR pressure vessels, nozzles (inlet/outlet, CRDM and instrumentation penetrations), safe-end welds, flange closure studs and beltline weld region are the possible sites of failure. In the evaluation of integrity and safety margins as well as lifetime assessment of the reactor pressure vessels the effects of variations in material properties, aging, mechanical, residual and thermal loads, flaws and other stress raisers, irradiation and reactor water chemistry are to be considered.

During service, irradiation induces changes in metal structure and degradation of the material properties both in the base metal including welds and also in the stainless steel cladding of the reactor pressure vessel. Irradiation of the materials usually increases the ductile-to-brittle transition temperature, decreases the upper-self energy and increases the yield strength as well as hardness, accompanied by a decrease in ductility and work hardening rate. Precipitates (Cu-rich, possibly also phosphides, and small carbides and nitrides), vacancy clusters (microvoids) and interstitial clusters (dislocation loops) are formed and segregation of certain elements, such as phosphorus and nickel, at the grain boundaries takes place. Irradiation, thus, enhances both diffusion and clustering of certain elements. Important parameters of irradiation embrittlement are neutron fluence, irradiation temperature (low temperature neutron exposure increases strongly the irradiation damage), steel composition and microstructure. Other phenomena, which may add synergistic effects to irradiation embrittlement, are thermal aging, strain aging and hydrogen embrittlement. The requirement for understanding the irradiation embrittlement process is a careful microstructural characterization of the microstructure of the irradiated steels at near atomic level. The effects of neutron irradiation on the degradation of the reactor pressure vessel steels are being monitored in each reactor by means of survaillance programs. In general, Charpy-V notch (CVN) specimens and tensile specimens are used to assess toughness values of the steels. In the safety analysis the irradiation effects on the changes of the Charpy fracture energy curve are assessed to obtain the fracture margin for the irradiated reactor pressure vessel, e.g., according to ASME code. Post-irradiation thermal annealing is the most promising remedy for restoring the toughness properties of an irradiated steel. There are also a number of unresolved technical issues in irradiation embrittlement, such as dose rate, neutron spectrum and irradiation temperature effects, material property variability etc. as well as limitations in the existing data bases. Additionally

there is always a problem on the transferability of the data obtained from the small specimens to a real reactor pressure vessel. (1)

Environment-sensitive cracking (corrosion (thermal) fatigue, stress corrosion cracking) of reactor pressure vessel steels, such as A533B and A508, have been studied extensively. Stress corrosion cracking of cladding in a Japanese BWR and thermal fatigue cracking in the feed water nozzle cladding of several US BWRs have occurred, where the cracks penetrated also into the base metal. The reasons for these cracks are now well understood and they have led to the accepted flaw estimation methods for heavy-section steel structures. Recently, a number of LWRs have experienced SCC in the pressure vessel safe-end and CRDM/instrumentation penetration Ni-alloy welds and the cracks have also sometimes propagated into the base metal of the pressure vessel. These serious cases of cracking are at the moment under very extensive examination and new research programs are started to clarify the reasons and the mechanisms of cracking in Ni-alloy weld metals. ASME code presents a procedure for estimating the remaining useful life of a cracked reactor pressure vessel or nozzle. This procedure combines a fatigue crack growth analysis with the maximum allowable flaw size. The fatigue crack growth reference curves of the ASME code are generally used. However, a rather large amount of new test data since the formulation of the reference curves indicates considerably higher crack growth rates than the ASME reference curves, which may need in some cases more accurate predictions. The new proposed methods are based on time-dependent rather than cycle-dependent analysis of the crack growth. The importance of metallurgical variables of the pressure vessel steels is quite well understood. It is related to the sulphur content of the steel and especially the MnS inclusion size, shape and distribution of the steel seems to be responsible for susceptibility to environment-assisted cracking (EAC) in reactor water conditions. Recently, it has been observed that the heat-to-heat variability between various steels and especially the weld metals may be caused by dynamic strain aging (DSA) phenomenon caused by the interactions of free nitrogen (and carbon) atoms and dislocations in steel at certain temperature and strain rate ranges.

Recently, a new form of cracking has been found first in BWR safe-end weld metals (Inconel 182), which has resulted in safe-end replacements and weld repairs in a number of reactors. More recently, these cracks have been observed in the safe-end welds (Inconel 182/82) of PWRs as well as in the CRDM penetration tubes (Inconel 600) and welds (Inconel 182) in the reactor heads,

which have been replaced in a number of plants. A more serious observation has been made concerning leakages at the bottom of the pressure vessels of PWRs related to the instrumentation penetrations where also the same susceptible Inconel 182 weld metal is used. These cracks affect markedly the ISI programmes for many diffult-to-acces components and their attachment welds where Ni-alloy weld metals are used.

3.2 Reactor piping and internals

Environment-assisted cracking of LWR pressure boundary components, which are made of various austenitic stainless steels (AISI 304 and 316 as well as also stabilized steels AISI 321 and 347), has been a common mode of material failure, especially in BWRs. Important factor affecting EAC is weld sensitization of austenitic stainless steels, which together with high stresses (and strains) in normal BWR environment is able to cause cracking. After welding the degree of sensitization is generally low, but it increases during operation due to low temperature sensitization (LTS). Sometimes the degree of sensitization can be very minor for cracking to occur and it has also been observed that a heavy cold work alone without sensitization is able to cause intergranular stress corrosion cracking (IGSCC) in stainless steels. Therefore, the high stress levels consisting of weld residual, operating, fit-up and fabrication stresses, which together may exceed the yield stress of the austenitic stainless steels are most important. As compared to IGSCC, fatigue cracking of stainless steel components accounts for a much smaller percentage of the total failures in BWR piping. Thermal fatigue cracks are typically transgranular and they occur similarly in BWR and PWR conditions. Thermal fatigue cracking can be prevented by modifying the pipe system design and installing mixers to minimize the thermal transients.

IGSCC cracking has resulted in significant forced outages with associated high costs of repairs and replacement power, significant personnel radiation exposures and occasional safety hazards. For example, material related capacity factor losses due to IGSCC of stainless steel coolant piping of BWRs in USA averaged more than 6% in 1980’s. In addition to stainless steel piping most of the components and used materials of nuclear power plants have been affected by some kind of corrosion damage which have led to replacement of the major components often after only a small fraction of their design life (2). A number of repair and mitigation measures against IGSCC have been developed and applied, e.g., narrow-gap welding, heat sink welding, induction heating stress improvement

and mechanical stress improvement, which are related to stress improvement, nuclear grade stainless steels (may crack in certain circumstances in cold-worked condition), which is related to sensitization, hydrogen water chemistry and lately the Noble Metal water chemistry treatment for the whole BWR plant, which are related to the electrochemical potential control. Implementation of these pipe crack remedies in the USA is generally thought to be complete and it is expected that the number of pipe cracks caused by IGSCC and their impact on plant operation in the future is relatively small. However, in other countries such as in Japan and Germany these cracks have had serious consequences to plant operation from the regulatory organizations even though the concept of leak-before-break has not been violated.

The internal stainless steel components of, especially, BWR pressure vessels are potentially susceptible to IGSCC, because materials, welding methods and environments for internals are similar to BWR piping. Therefore, failures of stainless steel internal components have been analogous to pipe cracking problems in many plants. However, in near-core components failures have also occurred in annealed stainless steel materials (3-5). This phenomenon has been named irradiation assisted stress corrosion cracking (IASCC), which occurs also in PWRs. IASCC describes intergranular environmental cracking of materials exposed to ionizing radiation, cracking is accelerated by radiation in combination to change in water chemistry, material microstructure and chemistry, etc. IASCC has been extensively studied but the phenomenon should be much better mechanistically understood to be able to develop the methodology to predict the component behavior in relation to IASCC and to identify the possible countermeasures to IASCC. Most of the internals affected by IASCC have been replaced without major capacity factor losses, even though there have been significant maintenance costs. The recent failures in the core shroud structures have been more difficult and replacements of the core shroud and its support structure have been very costly and in one case, KWW Wuergassen, the whole BWR plant was decomissioned after finding serious cracking in the core shroud.

3.3 Steam generators

Steam generators of a typical PWR plant contain 150…500 km of Inconel 600/Incoloy 800 heat transfer tubing which forms a thin-walled pressure boundary between the primary and secondary systems. The steam generators have normally an excess heat transfer area of about 20%. The major causes of steam

generator tube failures are primary side IGSCC, secondary side IGSCC or intergranular attack (IGA), pitting corrosion and wear. A large number of PWRs have replaced their steam generators due to these failure modes. Similar to primary side IGSCC in steam generator tubes is the pressure vessel head penetration cracking in thick Inconel 600 alloy. Materials selection in steam generator replacements has been the key remedy and in most of the cases Inconel 690 alloy has been selected even though Incoloy 800 alloy has not shown any tendency to cracking during its long operation experience. So far, also Inconel 690 alloy has performed well. In Russian VVER plants AISI 321 stainless steel tubes are used which are susceptible to chloride-induced SCC and require, therefore, extremely good water chemistry to survive against pitting corrosion and SCC. This has been possible in Loviisa VVER plant.

4. Conclusions

Concerns to material failures of nuclear power plant components have been changing during the last years. Corrosion related failures of stainless steel components have been the major concern, especially pipe cracking due to weld sensitization has caused outages and repairs in BWRs. IGSCC of locally cold-worked stainless steel components without sensitization is an emerging problem in aging plants. The major issue concerning failures of stainless steel components has also been environment-assisted cracking (IGSCC and IASCC) of reactor core internal components, where handling of highly active stainless steel materials in repairs is causing also a major concern. In PWRs the long-time concern has been the steam generator tube corrosion damage both on the primary and secondary side as well as the irradiation embrittlement of the reactor pressure vessel steel and its weldments. The new big issue is the Ni-alloy weld metal cracking in reactor pressure vessel safe-end welds and in reactor head and bottom penetrations. Many of these failure modes are time-dependent and, thus, are expected to become more prevalent when the plants are aging. Thus, these materials problems are of major concern when the safety margins and plant life extension problems are considered. For the safe operation of the primary pressure boundary materials various aging assessment techniques, such as non-destructive testing and evaluation, statistical methods, transient data collection, temperature, neutron spectrum and flux as well as continuous water chemistry monitoring and control, operational strategies and predictive models for various forms of failures, have been developed and need to be developed

further. The development of the predictive models relies on the mechanistic knowledge on failures. Therefore, in addition to development of the mitigation methods, basic research on materials science of nuclear materials and their failure mechanisms has to be carried out for understanding the phenomena and producing reliable data for predictive models.

References

1. Hänninen, H. Phenomena of Material Degradation with Time Relevant to Reactor Pressure Vessels. Int. J. Pres. & Piping 54(1993), pp. 9–30.

2. Hänninen, H., Aho-Mantila, I. & Törrönen, K. Environment Sensitive Cracking in Pressure Boundary Materials of Light Water Reactors. Int. J. Pres. & Piping 30(1987), pp. 243–291.

3. Hänninen, H. & Aho-Mantila, I. Environment Sensitive Cracking of Reactor Internals. Proc. 3rd Int. Symposium on Environmental Degradation of Materials in Nuclear Power Systems – Water Reactors. G. J. Theus and J. R. Weeks (Eds.). Warrendale, PA: The Metallurgical Society Inc., 1987, 77–92.

4. Andresen P. et al. State of Knowledge of Radiation Effects on Environmental Cracking in Light Water Reactor Core Materials. Proc. 4th Int. Symposium on Environmental Degradation of Materials in Nuclear Power Systems – Water Reactors. D. Cubicciotti (Ed.). EPRI, CA, 1990. Pp. 83–121.

5. Scott, P. A Review of Irradiation Assisted Stress Corrosion Cracking. J. of Nuclear Materials 211(1994), pp. 101–122.

Applications of the TVO piping and component analysis and monitoring system (PAMS)

Paul Smeekes[1], Olli Kuuluvainen[2] and Eero Torkkeli[3]
Teollisuuden Voima Oy[1], Olkiluoto, Finland
Rostedt Oy[2], Luvia, Finland
FEMdata Oy[3], Haukilahti, Finland

Abstract

To make fitness, safety and lifetime related assessments for piping and components, the amount of data to be managed is getting larger and larger. At the same time it is essential that the data is reliable, up-to-date, well traceable and easy and fast to obtain. At present the main focus of PAMS is still on piping, but in the future the component related databases and applications will be more and more developed.

This paper presents a piping and component database system, consisting of separate geometrical, material, loading, result and document databases as well as current and future applications of the system. By means of a user configurable interface program the user can generate indata files, run application programs and define what data to write back into the result database. The data in the result database can subsequently be used in new input files to perform postprocessing on previous results, for instance fatigue analysis, crack growth analysis or RI-ISI. The system is intended to facilitate the analyses of piping and components and generate well-documented appendices comprising significant parts of the input and output and the associated source references.

1. Introduction

The system is meant to contain all information necessary to perform most of the standard analyses associated with and monitor piping systems and components for an existing and operating plant [7]. At present most of the piping inside the containment of the TVO OL1, OL2 units and part of the piping inside the containment of the OL3 unit are entered into the system. Later more will be added. The system was initially meant as an “as built” system, but is now also used for the documentation review of the OL3 plant that is under construction.

All data in the system will be accompanied by the necessary information with regard to its source reference, dates, version and validity. It will be possible to keep models for system configurations that have existed during the history of the plant or even an “as-designed/standard” version and an “as-built/measured” version. It is clear that this requires sophisticated bookkeeping. The programming associated with the bookkeeping has just started.

In case a load definition is changed, a new load analysis and load summary report will be issued. These will make the old reports obsolete in the document database. The system will “know” that the subsequent strength analysis and the associated results are not valid anymore and issue warnings to the user.

With a growing importance of parameter studies and probabilistic analysis it is important to have the analysis input data readily available [9].

The system is build up of separate and stand-alone databases and program modules. Thus different parts can be separately developed and used for their own purpose without the whole system having to be completed or in use. As the programming languages are developing very fast and modern tools shall be used as they give more possibilities and improve the performance, the next development was the independence of the development program language.

For the subsequent analyses commercially available programs are used as much as possible (database development, piping analysis, FEM, CFD, EN/PED related component analysis etc.). As the updates of these programs are handled by professional organizations adaptations to the latest developments will always be available. Only for very special purposes, customised software has been developed, like RI-ISI, crack growth analysis and event monitoring.

The programmers perform extensive testing of the developed modules. Most modules provide immediate feedback by data visualisation. For example thermal, pressure and other transient loadings are animated directly within PAMS.

The main part of the development was performed by TVO and its consultants. Other partners involved have been the Helsinki University of Technology, Technical Research Centre of Finland, students of the Rauma school of Engineering, Rostedt Oy and FEMdata. As the system is developed and used by a small group, a unique approach was chosen. The main idea is that the system produces files and documentation that contain all references to associated source documentation thus enabling the user to efficiently check the indata. The PAMS-system itself only dumps information onto a structured file.

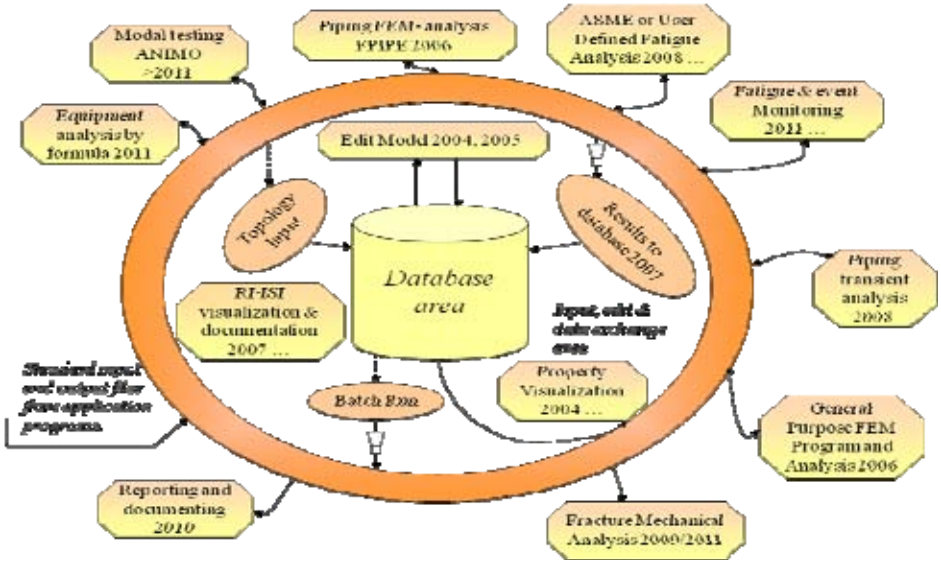

Figure 1. Structure of the pipeline and component analysis and monitoring system.

The pipeline and component analysis and monitoring system consists of the following main parts:

1. The database area with several interconnected databases, see Figure 1.

   The different databases are edited with their own user interface modules that are designed to give visual information alongside alphanumerical. Programs within the database area communicate directly with the databases, see Figure 1. These are for instance the indata visualisation modules and the RI-ISI application.

2. The database area contains the following Microsoft® Access 2000 [8] databases:

   a) The piping and component database, containing the geometry, material, contents, isolation, welds, loading, boundary conditions, detected cracks etc.

   b) The material database, containing information with regard to the material properties necessary for subsequent analysis, sometimes extending to charge information like chemical composition.

   c) The loading database [1] containing loads, loading combinations, design and service level limits, events, cycle quantities and measured histories of events that have occurred.

   d) The result database containing links to the full analysis input and results as well as all help files and automatically generated integrated result database tables for subsequent postprocessor analysis.

   e) The document database contains the documentation associated to the above items.

3. The external area with the application programs

   a) Apart from some analysis control the application programs get 100% of their indata from the databases and run in batch mode. Large result files (thermo-hydraulic analysis) will exceptionally be stored as files only. Two programs types are:

      1) Commercial programs for structural, flow, fatigue, fracture mechanical or other analyses.

      2) Tailor made programs for post processing of previously obtained results, event monitoring, fatigue analysis and monitoring, crack growth analysis and monitoring, definition of inspection intervals etc.

4. The neutral file area for the communication between the databases and application programs.

The neutral file is the batch indata file according to the application programs' user manual ("real" neutral files do not yet exist although many have tried to define them). Sophisticated user definable interface modules write data in the right format from the databases into the indata file and extracts data from the analysis program printout results back into the result database.

2. Elements of the database system

2.1 Piping and component database

The organisation of the piping and component geometry in the database is similar to the organisation of the TVO drawings that are associated to the piping systems and components and is thus well recognisable to TVO users:

* Level 1, system with the system identification number. Drawings at this level are called system-isometrics.
* Level 2, the main parts of the system are found. There are no separate drawings at this level.
* Level 3, the isometric drawings and associated part lists, the lowest and most detailed level of piping drawings available at TVO. Geometry, material and welding related information is entered at this level and linked to the isometric drawing and other associated source references in the document database.

The database contains nodes (topology, boundary conditions etc.) and elements (piping, component parts etc.) with associated properties. When entering data this is visualised and can immediately be checked for soundness. The database model is looking like a finite element model but actually contains an as-build and/or as-designed representation of the geometry. Additional structures necessary to perform a sound dynamic analysis can de added to the model, see also Figure 2. For the indata file the elements can be automatically divided in parts with a user definable maximum length.

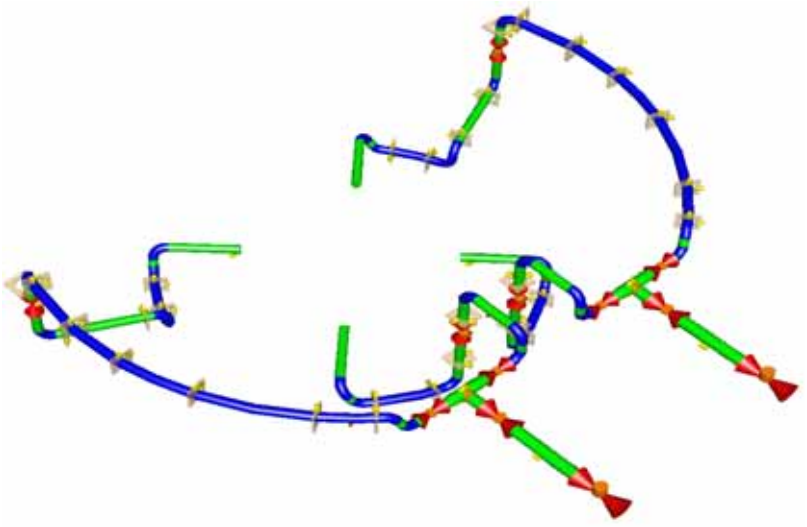

Figure 2. Visualisation of piping and supports with the piping database graphical user interface.

2.2 The material database MATDBS

The material properties of the materials used at the TVO powerplant are gathered in the material database [11], see Figure 3. This database contains both standard values from material standards and measured values from material certificates. For instance for the RI-ISI application it was necessary to assess the sensitivity to stress corrosion cracking and thus even the actual chemical composition was entered into the material database. From a database design point of view this addition is not very large, but the extra amount of indata that was entered into the system was huge.

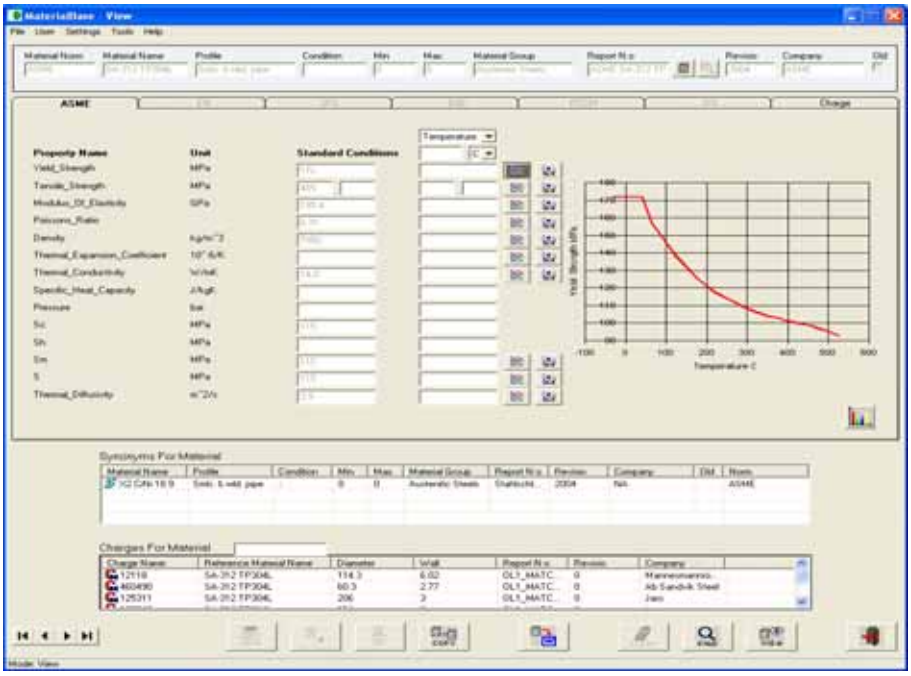

Figure 3. Visualisation of material input.

2.3 The document database

The document database, see Figure 4, contains documents that are linked to information items within PAMS. For instance, a load analysis report is coupled a load, see Figure 5 and material properties are coupled to their source reference, see Figure 3. Due to the links it is possible to open the document. The document database even contains information as to the validity of documents. Other modules of the database system can use this information to produce warnings or errors.

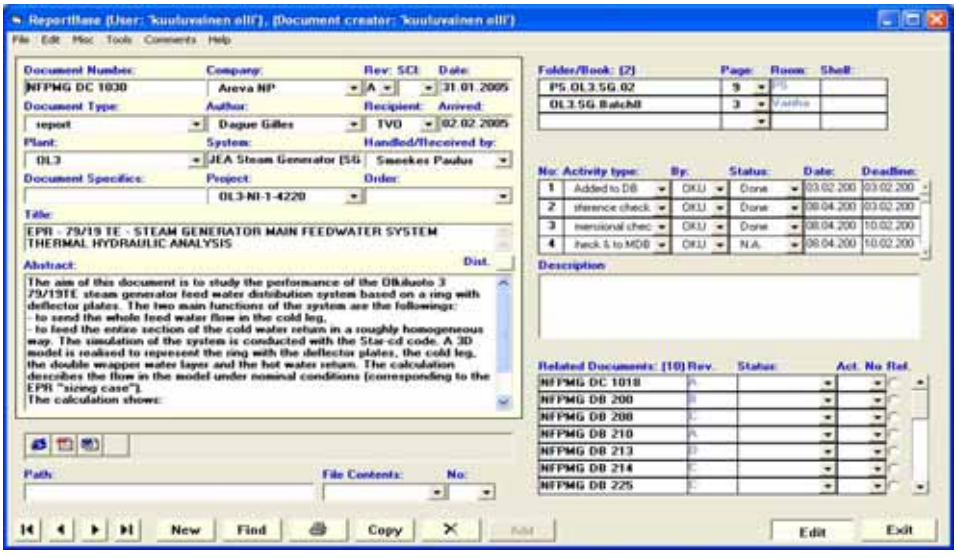

Figure 4. Example of visualization of a transient pressure-temperature load in the database.

2.4 The loading database

The loads, loading combinations, events and everything else related are saved in the loading database [1].

At present static or dynamic pressures, temperatures, weight, or forced displacements can be included as basic loads and linked to their source document, see Figure 5. These are stored in the database or, in case of large data quantities, coupled as structured files. A transient load can be entered and simultaneously visualized as shown below.

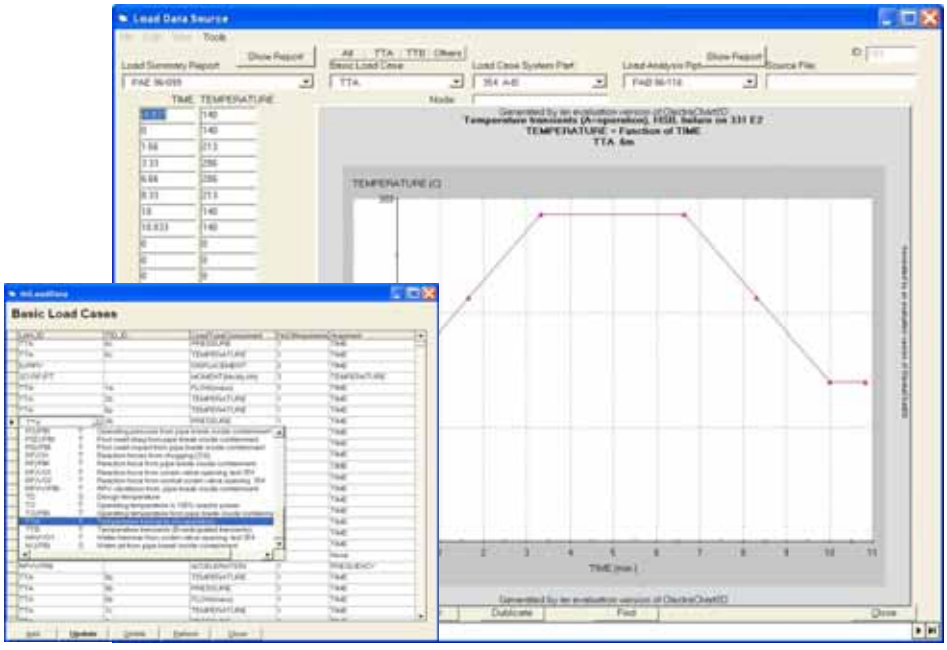

Figure 5. Example of visualization of a transient pressure-temperature load in the database.

Once the transient is entered it can be visualized with an animation. Animations can be made for any piping entity.

Once all transients are entered they can be checked automatically for soundness. The following rules apply:

1. All piping parts in an analysis entity shall have all necessary transients defined.
2. The transients shall start from the same operational state and end into the same operational state.
3. The length of similar transients shall be the same and all parts of the transient shall occur synchronous.
4. Transients that are combined into cycles shall fit together, i.e. start/end from the same operational state.

The four items above seem trivial but they are very important and unfortunately the loading analysis documentation did not use these same rules. When visualizing a transient in an animation it will show input errors that have been

made (issue 1 & 4). As PAMS make an exact copy of the data in the database into the batch input file application programs will not start in case of seemingly small mistakes (issue 1, 2, 3 & 4). Thus the system forces the users to make a "perfect" load input. After all corrections are made these will be incorporated in the loading analysis documentation.

The used operational states are:

- 100% operation: This state is as much as possible the start of cycles, even start-up and shut-down
- Hot standby (HSB).
- Cold, normal situation during the outage.
- Test, being a totally separate state.

3. Analyses and application programs

3.1 Piping strength analysis

The piping strength analysis is carried out with commercially available piping analysis programs. At present the Finnish program FPIPE [4] is in use, see Figure 6.

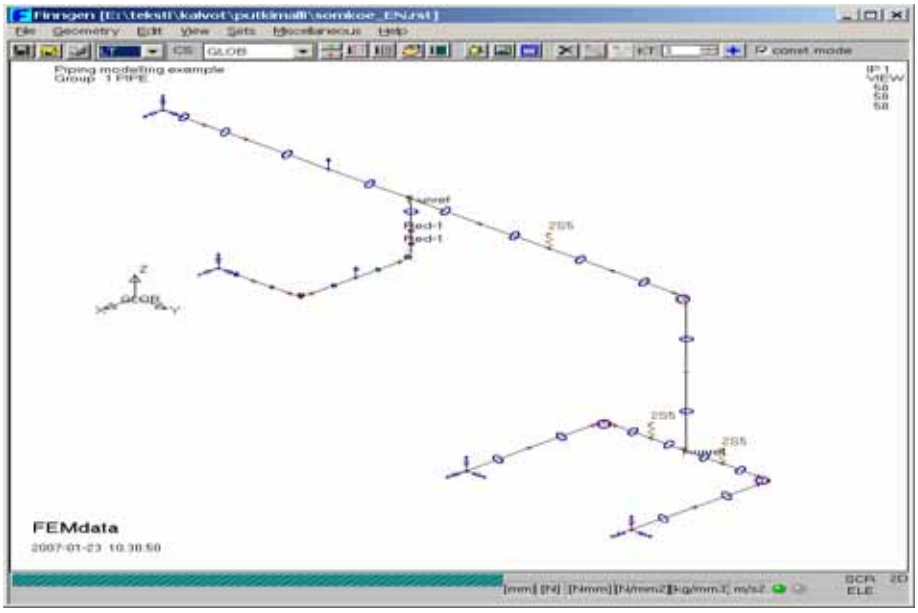

Figure 6. Wire-frame model of a piping model in FPIPE.

Basically it is possible to use any piping program using an alphanumerical batch input file. Analyses were also performed with ANSYS. When doing a dynamic analysis of the complete containment, RPV and class 1 piping inside the containment the database was used to generate the piping models inclusive piping supports, see Figure 7.

Figure 7. Results for a PAMS piping model inclusive supports that was generated for ANSYS.

3.2 Fatigue analysis

For a long time FPIPE has had a program module that performs fatigue analysis according to the ASME III – NB3600 standard [6] for class 1 piping. As the NB3600 analysis methodology is more or less an engineering tool it is mostly conservative and can only be applied in a semi-automatic way. With the OL1 and OL2 nuclear power plants becoming elder and elder the designed budget of fatigue cycles starts to fill up more and more. Already now the budget for one test-event is nearly full and in the near future it has to be classed as a different event not to have to immediately redo the fatigue analysis. Obviously the fatigue

analysis has to be repeated in the near future anyway. However, TVO wants to get a much better grip on the implication of events on different locations and has chosen for a completely different approach. The transients will be analysed in a fully time dependent way and separately for every location. First the piping analysis program FPIPE does this transient analysis for every single transient defined in the loading report and then the force and moment results are stored in the PAMS result database and thus available for postprocessing. Please note that in this global analysis FPIPE uses the average temperature over the cross-section after doing a 1 D thermal analysis over the defined cross-section.

The Femdata ASME NB3600 program has been further developed to perform analysis according to the ASME NB3650M. This postprocessing program does a full rainflow fatigue analysis. The input for this postprocessing program module is fully automatic generated both from the PAMS input database and the PAMS result database and consists of:

- The geometry of that part of the piping system being in the direct vicinity of the location to be analyzed, minimum one node and two adjoining pipe-elements inclusive cross-sectional and material information.
- For all involved transients the associated time dependant pressure, temperature and flow.
- For all involved transients the associated time dependant forces and moments on the analysed node.
- For the analysed node the necessary stress concentration factors according to the ASME.
- The number of cycles either for combined events (small histories of more than one transient) or single events.
- First the ASME III – NB3560M will then once again perform a 1D thermal analysis to determine the thermal stresses over the wall.
- After that full rainflow analysis is performed on different calculation points around the circumference, see figure below, and through the wall at the chosen cross section, see Figure 8 below. Obviously all involved transients and cycles are considered.
- After that the fatigue usage factor will be known at all requested points over the cross-section.

- Also the times from where the minimum and maximum stress values were taken are saved.
- These are then used to even do an additional ASME NB3600 analysis.
- The Figure below associated items to the ASME NB3560M analysis.

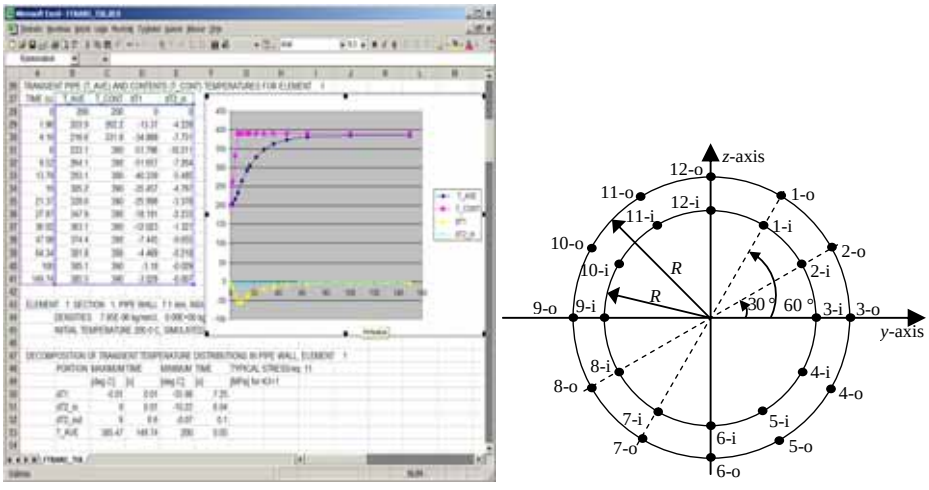

Figure 8. ASME NB 3200 postprocessing intermediate results and requested result points.

3.3 Load analysis (CONTANA project)

Ongoing OL1 and OL2 modernization has resulted in changes to plant design and operating parameters. Also changes in the YVL-guides of the Finnish Regulator have to be adapted for main system changes. Therefore certain internal and external dynamical design loads were revised affecting the dynamic response of the buildings and connected structures. This again has an effect on the loading specifications for piping, components and equipment. In order to update the design loads and associated background material of and affected by the containment and associated structures, the structural response for some dynamic loadcases was reanalyzed for the building, connected structures and piping systems. The PAMS system was used to generate ANSYS models of 31 different piping analysis entities that were incorporated in the containment model. New features that were built to accommodate this project were:

- Free choice of the starting number for the model nodes and elements. After that they are numbered consecutive. Thus the models could just be “added” to each other and to the containment model.
- Modelling of support beams in PAMS and generation of ANSYS models inclusive these support beams. As beams are not axi-symmetric this was a total ne field for definition and visualisation.
- Division of logical piping parts into more than one piping element according to some predefined rule.

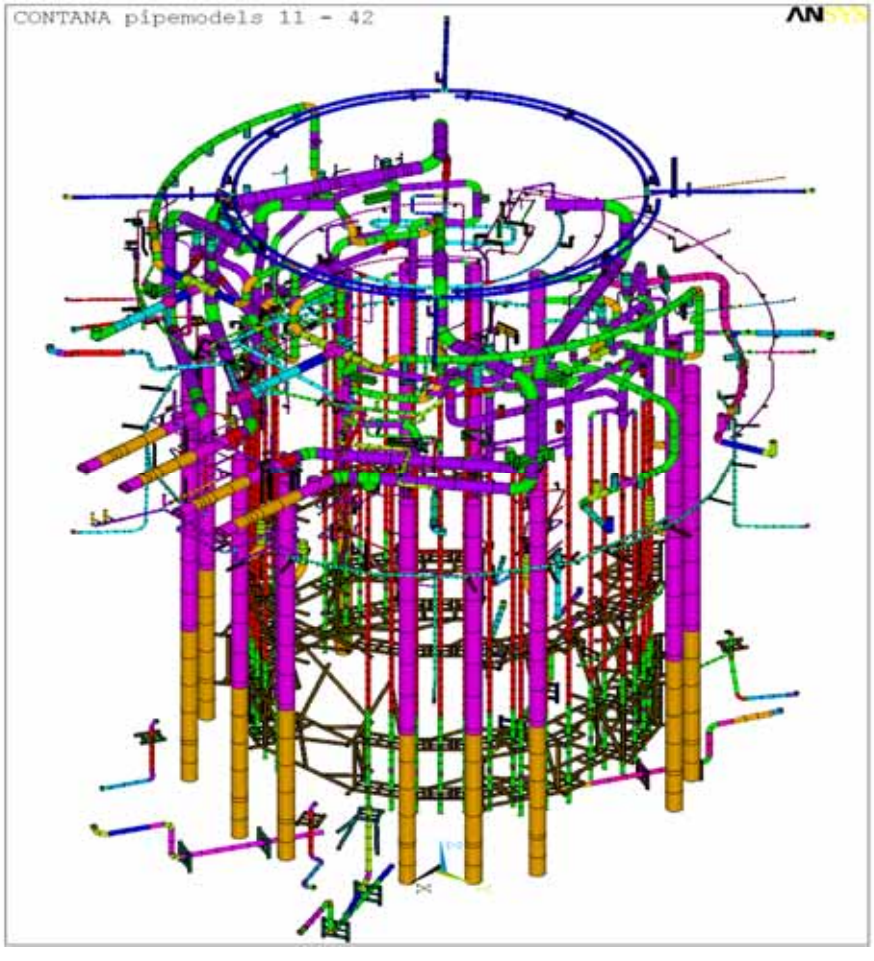

Figure 9. CONTANA – 31 piping models inclusive supports.

3.4 RI-ISI

Actually the first application of the PAMS system that was used to directly generate a complete official documentation was the RI-ISI-application according to the ASME – Boiler & Pressure Vessel Code, Section XI [14], Appendix R, Method B. This application was developed in 2007/2008, mainly applied in 2008 and the resulting documentation was approved by the Finnish Regulator STUK in early 2009. In Figure 8 the segment division for the feedwater lines and the visualized risk class for one of the segments are shown. The results of the PRA (CCDP and CLERP) were directly entered to the piping segments as input to PAMS. Some damage related rules taken into account are listed in Table 1 below.

Table 1. Different rules that are automatically taken into account by the PAMS RI-ISI application.

Damage potential	**Damage mechanism**
High	**Stress corrosion cracking IGSCC** (SS C>= 0.040%), I-182 welding material & $T_{water} \geq 150\ ^{o}C$ **Significant thermal cycling** (mixing areas) (SS $\Delta T \geq 50\ ^{o}C$, CS $\Delta T \geq 70^{o}C$) **Fatigue,** cumulative usage factor = 0.8–1.0 **Stress intensity** primary & secondary > **2.6 S_m** **Flow accelerated corrosion** (FAC) **Water hammer** (possibly combined with other mechanisms)
Middle	**IGSCC** (SS C = 0.035–0.040%) & $T_{water} \geq 150^{o}C$ **Thermal Cycling** (SS $\Delta T \geq 40^{o}C$, CS $\Delta T \geq 60^{o}C$) **Fatigue,** cumulative usage factor = 0.4–0.8 **Stress intensity** primary & secondary $\geq$ **2.4 S_m** **MIC, PIT ja CC (**SS with no flow) **Water hammer** (possibly with other mechanisms, decided in committee meeting)
Low	No known damage mechanisms

Apart from figures like the ones shown below the document consists of explanatory text and tables containing all significant information related to the

system under consideration and obviously all the necessary intermediate and final results. The largest effort was to generate and enter the indata into the system.

The next step in the TVO RI-ISI development will be the introduction of probabilistic fracture mechanics to determine failure probabilities and risks. Furthermore the inspection history and future will be entered into the system.

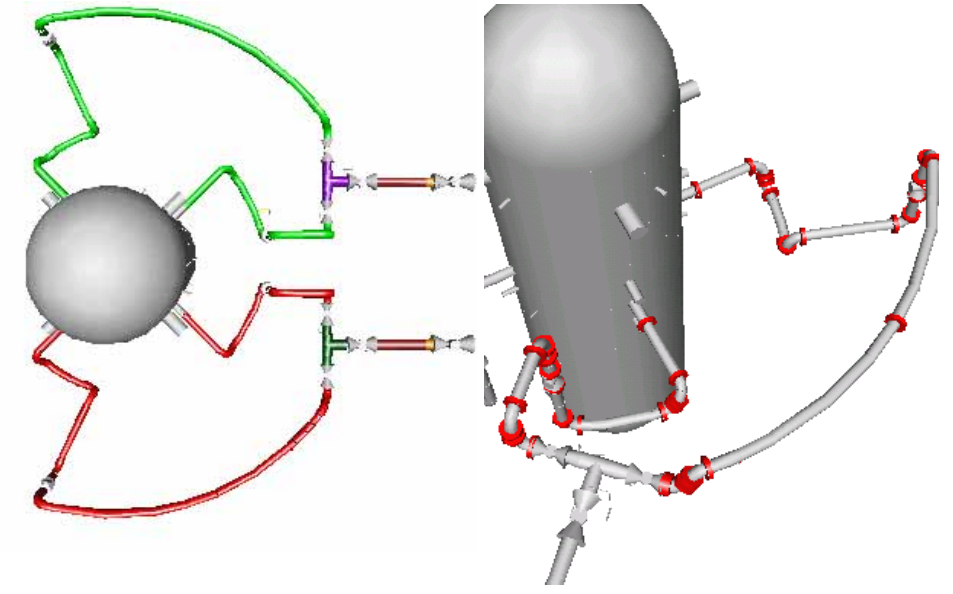

Figure 10. PAMS piping model generated segment division for the feedwater lines and the visualized risk class for one of the segments.

3.5 Fracture analysis

When performing fracture analysis, several crack growth mechanisms have to be considered, like crack growth due to cyclic mechanical loading or IGSCC. As these mechanisms are dependent upon the material and the environment these method(s) can be chosen automatically. These analyses have been performed performed using the VTT-BESIT program [5] but the indata file is still made partly by hand. In 2009 the work to connect this program to PAMS was started. The largest problem is the format of the indata and output files of VTTBesit and its pre-processor DIFF. Their format is unstructured and basically only fit for input by hand. These programs will anyhow be fully connected to the PAMS system in 2010/2011. The analysis can then be performed for indications that are detected during inspection or for postulated cracks in a predefined group of

welds. These cracks could then be located in the cross section in a similar way as the usage factor determination locations shown in figure.

As the trend is to go to probabilistic crack analysis this database approach is very important as it makes the variation of locations and all sorts of parameters possible through automatic analysis.

Location	**312-Nozzles Safe end/Pipe weld**
Material used for the analysis	**SA376 type 304**
$D_i/D_o/t$ [mm]	**292/323.6/15.8**
Flaw Characteristics	**Internal circumferentially orientated crack**
Specified crack a/c [mm]	
Degradation mechanism	**Fatigue induced cracking**
Crack growth law	**$da/dN = C\cdot(\ K_J)^n$, C = 2.467E-08, n = 3.82**
Applied software	**VTTBESIT 2.0**
Weld residual stresses	**None**
Allowable crack determination	**ASME sect. XI, div. 1, app. C, C-3000 /20/**
Reference(s)	**/13/**

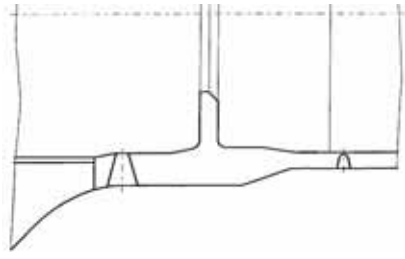

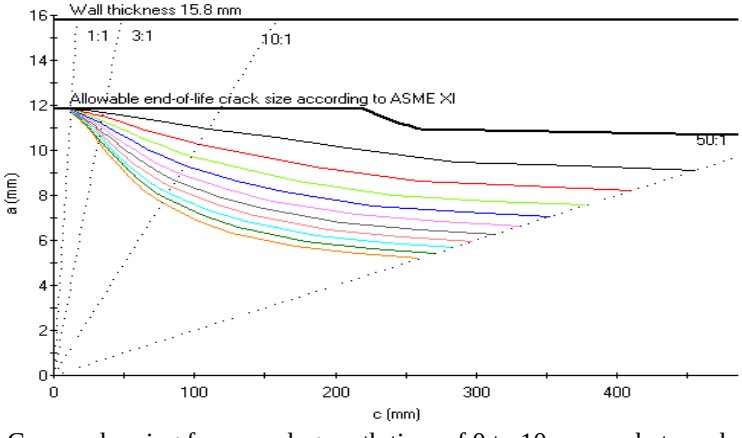

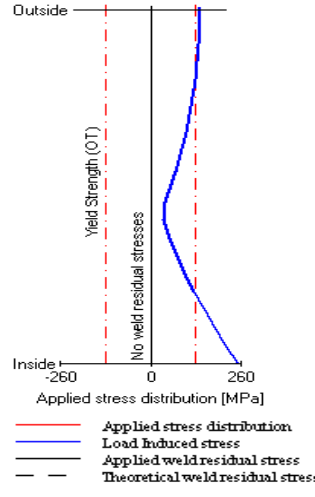

Curves showing for a crack growth time of 0 to 10 years what cracks will grow to the allowable end of life crack. The colour codes used in the diagram are defined in the table below.

years / c/a	**1**	**2**	**3**	**4**	**5**	**6**	**7**	**8**	**9**	**10**
1	**11.83**	**11.82**	**11.80**	**11.78**	**11.77**	**11.75**	**11.73**	**11.72**	**11.70**	**11.68**
2	**11.81**	**11.76**	**11.72**	**11.67**	**11.63**	**11.59**	**11.55**	**11.51**	**11.47**	**11.43**
3	**11.77**	**11.69**	**11.61**	**11.53**	**11.45**	**11.38**	**11.31**	**11.24**	**11.18**	**11.11**
4	**11.57**	**11.30**	**11.06**	**10.84**	**10.64**	**10.45**	**10.28**	**10.11**	**9.96**	**9.81**

Figure 11. Presentation of the short documentation for a crack growth analysis.

4. Bookkeeping and validation

As the database will be quite complex, a good design and bookkeeping is very important. The records to be kept shall contain such information as date of installation and possible exchange, as-build geometry, welding, inspection and repair. Design loads and a complete load history shall be available. Also the validity of the data shall be indicated. The date is important as for instance thermal cyclic loading that has occurred before a part was replaced shall be ignored with regard to the fatigue of the replaced part. Thus analysis can be performed based on reliable and up-to-date information. Programming of the bookkeeping has been started in 2009 and will be continued in the coming years. For the moment all changes made to the database are only recorded.

5. Topics for future studies and development

There are many ideas for further future development:

* For instance the piping models can be enhanced with models of the vessels they are connected to. In FPIPE this is possible with a combined 3D shell and piping model, see Figure 12 below.

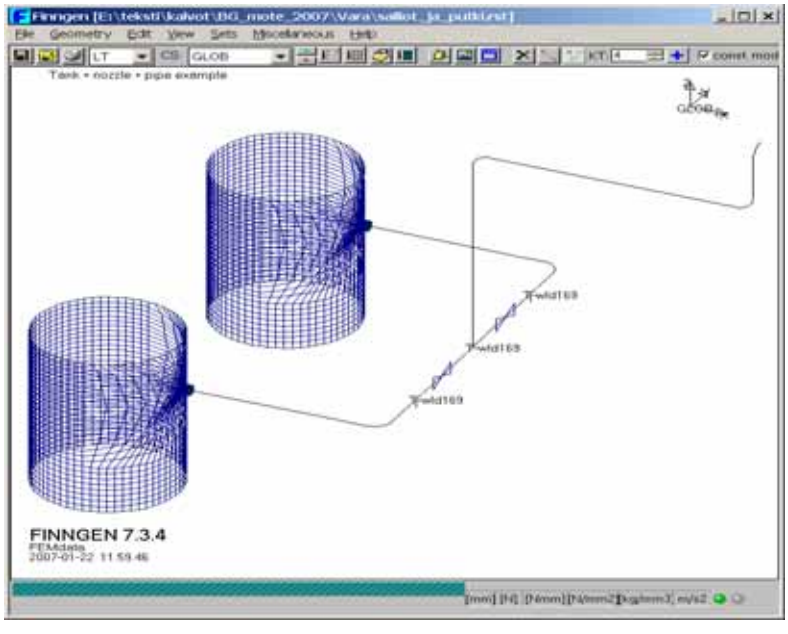

Figure 12. FPIPE combined 3D shell and piping model.

* Also some macros have been developed to generate 3-D solid models for ANSYS. An example for a Tee is shown in Figure 13 below. Input is again directly generated from PAMS. Some continuation to this step can be:

  • Develop a full 3D solid model of a piping system analysis entity directly from PAMS.

  • Develop a local 3D solid model a piping system around a detail to be investigated in very large detail. This could be a crack in a weld, then to be modelled with a crack growth processor program. An example like this is at present developed with a combination of the programs ANSYS and Zencrack. This model can then automatically get boundary conditions from previously performed FPIPE-analyses.

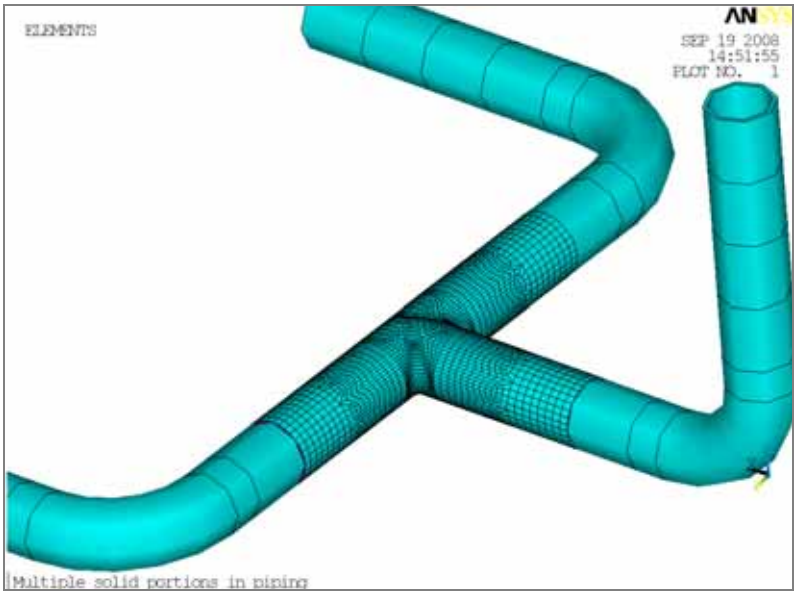

Figure 13. Combined piping model and macro generated 3D solid model of a Tee.

* Transient thermal- and flow analysis and flow induced loads, like water hammer or pump transients and pipe break loads. Will it be possible to generate an input file to a thermo-hydraulic program and write the analysis results back into the database? This is probably only a question of time and the choice of a suitable program.

* Back coupling of pressure and temperature measurements. The inside temperature transients to be determined from the measured outside temperature transients. A study on available techniques and tools will be performed and the possible application studied.
* Coupling of a program performing EN/PED piping and component analysis according to the EN Standards.
* Bimetallic weld analysis. This would involve a complicated FEM analysis to be coupled to the database. Some efforts have been made to make 3D model macros for Tees.
* Transient and event monitoring based on events and/or measurements.
* Bookkeeping of inspection results. This will already be started in the end of 2009.
* Multiple run development. This already functions for the analysis of different transients in one analysis entity. The automatic analysis of all transients in multiple analysis entities followed by fatigue analysis of all analysis nodes in the analysed analysis entities will be developed in the near future.
* Valve strength analysis. Some analysis tools have already been developed. Coupling to the database is under development, but has a low priority and may be shifted forward.
* Continuous development of visual input and output interfaces.
* Addition of the associated-report information to the input given
* Automatic update after changes to loading or geometry. This will be developed when the bookkeeping routines are more mature.
* Probabilistic analysis will be developed in parallel with the development of suitable postprocessing programs.
* Improve the load handling in three stages as described below:
    - In the first stage of the load input project all design transients from the final safety analysis reports (FSAR) will be entered into the PAMS system together with their designed number of occurrences. This has been done already.
    - In the second stage of the load input project the designed number of occurrences will be replaced by the number of occurrences from the actual event history plus the number of occurrences that is extrapolated from that

same event history. At the same time the events get a time stamp. Some preparation work has been done for this.

- o In the third stage of the load input project the design transients will be redefined with help of the temperature and flow measurements in the units and a new software tool. The have been gathered since a long time.

* Feasibility studies will be performed with regard to interfaces to one-dimensional pipe loading analysis programs, CFD-programs, modal analysis and update, general-purpose FEM programs and true neutral files.

References

1. Raiko, H., Lipponen, A., Smeekes, P. & Talja, H. Load-Case, and -Combination Database. SMiRT 16 Paper 1869, 2001.

2. Talja, H., Smeekes, P., Torkkeli, E., Laaksonen, J., Rostedt, J., Haapaniemi, H., Lipponen, A., Saarenheimo, A. & Solin, J. Lifetime of pressure retaining components (PUKK). Espoo: VTT Manufacturing Technology, 2000. Report VAL64-001549. 22 p.

3. Smeekes, P., Talja, H., Saarenheimo, A. & Haapaniemi, H. Numerical Simulation of Piping Vibrations Using Modal Correlation. SMiRT 16 Paper 1866, 2001.

4. FPIPE, a finite element method (FEM) based piping analysis program developed at FEMdata Oy, Finland.

5. VTT BESIT 1.0 by VTT Manufacturing Technology, Finland.

6. ASME Boiler And Pressure Vessel Code, Section III, Nuclear Power Plant Components, Division 1, Subsection NB, Class 1 Components.

7. Smeekes, P., Lipponen, A., Raiko, H. & Talja, H. The TVO Pipeline Analysis and Monitoring System. SMiRT 16 Paper 1868, 2001.

8. Microsoft® Access 2000, Relational Database Management System for Windows.

9. Simola, K., Talja, H. & Smeekes, P. Use of plant specific information in life management, PLIM 2002 IAEA-CN-92 /10

10. Smeekes, P., Lipponen, A., Raiko, H. & Talja, H. The TVO Pipeline Analysis and Monitoring System, SMiRT 17, 2003.

11. Smeekes, P., Alhainen, J., Lipponen, A. & Talja, H. The TVO/VTT material database, SMiRT 17, 2003.

12. NUREG/CR-6909 ANL-06/08, Rev. 0, 1.2.2006, Chopra O. K., Argonne National Laboratory, Effect of LWR Coolant Environments on the Fatigue Life of Reactor Materials.

13. Smeekes, P. The TVO Pipeline Analysis and Monitoring System, SMiRT 19, 2003.

14. ASME – Boiler & Pressure Vessel Code, Section XI.

Fatigue of stainless steel

Jussi Solin
VTT Technical Research Centre of Finland
Espoo, Finland

Abstract

The 2009b update of ASME III introduces a new set of fatigue design curves. The new curve for austenitic stainless steels is exactly matching with the one endorsed in 2007 by the US NRC for new designs only. This has a notable effect in usage factor calculation at strain amplitudes below 0.5%. However, experimental results clearly demonstrate that a new air curve would not be needed for the studied stainless steel grades. Our current results suggest arguments for use of stabilized stainless steels in NPP piping components, where high cycle fatigue ($\varepsilon_a \leq 0.5\%$) is a concern.

1. Introduction

The ASME III design by analysis philosophy and local strain approach assume that the designer has relevant material data available [1]. Although generalized design curves have been included in the codes to reduce need for material testing, choice and applicability of the code curve – or an experimental curve – for the particular application remains the responsibility of the designer. However, the proposed design curves are introduced in a “mandatory” appendix. Perhaps this is one reason for the general mistake of assuming the ASME design curves as the only alternatives.

Particular care should be taken when adding or modifying the code curves. This is not the case in a current attempt to introduce a complex set of new design curves into ASME III aiming to count for environmental effects of primary water in fatigue [2]. But the air curve for stainless steels was already modified in

the 2009b update for ASME III [3]. This presentation will discuss and take a critical position to such modifications into the ASME code.

Aim of the current presentation is to test and discuss the existing and proposed design criteria. For that purpose relevant material batches, which would be ready for plant use are needed[4]. Experimental strain life fatigue data was determined to be used as a base line for component specific evaluations and for comparison with the reference curves. Monotonic and cyclic stress strain responses were analyzed to clarify the deformation and fatigue mechanisms for the studied stainless steel grades. Understanding of fatigue mechanisms is needed in evaluating applicability of design criteria for different grades and manufacturing batches of stainless steel.

2. Design curves for stainless steel

Fatigue design curves given in the ASME Code Section III were derived from reference mean curves proposed by Langer. They are based on strain controlled low cycle fatigue tests in room temperature. Arbitrary design margins, 20 against life and 2 against strain, were considered appropriate for ensuring transferability of the data to plant components [1].

2.1 Relevant curve as design basis

Consideration of operation environment is a good example on the generic problem of selecting the design basis. The code itself does not give specific curves or factors for adopting influence of reactor coolant to fatigue calculation. Moderate environmental effects are accounted for through the design curve definition (within the margin of 20 in life), but the responsibility of considering eventual environmental effects was left to the designer as clearly stated in the ASME (1972) Criteria Document for the ASME III Design by analysis procedure as follows: “protection against environmental conditions such as corrosion and radiation effects are the responsibility of the designer” [1].

It is obvious that the designer may choose to use an appropriately determined and more relevant experimental curve. This is literally recommended by STUK

[4] Finding of relevant nuclear grade steel samples turned out to be surprisingly difficult, but two completely relevant batches were obtained.

(2002) in the Finnish YVL guide for ensuring strength of NPP pressure equipment. According to YVL guide 3.5, “fatigue assessment shall be based on S-N -curves applicable to each material and conditions” [4]. However, an effect corresponding to modification of design curve can be realised through appropriate factors. For example, F_{en} is used in case of environmental effects.

2.2 Air curve for stainless steels by NRC (2007)

The development of the ASME code was focusing on severe but rare thermal transients that can cause notable low cycle fatigue damage in heavy equipment. Later on, higher numbers of small stress cycles acting in the piping have been addressed, in particular for small bore pipes. Simultaneously fatigue tests have been conducted to longer lives. Encouraged by new experimental data and the proposal by Chopra and Shack in NUREG/CR-6909 [5], the US NRC endorsed a new air curve for stainless steels as part of a Regulatory Guide 1.207 for new designs in USA [6].

It should be noted that in the LCF regime all air data for austenitic stainless steels lie practically within a common scatter band and the later proposed curves do not much differ from the Langer curve. The difference grows to an order of magnitude in life in the HCF regime ($N_f > 10^5$ cycles), where the “Chopra curve” – and also some other published data, e.g. by Jaske, Higuchi, Solomon and others [7–9] – becomes more conservative.

2.3 New air curve for stainless steels in ASME III (2009)

The 2009b update [3] of ASME III introduces a new set of fatigue design curves. The new curve for austenitic stainless steels is exactly matching with the one introduced in NUREG/CR-6909 [5] and subsequently endorsed by the NRC [6].

The new curve is compared to the previous one in Figure 1, where the reference mean curves and design curves are given for both cases. Based on new reliability analysis, the margin in number of cycles was reduced from 20 to 12, but the design margin in stress (or strain) amplitude direction remained as 2.

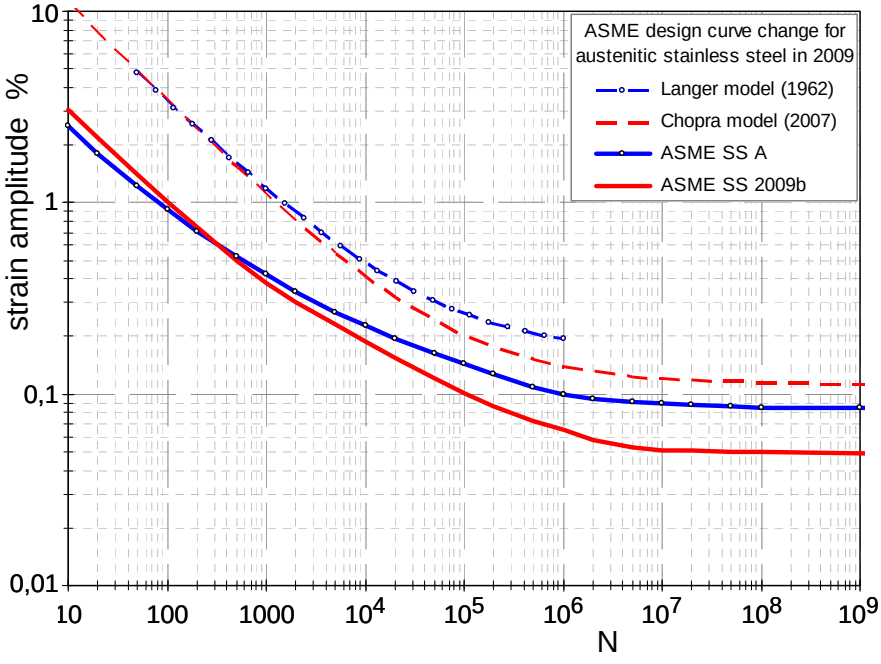

Figure 1. Traditional and new fatigue design curves for austenitic stainless steels.

3. Experimental results

3.1 Test materials

Two fully relevant material batches are currently being studied at VTT. A comprehensive reference fatigue curve was determined for a solution annealed niobium stabilized austenitic stainless steel (X6CrNiNb1810 mod). It was received as a $\phi 360 \times 32$ mm pipe, which fulfils all KTA material requirements for primary components in BWR and PWR [10]. So far, a few fatigue tests have been performed for a titanium stabilised steel (08X18H12T; $R_{p0.2}$ = 284 MPa; R_m = 510 MPa) in form of a ϕ460x32 mm pipe, which fulfils all requirements for primary piping in VVER. Additional data for materials (including 316 and 316NG) obtained as small scale bars would support the current discussion, but emphasis is given for the NPP relevant batches, and in particular, for the Nb stabilised steel, which was more extensively tested.

Tests were performed in a MTS 100 kN rig with precision alignment grips. Alignment of load train was adjusted with the help of strain gauged specimens

according to the ASTM E 1012-05 procedure.[5] Strain controlled low cycle fatigue tests were performed according to the ASTM E 606 procedure using sinusoidal waveform. The LCF specimen dimensions are shown in Figure 2. For further experimental details, see [10].

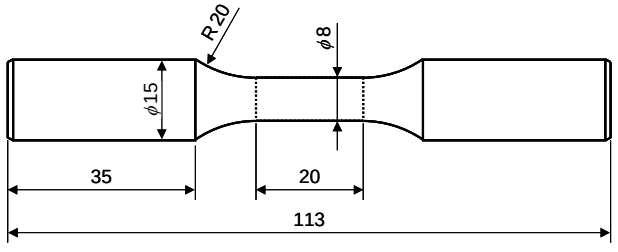

Figure 2. Fatigue specimen and dimensions in mm.

3.2 Stress strain response

Results of monotonic stress strain measurements together with the material specification report on the tensile test results for the niobium stabilized austenitic stainless steel are summarized in Table 1.

Table 1. Tensile test results for the niobium stabilized steel [10].

Data source	E	$R_{p0,2}$	UTS
minimum of 5 tests	195 GPa	224 MPa	535 MPa
maximum of 5 tests	201 GPa	249 MPa	559 MPa
average of 5 tests	197 GPa	238 MPa	544 MPa
material report / pipe	-	239 MPa	548 MPa
material report / melt	-	251 MPa	544 MPa

[5] Importance of alignment is emphasised, because of care needed and consequences. Insufficient alignment would lead to decrease of fatigue endurance in HCF regime.

3.2.1 Hysteresis loops

The stress strain responses can be studied through hysteresis loops and hardening softening curves. During a constant strain amplitude test stress amplitude and mean stress depend on the material response. Hysteresis loops at half-lives ($N = N_{25} / 2$) of tests for the niobium stabilized steel at different strain amplitudes are shown in Figure 3. The general tradition of reporting the half-life data is applied here, although this practice may be questioned for stainless steels. The cyclic response does not stabilize as assumed for the standard half-life definition of stress strain response.

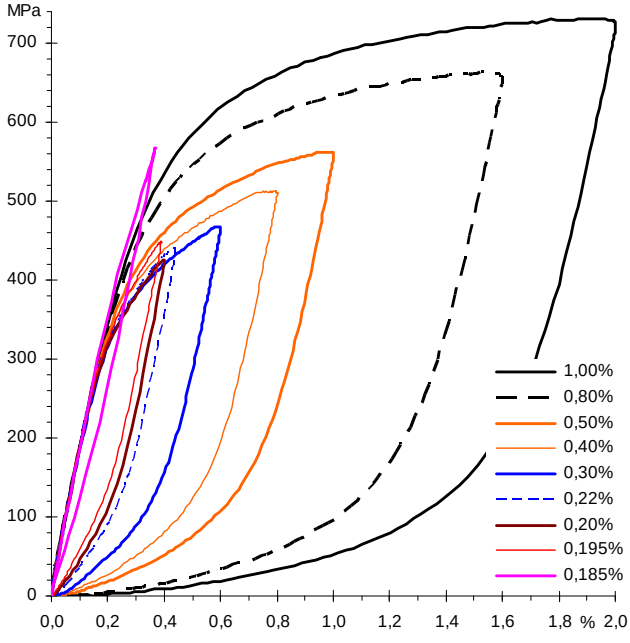

Figure 3. Hysteresis loops at half-lives for the niobium stabilized steel [10].

The hysteresis loops in Figure 3 were positioned to reveal different strain hardening paths in tensile direction. According to Bayerlein et al. [11], different strain hardening paths (non-Masing behaviour) indicate that the dislocation microstructures and/or cyclic deformation mechanisms are amplitude dependent. But for many austenitic stainless steels the deformation mechanisms change even during a single test. Figure 4 shows evolution of hysteresis loops during a constant amplitude test at the endurance limit region. More than one third of the

total strain (ε_a = 0.185%) was inelastic before secondary hardening eliminated most of the hysteresis.

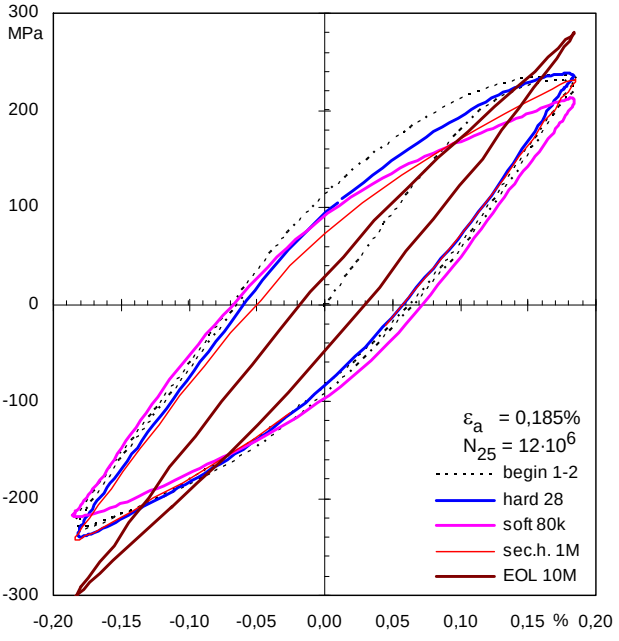

Figure 4. Hysteresis loops at different stages of a low strain amplitude test.

3.2.2 Cyclic softening and hardening

Change of cyclic stress response during a test is best visualized by softening - hardening curves. They show stress responses ($S_a = \Delta S / 2$) as a function of number of cycles during constant strain amplitude tests, Figure 5.

Consistent and well repeatable cyclic stress strain responses including initial hardening, softening and secondary hardening were observed for both steels. Dislocation density and internal stresses are increased during the first 10 to 50 hardening cycles. Subsequent dislocation activity utilizes the driving force and repeated opportunities to optimize the dislocation structures. This is seen as cyclic softening, which lasts for 2 000 to 100 000 cycles depending on the strain amplitude. During softening the stress response may be lowered below that for the soft annealed material. When strain amplitude is low enough to provide long life before cracking, softening is followed by secondary hardening.

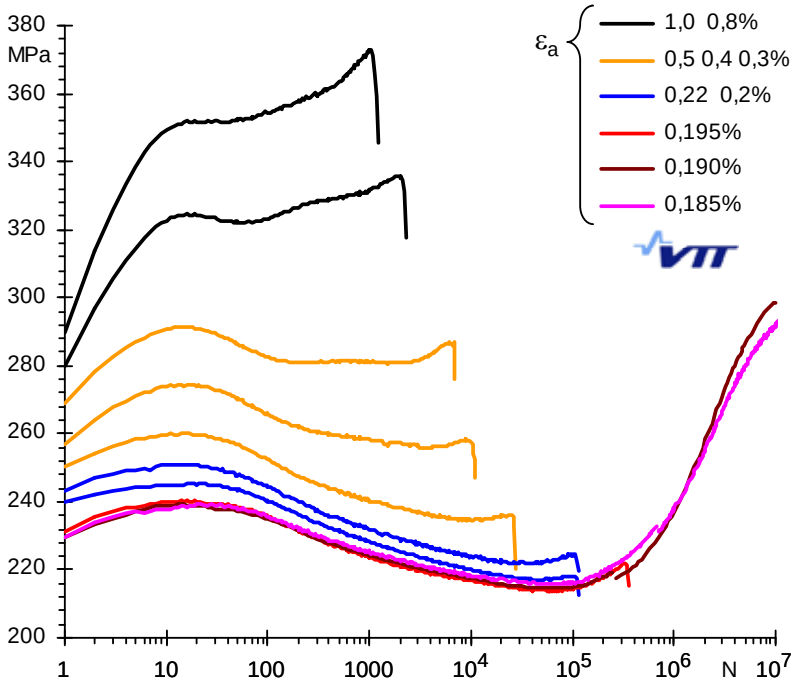

Figure 5. Hardening – softening curves for the niobium stabilized steel [10].

3.2.3 Elastic modulus

The elastic modulus of the niobium stabilised stainless steel was determined to 197 GPa, but unloading – reloading modulus was not constant. The apparent elastic modulus reached a maximum just when small scale yielding began (well below $R_{p0,2}$) and then gradually decreased with increasing strain. A decrease of modulus was observed also in cyclic straining, when linear parts of the hysteresis loops were consistently determined from a huge amount of loops.

As the results deviate from the standard elastic modulus, we assign them as “apparent modulus”. A drop of this apparent modulus was systematically observed at all strain amplitude levels and during the whole fatigue life as demonstrated in Figure 6.

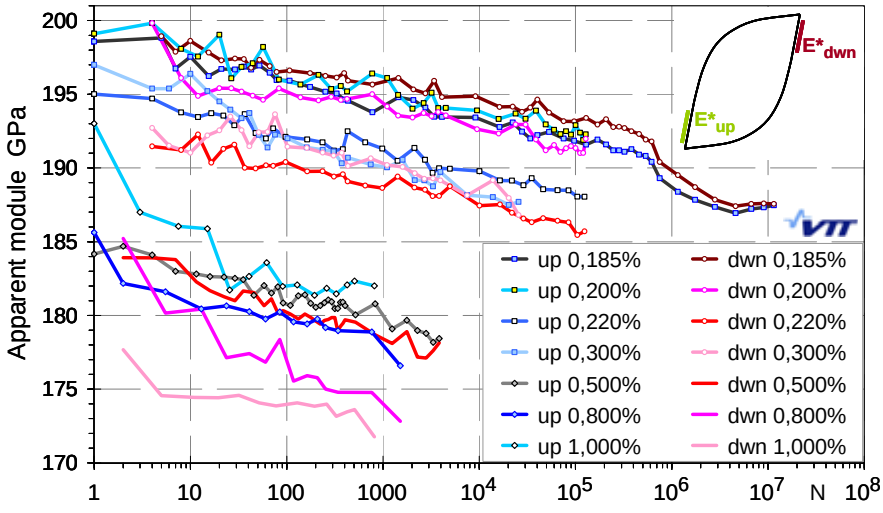

Figure 6. Change of modulus in increasing and decreasing ramps during cyclic straining.

3.3 Strain-life curves

For the studied stabilised steels obtained fatigue lives are summarized in Figure 7. The individual data points are shown together with the reference curves by Langer and Chopra. Also the traditional and recently modified ASME design curves are shown. Our data is within the scatter band of Langer's data set and well above the traditional ASME design curve.

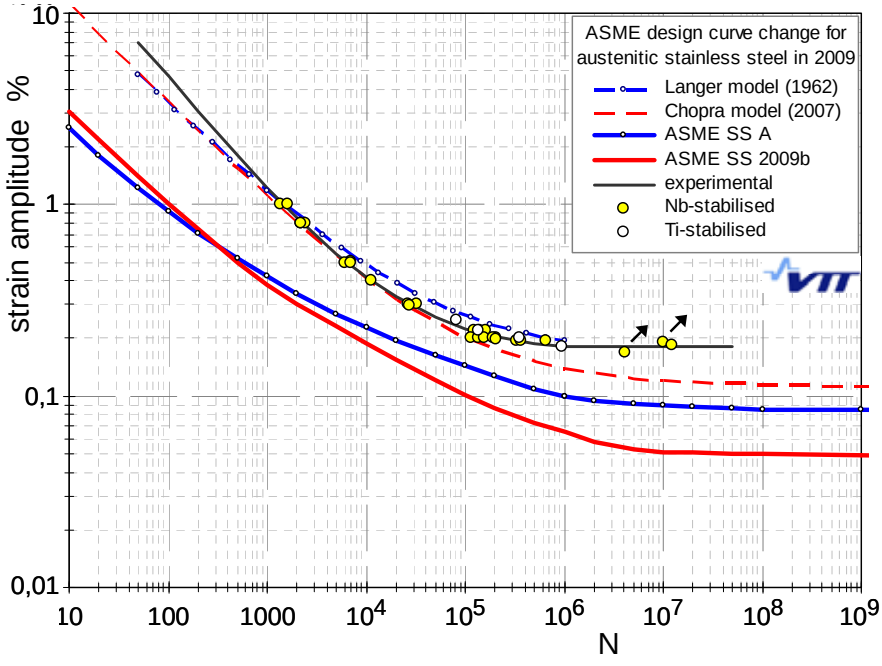

Figure 7. Strain life data for two relevant primary piping steels compared to ASME 3 design curves and reference curves behind the old and new design curves.

4. Discussion

4.1 Comparison of old and new design curves

The new curve was compared to the previous one in Figures 1 and 7, where the reference mean curves and design curves were given for both cases. The reference curves are identical in short lives (LCF) region, but based on new reliability analysis, the margin in number of cycles was reduced from 20 to 12 in NUREG/CR-6909 [5] and thus the new curve gives longer lives in the very low cycle region. However, the design margin in stress (or strain) amplitude direction was not similarly considered and it remained as 2.

Together with lowering of the reference curve, this has a notable effect in usage factor calculation. As shown in Figure 8, there is no change at 0.6 % strain amplitude, but for lower amplitudes the usage factor needs to be multiplied by an increasing number, when switching to the new curve. The change is shown also in terms of allowable strain.

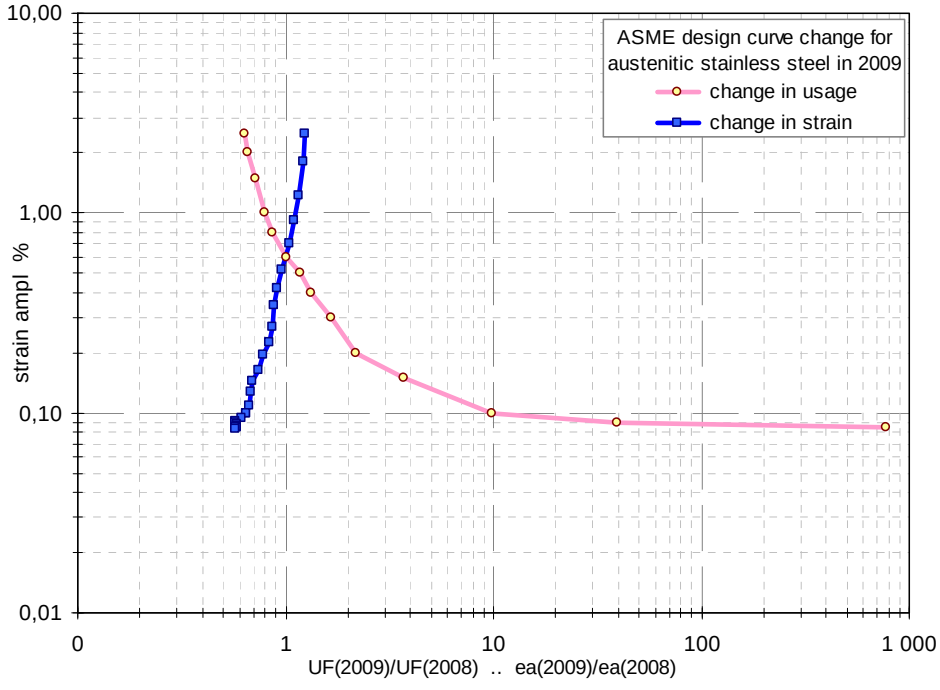

Figure 8. Effect of new fatigue design curve for austenitic stainless steels in terms of change in fatigue usage factor and allowable strain amplitude to provide similar usage.

4.2 Comparison of experimental and design curves

For the niobium stabilised steel determined mean curve[6] is shown in Figure 9 together with the mean curve model developed by Chopra for various grades of stainless steels (304, 316, 310, 347, 348, …) [5]. Our data is within the same scatter band in LCF regime, but scales off in HCF. A remarkable difference is seen for long lives ($N_{25} > 10^5$). For comparison with the design curve endorsed by NRC [6] for new designs in US – and included in the ASME 2009b update [3], we determined an experimental design curve with the design margins proposed by Chopra [5]. We can see in Figure 9 that the NRC design curve would be very conservative for this particular material batch in HCF.

[6] Some data points should be marked with validity concerns, because the crack locations may have led to early acceleration of crack growth and reduced total life, but even those data points were included in determining of the mean curve.

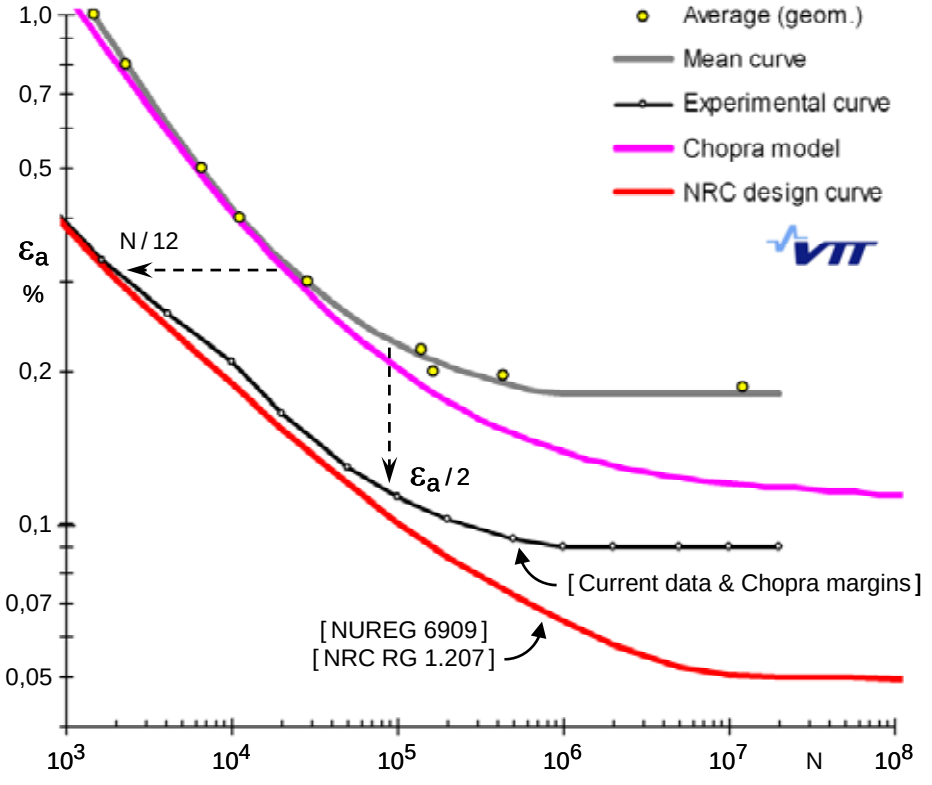

Figure 9. Comparison of experimental curve for Nb stabilised steel with the new design curve by NRC and in ASME 2009b. [12]

Our current data for the stabilized steel has a low slope and extends even above the Langer curve in high cycle region, Figure 7. Good HCF properties for these grades can be explained by a hardening effect of carbides and with the general correlation of material strength and strain life curve slope, Figure 10. According to the model, it may be assumed that harder grades of otherwise similar materials exhibit superior HCF strength.

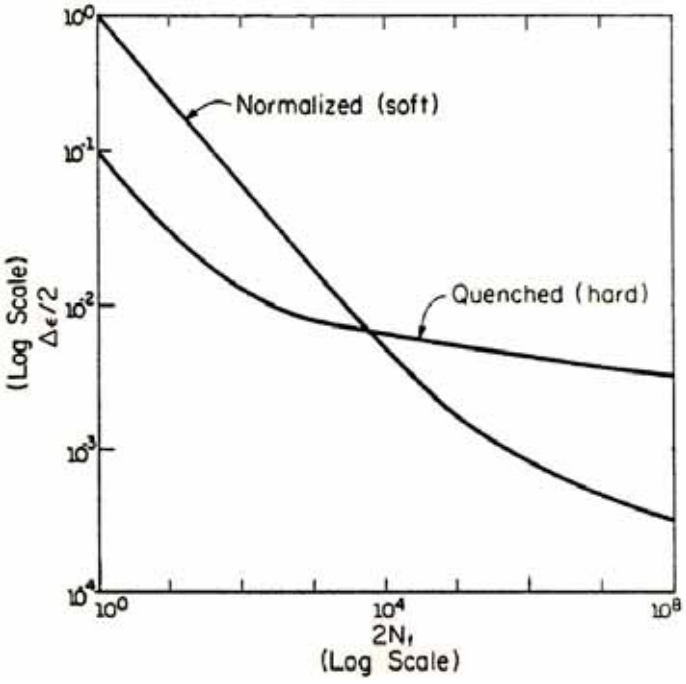

Figure 10. Comparison of strain-life curves for hard and soft material as observed for ferritic steels [13].

4.3 Endurance limit

In addition to good HCF performance, the strain-life curve for the studied steel grades seems to turn horizontal. This phenomenon deserves a closer look.

4.3.1 Hardening, softening and internal stresses

Austenitic stainless steels are known for strain hardening and ability to generate large internal stresses by plastic strain. But they also exhibit cyclic softening as seen above. Evolution of microstructure and internal stresses cause changes in hysteresis loop shape. Rearrangement of elastic and plastic strain components[7] is particularly notable during the secondary hardening phase of long life tests and can be seen as narrowing of the hysteresis loops, Figure 4.

[7] When their sum, total strain amplitude is constant.

Kuhlmann-Wilsdorf and Laird [14] divided the shear stresses acting on the slip planes into thermal (rate dependent) “friction stress” and athermal (elastic type) “back stress” rising from short distance dislocation motion. The friction and back stress components can be used for modelling hysteresis loops.

4.3.2 Origins of fatigue limit

The range of linear elastic stress strain response is very small for solution annealed austenitic stainless steels. Notable amount of inelastic strain and hysteresis occurs even at low strain amplitudes leading to immeasurable fatigue lives. But in spite of this, fatigue limit type behaviour[8] is prominent as the strain life curve turns horizontal.

Secondary hardening is observed in long or infinite life tests. Together with decrease of apparent modulus, secondary hardening leads to decrease of inelastic (plastic) strain during the test. Precipitates, dislocation density and microstructure influence hardening. The simultaneously created sub-grain internal stresses probably cause evolution of the apparent modulus, which may actually be just another manifestation of the back stress. But in any case, change of modulus is another contributor to transformation of plastic strain into elastic.

To demonstrate importance of apparent modulus change, let us consider the end-of-life hysteresis loop in Figure 4. The total strain amplitude can be divided into plastic and elastic strains to get:

$$\varepsilon_{tot} = \varepsilon_{pl} + \varepsilon_{el} = 0{,}025\% + 0{,}160\% = 0{,}185\% \quad (1)$$

A 5 % drop of apparent elastic modulus during this test can be deduced from Figure 6. So, if we assume constant strain and stress amplitudes and increase the elastic modulus by 5 % corresponding to initial condition, we rearrange to

$$\varepsilon_{tot} = \varepsilon_{pl,0} + \varepsilon_{el,0} = 0{,}033\% + 0{,}152\% = 0{,}185\% \quad (2)$$

In other words, we obtained approximately a 1/3 change in plastic strain amplitude, just due to modulus change. This is already a significant contribution

[8] The term ”fatigue limit” might be used in this case, because the endurance limit value becomes insensitive to the cycle count beyond 10^6 cycles. Endurance limit is often defined as the amplitude leading to fatigue life of 10^7 cycles.

to reduce the fatigue damage rate. Together with cyclic hardening (increase of stress amplitude and change of loop shape) modulus change ensures that an endurance limit exists. As the specimen does not fail, secondary hardening and modulus drop get a chance to decrease the damaging inelastic strains, thus effectively ensuring that the specimen endures even longer. Further details and discussion on the secondary hardening phenomena go beyond this presentation, but it is worth of noting that it may occur also in operation temperatures.

4.4 Applicability of the new design curve

In recent decades, mitigation of susceptibility to stress corrosion cracking has been a major challenge for material scientists in the nuclear industry. Sensitization has been prevented by reducing carbon content of the steels. As a side effect, strength properties of the nuclear grade stainless steels (304L, 316L, 316NG, …) have changed. If the model in Figure 10 is applicable also for austenitic steels, evolution in material properties may partly explain reduction in HCF data in recent experimental data.

Together with other results[9] by Solin [15-16] the experimental results clearly demonstrate that different grades of stainless steels exhibit different fatigue performance, and that the new air curve is better applicable only to part of the stainless steel grades. Based on general experience, it seems probable that many soft grades developed particularly to exclude sensitivity to stress corrosion cracking will comply with the Chopra curve, but many grades used in the existing plants will not.

4.4.1 Different grades and different curves for different purposes

As the NRC emphasised, the Regulatory Guide 1.207 as such is applicable to new designs only. However, the same curve has now been imported to the ASME code, which is generally used also for assessing earlier designs.

As a consequence, questions arise:

[9] Only base materials are considered in this presentation, but the available data on weld materials indicate also good HCF performance, which is also expected for overmatching strength welds.

- Which curve should be used for fatigue assessment of existing NPP components?
- or new components made of steels grades with good HCF resistance?

To motivate R&D efforts and optimisation of stainless steel fatigue properties, designers should be encouraged to consider and compare material specifications for different grades. Determining more relevant experimental curves for material grades to be used in building of new nuclear power plants is recommended. The updated code curve should not be considered mandatory, but it needs to be used, when relevant experimental data is not available.

Finally, our current results provide supporting arguments for use of stabilized stainless steels in components where high cycle fatigue ($\varepsilon_a \leq 0.5$ %) is a concern. Further research would naturally be recommended before final conclusions.

5. Conclusions

Strain controlled fatigue tests for austenitic stabilized stainless steels in room temperature air led to the following conclusions:

- The data demonstrates fatigue limit type behaviour for these materials.
- This limit coincides with a marked transition in cyclic stress response.
- Secondary hardening and drop of apparent elastic modulus reduce the inelastic strains and thus reduce further fatigue damage.

Our LCF data for stabilized austenitic stainless steels extends to very long lives, where it is in better agreement with the Langer curve than some newly proposed air curves. This means that the original basis of ASME 3 design criteria is valid for some material batches, which are completely relevant for NPP primary loop piping in certain operating PWR's.

Applicability of the new air curve endorsed in NRC RG 1.207 and recently adopted also into ASME III (2009b) may be questioned for existing NPP's and also for new designs utilizing stabilised stainless steel grades. Determining more relevant experimental curves for material grades to be used in building of new nuclear power plants is recommended.

Acknowledgements

This presentation is part of the Finnish national research programme on nuclear power plant safety, Safir, funded by VTT, TVO, VYR and Fortum. However, much of the reported experimental data was separately funded by E.ON Kernkraft GmbH. The experiments were carried out at VTT by Mr. J. Alhainen and E. Arilahti. The analysis of results was partly funded also by the Academy of Finland decision 117700.

References

1. ASME 1972. Criteria of the ASME Boiler and Pressure Vessel Code for design by analysis in sections III and VIII division 2. Pressure Vessels and Piping: Design and Analysis, A Decade of Progress, Volume One. Pp. 61–83.

2. ASME, 2009. ASME Code Section III, Division 1, Draft code case N-XXX. Fatigue Design Curves for Light Water Reactor (LWR) Environments. 6 p.

3. ASME, 2009. ASME Code, Section III, Division 1, Appendices, Mandatory Appendix 1 Design Fatigue Curves. Addendum 2009b.

4. STUK, 2002. YVL-guide 3.5, Ensuring the strength of nuclear power plant pressure devices, issue 5.4.2002. (in Finnish, translations exist)

5. Chopra, O., Shack, W., 2007. Effect of LWR Coolant Environments on the Fatigue Life of Reactor Materials, Final Report. NUREG/CR-6909, ANL-06/08, Argonne National Laboratory. 118 p.

6. NRC, 2007. U.S. Nuclear Regulatory Commission Regulatory Guide 1.207, 2007. “Guidelines for evaluating fatigue analyses incorporating the life reduction of metal components due to the effects of the light-water reactor environment for new reactors”. 7 p.

7. Jaske, C. E. & O’Donnell, W. J., 1977. Fatigue Design Criteria for Pressure Vessel Alloys, Trans. ASME J. Pressure Vessel Technol. 99, pp. 584–592.

8. Higuchi, M. 2004. Japanese program overview. 3rd International Conf. on Fatigue of Reactor Components, 3.–6.10.2004, Seville, Spain, EPRI/OECD, 15 p.

9. Solomon, H., DeLair, R. E., Vallee, A. J. & Amzallag, C. 2004. 3rd Int. Conf. on Fatigue of Reactor Components, 3.–6.10.2004, Seville, EPRI/OECD. 22 p.

10. Solin, J., Nagel, G. & Mayinger, W. 2009. Cyclic behavior and fatigue of stainless surge line material (PVP2009-78138). Proceedings of ASME Pressure Vessel and Piping Division Conference, Prague, Czech Republic, July 26–30, 2009. 9 p.

11. Bayerlein, M., Christ, H.-J. & Mughrabi, H. 1987. A critical evaluation of the incremental step test. In: Rie, K.-T. (ed.). Low Cycle Fatigue and Elasto-plastic Behaviour of Materials. Essex, Elsevier. Pp. 149–154.

12. Solin, J., Nagel, G. & Mayinger, W. 2009. Fatigue curve and stress strain response for stainless steel (SMiRT 20-Division 1, Paper 3135). 20th International Conference on Structural Mechanics in Reactor Technology, Espoo, Finland, August 9–14, 2009. 10 p.

13. Bannantine, J. A., Comer, J. J. & Handrock, J. L. 1990. Fundamentals of metal fatigue analysis. Prentice Hall. ISBN 0-13-340191-X. 273 p.

14. Kuhlmann-Wilsdorf, D. & Laird, C. 1979. Dislocation behavior in fatigue II: friction stress and back stress as inferred from an analysis of hysteresis loops. Materials Science and Engineering 37, ss. 111-120.

15. Solin, J. 2006. Fatigue of stabilized SS and 316 NG alloy in PWR environment. Proceedings of PVP 2006-ICPVT11 2006 ASME Pressure Vessel and Piping Division Conference, July 23-27, 2006, Vancouver, BC, Canada. Paper PVP2006-ICPVT11-93833.

16. Solin, J., Alhainen, J. & Karlsen, W. 2009. Fatigue of primary circuit components (Fate-Safir) – cyclic behaviour and fatigue design criteria for stainless steel. SAFIR2010 – The Finnish Research Programme on Nuclear Power Plant Safety 2007–2010, Interim Seminar, 12–13.3.2009. 13 p.

Description of the Posiva repository for spent fuel

Heikki Raiko
VTT Technical Research Centre of Finland
Espoo, Finland

Abstract

In Finland, the spent nuclear fuel will be emplaced in the bedrock at a target depth of 420 metres. Posiva Oy is the company responsible for high active nuclear waste management in Finland. Currently, an underground rock characterization facility ONKALO is under excavation since summer 2004 at the selected final disposal site Olkiluoto on the west coast of Finland. Construction of the actual final disposal facility will begin after the accepted construction license that will be applied by the end of 2012 and the facility is planned to be operational in 2020. According to the present plans, the final disposal will be implemented in a way that fuel bundles as a whole will be sealed in canisters that are made of nodular cast iron, enclosed in a corrosion resistant, 50 mm thick copper shell. The canisters will be emplaced in holes drilled at the bottom of the tunnels excavated in the bedrock. The canisters are surrounded with compacted bentonite clay. Deep repository prevents unintentional human intrusion into the final disposal facility and the depth will damp the possible effects acting on ground surface even in very long time perspective. The disposal facility is described in more detail in the reports named in Reference list. The Finnish design is nearly similar to the Swedish concept introduced by Swedish Nuclear Fuel and Waste Management Co (SKB). Posiva and SKB are in close co-operation in developing of the concept and technology.

The materials technology challenge in the spent fuel disposal is concentrated on the manufacture, sealing and inspections of the iron-copper canister that is expected to survive for 100 000 years in the reposity conditions.

1. Introduction

In Finland, there are two companies producing electricity using nuclear power, Fortum Power and Heat Oy (Fortum) and Teollisuuden Voima Oyj (TVO). Under the Nuclear Energy Act, Fortum and TVO are responsible for the safe management of the waste and for all associated expenses. Each company is responsible for processing and disposal of its own low and medium level radioactive waste, as well as for all operations included in the decommissioning of the plants. Posiva Oy, a joint company owned by Fortum and TVO, is responsible for research and technological development concerning spent fuel disposal, as well as construction and operation of the disposal facility. All existing and future spent nuclear fuel from the Loviisa and Olkiluoto plants is to be disposed of in the Finnish bedrock. Parliament approved in 2001 the Government's Decision in Principle on Posiva's application for a construction licence for a disposal facility for spent.

When providing for disposal to be carried out in Finland, the starting point is that spent fuel removed from the reactor shall be stored in interim stores until the disposal operation starts in 2020. Before 2020 the spent fuel will be temporarily stored in intermediate stores in the plant areas.

TVO and Fortum shall be prepared to submit clarifications and designs required for the construction licence for a spent fuel disposal facility by the end of 2012, on the basis of which the disposal can take place in 2020.

2. Starting point for design

2.1 Safety concept for disposal

Posiva's repository design is based on the KBS-3 concept, which was developed by the Swedish SKB. The disposal concept and the repository are based on the multi-barrier principle, in which several engineered barriers support one another so that insufficiency in the performance of one barrier (or subsystem) does not jeopardize the long-term safety of the disposal system.

The safety concept starts from the premise that the repository materials are available in nature. Safety is achieved under the natural conditions of the deep bedrock during the construction of the repository, as well as under future conditions caused by climatic change. Furthermore, the repository design leans on simple subsystems, on the coherent results of a long-term programme of

research and on the knowledge that proven technology for implementing the repository is available. The safety concept reflects the view of how long-term safety can be achieved, taking into account existing constraints related to disposal and by using technical solutions that meet the requirements imposed by Posiva.

2.1.1 Long-term safety issues

The safety concept is based on long-term isolation and the disposal system is planned to retain radioactive releases within the geosphere and the biosphere for at least 100 000 years. The underground repository is built at a depth of 420 meters. The spent fuel assemblies are placed into copper canisters. Before the canister is emplaced into a deposition hole, the deposition hole is lined with highly compacted bentonite blocks to fill the empty space between the disposal canister and the bedrock. The disposal tunnels and the surface connections are backfilled and sealed.

The backfilling ensures the restoration of the natural state of the repository and the surrounding bedrock and prevents the excavated rooms from becoming conductors for groundwater. The backfilling also prevents unauthorized access to the repository.

For as long as the copper canister remains intact the interaction of the spent fuel with its surroundings takes place only in the form of thermal flows and by small amounts of gamma- and neutron radiation that penetrate the canister's wall.

2.1.2 Olkiluoto baseline and monitoring of changes

The baseline conditions at Olkiluoto have been comprehensively studied and investigated prior to construction to distinguish how the excavation of the ONKALO and the repository will affect the bedrock and the groundwater conditions. At later stages and partially already now the selected follow-up points are monitored and the values are compared with the reference values from the baseline studies.

2.1.3 KBS-3 concept

This facility description presents the disposal concept or the basic concept that is based on the long-term isolation with multiple engineered barriers complementing

each other, where the engineered barrier closest to the spent fuel, i.e. the canister, is emplaced in the deposition hole drilled to the solid bedrock.

According to the disposal concept, the spent fuel assemblies are installed and enclosed within the cast iron insert, which is surrounded by a copper canister. The copper canister lid and the shell are sealed tightly, so that the groundwater flowing in the bedrock does not come into contact with the cast iron insert or the spent fuel. This ensures isolation of the spent fuel and prevents release of radionuclide to the groundwater and thereby to the geosphere and to the biosphere. The single copper canisters are emplaced in the deposition holes at the bottom of the excavated disposal tunnels in the solid bedrock at a depth of 420 meters. Each vertical deposition hole is lined with bentonite, i.e. swelling natural clay material that serves as a buffer material between the host rock and the canister. Once the canister has been emplaced in a deposition hole lined with bentonite, an additional bentonite buffer is placed on top of the canister in order to fill the hole up to the level of the disposal tunnel floor. The purpose of the bentonite, after being saturated, is to severely limit the flow of groundwater around the canister, to conduct the heat produced by the spent fuel from the canister to the rock, to provide sufficient permeability to gases that are mainly formed inside the canister as a result of corrosion and, simultaneously, to absorb radio-nuclides, which could be released from the canister. The bentonite also provides mechanical support to the canister so that it remains in its original position. Bentonite, which is more elastic than the canister and the bedrock, protects the canister against minor rock movements. The near-field bedrock surrounding the deposition hole protects the canister against unfavourable disposal conditions and, as the last release barrier; the rest of the surrounding bedrock retards and dilutes any release of radio-nuclides from the canister.

The disposal tunnels will be filled with compacted blocks of expanding clay, which will ensure that the bentonite buffer, while swelling, stays in the deposition hole and will prevent the disposal tunnels from becoming preferential conductors for groundwater. The backfill will also prevent unintentional and un-declared intrusion into the repository. The following describes the technical design, subsystems, operational requirements and operation principals related to the different release barriers.

2.1.3.1 Canister

The purpose of the canister, as an airtight and watertight unit, is to insulate the spent fuel. After several decades in interim store the spent fuel assemblies are loaded into a cast iron insert, which is surrounded by a copper overpack. The empty space inside the canister is filled with an inert gas in order to decelerate and minimize the internal corrosion caused by moisture and radiation.

The canister has to meet the following requirements:

- the corrosion lifetime in the bedrock conditions shall be at least 100 000 years
- the canister shall be mechanically robust, i.e. it shall tolerate handling operations, deformations, internal pressure, hydrostatic pressure, swelling pressure of the surrounding buffer, minor rock movements and the load caused by future glaciations
- the sealing method shall not reduce the required long-term performance of the canister
- the canister shall have sufficient radiation shielding and thermal conductivity properties
- the cast iron insert shall provide a significant chemical buffering capacity.

Furthermore, the spent fuel isolated in the canister shall be and remain sub-critical. Manufactured prototype canister can be seen in Figure 1.

2.1.3.2 Buffer material and backfill materials

Buffer material is used in the deposition hole where its function between the canister and the rock is

- to isolate the copper canister from the near-field bedrock and the processes in it
- to support the canister in its installation position
- to absorb minor near-field rock movements
- to prevent groundwater flows in the gap between the canister and the bedrock in such a way that mass transport (most significantly radio-nuclide transport) between the bedrock and the canister occurs mainly by diffusion.

Figure 1. Canister insert for BWR-fuel made of nodular cast iron on the right and a copper overpack on the left (H. Raiko).

The buffer material is bentonite, which is installed into the deposition hole around the canister. Bentonite is clay which, after saturation, swells and becomes plastic.

A disposal tunnel is backfilled after emplacement of all canisters and the installation of the buffer material, and this backfilling is carried out in stages throughout operation of facility. Finally, the surface access routes, i.e. the access tunnel and the shafts, are backfilled as the disposal process is complete.

2.1.3.3 Bedrock in the near field and in the disposal area

The main functions of the bedrock as part of the multi-barrier principle are:

- to isolate the repository from the biological environment and to protect it against external impacts and processes taking place near the ground surface
- to provide favourable and predictable mechanical, chemical and hydro geological conditions for the long-term isolation of the canister and the buffer and backfill material

- to limit the amount of groundwater coming into contact with the buffer and the canister and
- to retard and retain potential releases from the repository.

The host rock that is suitable for disposal is also well suited for the construction of underground spaces. The repository design aims to avoid fracture zones in the bedrock and mechanically or chemically unstable areas, as well as major water flow paths.

2.2 Design basis

2.2.1 Legislative requirements

The Government Decision dating from 1999 for the safety of spent fuel disposal is of particular importance to the disposal facility. In this decision, the dose limits for the disposal facility are stricter than those given to nuclear power plants. Radiation and Nuclear Safety Authority (STUK) specifies the regulations given in Government Decision (1999) and points out that the disposal shall not under any assessment period have such an impact on health or the environment that would exceed the maximum level regarded as acceptable during the disposal implementation.

2.2.2 General design basis

The purpose of the spent fuel disposal facility is that the nuclear fuel assemblies generated in Finnish nuclear power plants are encapsulated in a form necessary for permanent disposal and are permanently disposed of in Finnish bedrock.

The disposal facility consists of two parts:

- facilities above ground, of which the most important building is the encapsulation plant. In the encapsulation plant, the spent fuel from Loviisa and Olkiluoto nuclear power plants, after having cooled in interim store facilities over several decades, is received, dried and packaged into disposal canisters
- repository, which consists of tunnels and deposition holes in the deep bedrock, where the spent fuel, packaged into canisters, is emplaced. Also necessary underground auxiliary rooms and access routes are included.

The total land area of the facility above ground, i.e. the area for buildings, roads, stores and fields, is approximately 15 hectares. There is one access tunnel leading from the surface to the repository plus the required number of vertical shafts for ventilation, personnel and canister transfer.

2.3 Timetable for disposal operations

Currently in the facility design, the expected operating lifetime for the Loviisa units is 50 and for the Olkiluoto units 60 years. Therefore Loviisa units would cease operation around 2030 and Olkiluoto units around 2040. Currently, a third unit (Olkiluoto 3) is under construction in Olkiluoto and the spent fuel from it is also planned to be disposed accordingly in the same repository.

The preliminary timetable is based on the above-mentioned calculations. Because the decay heat is governing the time when each canister can be disposed, this leads to that the spent fuel from each plant unit has to be disposed of at the same rate as it is being generated. Therefore, the total span of time needed for the disposal operations is about 100 years, at least.

3. General description of the disposal facility

The disposal facility consists of surface structures, buildings and related components, an underground repository and its access and maintenance routes. Besides traffic arrangements (roads and parking areas), the surface structures, buildings and related components include:

- encapsulation plant and operating building
- ventilation shaft building
- research building (incl. warehouse)
- building for tunnel technique (for the repository)
- repair shop
- information building
- crushed rock storage area and crusher station
- bentonite container storage area
- backfill material mixing station
- fuelling station and storage tank.

The underground repository consists of the following components and rooms:

- canister shaft and personnel shaft with lifts
- ventilation shafts
- access tunnel
- repair shop and washing and refuelling hall for vehicles
- central tunnels
- characterisation tunnels and levels
- disposal tunnels and deposition holes
- parking hall
- operation and decommissioning waste hall at about -200 m level
- testing and demonstration rooms
- rescue chamber/office, brake and personnel rooms
- technical rooms, such as pumping station and sedimentation pools, fire-fighting water pools, electrical rooms and technical rooms.

The most significant stages in the operation of the disposal facility are waste transport, encapsulation, canister transfer and canister emplacement in the deposition holes. Several preliminary stages are needed to support these operations, as described below.

Spent fuel generated in the nuclear power plants and cooled in the interim stores is transported from the Loviisa and Olkiluoto interim stores in transport casks to the encapsulation plant.

In the encapsulation plant, the transport cask is opened, spent fuel assemblies are lifted from the casks to be dried in the autoclave and placed into the canisters. The canister lid is sealed by welding, the weld surface is machined and the weld quality inspected. The canister that has passed inspection is transferred into the encapsulation plant's buffer store.

Canisters, which are ready for disposal, are transferred from the buffer store down to the repository using a canister lift. An optional way to transfer the canister down to the repository is to use a transfer vehicle and the access ramp. In the repository, the canister is moved from the lift to the canister transfer and emplacement vehicle and transferred to the deposition hole in the disposal tunnel in order to be emplaced. The same vehicle is used for both emplacement and transfer of the canister. Before the canister is emplaced in the deposition hole, the vertical hole is lined with bentonite discs and rings. When the canister has been lowered into the hole, bentonite blocks are placed on top of the canister using a special vehicle.

Disposal tunnels are backfilled gradually as canisters are disposed of in them. Before filling, ventilation, electricity and water systems are removed from the disposal tunnel, and the tunnel is cleaned. During the operational stage, new disposal tunnels are excavated gradually as they are needed. Canister deposition holes are bored with full profile boring in the disposal tunnel floor.

4. Structure of the disposal facility

4.1 Surface structures and buildings

The disposal facility at Olkiluoto comprises an independent operating system located above the repository. At the early stage of plant operation, the disposal facility and facility area utilize the existing infrastructure of the Olkiluoto nuclear power plant.

4.1.1 Encapsulation plant

The encapsulation plant is the most important building of the disposal facility. The interim store for bentonite blocks will be built in conjunction with this plant. According to the preliminary plans, the encapsulation plant is 65 meters long and 36 meters wide. The building is approximately 15 meters high and the building volume is approximately 40 000 m^3. The building will have six storeys.

Heavy traffic will be limited to the ground level of the plant through doors opening directly out. Fuel transport casks are delivered to the reception area by a road transport trailer. The reception area is a drive-thru area. New disposal canisters are transferred to the plant by lorry.

The average encapsulation rate at the encapsulation plant is 40 canisters per year, with the maximum rate being 100 canisters per year.

The encapsulation plant is designed in compliance with all current safety regulations so that in the event of disturbance or accident, the release of radioactive materials into the environment remains insignificant. All operations in the encapsulation plant are to be carried out safely and without any significant releases and personal doses. Image from 3D plan of the encapsulation plant is shown in Figure 2.

Figure 2. Section of encapsulation plant (Posiva).

4.2 Repository

The planned total excavated volume of the repository for a 6 000 tU is approximately 1 110 000 m^3. The volume of momentarily open excavations at any time is a maximum of approximately 700 000 m^3.

Thermal analysis provides a starting point for repository design and has an important influence on the effectiveness of the disposal operation. These on the other hand affect the volume of rock reserve needed for excavating tunnels and the disposal facility lifespan.

In the one-storey layout option, all spent fuel is disposed of on one level. The repository length in a north-south direction is around 1.1 km and its width in an east-west direction around 2.2 km.

There are plans to make the repository wider, if the plans for additional nuclear power plant units are accepted and realised. The current layout of the repository is shown in Figure 3.

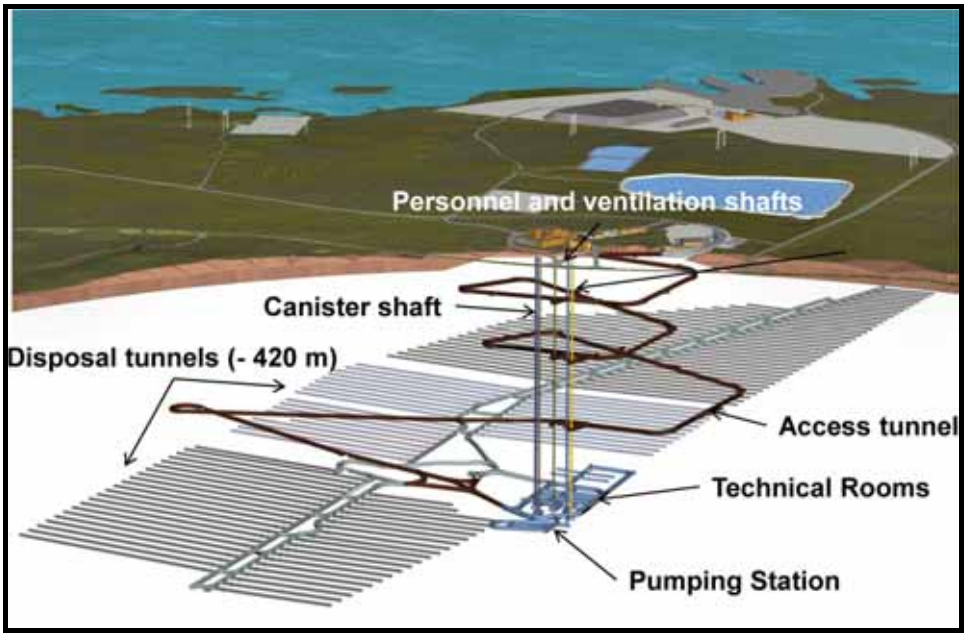

Figure 3. Section of repository with access and ventilation shafts. (Posiva).

4.2.1 Access routes

According to the current repository design, one access tunnel and several shafts (canister shaft, personnel shaft and ventilation shafts) are constructed. The access tunnel and the ventilation shafts are built in association with the construction of the ONKALO.

The access tunnel descends clockwise, making it possible for vehicles driving upwards to use the less steep outer curve of the tunnel. The access tunnel floor is made of concrete. Characterisation niches will be constructed at different depths in the access tunnel to investigate the bedrock. The access tunnel's length will be about 5 500 m with an inclination of 1:10, the excavation height will be 6.3 m (free height of 4.5 m), and the width 5.5 m. The tunnel is wider and has an increased gradient in passing lanes and around curves.

4.2.2 Central and disposal tunnels and other rooms for disposal operations

The repository comprises central tunnels, disposal tunnels and auxiliary rooms relating directly to the disposal operations and is divided into controlled and uncontrolled areas. The controlled area, which is part of the nuclear plant, comprises technical rooms, the canister shaft, the personnel shaft, part of the central tunnels and the disposal tunnels where spent fuel is disposed of in each operational stage.

5. Disposal facility operations

The disposal facility starts to operate in 2020 after the operating license under the Nuclear Energy Act has been obtained. The operation includes among other things encapsulation, canister emplacement, tunnel backfilling, construction during operation (repository enlargement), transfer and control.

5.1 Construction in phases

The actual implementation of the facility is carried out in phases. By the year 2020, only a small part of the disposal tunnels will have been constructed. Initially, disposal tunnels covering a few years' disposal needs will be constructed at level – 420 m. The need for heating, ventilation and seepage drainage is also lower, as the volume of excavated underground room open at the same time remains small. Constructing in phases also avoids need for construction overcapacity.

More rooms are excavated as the disposal progresses. Both disposal and excavation are thus being carried out at the same time, but in separate tunnels. The chosen implementation strategy determines the excavation and construction volume to be undertaken in an enlargement stage at a time.

5.2 Facility personnel

Some 120 persons with various tasks relating to facility operation, maintenance, control and administration will be working in the disposal facility. There are several different tasks and operations: spent fuel reception and encapsulation, disposal operation, control room operations, cleaning and maintenance of

premises and equipment, as well as administration and finance, radiation control, security operations and operations in the visitor centre.

5.3 Spent fuel transport and transfers to the encapsulation plant

Currently the spent fuel is stored in the interim stores in the Loviisa power plant at Hästholmen and in the TVO power plant at Olkiluoto. From these interim stores the spent fuel will be transported to the encapsulation plant in special transport casks as special transports.

5.4 Encapsulation plant operations

Fuel assemblies are transferred in transport casks from the spent fuel interim store and sealed in copper canisters in the encapsulation plant. In the hot cell, fuel assemblies are placed into the fuel channels inside the canister's insert. The canister lid is sealed by welding and the seam is inspected by an ultrasonic inspection device and with an X-ray system. If the inspection result meets the requirements, the canister is then ready for disposal and transferred to the buffer storage for transfer down to the repository. Otherwise the canister is sent back, either to be repaired or dismantled.

5.5 Canister transfers from the encapsulation plant to the repository

The canister is transferred to the repository by the canister lift or in an optional using a transfer vehicle and the access ramp. The canister lift's load needs to be minimised (lift total load is ca. 30 tonnes). The canister lift cage is a one-store cage. In the encapsulation plant and in the repository, the lift has two station levels: the lower level is for disposal canisters and the upper level for bentonite blocks.

In the encapsulation plant, the canister is taken to the canister shaft lift by an automatic guided vehicle. At the repository level, the same vehicle takes the canister out of the lift to the canister loading station and further to the canister transfer and emplacement vehicle.

5.6 Repository operations

5.6.1 Excavation and construction of the repository

The construction of the repository comprises excavation work, construction engineering works and mechanical works. Excavation work includes (among other things) excavation, reinforcement and the boring of deposition holes. Construction engineering includes building floors in the disposal tunnels, walls in the shafts and building pumping station and sedimentation pools. Mechanical works include the implementation of various systems, such as ventilation and electrical systems.

5.6.2 Canister emplacement

Emplacement of canisters starts in the tunnels nearest to the canister shaft. The deposition hole is lined with bentonite (bottom and sides) before the canister is emplaced.

The bentonite blocks are transferred in transfer frames from the encapsulation plant buffer store to the repository by the canister lift or via the access ramp. The bentonite blocks are moved from the canister lift lower station and taken to the deposition holes in the disposal tunnel and installed in the deposition hole by the transfer and installation vehicle for bentonite blocks. Canister installation vehicle and principle of canister disposal is shown in Figure 4.

5.6.3 Backfilling of disposal tunnels

The disposal tunnels are backfilled as canisters are emplaced in them. The canister disposal and the backfilling of tunnels can be processed in cycles. The cycle length depends on the desired disposal efficiency, but it cannot be much longer than one month. The disposal canisters should not be kept for weeks in open deposition holes, because the water inflow into the holes cannot be completely prevented before the tunnel above the hole is backfilled.

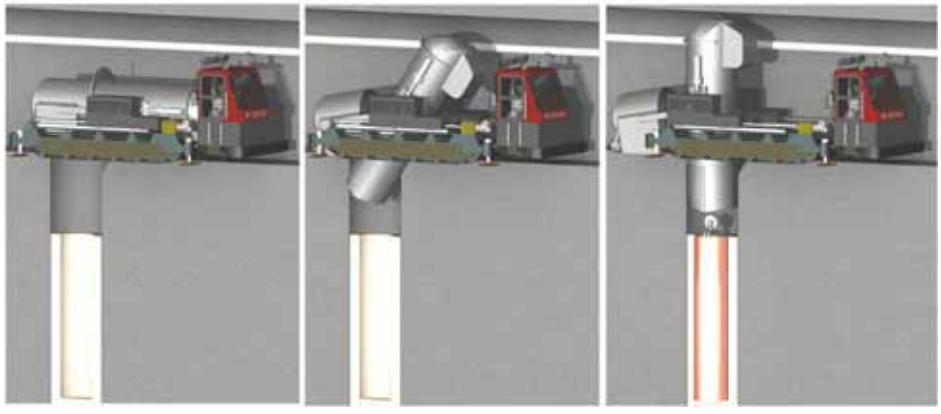

Figure 4. The canister transfer and installation vehicle is disposing the canister into the buffer lined disposal hole (Posiva).

6. Repository closure and retrievability

6.1 Closure in phases

The lifespan of the nuclear power plants of the different operators vary. In the disposal facility design, provisions are made for spent fuel from the different operators to be disposed of in such a way that the locations and numbers of the emplaced disposal canisters can be verified. Furthermore, all disposal canisters are to be emplaced in sealed disposal tunnels and the central tunnel or disposal panel tunnel connected to them shall also be sealed. Spent fuel from a single power plant or power plant unit will thus be disposed of behind two backfilled and sealed tunnels in the repository.

The closing of disposal panels is carried out by dismantling the built structures in the associated disposal tunnels and central tunnels, by backfilling the excavated rooms and by constructing the sealing plugs for the disposal tunnels.

6.2 Decommissioning

Decommissioning refers to the operations that are carried out after the operation of a nuclear facility has ceased. The nuclear facility is made environmentally safe by dismantling it and taking care of any waste that has been produced. The closure of the repository is carried out partly during the operational stage and partly during the decommissioning stage.

7. Summary

Spent fuel generated in TVO and Fortum owned nuclear power plants will be disposed of at Olkiluoto in Eurajoki. A disposal facility comprising an encapsulation plant on the surface, other buildings and structures on the surface and a repository in the deep bedrock will be built at Olkiluoto.

The repository planning has been divided into three-year periods and aims at being prepared for submitting an application for a construction licence to the authorities in 2012. This facility description is based on the preliminary design dating from 2009. The next updated facility design and facility description will be presented in 2012.

Posiva's disposal plan is based on the KBS-3 concept, or vertical disposal concept. Long-term safety is based on the multi-barrier principle, which refers to several release barriers that support one another so that insufficiencies in the performance of one barrier do not jeopardize the long-term safety of the disposal system.

For underground investigation purposes, the construction of the underground rock characterisation facility, the ONKALO, was started in 2004. The ONKALO was designed in such a way that it can later be used as part of the repository. The underground research aims to ensure the suitability of the chosen site by identifying the favourable parts of the rock mass for disposal by characterising the rock conditions in detail.

The repository and its operation are designed in accordance with existing legislation and regulatory guides concerning the use of nuclear energy. An access tunnel and three shafts with lifts provide access routes to the surface. Apart from the underground rooms for disposal operation, such as disposal tunnels and deposition holes in the disposal panels, central tunnels and auxiliary and technical rooms in the controlled and uncontrolled area will be provided. The repository will be enlarged in stages as disposal progresses. The access tunnel is mainly used for the transfer of large material flows, such as blasted rock, backfill material and building materials. The repository and the encapsulation plant will be constructed in late 2010s.

The aim is to start disposal facility operations in 2020. According to current knowledge, the disposal operations continue into the 2120s. At the start of operations, spent fuel from Loviisa and Olkiluoto power plants is transported in transport casks by road to the encapsulation plant. In the encapsulation plant, the transport casks are opened; the fuel assemblies are lifted out of the cask one at a

time and placed in a drying unit. After drying, the fuel assemblies are placed into disposal canisters.

The disposal canister comprises an inner nodular cast iron insert provided with a lid and an outer copper overpack, which is 5 cm thick and corrosion proof. The copper lid is sealed by welding. After weld machining and weld inspection, the canister that meets the criteria for disposal is transferred to the buffer storage in the encapsulation plant. From the buffer store, canisters are taken to the repository by the canister lift or via the access ramp. In the repository, the canister transfer and emplacement vehicle takes the canister from the lift to the deposition hole in the disposal tunnel. The same vehicle places the canister into the deposition hole bored in the rock. Before canister emplacement, the hole is lined with bentonite blocks and rings. After the canister has been emplaced, additional bentonite blocks are placed on top of the canister.

The disposal tunnels are backfilled as the canisters are emplaced. Before backfilling, the concrete floor and the ventilation, electrical and water systems are dismantled and the tunnel cleaned. The backfill material is spread and compacted into the tunnel. After the entire tunnel has been filled, a concrete plug will be built at the tunnel opening. During the operational stage, disposal tunnels are excavated as disposal progresses. Disposal is thus carried out in stages.

At the end of the disposal operation, the encapsulation plant is demolished and decommissioned appropriately. The repository and the access routes are backfilled and concrete structures will be built at tunnel openings; thus no subsequent monitoring has to be organised at the site in order to ensure long-term safety.

References

1. Tanskanen, J. Facility Description 2009. Working Report 2009-123. Posiva Oy, Olkiluoto. 164 p. (In Finnish)

2. Saanio, T., Ikonen, A., Keto, P., Kirkkomäki, T., Kukkola, T., Nieminen, J. & Raiko, H. Outline Design of the Disposal Facility 2009. Working Report 2009-60. Posiva Oy, Olkiluoto. 148 p. (In Finnish)

3. Kukkola, T. Encapsulation Plant Design – Outline Planning Stage – Repository Connected Facility. Working Report 2009-59. Posiva Oy, Olkiluoto. 62 p.

Dynamic behaviour of pipelines in power plants

Kim Calonius
VTT Technical Research Centre of Finland
Espoo, Finland

Abstract

Dynamic excitation due to a pipe break can cause pipe to abruptly displace and hit the components, instrumentation and equipment nearby. In order to minimize the risk of such damage by pipe whips in a power plant, different types of restraints and supports are designed for the pipelines.

The usability of different types of elements provided by Abaqus, a commercial general-purpose finite element code, in modelling the dynamic behaviour of pipelines is tested. A relatively short pipe line section with one bend and one restraint is chosen as a test case. Simple and typical nuclear power plant pipeline geometry and materials are chosen. The stiffness of the restraint as well as the flexural stiffness of the pipe cross-section are solved with static compression simulations with a detailed model using three-dimensional solid and shell elements. After that, the model is substituted with couple of simpler models using pipe and/or elbow elements for the pipe and a spring element for the restraint.

The eigenmodes of models are calculated and compared with each other. The pipe whip is simulated with nonlinear dynamic analyses with the most adequate models according to the preliminary linear analyses. The displacement and stress results of different models are compared with each other and the reliability and adequacy of different element types are discussed. Sensitivity study is made by varying analysis type, material properties, mesh density, element properties and inner pressure.

The results of the most adequate simple models with the right combinations of special-purpose elements provided by Abaqus corresponded well to the ones of the much larger three-dimensional solid and shell element models.

The post-yield behaviour of the pipe steel material has some notable effect on the behaviour of the pipe in a guillotine pipe break. Obviously, rate dependence makes the structure slightly dynamically stiffer. The inner pressure of the pipe and its assumed decay after the pipe break has a major influence on the results.
It is shown, how the stress distribution along the pipe axis, around the cross-section and through the thickness of the wall can be solved with elbow elements on a fairly detailed level. Long pipe runs with many supports and restraints should preferably be modelled with simple structural elements such as pipe and elbow elements and special-purpose elements in order to save time and numerical errors due to overly large models.

1. Introduction

Every continuum structure can be modelled and solved with general-purpose solid continuum volume elements. However, that can be very ineffective and time-consuming, since usually very large amount of volume elements are needed to catch the right behaviour. That is why it is useful to have structural and special-purpose elements instead.

The pipes in power plants are long, slender structures with relatively thin walls. Therefore, it is convenient to model them with shell elements. Since the beam theory can be used to calculate their behaviour quite accurately, also pipe elements can be used. Pipe, elbow, shell and solid volume elements are used in this study for modelling the pipe.

There are many types of supports and restraints in power plants. They support components and pipelines mainly against the gravitational forces in vertical direction. Either the components rest on the support or they are suspended by the so-called hangers. The function of restraints is to take the dynamic loads in case of accidents such as pipe breaks or earthquakes when the pipes can have exceptionally large movements and velocities. The thermal expansion is taken into account by leaving sufficiently large gaps between the pipe and restraints.

If special-purpose elements are not used, contact behaviour has to be formulated between the pipe and restraint surfaces. That is why it is also useful to have special-purpose elements instead, which can include the gap, contact,

stiffness and even possible viscous properties. Solid volume, spring and so-called pipe support elements are used in this study for modelling the restraint.

This study concentrates on simulating the dynamic behaviour of a certain relatively short pipe section with one restraint. Its stiffness is first calculated with a relatively detailed finite element model, which is then substituted with a simpler model using structural and special purpose elements. A pipe guillotine break is chosen as a dynamic test case that is simulated with different kinds of models. The main aim is not simulate the pipe break as realistic as possible, but to compare different model and analysis types with each other.

A model with elbow elements is found out to be the most adequate and suitable one. Sensitivity study is conducted with that model by varying some properties and characteristics.

This study is reported more thoroughly in [1], [2].

2. Model description

Since all kinds of sensitivity study is made and adequacy of different model types is assessed, it is practical that the structure is not too complex with many variables. A relatively short pipe section with one restraint and one bend is studied by finite element calculations with Abaqus code [3]. The whole combined model consists of three parts: the pipe, the restraint with a small gap (6 cm in size), and a concrete block which represents the surrounding structures such as part of containment wall near the pipeline. Figure 1 shows the example pipeline geometry simulated in this study with main dimensions. The lower right end of the pipe is rigidly fixed and the postulated pipe break takes place in the upper left end of the section.

The different finite element model types are shown in Figure 2. The concrete block and the restraint are modelled either with solid volume elements (referred as C3D8R in Abaqus) or with a nonlinear spring element (SPRINGA). The pipe is modelled with solid volume, shell, pipe or elbow elements. The detail of the solid volume element model of the pipe is shown in the upper left hand corner. It has four linear 8-noded elements through the wall thickness and altogether 272 136 elements (C3D8R). The pipe (or elbow) element model is shown in the upper right hand corner. Depending on the mesh density, it has either 18 or 36 elements (6 or 12 elements along the bend) (PIPE31, PIPE32, ELBOW31, ELBOW31B, ELBOW31C or ELBOW32). There are three different cases regarding the element types: 1) only pipe elements are used, 2) only elbow

elements are used or 3) pipe elements are used for the straight sections and elbow elements for the bend section. The spring element can also be seen near the bend in the horizontal section in Figure 2. The shell element model with a fine mesh is shown below the other two models. It has 44 shell elements (S4R) around the pipe circumference and the total number of elements is 6 864. The model with a coarse mesh has only 12 elements around the pipe (total number of elements 456).

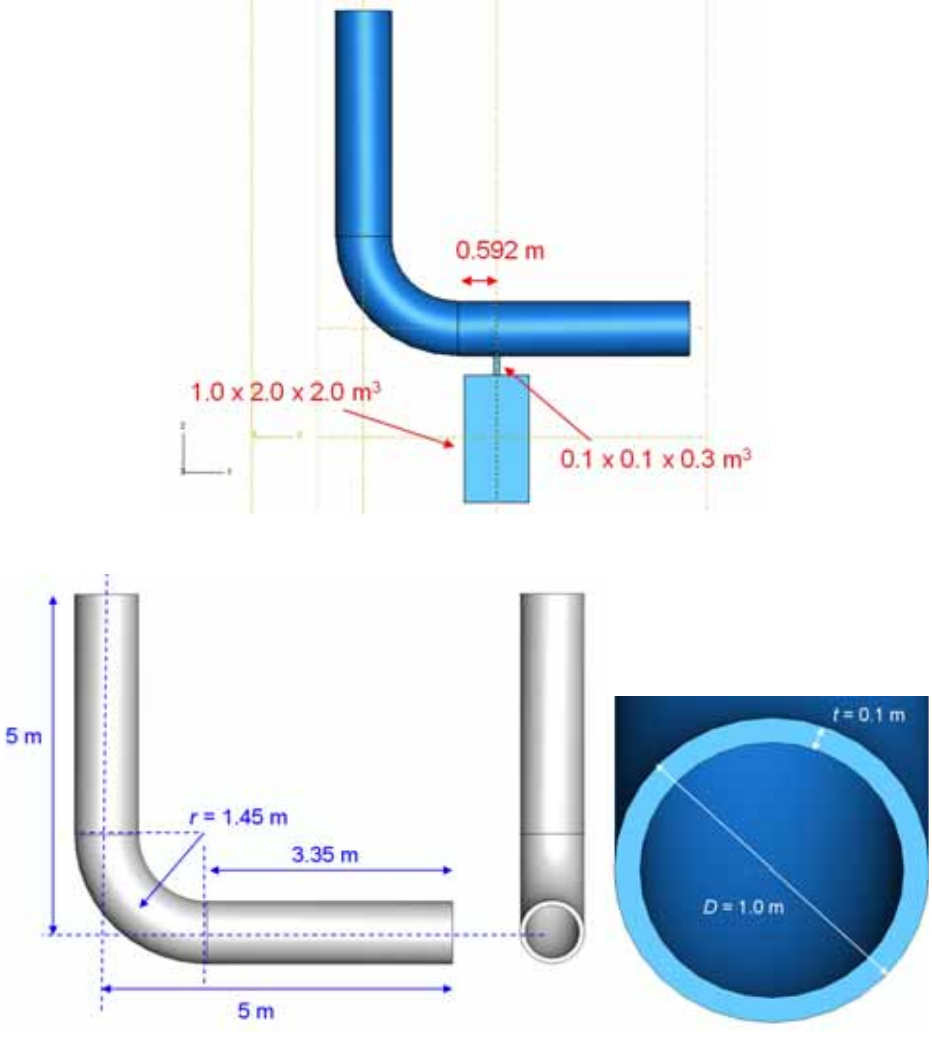

Figure 1. The pipeline model and its main dimensions.

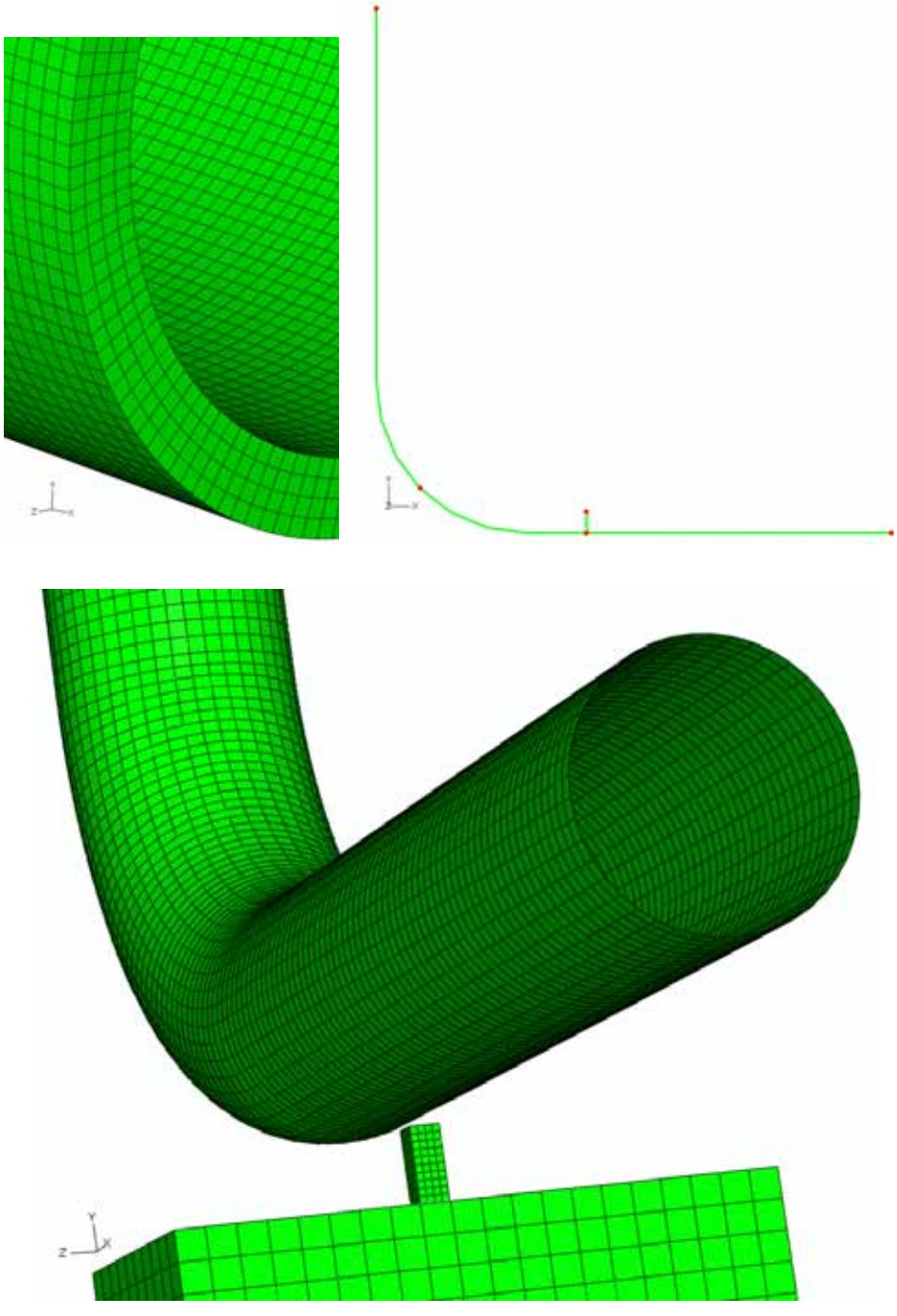

Figure 2. Solid volume (above left), pipe/elbow (above right) and shell element (below) models.

If all the analyses considered, five materials are used – one elastic steel material, three inelastic steel materials and one elastic concrete material type. Depending on the analysis, the pipe is assigned either inelastic material properties A, B, C or only elastic properties of A. The simple steel rod of the restraint with a square cross-section is always assigned steel type B. Water is not included, but its mass is taken into account in one of the analyses. The high inner pressure is applied in each one of the final analyses. Table 1 shows the linear material property values.

Table 1. Elastic material properties.

Material	**Steel (A, B)**	**Steel (C)**	**Concrete**
Density, ρ [kg/m^3]	7 850	7 830	2 400
Young's Modulus, E [GPa]	210	176	35
Poisson Coefficient, ν	0.3	0.3	0.2

According to Haar et al. [4] the density of the water at temperature of 300^{o}C is 727 kg/m^3. If it is taken account in the density of the steel C, the new "combined" density increases from 7 830 kg/m^3 to 9 121 kg/m^3.

Figure 3 shows the nonlinear stress – plastic strain curves for different steel materials. Material C is the most realistic one in this case. It is the normal austenitic stainless steel SS-2333 in operational temperature.

In order to find out the adequacy of different element types and the sensitivity of the models to different parameters many different cases are studied by extracting their natural frequencies and comparing them with each other. The lower end of the pipe is fixed and the upper end is free. Altogether 19 different cases were solved. Following characteristics were varied: Element type and interpolation, mesh density, number of integration points and ovalization modes, whether the rotations are free in the fixed end of the shell element model, the inner pressure type with elbow elements (open or closed) and the inner pressure with shell elements. First ten eigenfrequencies were solved with Lanczos method.

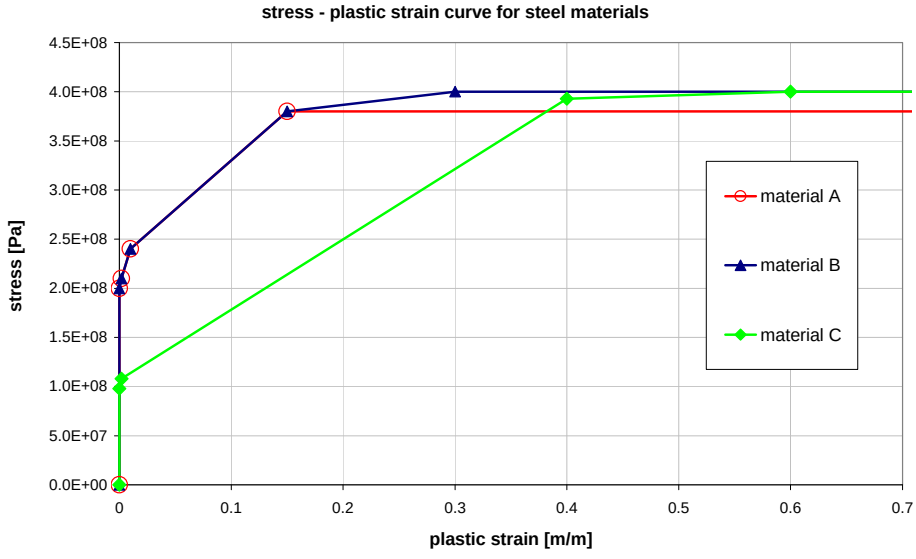

Figure 3. Stress – plastic strain curves for different steel materials used in the analyses.

The masses are really close to each other in every case, which partly verifies the models. The most accurate model can be assumed to be the one with solid volume elements or the one with a very fine shell element mesh. Their eigenfrequencies are very similar. The model with only linear pipe has some discrepancies and is not accurate enough. The ones with also elbow elements correspond better with the detailed models. The inner pressure makes the models slightly stiffer. The model that used both pipe and elbow elements is really close to the detailed models when it comes to eigenfrequencies, even closer than the coarse shell model. Mesh refinement slightly enhances the accuracy in a global sense. Two pipe model types are chosen for the nonlinear dynamic analyses: the model with a fine shell element mesh and the model with 18 linear elbow elements.

3. Dynamic analysis of a guillotine pipe break

A guillotine pipe break is chosen as a nonlinear dynamic analysis case. It is first analysed using the combined model shown lowermost in Figure 2. That is a relatively large model using shell elements for the pipe (chosen based on the eigenfrequency results above) and solid volume elements for the concrete and the steel restraint. After that, as a comparison, the same case is analyzed with a model using only structural and special-purpose elements; elbow elements for

the pipeline and a nonlinear spring element for the support. The properties such as the stiffness of the spring element are determined by preliminary static compression simulations with the large combined model. Nonlinear spring element (SPRINGA) with a stiffness of 1 GN/m and a gap of 6 cm is used.

The release of fluid from a break in high-energy piping can result in significant changes in flow characteristic within the piping system, creating reaction forces, which dynamically excite the piping and cause a so-called pipe whip.

The fluid forces acting on the ruptured pipe are a function of time and space, and depend on the fluid state within the pipe prior to rupture, the break flow area, frictional losses, and plant system characteristics. Break flow area is often assumed to develop within one millisecond after break initiation. Fluid forces can be divided into two parts: initial thrust force and steady state thrust force. The former is:

$$F_{in} = P_0 A_e \tag{1}$$

where P_0 is the initial pressure in the pipe and A_e the break plane area. The steady state thrust coefficient is dependent on the fluid state and the frictional effects. In this case, the initial thrust force is 9.54 MN.

Normally, a dynamic time history analysis shall be conducted of the ruptured piping to determine its response to the exciting forces. The pipe whip constraints and other objects that can modify the pipe whip motion shall be considered in the analysis. Absorption of energy via plastic pipe deformation is typically the most desirable method in the design of piping and restraints for protection against pipe whip effects. The elastic and plastic behaviour of the pipe material shall be taken into account in the analysis as mentioned in [5, 6].

According to a study by Robbe et al. [7], there are three phases of pressure drop in a PWR Primary Circuit pipe break. During the first 5 ms, pressure drops from 155 bar to around 70 bar. When it gets to the saturation pressure, the water vaporizes. The flow rate increases until the critical flow rate. From 5 ms to 100 ms, a general pressure loss to around 80 bar takes place in the whole circuit. After 100 ms, a slow diphasic pressure decrease takes place in the whole circuit. In this study, fluid-structure interaction (FSI) phenomena were not taken into account.

A large-break loss of coolant accident with a guillotine break of one of the main coolant pipes near the reactor pressure vessel has been studied by Brandt et al [8]. It initiates a pressure wave which propagates inside the vessel. The simulation of bidirectional FSI phenomena was found to be important for accurate prediction of the resulting deformation and loads. Fully coupled simulation

results were validated against the German Heißdampfreaktor experiments. Regarding the pressure near the break point, however, results by [7] and [8] are in agreement with each other. Of course, the first milliseconds are sensitive to the assumed pipe break opening time and rate.

The analyses in this study consist of two steps. The first step is static during which an inner pressure is applied to the pipe. It is linearly ramped up in one second time. The upper end and the lower right end of the pipe are fixed during this step. The second step is dynamic with automatic time incrementation. Right in the beginning of it the free end is released, which initiates the pipe break condition instantaneously.

Only some of the results are shown here. All the analyses were successful. The energy balance was maintained and the results of shell and elbow models had a good correlation, with both plastic and elastic material properties. The stress results were in good agreement. In elbow elements, stresses can be defined around the circumference of the pipe and through its wall thickness. Also, the deformed shape of the cross-section is possible to be plotted. The results with explicit time integration corresponded well to the ones with implicit integration. Elbow elements are provided only for implicit integration.

In the elastic cases, the pipe vibrates dominantly according to its second mode and hits repeatedly the restraint near the highest point of its natural path (that would be unobstructed). Since the restraint or the pipe do not give in, there are only small displacements and the models are in good correlation with each other. In plastic cases, the stress wave reaches the fixed end 2 ms and the pipe hits the restraint 17 ms after the pipe break. Figure 5 shows the deformed shapes of the shell and elbow element models 0.06 s after the pipe break. The von Mises stress distribution on the outer surface is also shown. In elbow element model, the stresses are plotted from the side closest to the viewer. The plastic hinge has been formed first in the fixed end and then near the restraint in both cases. These models had slightly different dimensions than the final ones shown in Figure 1, they had steel material of type A and constant inner pressure.

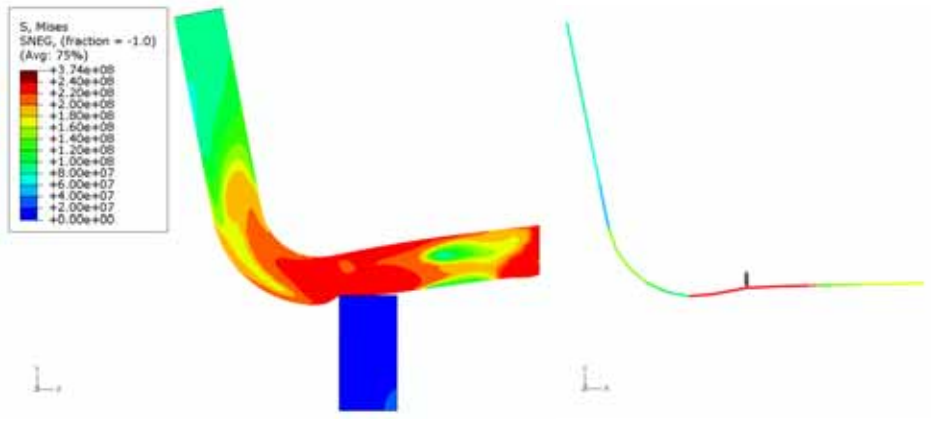

Figure 4. Deformed shapes with von Mises stress distributions on the outer surface 0.06 seconds after the pipe break of the shell (left) and elbow (right) element models.

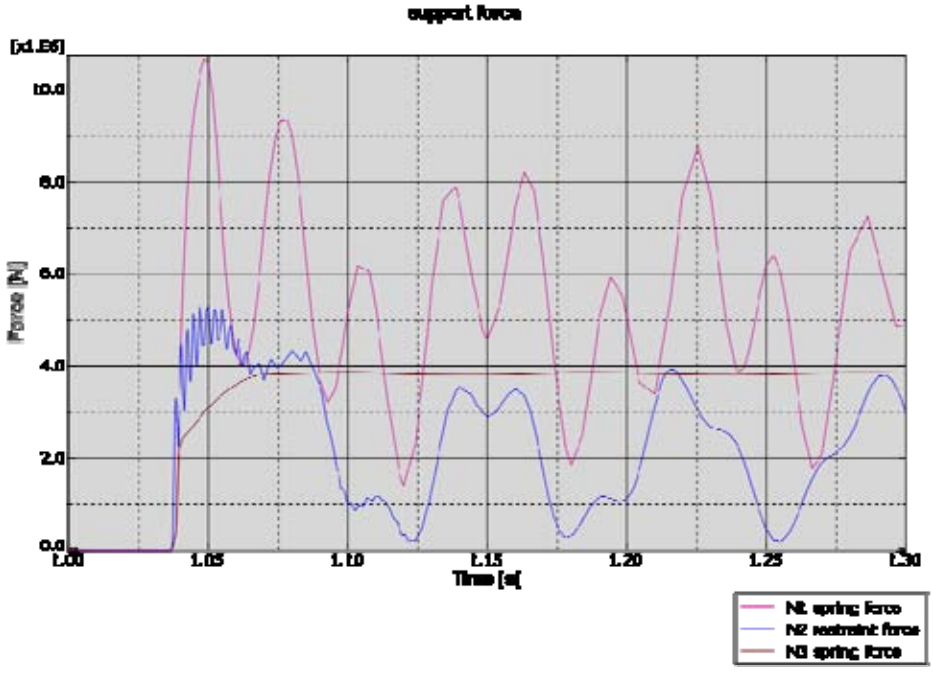

Figure 5. Vertical forces as functions of time in the restraint or spring in different cases (N1, N2 and N3).

In the final dynamic analyses, a pressure which decreases from 15 MPa (or 150 bar) to 5 MPa (or 50 bar) in 1 ms is used. This kind of decrease very near the break point is based on several previous studies [4, 7, 8].

They were conducted with Abaqus/Standard version 6.9-2 [3]. Material C with rate dependency according to Cowper-Symonds equation with parameter values D = 1 522 and q = 5.13 was used. Figure 5 shows the vertical forces as functions of time in the restraint or spring in different cases (N1, N2 and N3). In case N1, the spring acts in one direction and has a gap of 6 cm. In case N3, the spring stiffness curve in not linear but has also some softening.

4. Conclusions

Different kinds of ways to numerically model with finite element method the pipe runs and their supports are studied. A pipe guillotine break with whipping is chosen as a dynamic analysis case. Simple and typical nuclear power plant pipeline geometry and materials are chosen. It is seen that in respect to the eigenmodes, the pipe element model is adequate and almost as accurate as a shell element model with a fine mesh, especially when the pipe bend is modelled with elbow elements. The chosen restraint type is relatively stiff when having elastic material properties. Sensitivity study is conducted further on with the elbow element model.

Dynamic analyses of a pipe break are conducted. The calculated forces and stresses correspond to theory and the ones found in literature.

Nonlinear spring elements are found to act realistically and seem very suitable to model restraints for this kind of dynamic problem. The displacement and cross-section deformation results of the elbow element model corresponded reasonably well to the ones of the much larger shell element model. The situation is naturally different on a detail level near the restraint. There are some local discrepancies in the stress results.

The post-yield behaviour of the pipe steel material has some notable effect on the behaviour of the pipe in a guillotine pipe break. The maximum forces were of different magnitude by several percentages, but in every case with otherwise same parameters a plastic hinge was formed at the restraint and the analysis terminated. Obviously, rate dependence makes the structure slightly dynamically stiffer. The behaviour is smoother but after some 0.1 seconds, the spring forces are of the same magnitude.

The inner pressure of the pipe and its assumed decay after the pipe break has a major influence on the results. If the pressure rapidly decays instead of being constant, the pipe still hits the restraint, but the force is less than half and no plastic hinge is formed.

By comparing the results with different types of spring behaviours and a detailed finite element modelling of the pipe and restraint, is was seen, that the spring element should include the gap and some softening, i.e. curvature in the stiffness curve, but preferably not directly the stress-strain curve of the material.

The pipe support element (ITSUNI) provided by Abaqus acts in an equal way to the spring element, when the same spring behaviour is included. In a case of a single rod-like restraint, separate spring elements are more adequate, but in case of several beams, trusses or a grid, pipe support element can be more adequate.

The mass of the water has only minor effect on the dynamic behaviour of the pipe in this kind of highly dynamic loading. The maximum forces were almost the same with of without the water mass.

This is not an extensive study but gives a good base for the future study and for making the decision how to solve similar kinds of problems. First of all, it should be remembered that comparisons were made between several FE models instead of an actual structure and FE models. All the different ways and combinations to model these cases were not studied, but a few adequate ways were found. Long pipe runs with many supports and restraints should preferably be modelled with simple structural elements such as pipe and elbow elements and special-purpose elements in order to save time and numerical errors due to overly large models. It is shown, that the stress distribution along the pipe axis, around the cross-section and through the thickness of the wall can be solved with elbow elements on a fairly detailed level even in highly dynamic problems.

References

1. Calonius, K. Preliminary numerical studies on dynamic behaviour of pipelines. Espoo: VTT, 2008. VTT Research Report VTT-R-01637-08.

2. Calonius, K. Numerical studies on dynamic behaviour of pipelines. Espoo: VTT, 2009. VTT Research Report VTT-R-01025-09.

3. Abaqus Manuals, 2009. Version 6.9-2. Dassault Systèmes.

4. Haar, L., Gallagher, J. S. & Kell, G. S. NBS/NRC steam tables. National Standard Reference Data System. USA, 1984.

5. Vörös, G. & Zsidi, Z. Analysis of the effects of postulated pipe rapture. Gépészet, Budapest, 2002. Pp. 307–310.

6. Micheli, I. & Zanaboni, P. An analytical validation of simplified methods for the assessment of pipe whip characteristics. Transactions of the SMiRT Conference, 2003. Paper #J05-4.

7. Robbe, M., Lepareux, M. & Trollat, C. Hydrodynamic loads on a PWR primary circuit due to a LOCA-pipe computations with the CASTEM-PLEXUS code. Transactions of the SMiRT-15 Conference, 1999. Paper #J05-4.

8. Brandt, T., Lestinen, V., Toppila, T., Kähkönen, J., Timperi, A., Pättikangas, T. & Karppinen, I. Validation of fluid-structure interaction calculations in a large-break loss of coolant accident. Proceedings of the 16th International Conference on Nuclear Engineering, Vol. 2. ICONE16. Orlando, Florida, USA, 11–15 May 2008. ASME. Orlando, Florida. Pp. 245–254.

On welding residual stresses in structural integrity analyses of NPP components

Otso Cronvall
VTT Technical Research Centre of Finland
Espoo, Finland

Abstract

It is typically assumed that weld residual stresses (WRSs) in the pipings of nuclear power plants (NPPs) are confined to the weld region and its immediate vicinity and have locally relatively high values, of the order of tensile yield stress in and near the inner surface. In many cases the welds have not been post weld heat treated, and thermal relaxation of the WRS levels is small due to the relatively modest operational temperatures. Therefore, the WRSs in NPPs can potentially affect the structural integrity through the risk of stress corrosion cracking (SCC). In this study the WRS assumptions of commonly used fitness-for-service procedures are compared for a set of representative NPP pipe sizes. Also, the behaviour of WRSs as a function of typical load transients, corresponding to several years of plant operation, is simulated with finite element analysis (FEA) for a nozzle connected to a safe-end and pipe. Finally, from the results of the computational analyses, conclusions and recommendations are given on the application of WRS assumptions.

1. Introduction to WRS assumption procedures

The weld residual stress (WRS) assumption procedures covered here are the ASME recommendations [1, 2], the British Standard BS 7910: 1999 [3], the R6 Method, Revision 4 [4], the SSM handbook [5], the SINTAP Procedure [6], the API 579 procedure [7] and the FITNET Procedure [8]. The examined WRS and

weld types are as-welded state WRS distributions in circumferential nuclear power plant (NPP) piping/nozzle welds.

According to experimental measurements and the above mentioned seven procedures the WRS values are typically relatively high in NPP component welds in the as-welded state. Thus it is of vital importance to take them into account in the analyses of structural integrity analyses, e.g. on crack growth sensitivity. The WRS distributions present in a structure are the result of the manufacturing history and the elastic-plastic properties of the structure. The former is referring to the mechanical and thermal processes executed during the whole production sequence and the latter to the elastic-plastic behaviour of the structure. After PWHT the WRSs are typically remarkably lower.

The published experimental WRS data have a substantial scatter. Consequently the defined WRS distribution assumptions have been developed as tensile upper bound solutions based on the data. However, according to [9, 10, 11, 12, 13], this approach not only lacks consistency for the same type of joints and welding parameters, but can either significantly overestimate the WRSs in some cases, or underestimate them in others.

Over the last decade or so, welding process induced residual stresses have received increasing attention in the pressure vessel and piping research community. The driving force for this interest can be attributed to the fact that application of modern structural integrity assessment procedures for defective welded components, e.g. the R6 Method, Revision 4 [4], SINTAP Procedure [6], API 579 procedure [7] and FITNET Procedure [8], require considerably more input data to give a more realistic WRS assessment. All WRS assumption procedures covered here base their definitions on material yield strength, so that typically the maximum absolute WRS values are nearly at yield strength, usually acting in and near weld inner/outer surfaces. The variation of the yield stress values within the typical operational temperature range in Light Water Reactor (LWR) NPP piping systems, being approximately from 20 to 330°C, is of the scale of 10%. For austenitic NPP piping stainless steels (SSs) the stress values at 1.0% strain should most often be used for yield strength, whereas for corresponding ferritic steels the stress values at 0.2% strain should be used, respectively. The input data needed in using the WRS assumptions in the above mentioned seven procedures vary so that with the older procedures geometry and basic material strength data suffices, whereas in case of more recent procedures also data concerning the conduct of the welding process are needed.

The examined seven WRS assumption procedures provide a range of approaches to define the WRS distributions. In older WRS procedures, such as ASME recommendations [1, 2], only one approach in the form of a few simple functions is given, whereas in more recent WRS procedures, such as R6 Method Rev. 4 [4], several levels for defining WRSs are presented, ranging from coarse level 1 definitions giving single values, to level 2 with WRS assumptions as analytical functions, to subtle and computationally laborious level 3 approaches, requiring e.g. the use of advanced non-linear 3D FEM analysis tools. In general, the WRS assumptions are defined in all of the examined seven procedures also (or only) with analytic functions, such as polynomials and exponent function. On the behalf of the more recent WRS assumption procedures, these correspond to level 2 definitions. Separate WRS distribution sets are typically given for austenitic SS and ferritic steel materials, weld types and weld wall thickness ranges. Also, overall validity ranges are given in most procedures for WRS assumptions, as a function of e.g. weld wall thickness and yield strength.

One unfortunate departure from realism in case of some of the more recent WRS assumptions, e.g. R6 Method Rev. 4 [4], API 579 procedure [7] and FITNET [8], is that in the transverse to weld direction the WRSs are not self-balancing. While making local crack growth calculations with a fracture mechanics based analysis tool this feature may not pose remarkable problems, but in case of corresponding 3D FEM analyses it is quite the other way around, as in order to achieve equilibrium FEM automatically modifies the WRSs towards self-balanced distributions over the component model walls, and thus the original WRS distributions are not maintained.

2. Application of WRS assumption procedures

2.1 Analysis input data and scope

In this study the WRS distributions are calculated with the above mentioned seven procedures for representative small, medium and large NPP piping component cross-sections in Finnish Boiling Water Reactor (BWR) NPP units. The dimensions of these pipes are [14]:

- Small pipe; outer diameter = 60 mm, wall thickness = 4.0 mm,
- Medium pipe; outer diameter = 170 mm, wall thickness = 11.0 mm,
- Large pipe; outer diameter = 510 mm, wall thickness = 26.0 mm.

For these three pipe sizes WRS distributions through wall are calculated for both austenitic and ferritic materials in perpendicular to weld direction. The examination of WRS distributions was limited to this direction as worldwide more than 90% of the detected piping cracks have been oriented parallel to weld, see e.g. ref [16], and it is mainly perpendicular to weld stresses that make such cracks grow. The covered weld condition in the calculations is as-welded state.

The temperature is set to 286 °C in all calculations, corresponding to operational temperature in Finnish BWR NPP units. In this temperature the stress at 0.2% strain of the considered austenitic and ferritic materials are 125 and 184 MPa, respectively. Of the covered WRS assumption procedures, those in BS 7910: 1999 [3] and API 579 [7] consider the stress at this strain for austenitic SS as the yield strength, whereas according to R6 Method, Rev 4 [4], SSM handbook [5], SINTAP [6] and FITNET [8], the yield strength for these materials is taken to correspond the stress at 1.0% strain, respectively. Here 1.5 times the stress at 0.2% strain, i.e. 187.5 MPa, was taken to correspond to the stress at 1.0% strain for austenitic SS, as according to [6]. As for more robust ASME recommendations [1, 2], the yield strength is simply taken as 207 MPa (30 ksi) in all temperatures, corresponding on average to the room temperature yield strength of the SS weld test specimens used to provide part of the associated WRS data [15]. The tensile strength of the considered austenitic and ferritic materials are 412 and 540 MPa, respectively. The values of Young's modulus in the considered temperature are for these two materials 176 and 204 GPa, respectively, and for both of them the value of the Poisson's coefficient is 0.3.

2.2 WRS distribution application results

In the following Figures 1, 2 and 3 are presented for the three considered NPP pipe weld cross-sections the as-welded state WRS distributions through wall and perpendicular to weld, as computed with the earlier mentioned seven WRS assumption procedures. In these figures the horizontal axis is radial coordinate through pipe wall with origin on the inner weld surface, and the vertical axis presents the WRS values. In the legend "-Au" in the end of procedure name means that the curve in question is for austenitic SS, and correspondingly "-Fe" for ferritic steel. In case of pipe size Small, having wall thickness of 4.0 mm, no WRS results are presented for R6 Method, Rev 4 [4], SINTAP [6] and FITNET [8], because in these three procedures the validity range for as-welded WRSs are limited for this material type to thickness range of 9 to 84 mm.

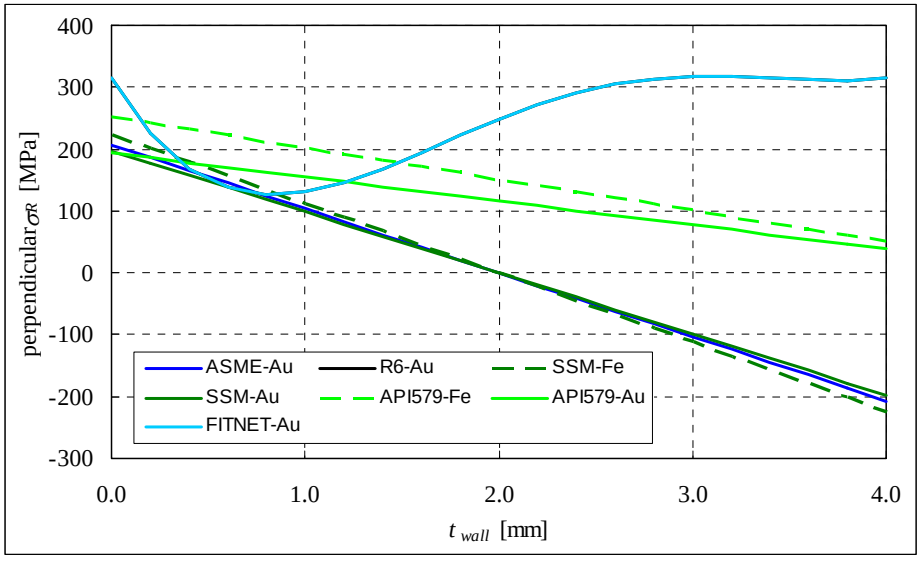

Figure 1. As-welded state WRS distributions through wall and perpendicular to weld for the pipe with cross-section Small.

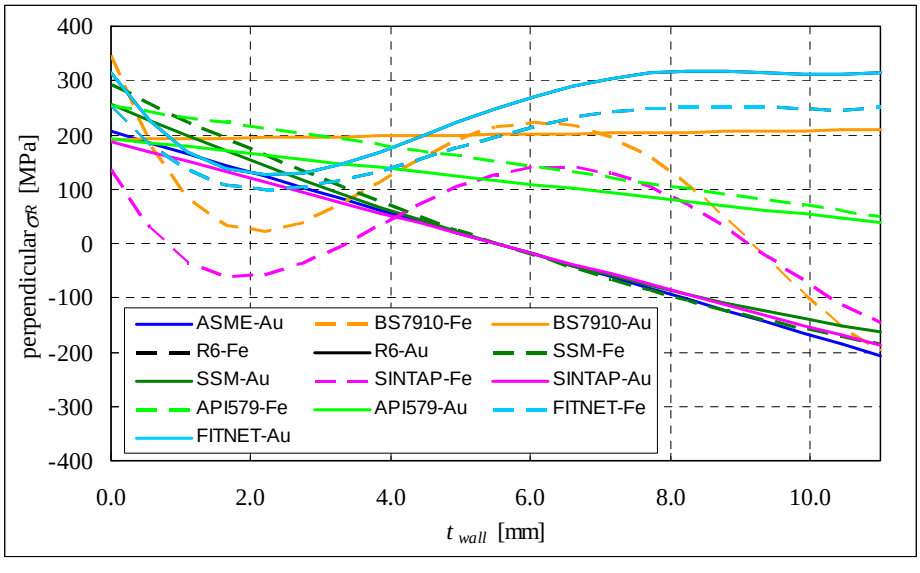

Figure 2. As-welded state WRS distributions through wall and perpendicular to weld for the pipe with cross-section Medium.

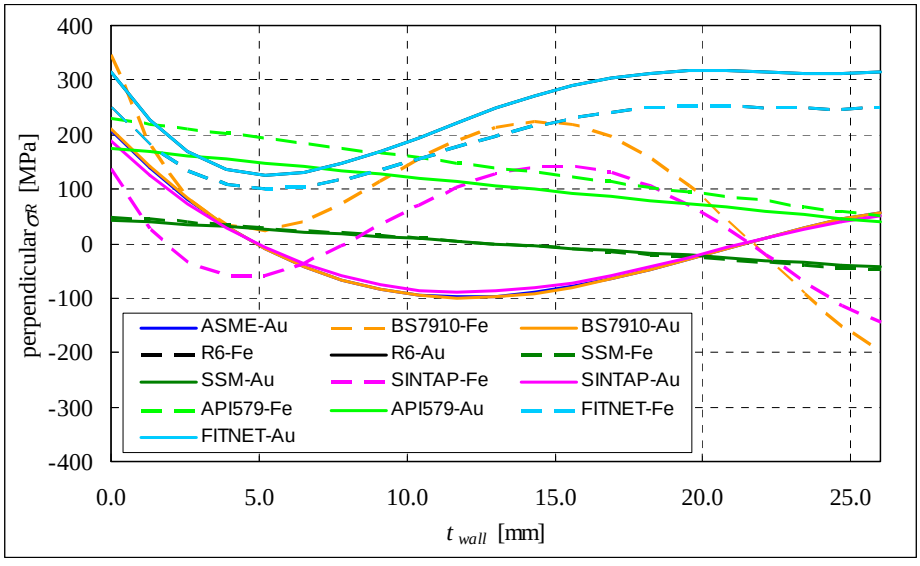

Figure 3. As-welded state WRS distributions through wall and perpendicular to weld for the pipe with cross-section Large.

As can be seen from these figures, for the selected NPP pipe weld cross-sections and material types the resulting as-welded state WRS distributions perpendicular to weld differ remarkably from each other, both in shape and by their values.

Depending on the wall thickness and WRS assumption procedure in question, in and near the inner surface the WRS values vary approximately between 50 to 350 MPa of tension, where the highest values are most often given by the R6 Method, Rev 4, BS 7910: 1999, API 579 and FITNET procedures. According to the same procedures for austenitic SS the WRS values also completely/mostly stay in tension through the wall all the way to the outer surface, giving there values of the same scale as in the inner surface. This is hardly realistic as such distributions are not self-balancing. Whereas according to the ASME recommendations, SINTAP and SSM procedures the WRS values for austenitic SS turn to compression when approaching the outer surface, so that self-balanced distributions are achieved, which is realistic. For ferritic steel, only SSM handbook gives self-balancing WRS distributions for Small and Large cross-sections, whereas for Medium cross-section only SINTAP procedure gives a self-balancing WRS distribution, respectively. However, for this material type also SINTAP and BS 7910: 1999 procedures give WRS values of compression in and near the outer surface, though the through wall WRS distributions

obtained with these two procedures are not self-balancing. ASME recommendations are for the time being limited to cover only austenitic SSs.

When comparing to material strength values, R6 Method, Rev 4 and FITNET procedures give at both inner and outer surfaces WRS values that are for austenitic SS approximately 65% higher than the yield stress (corresponding here 1.5 times the stress corresponding to the 0.2% strain), whereas for ferritic steel they are approximately 35% higher than the yield stress, respectively. In case of ferritic SS also BS 7910: 1999 gives high tensional WRS values in the inner surface, being approximately 90% higher than the yield stress. In case of other WRS assumption procedures the WRS values in the inner and outer surfaces and their vicinity are considerably lower, except for API 579 the WRS values at the inner surface are for ferritic steel approximately 30% higher than the yield stress. For all WRS assumption procedures the WRS values remain in all points for all three considered pipe sizes below the tensile strength, and thus the realism concernning ultimate material strength is not violated.

Partly the result curves in the Figures 1, 2 and 3 were taken from the background ref. [17], and the rest from computations performed within this study.

For the considered NPP pipe weld cross-sections the as-welded state WRS distributions parallel to weld, though not shown here with figures, are quite similar, varying approximately between 100 to 200 MPa of tension, and barely changing as a function of the wall thickness. The only exception here is API 579 procedure, as it gives linearly altering distributions with on average 200 MPa of tension in the inner surface and on average 50 MPa of tension in the outer surface, respectively. The SSM procedure gives the highest WRS values for all analysed pipe sizes. At maximum the applied procedures give WRS values exceeding the yield strength by approximately 10%. Thus none of them exceeds the tensile strength. Here in case of FITNET, R6 Method Rev. 4, BS 7910: 1999 and API 579 procedures, low heat input was conservatively selected.

The differences between the recommended WRS distributions through wall and perpendicular to weld in as-welded state stem from several reasons, mainly relating to the available measured WRS data and/or FEM analysis result data, based on which they have been defined, and procedure scope concerning e.g. geometry, material and weld procedure parameters. The WRSs depend on complex interacting factors, which are difficult to simulate consistently using solely FEM. Defining reliable WRS distributions from measurements is also problematic because of the complex local and global spatial distributions of stress, the innate

variability of WRS fields (even in welds fabricated to identical procedures) and because of the limitations of the measurement techniques themselves.

In the light of the WRS analysis results for cases concerning austenitic SS, only ASME recommendations and SINTAP procedure in all cases, and SSM handbook in most cases, give WRS distributions that are self-balancing in the transverse to weld direction. Of them the least over conservative WRS procedure appears to be SINTAP. As for the corresponding analysis results for cases concerning ferritic steel, for Small and Large cross-sections SSM handbook gives self-balancing WRS distributions, whereas for Medium cross-section only SINTAP procedure gives a self-balancing WRS distribution, respectively.

3. Numerical simulations of WRSs

The NPP components analysed here are a safe-end connecting to a nozzle and pipe, resembling those that connect the feed water system to the Reactor Pressure Vessel (RPV) in BWR units. In particular, it is examined how to simulate with FEM the WRS distributions and their behaviour as a function of typical NPP load transients in the safe-end/pipe weld joint. The as-welded state WRS distribution for this weld is assumed according to SINTAP procedure [6]. The main background document for the presented numerical simulations is ref. [18].

3.1 Input data for numerical simulations

The general geometry of the analysed NPP component assembly is presented in Figure 4 in the following. The relevant numerical geometry, material, WRS and loading input data values are presented in Table 1 and Table 2, respectively. Types of considered materials are for nozzle; ferritic steel, for base metals of safe-end and pipe; austenitic stainless steel, and for the examined safe-end/pipe joint weld material same properties are assumed as for the associated base materials.

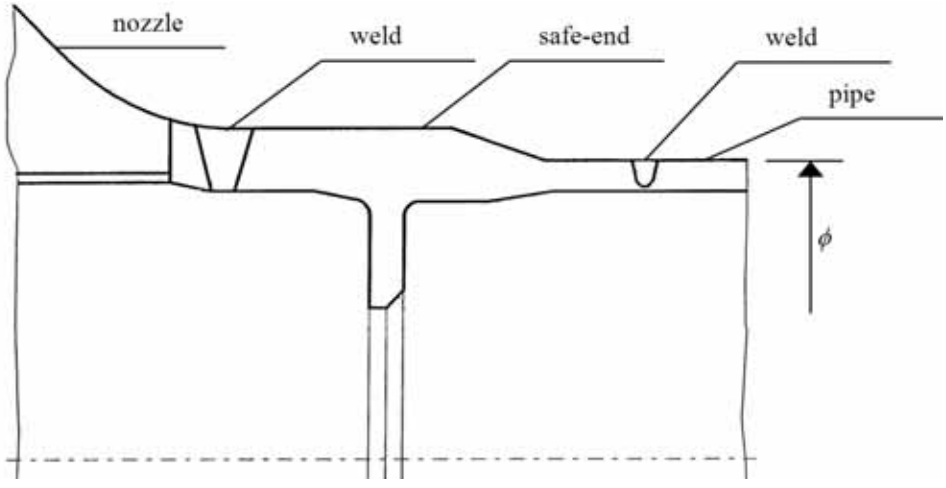

Figure 4. The overall geometry of the safe-end connecting to nozzle and pipe; horizontal section of the components at the level of their common symmetry axis.

Table 1. Geometry, material and WRS input data for numerical simulations concerning the safe-end connecting to nozzle and pipe.

Geometry & Material Property Data		**WRS Data**	
Outer diameter [mm]	a few hundreds	WRS definition procedure	SINTAP
Wall thickness [mm]	~ 16	Axial WRS, inner surface [MPa]	245
Yield strength at 286°C [MPa]	220	Axial WRS, outer surface [MPa]	-245
Young's modulus at 286°C [MPa]	200	Variation of axial WRS between inner/outer surface	linear

Table 2. The load sequence applied here as a single load history in the time dependent numerical simulations concerning the safe-end connecting to nozzle and pipe.

Event no.	**1**	**2**	**3**
Event description	STS => WRS => STS	STS => LC1 => STS	STS => SO => STS
Event no.	**4**	**5**	**6**
Event description	STS => LC2 => STS	STS => LC3 => STS	STS => LC4 => STS
Event no.	**7**	**8**	**9**
Event description	STS => LC2 => STS	STS => LC5 => STS	STS => LC2 => STS
Event no.	**10**	**11**	**12**
Event description	STS => LC3 => STS	STS => LC2 => STS	STS => LC4 => STS
Event no.	**13**	**14**	**15**
Event description	STS => LC2 => STS	STS => LC3 => STS	STS => LC2 => STS
Event no.	**16**		
Event description	STS => SDS => STS		
Notations	• STS; static loading to steady state • WRS; loading of WRSs • SO; Start of operation • SDS; shut-down state (i.e. static pressure of 1.0 bar and temperature of 20°C, respectively) • LC1; System pressure test	• LC2; Cold shut-down & Cold start-up • LC3; Feed water line opened at 320 kg/s & Reactor scram, during normal operation with normal feed water flow • LC4; Feed water line opened at 320 kg/s & Feed water line closed at 320 kg/s • LC5; Feed water line opened at 320 kg/s & A – isolation	

3.2 Numerical heat transfer and stress/strain simulations

All heat transfer and stress/strain analyses were performed with FEM code Abaqus, version 6.8-2 [19, 20]. The analyses were performed as fully coupled, i.e. the heat transfer and stress/strain analyses were performed simultaneously.

As all considered loads, including WRS distributions, are symmetric in relation to geometry symmetry axis of the examined safe-end, pipe and their joint weld, it sufficed to prepare an axisymmetric FEM model for the numerical simulations. The examined safe-end/pipe joint weld region of the prepared FEM model used in the simulations is shown in Figure 5, in the following.

The thermal boundary conditions of the overall FEM model are such that for the outer surfaces and for the two cut-off sections with which the model was cut from the global structure, adiabatic boundary condition was applied, whereas for the inner surfaces, where heat will be exchanged between the water and the metal, the value of the heat transfer coefficient, α_{HT}, varied between 1 000 and 70 000 W/m^{2}K.

The displacement boundary conditions of the overall FEM model are such that for the safe-end side vertical cut-off surface, the horizontal displacements are set to zero, whereas the pipe side vertical cut-off surface is set to remain vertical and straight, but allowed to deform perpendicular to itself.

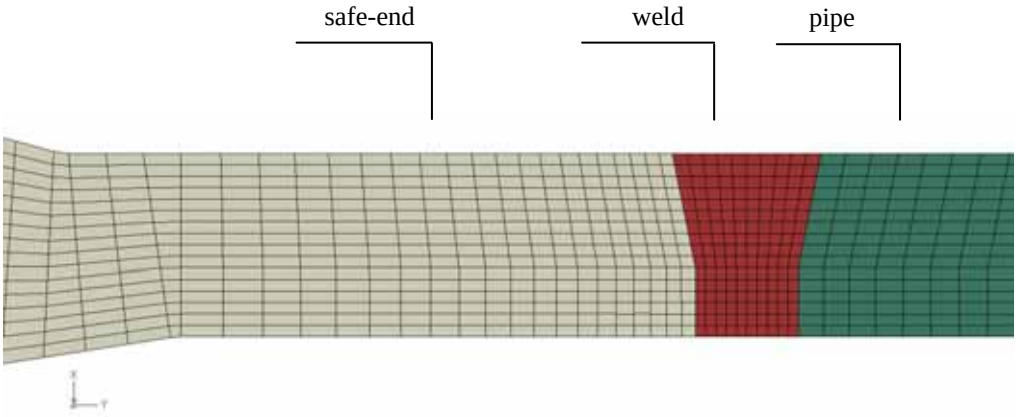

Figure 5. Detail of the element mesh of the axisymmetric FEM model of the examined safe-end, pipe and their joint weld, showing all involved material regions emphasised with different colours.

The axisymmetric FEM model was meshed with general purpose continuum elements. The selected element type from the Abaqus element library is CAX4RT, which is a 4-node rectangular bilinear displacement and temperature element, with reduced integration and hourglass control. Active degrees of freedom are the two displacements in the model plane, i.e. in the vertical (x-axis) and horizontal (y-axis, being here also the FEM model symmetry axis) directions, and temperature. The number of the nodes and elements in the model are 2836 and 2650, respectively.

As a starting point, almost any approach to create a locally high stress state matching the selected WRS distribution to a FEM model can be applied, as long as it remains as such when the loading with which it is created is removed. In

practise this means that if in the analysis steps following the one during which WRS distribution was created, which obviously should be the very first analysis step, no other loading is introduced to the analysis run, the total stress state in the examined weld region should stay as the created WRS distribution. Obviously the total stress state changes in the FEM model weld region when other loads are introduced to the model further in the analysis run, and if the yield strength is exceeded, maximum values of WRSs and other stress components may lower to some extent as the stresses further distribute to the neighbourhood of the weld region.

When creating a local WRS distribution to a FEM model, it is generally not possible to apply the most commonly used load types, such as pressure, line and point loads against a surface. Thus other load types must be resorted to. The number of available load types depends also on the used FEM analysis code. With Body Force load type of Abaqus, having the unit of N/m^3, it was possible to create such a local stress field in the safe-end/pipe joint weld region of the FEM model that after continuing the WRS analysis step to steady state the result was a somewhat correct local WRS distribution, both concerning maximum and minimum values and distribution shape. However, this took a number of attempts.

As mentioned earlier, a history of anticipated load transients were analysed. This means that they were all included in a single analysis run in a realistic chronological order and separated from each other by static loading conditions long enough for steady state to take place. Thus the effect of structural memory, i.e. the effect to each present material elastic-plastic stress/strain state of all earlier loads, was fully included. The von Mises material yield model with associated flow rule and isotropic work hardening were used in the performed FEM analyses.

3.3 Results from numerical simulations

A brief result summary concerning the performed numerical simulations is presented in the following. It is limited to cover the transverse to weld stress results in the safe-end/pipe joint weld region. In Figure 6 are presented the simulated stress distribution after the first loading event; loading of the WRSs. In Figure 7 are presented the simulated stress distribution after the 15th loading event, loading of the Cold shut-down & Cold start-up. In Figure 8 are presented the WRS distributions through wall from a selection of instants of the covered load event sequence.

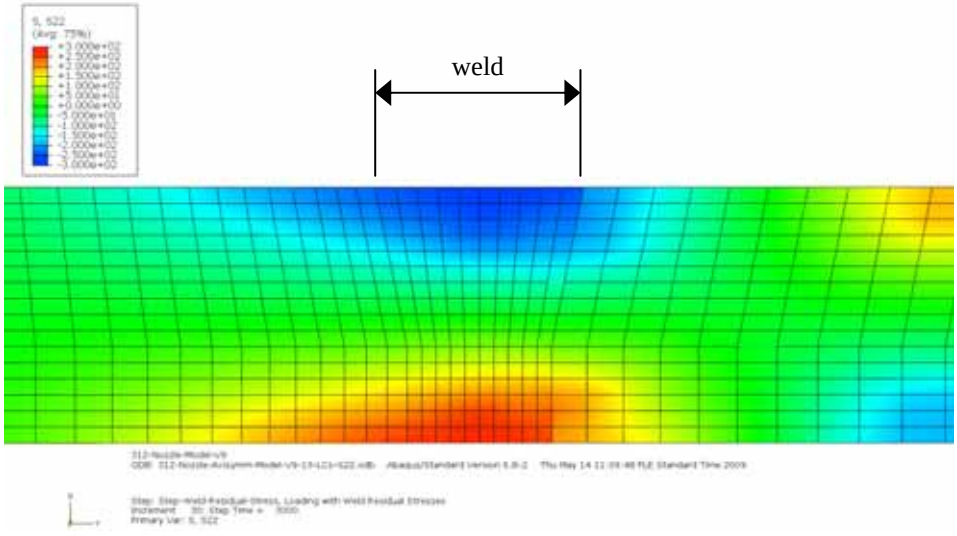

Figure 6. Transverse to weld stresses for the safe-end/pipe joint weld and adjacent regions. The examined time instant is the steady state after the ending of the load event 1; loading of the WRSs. Here the unit of S22 in the legend is MPa.

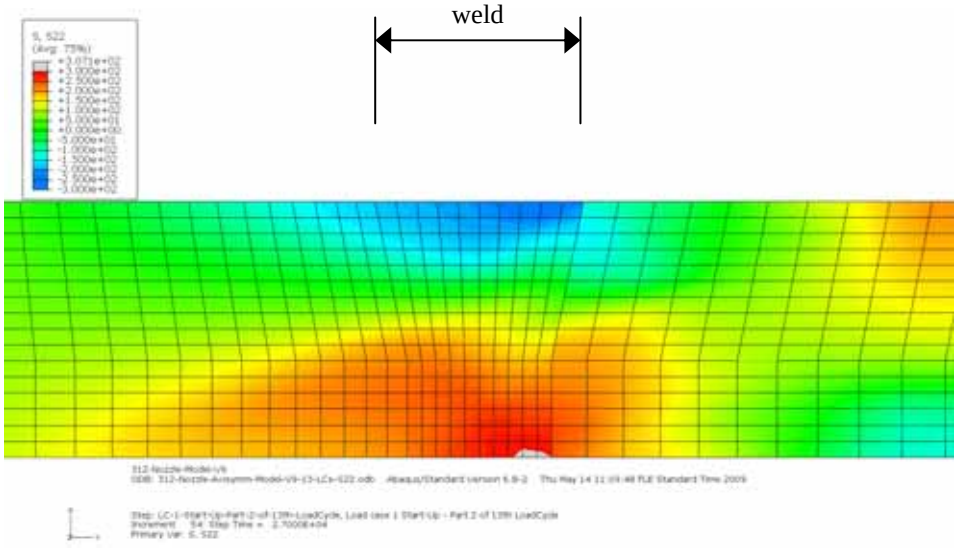

Figure 7. Transverse to weld stresses for the safe-end/pipe joint weld and adjacent regions. The examined time instant is the steady state after the ending of the load event 15; loading of the Cold shut-down & Cold start-up. Here the unit of S22 in the legend is MPa.

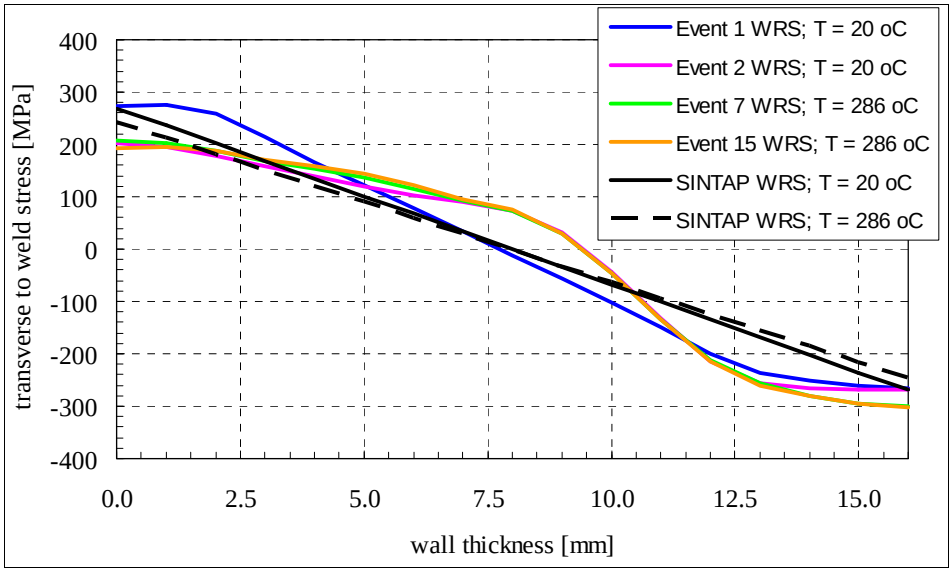

Figure 8. Transverse to weld WRS results for the safe-end/pipe joint weld centre line, together with the corresponding WRS distributions in the as-welded state defined according SINTAP procedure [6]. The examined time instant concerning each load event is that when the steady state after the ending of the load event has been reached. The origin of the radial through wall coordinate axis, horizontal axis in the figure, is at the inner weld surface.

As can be seen from the Figure 8, after 15 load events the transverse to weld WRSs in the centre line of the examined weld have decreased in and near the inner and outer surface approximately 50 MPa. Within the wall the WRSs levels have on the other hand to some extent climbed higher, somewhat suggesting that the continuing distribution of the maximum WRSs to the adjacent material regions occurs also in the through weld wall thickness direction. The relaxing of the WRSs was on the weld edges approximately of the same scale as on the centre line. It can also be seen that the first load event after the loading of the WRSs has the most remarkable redistributing effect to maximum WRS values, whereas due to load events following that only relatively small changes to WRS distribution occur. For comparison against how FEM modifies the initial WRS distributions as defined in the applied fitness-for-service procedure, also shown in the Figure 8 are with black colour the WRS distributions according to SINTAP procedure, with continuous line for temperature of 20°C, and with broken line for temperature of 286°C, respectively.

4. Crack growth sensitivity analyses

4.1 Input data considerations and analysed cases

The geometry and necessary material properties of the analysed safe-end/pipe joint weld are already presented in Figure 4 and Table 1, respectively. The process loads considered here are pressure of 70 bar and temperature of 286°C, corresponding to operational conditions in Finnish BWR NPP units. The analysed degradation mechanism is intergranular SCC (IGSCC).

SCC is a localised non-ductile progressive failure mechanism that occurs only in case the following three conditions are fulfilled simultaneously, see e.g. refs. [21, 22]:

- Stress around the crack-tip is tensile.
- Environment is aggressive.
- Material is susceptible to SCC.

In crack growth analyses the considered crack postulate is a circumferentially oriented inner semi-elliptic surface crack, with aspect ratio, i.e. crack depth divided by half of crack length, set to a constant value of 1/3. This is equal to the aspect ratio of the reference crack as defined in Section III of the ASME code [24], corresponding to the crack shape having the highest growing potential. The analyses cover an assumed operational plant lifetime of 60 years. As for the considered crack postulate the opening mode (mode I) is assumed in the analyses, for which the stresses driving the crack growth are taken in the transverse to weld direction. The effect of load transients to IGSCC is omitted, as concerning loads only static operational conditions and WRSs need to be considered in the analyses. It is assumed that the yearly time spent under operational conditions is altogether 8000 h.

The fracture mechanics based crack growth equation used in the SCC analyses, as according to ref. [22], is as follows:

$$\frac{da}{dt} = C \cdot K_I^n \tag{1}$$

where a [mm] is crack depth, t [year] is time, K_I [MPa√m] is mode I stress intensity factor, and C and n are constants characterising the material properties as a function of temperature and environment, and the values for which are given in Table 3. No K_I threshold value was considered in the IGSCC induced

crack growth analyses. Also other necessary input data used in the fracture mechanics based SCC sensitivity analyses are presented in the Table 3.

Table 3. Input data used in the fracture mechanics based SCC sensitivity analyses.

SCC Analysis Part of Input Data		**Stress Data**	
Fracture toughness [MPa√m]	350	Axial WRS distribution acc. to SINTAP procedure	for values, see Table 1
Initial crack depth & length [mm]	0.1 & 0.6		
SCC equation parameter values [23];		Axial membrane stress caused by operational conditions [MPa]	ca. 90
C [(mm/year)/((MPa√m)^n)]	1.42E-04		
n [-]	3.0		

In all analyses, the K_I values were calculated with analysis tool VTTBESIT, the characteristics of which are briefly described in the following.

The fracture mechanics based more robust crack growth analyses were performed with the analysis code VTTBESIT. This analysis code comprises parts developed by the Fraunhofer-Institut für Werkstoffmechanik (IWM), Germany and by VTT. The theoretical background and analysis procedures of VTTBESIT are presented in refs. [25, 26, 27].

With VTTBESIT it is possible to calculate stress intensity factor values in several points along the crack postulate fronts, including deepest point (crack tip) and edge/end points. The analysis code treats only the mode I loading in which the direction of the loading is perpendicular to the crack surface (crack opening mode), and the analysis procedure is linear-elastic. These calculations are carried out with program BESIT60, developed by IWM. This program is based on the weight/influence function method. Solutions are provided for “infinite” and semi-elliptical surface crack postulates in straight plates and cylinders.

VTTBESIT uses the BESIT60 program code as a pure stress intensity factor value computing subroutine and applies the results as starting values for crack growth assessments. Two crack growth models are provided in the analysis code: Paris-Erdogan equation [28] for fatigue induced crack growth, and rate equation for SCC [29], here equation (1).

For the examined safe-end/pipe joint weld three crack growth analysis cases are considered:

1. The WRS component of the stresses acting in the weld remaining at as-welded state as defined according to the SINTAP procedure [6], and with

stresses caused by operational conditions as presented in Table 3, respectively. In this case all stress components are set to remain as such, i.e. they are time independent. Here the WRSs were added to other stress components by superposition to obtain the total stress distribution.

2. The WRS component and other stresses are taken time dependently from the results of the performed FEM analyses In this case it was assumed that the stress distributions within the weld region remain as they are after the last analysed load event.

3. For comparison, a case where the WRSs are excluded, so that only time independent stresses caused by operational conditions as presented in Table 3 are considered.

4.2 Crack growth analysis results

The main results from the three cases of fracture mechanics based crack growth analyses performed to the examined safe-end/pipe joint weld are presented in Figure 9, which shows the crack growth as a function of plant years in operation. As can be seen for the two cases including WRSs, the calculated crack growth is relatively quick, once the crack depth has exceeded approximately 1.5 mm. Concerning the resulting K_I distributions over the crack fronts, their maximum values stayed in both analysis cases below 50 MPa$\sqrt{}$m. In the second analysis case where the relaxing of maximum values WRSs and other stress components had been taken into account with FEM simulations, the calculated crack growth was to some extent slower than in the first case where the as-welded state WRSs and other stress components were maintained in their original values time independently throughout the analysed time span. For instance, in the second case the crack grows to 50% and 90% depths of wall thickness in 8.2 and 10.6 years, whereas the same results are for the first case 7.7 and 9.9 years, respectively. On the other hand, concerning the crack growth results for the last 10% of wall thickness, one should view them with some caution as the accuracy of the results is not as good there as for shallower cracks. The slowing down of the crack growth rate (CGR) in both analysed cases when approaching the outer wall surface is caused by the compressive WRS values in that part of the wall, the compression reaching the maximum value in the outer surface. As for the third crack analysis case without WRSs and including only stresses caused by static operational conditions, it can be seen that for the considered time span the

crack growth remains remarkably slow, which demonstrates how dominant a stress component in the total stress distribution the WRSs is. In this case the crack grows according to computations within the considred time span only 0.1 mm in depth.

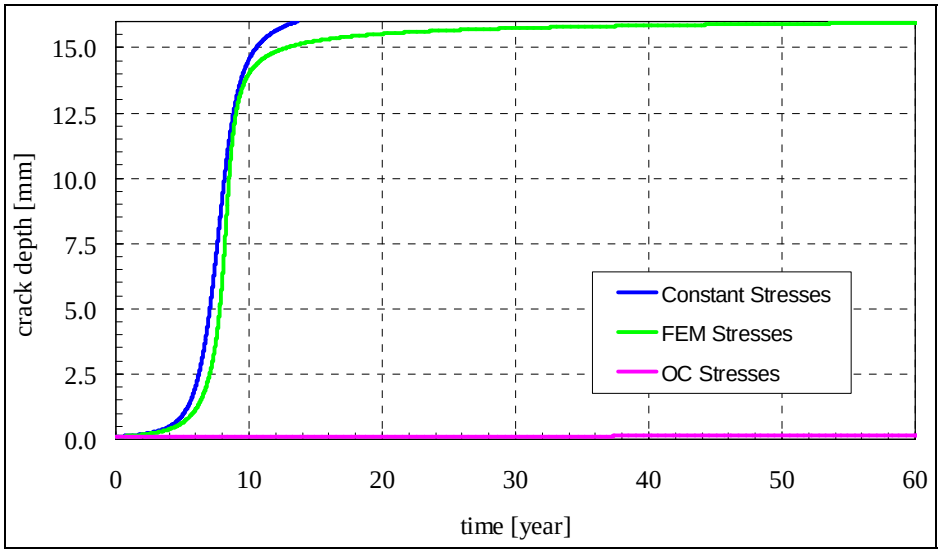

Figure 9. For semi-elliptic inner circumferential surface crack postulate under axial stresses, the crack growth histories through the safe-end/pipe joint weld for three IGSCC analysis cases: 1) stresses including WRSs acc. to SINTAP remain as they are at the start of analysis (Constant Stresses in the legend), 2) stresses including WRSs acc. to SINTAP are taken from the results of the time dependent FEM analyses (FEM Stresses in the legend), and 3) stresses excluding WRSs correspond to those caused only by static operational conditions (OC Stresses in the legend).

5. Discussion

One unfortunate departure from realism in case of some of the more recent WRS procedures, e.g. R6 Method Rev. 4, API 579 and FITNET, is that in the transverse to weld direction the WRSs are not self-balancing. While making local crack growth calculations with a fracture mechanics based analysis tool this feature may not pose remarkable problems, but in case of corresponding 3D FEM analyses it is quite the other way around, as in order to achieve equilibrium FEM automatically modifies the WRSs towards self-balanced distributions over the component model walls, and thus the original WRS distributions are not

maintained. Thus for FEM analyses of NPP components of austenitic SS and including WRSs the use of SINTAP procedure and ASME recommendations, which in all cases appear to give self-balancing WRS distributions over weld, are recommended, respectively. The less over conservative of these two procedures appears to be SINTAP. As for the corresponding FEM analyses of components of ferritic steel, for Small and Large cross-sections the SSM handbook gives self-balancing WRS distributions, whereas for Medium cross-section only the SINTAP procedure gives a self-balancing WRS distribution.

In the numerical simulations concerning the safe-end/pipe joint weld WRSs a history of anticipated load transients were covered. With FEM such an analysis can be computationally very laborious. Thus it is essential to use as small a model as possible so that all necessary and relevant physical phenomena and characteristics remain included in it, i.e. to minimise the total number of degrees of freedom (DOFs) in the analysis. If it is possible to use an axisymmetric FEM model, as it was here, it remarkably reduces the computational work as compared to a full 3D FEM model. The sizes of the models of the latter type can be prohibitively large, allowing the inclusion of only a few load transients to a single analysis run, when tens of them should be covered when simulating plant operation spanning only a few years. One possibility to overcome this would be to use sub-modelling, so that the more densely meshed sub-model would include the examined weld.

When creating with Body Force load type the WRS distribution to the safe-end/pipe joint weld it was soon noticed that the stiffness of the model, as e.g. dependent on the length of the model in relation to its thickness/width, and applied boundary conditions strongly affect how the FEM model responds to these loads, i.e. how it further distributes them within the model. Thus the set of load values with which a correct local WRS distribution is achieved, is always unique to the FEM model in question. Here the prepared FEM model was quite long as compared to its other dimensions, i.e. relatively slender, to ensure that possible boundary condition disturbances even out well before the examined weld.

So, creating local stress fields of WRS type to a FEM model is in practise an iterative process. First an applicable load type must be selected. Then as an initial approximation a set of load values must be selected. Based on the obtained local stress field in the end of WRS analysis step, the load values are to be justified, providing higher values if the resulting WRS distribution had too low maximum values and vice versa. This iterative process is continued until a correct enough WRS distribution has been achieved.

According to FEM results, after the analysed load events the transverse to weld WRSs in the centre line of the examined weld have decreased in and near the inner and outer surface approximately 50 MPa. Within the wall the WRSs levels on the other hand climbed to some extent higher, suggesting that the continuing distribution of the maximum WRSs to the adjacent material regions occurs also in the through weld wall thickness direction. The relaxing of the WRSs was on the weld edges approximately of the same scale as on the centre line.

Here the von Mises material yield model was used in the FEM simulations, as it is often applied for metals in elastic-plastic analyses, and it is also computationally relatively easy to use. Likewise it is appropriate to use associated flow rule in this connection. However, isotropic work hardening, which was used here, is not necessarily the most appropriate model to depict the elastic-plastic behaviour history of the ductile austenitic SS weld material in question here. Instead, kinematic or combined isotropic and kinematic work hardening model could better and more realistically suit for the analysis task in question. However, due to lack of available material data during the preparation of the FEM analyses, it was not possible to apply either of these two mentioned work hardening modelling options.

For the safe-end/pipe joint weld three crack growth sensitivity analysis cases were considered. The analyses were performed with a fracture mechanics based analysis tool, the considered crack postulate is a circumferentially oriented inner semi-elliptic surface crack, the dimensions of which are: depth x length = 0.1 x 0.6 mm. The analyses cover an assumed operational plant lifetime of 60 years. The considered degradation mechanism and load case were IGSCC and static operational conditions, respectively.

For the two analysis cases including WRSs the calculated crack growth was relatively quick, once the crack depth had exceeded approximately 1.5 mm, with both cases reaching the wall depth of 80% within 10 years. As for the third crack analysis case without WRSs and including only stresses caused by static operational conditions, the crack growth remains remarkably slow, according to computations within the considred time span only 0.1 mm in depth.

One feature increasing the CGR in the calculations is the applicable but somewhat conservative CGR equation used here, see equation (1). Namely, the values for the temperature and environment dependent parameters C and n, see Table 3, in this equation have been defined so that the resulting CGR curve envelops almost all associated laboratory data points, i.e. an upper bound approach. The conservative nature is moreover even emphasised in this approach,

as the vertical axis presenting the CGR is typically logarithmic, i.e. a seemingly small rise of the CGR curve in the diagram leads to a considerable increase in the corresponding growth rate. All other available applicable CGR procedures for SCC in NPP components in BWR environment appear to be based on the same approach as the one used here, i.e. their temperature and environment dependent parameters have been defined so as to obtain an upper bound CGR curve, see procedures e.g. in refs. [30, 31]. Also, these CGR approaches mostly concern sensitised component materials, whereas presently in many/most NPP units in operation the primary circuit components have been replaced with ones of such materials that are not prone to become sensitised.

One possible way to relieve the conservatism in these CGR assessment procedures would be to apply best estimate approach, i.e. so that the CGR curves would rather be formed as to correspond to the mean values of the underlying laboratory data, than as the mentioned upper bound. This would require access to the underlying measurement data, however, which invariably are proprietary and not available, as CGR tests are expensive to perform, among other things because the test durations are typically of the scale of years. However, for the time being it seems that such best estimate approach, or optionally a probabilistic one, would be the best (and perhaps only) ways to relieve the conservatism in the mentioned CGR procedures. Hopefully this would be possible in the future, which obviously requires first gaining access to the mentioned CGR laboratory data sources. Having less conservative CGR procedures available would arguably lead to more realistic structural integrity and fitness-for-service analysis results. However, in these analysis procedures at least a reasonable level of conservatism should be maintained at all times, so as to ensure a sufficient and adequate structural margin against e.g. weaker than designed materials, more severe than anticipated loads and longer than originally designed operational lifetimes.

6. Conclusions

The more recent WRS procedures are backed by more measured data and more accurate FEM analysis result data than the corresponding older ones. So for the assessment of the WRS distributions through wall and perpendicular to weld in as-welded state these procedures are recommended, i.e. API 579, SINTAP, R6 Method Rev. 4 and FITNET, even though their match is not so good in some cases. These more recent procedures are also recommended for the assessment of WRSs in all other directions and for all other weld types and treatments.

However, the more recent WRS procedures are also more complex to apply than the older ones, as the equations are both longer and more numerous. Also, considerably more input data are needed, and if measured data are not available, somewhat conservative assessments and/or standard/handbook values have to be used.

When looking from the viewpoint of avoiding excess conservatism in structural integrity analyses, it is recommended to use such a more recent procedure that gives the lowest WRSs for the analysed weld in question. Possibly this requires making the crack growth analyses using several of the more recent WRS procedures, as it is not necessarily in advance obvious with which of them the slowest crack growth will be achieved. This is because in addition to the magnitude of the WRS values, also the shape of the stress distribution affects the crack growth in the analyses.

References

1. Section XI Task Group for Piping Flaw Evaluation, ASME Code. Evaluation of Flaws in Austenitic Steel Piping. Journal of Pressure Vessel Technology, Vol. 108, 1986. Pp. 352–366.

2. Shack, W. J. et al. Environmentally Assisted Cracking in Light Water Reactors: Annual Report, October 1981 – September 1982. NUREG/CR-3292, Washington D.C., U.S. Nuclear Regulatory Commission, June 1983.

3. British Standard BS 7910: 1999, Guide on methods for assessing the acceptability of flaws in fusion welded structures, 4th draft after public comment. England, 8 April, 1999.

4. R6 Method; Assessment of the Integrity of Structures containing Defects, Revision 4. 2004 update of 2001 edition. British Energy (BE).

5. Dillström, P. et al. A Combined Deterministic and Probabilistic Procedure for Safety Assessment of Components with Cracks – Handbook. SSM Research Report 2008:01, Swedish Radiation Safety Authority (Strålsäkerhetsmyndigheten, SSM). Stockholm, Sweden, 2008. 27 p. + app. 196 p.

6. SINTAP; Structural Integrity Assessment Procedures for European Industry; Final Procedure: November 1999. Project funded by the European Union (EU) under the Brite-Euram Programme: Project No. BE95-1426, Contract No. BRPR-CT95-0024.

7. American Petroleum Institute (API). Recommended practice for fitness-for-service. API 579. Washington, DC, American Petroleum Institute, 2000.

8. FITNET Fitness-for-Service PROCEDURE – FINAL DRAFT MK7. Editor(s) Koçak, M. et al. European Fitness-for-Service Thematic Network – FITNET. Germany. 1.5.2006.

9. Bradford, R. Through-thickness distributions of welding residual stresses in austenitic steel cylindrical butt welds. Proceedings of sixth international conference on residual stresses (ICRS-6). London: IOM Communications Ltd: 2000, p. 1373–381.

10. Dong, P., Osage, D. & Prager, M. Development of weld residual stress distributions for fitness for service assessment. Proceedings of ASME Pressure Vessels and Piping. New York: ASME, 2000, PVP-411: 53–64.

11. Bouchard. P. & Bradford, R. Validated axial residual stress profiles for fracture assessment of austenitic stainless steel pipe girth welds, pressure vessel and piping. Proceedings of ASME conference, New York: ASME, 2001, PVP-423: 93–99.

12. Dong, P. & Brust, F. Welding residual stresses and effects on fracture in pressure vessel and piping components: a millennium review and beyond, ASME Trans. J. Press. Vessel Technol. 2000; 122(3): 328–38.

13. Dong, P., Rahman, S., Wilkowski, G., Brickstad, B., Bergman, M., Bouchard, P. & Chivers, T. Effect of weld residual stresses on crack opening area analysis of pipes for LBB applications. Proceedings of ASME Pressure Vessel and Piping Conference. New York: ASME, 1996, PVP-324: 47–64.

14. Cronvall, O. Review and Comparison of Welding Residual Stress Definitions. Espoo: VTT, 2008. VTT Research Report VTT-R-01415-08. 102 p.

15. Brust, F. W. & Rudland, D. L. Three Dimensional Aspects of Computational Weld Modelling, 2008 ASME PVP Conference, PVP 2008-61558, Chicago, Illinois, USA.

16. Brickstad, B. The Use of Risk Based Methods for Establishing ISI-Priorities for Piping Components at Oskarshamn 1 Nuclear Power Station. SAQ/FoU-Report 99/05, SAQ Kontroll AB, 1999. 83 p.

17. Cronvall, O. On welding residual stresses and their practical inclusion in structural integrity analyses. Proceedings of the 20th International Conference on Structural Mechanics in Reactor Technology (SMiRT 20). Espoo, Finland, August 9–14, 2009. 9 p.

18. Cronvall, O. Practical inclusion and behaviour of welding residual stresses in structural integrity analyses of NPP primary circuit components. Espoo: VTT, 2009. VTT Research Report VTT-R-00962-09. 53 p.

19. Abaqus/Standard User's manual, Version 8.2. Dassault Systèmes Simulia Corp., 2008. Providence, Rhode Island, U.S.A.

20. Abaqus Theory manual, Version 8.2. Dassault Systèmes Simulia Corp., 2008. Providence, Rhode Island, U.S.A.

21. Jones, H. R. (Editor). Stress-Corrosion Cracking. ASM International, Ohio, 1992. 448 p.

22. Congleton, J. & Craig, I. H. "Corrosion Fatigue" in Corrosion Processes, Parkins, R. N., (Ed.). Applied Science Publishers, 1982.

23. Jansson, C. & Morin, U. Assessment of Crack Growth Rates in Austenitic Stainless Steels in Operating BWRs. Proc. of Eighth International Symposium on Environmental Degradation of Materials in Nuclear Power Systems – Water Reactors, August 10–14, 1997. Amelia Island, Florida. Pp. 667–674.

24. ASME Boiler and Pressure Vessel Code Section III, Division 1, Article G-2000. 2005 Update of 2004 Edition.

25. Varfolomeyev, I. et al. BESIF 1.0: Stress Intensity Factors for Surface Cracks under 2D Stress Gradients. IWM-Report T 14/96, Fraunhofer-Institut für Werkstoffmechanik (IWM), July 1996. 42 p.

26. Busch, M. et al. KI-Factors and Polynomial Influence Functions for Axial and Circumferential Surface Cracks in Cylinders. IWM-Report T 18/94, Fraunhofer-Institut für Werkstoffmechanik (IWM), October 1994. 41 p.

27. Busch, M. et al. Polynomial Influence Functions for Surface Cracks in Pressure Vessel Components. IWM-Report Z 11/95, Fraunhofer-Institut für Werkstoff-mechanik (IWM), January 1995. 88 p.

28. Paris, P. C. & Erdogan, F. A Critical Analysis of Crack Propagation Laws. Journal of Basic Engineering, 85(1960): 528–534.

29. Vepsä, A. Verification of the stress intensity factors calculated with the VTTBESIT software. Technical Research Centre of Finland (VTT), Research Group Structural Integrity, Research Report TUO72-044578. 40 p. + app. 2 p.

30. Morin, U., Jansson, C. & Bengtsson, B. Crack Growth Rates for Ni-base Alloys with the Application to an Operating BWR. Sixth International Symposium on Environmental Degradation of Materials in Nuclear Power Systems – Water Reactor Systems, August 1–5, 1993. San Diego, California. Pp. 373–378.

31. Japanese Society of Mechanical Engineers, JSME Codes for Nuclear Power Generation Facilities, JSME S NAI-2004, Rules of Fitness-for-Service for Nuclear Power Plants. 2004, JSME, Tokyo, Japan.

Mechanical performance and life prediction for canister copper

Juhani Rantala, Pertti Auerkari, Jorma Salonen, Stefan Holmström,
Anssi Laukkanen and Tapio Saukkonen*
VTT Technical Research Centre of Finland, Espoo, Finland
*Aalto University School of Science and Technology, Espoo, Finland

Abstract

The creep response of the OFP copper at 175°C has been studied by uniaxial, multiaxial creep testing, metallography and surface inspections. Surface cracks have been observed in a uniaxial test which has been running for more than 70 000 h (eight years). In a CT-specimen creep cavities have been observed after an exposure of 25 000 h. A purpose-built creep strain model has been implemented into FE analysis to characterize the stress multiaxiality and the stress state of the CT specimen. The results have been applied for life prediction of copper at foreseen levels of stress and temperature at the repository.

1. Introduction

This paper describes the mechanical performance of the copper overpack that provides corrosion protection to the final repository canister of spent nuclear fuel. In the current concept of the final repository, the canisters are placed some 400 m underground into the granite bedrock, and should withstand one or more glacial cycles without raising the background level of radiation. Of particular interest is the friction stir (FSW) or electron beam (EB) welded joint between the cylindrical overpack shell and its cover (Figure 1). Considering the mechanical strength of the overpack, the most important period could be the first 500−1000 years, when the peak temperatures could conceivably reach some 90°C (Figure 2).

This is within the range where copper may experience significant creep in case of sufficiently high stress levels [1].

2. Materials and methods

Parent material and welded (FSW) sections of oxygen free phosphorus-doped (OFP) copper was provided by SKB, Sweden. The chemical compositions of the tested materials are shown in Table 1.

Table 1. Chemical composition of the tested OFP copper materials (PM1 & PM2 – parent material of the cylinder; PM3 - section of the cover, W = material from the centre of the weld); in ppm if not otherwise indicated.

Mat'l	Cu%	P	Ag	As	Bi	Pb	Fe	Ni	Cr	S	O
PM1	99.993	42	12.4	1.5	0.36	0.60	1.4	0.9	0.16	6.8	2.6
PM2	99.993	41	11.4	1.5	0.36	0.71	1.2	0.8	0.14	6.7	3.0
PM3	99.993	40	10.5	1.0	0.22	0.35	1.5	1.0	0.14	6.4	2.6
W	99.993	39	10.7	1.4	0.34	0.60	1.3	0.8	0.12	6.3	2.8

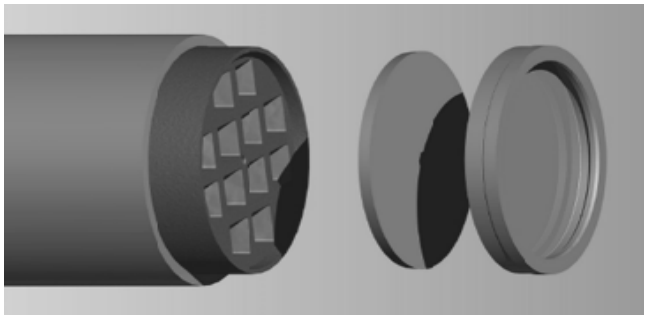

a)

b)

Figure 1. a) Schematic structure of the canister with copper overpack; b) friction stir welding of the cover.

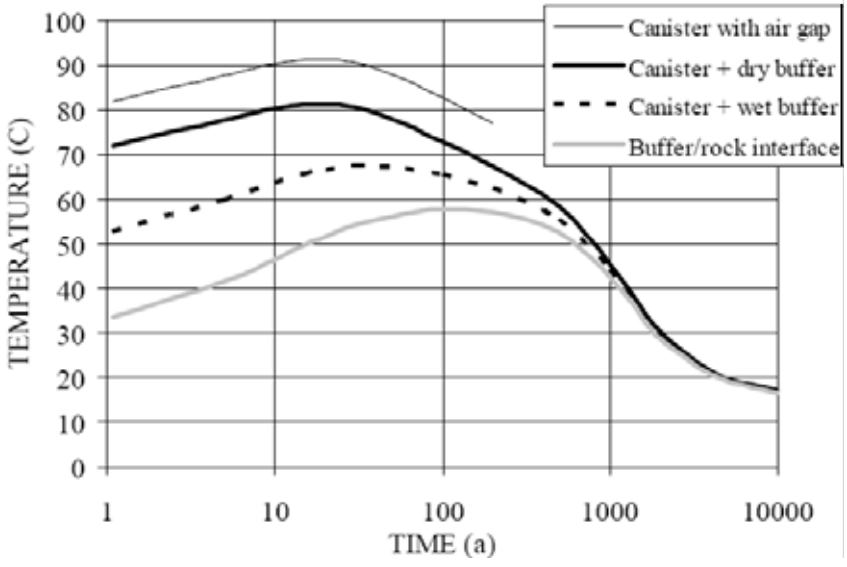

Figure 2. Expected temperature history of the canister for the first 10 000 years; note that some time after closure, the repository will be flooded with groundwater [2].

For testing the creep performance of the welds, ∅ 8 and 10 mm cross-weld uniaxial specimens and W50 mm compact tension (CT) specimens were extracted from the welded section as shown in Figure 3a. The CT specimens were prepared so that the joint line tip was the crack tip in the machined slit, to provide a natural defect. Uniaxial cross-weld specimens were extracted both in axial and radial direction as shown in Figure 3b. The creep testing was performed at 175°C at initial stresses of 80 to 136 MPa. The CT specimen testing was interrupted after every 5000 h of testing at 35 MPa reference stress at 175°C.

The strategy chosen for assessing the long-term performance of copper under repository conditions is to keep the stresses close to the expected range of in-service stress levels and to increase the temperature to accelerate creep in laboratory conditions. This is to avoid non-conservative predicted life when extrapolating from the laboratory results to the actual conditions. Uniaxial creep tests were performed in order to provide the necessary base line data for creep modelling. The multiaxiality effects were tested by using standard CT specimens (W 50 mm), which provide the highest degree of multiaxiality of the normal laboratory specimen geometries as has been shown in the LICON project [3].

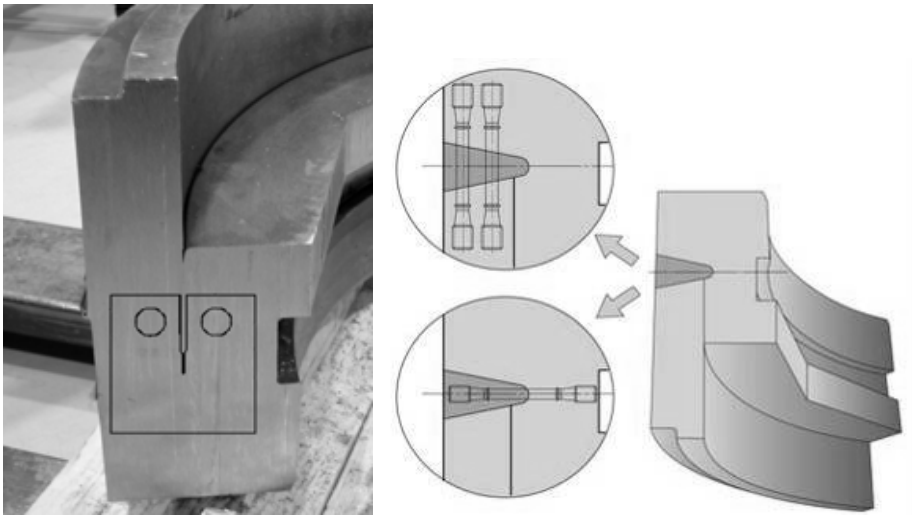

Figure 3. Extraction of a) compact tension (CT) specimens and b) uniaxial cross-weld specimens from a section of a welded (FSW) copper overpack.

3. Results

3.1 Uniaxial specimen testing

The longest uniaxial test for the OFP copper has been running for > 70 000 h at 150°C/120 MPa. At 63760 h the test was interrupted for visual inspection and physical measurements. At that point small apparently intergranular surface cracks were observed (Figure 4), before any clear necking of the specimen. After inspection, the test was continued at the same loading conditions as before.

Figure 4. Surface cracks in a uniaxial creep testing specimen after 63 760 h at 150°C. Scale bar 0.5 mm. Loading direction is horizontal.

3.2 CT specimen testing

The compact tension (CT) specimens with natural defects (sharp-tip FSW joints) were subjected to metallography at the joint tip region on both specimen sides. Slight surface oxidation and opening of the original tip region along the principal defect (inclusion) track was observed particularly after the first two 5 000 h periods of testing.

After 20 000 h of testing first indications of grain boundary cavitation were found as shown in Figure 5. At 25 000 h the cavity density had clearly increased, see Figures. 6 and 7. The cavity densities as observed in SEM are shown in Figure 8. The cavities observed in the CT specimen are small in size and have a high number density. Their appearance differs clearly from the large cavities which form at a low number density during ductile tearing near the fracture surface.

Figure 5. Grain boundary cavitation in EBSD image after 20 000 h. Scale bar 200 µm. Loading direction is vertical.

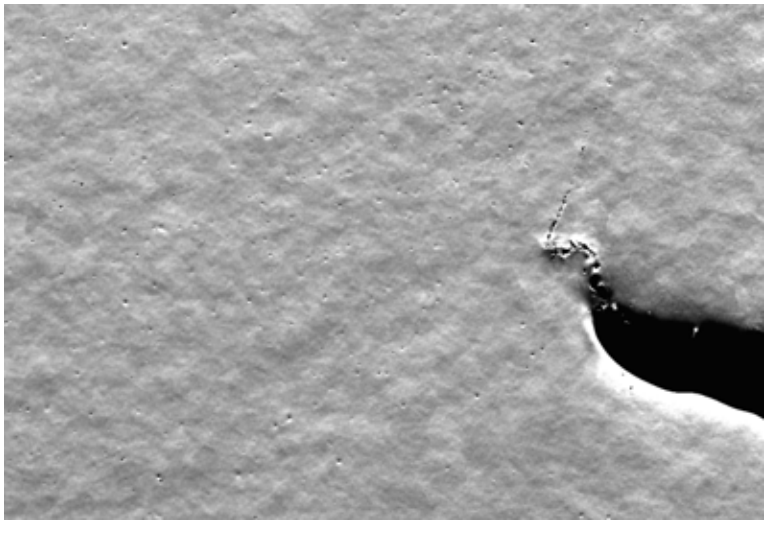

Figure 6. CT tip after 25 000 h. Width of the figure is 1.07 mm. The line of cavities towards 1 o'clock position from the crack tip are oxide particles of the original joint surfaces deformed by the FSW process. Loading direction is vertical.

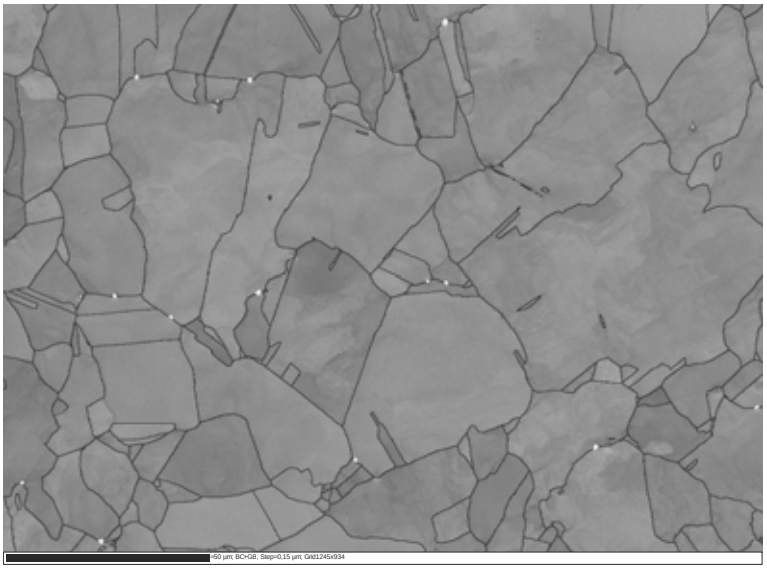

Figure 7. Grain boundary cavitation in EBSD image after 25 000 h. Scale bar 50 μm. Loading direction is vertical.

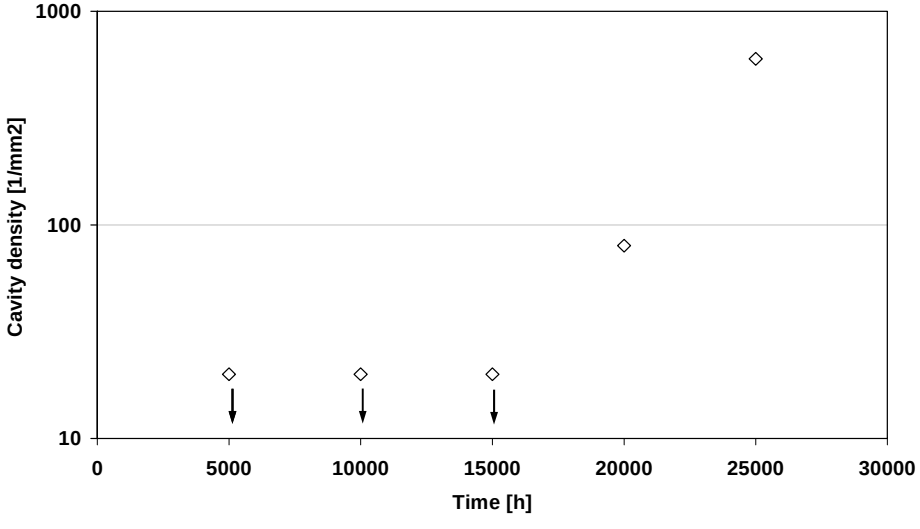

Figure 8. The measured maximum cavity densities from interrupted CT tests. The cavity density before 20 000 h was below the resolution of inspection.

3.3 Creep modelling and FE analysis

The Wilshire approach has been used for creep rupture modeling. The applied (engineering) test stress σ is normalised by the ultimate tensile stress σ_{TS} at test temperature and the rupture time t_f can be calculated from Equation (1):

$$\frac{\sigma}{\sigma_{TS}} = \exp\{-k_1[t_f \exp(-\frac{Q_c^*}{RT})]^u\} \quad (1)$$

where k_1 and u are constants extracted from the data fitting. For life assessment of axial and radial cross-weld specimens, the creep strain and rupture results were compared with the available base material data [1, 5].

The base material master curve was obtained by fitting the available creep rupture data to the Wilshire model by minimizing the root mean square of the difference in measured and predicted logarithmic rupture times [5]. The resulting model fit and the parameter values of the rupture model are shown in Figure 9.

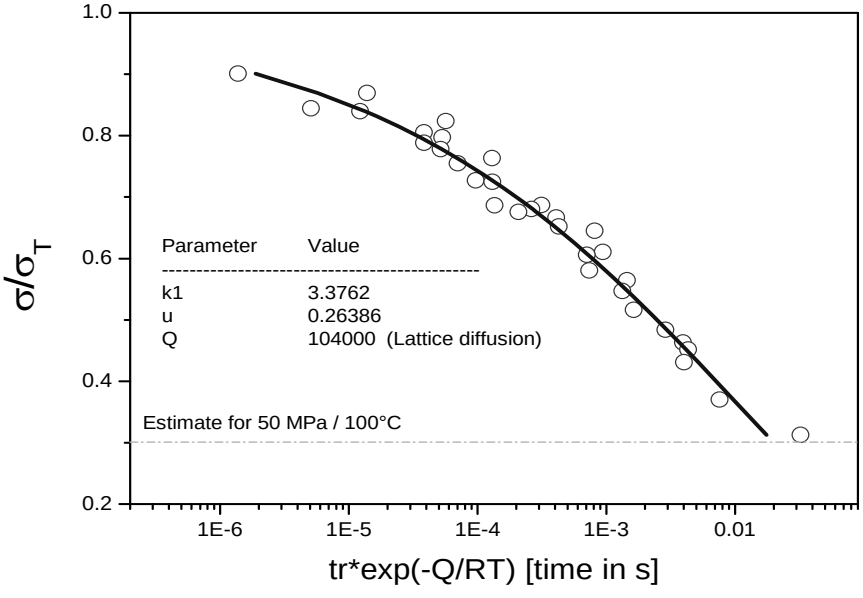

Figure 9. Creep data fit to the parent material model of OFP copper.

The creep strain response of copper is modelled by using the LCSP creep model, which includes primary, secondary and tertiary terms [5]. This creep model has been implemented into FEM. The principal stresses ahead of the crack tip in a

standard W 50 mm CT specimen with a notch radius of 0.07 mm after an exposure of 10 000 h are shown in Figure 10. It should be pointed out that when using the LCSP creep model the stresses at the crack tip have a finite value and don't approach infinity like in the case of using a standard Norton creep model. The peak stresses appear at a distance 0.1 mm ahead of the crack tip. It should also be noted that from a distance of 0.4 mm onwards the highest vertical stress component is the stress acting in the direction of crack extension.

The von Mises effective stress distribution ahead of the crack tip plotted at three different load levels (plane stress Tresca effective stress = 55.2/43.2/24.6 MPa) in Figure 11 shows that at a distance of 0 to 0.1 mm there is a zone which can be seen as analogous to the process zone in elastic-plastic fracture mechanics. In this zone the material is at tertiary stage. At all three stress levels the stresses in this zone overlap and start to differ only further away from the crack tip.

In the LICON method [4] the multiaxiality is quantified by using the multi-axiality parameter H which is defined as the ratio of maximum principal stress over von Mises effective stress:

$$H = \frac{\sigma_1}{\sigma_{VM}}$$

The distribution of this parameter H at three different load levels after 10 000 h is plotted in Figure 12. The distributions differ at locations close to the crack tip but settle to a stable value of 2.65 after a distance of 0.4 mm.

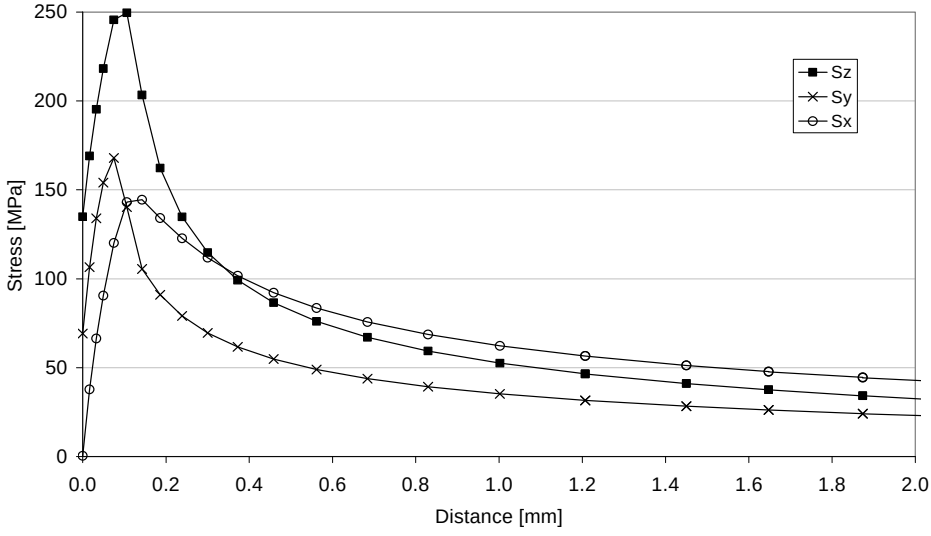

Figure 10. Stress components ahead of the crack tip after 10 000 h at a load of 5.6 kN, plane stress Tresca effective stress = 24.6 MPa.

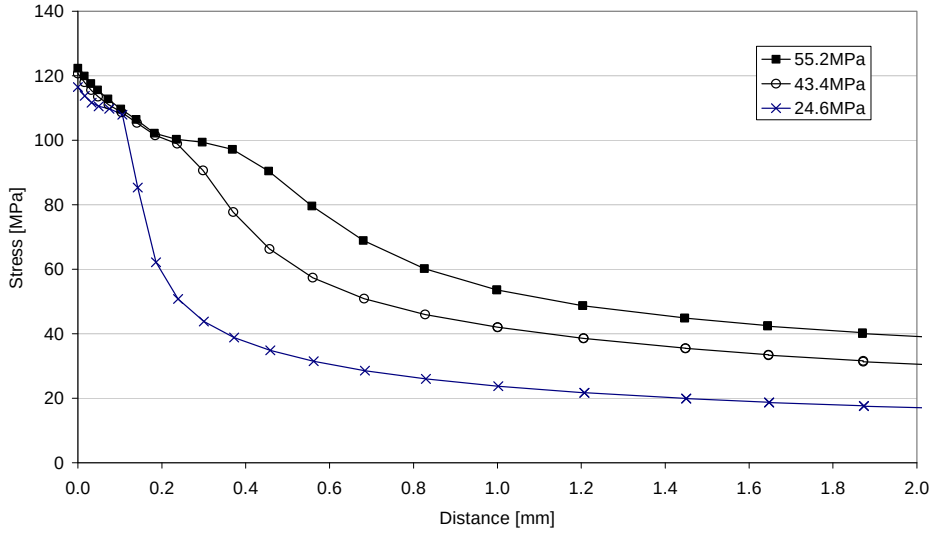

Figure 11. von Mises effective stress distribution ahead of the crack tip at three different reference stress levels.

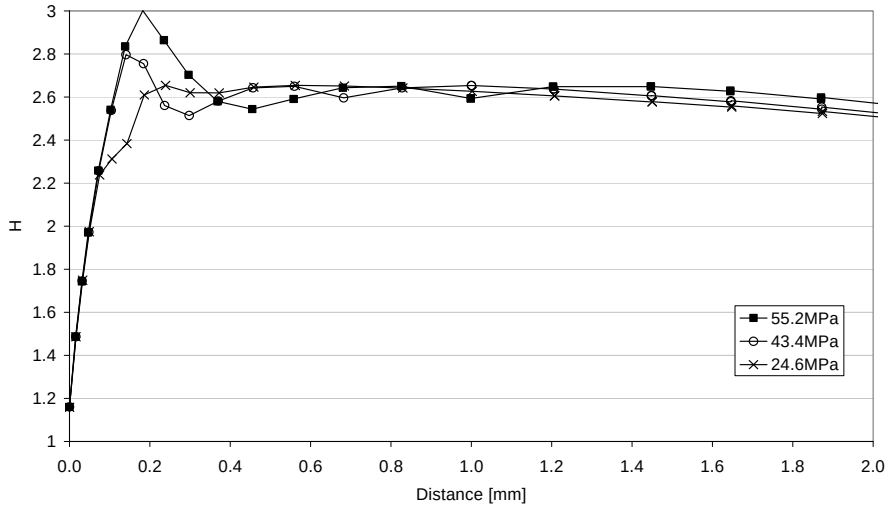

Figure 12. Distribution of the multiaxiality parameter H at three reference stress levels.

4. Life prediction

Extrapolating the creep models for the OFP canister copper (corresponding to all available creep data combined), the expected life at 50 MPa and 100°C requires extrapolation of the model to a normalised stress (σ/σ_{TS}) of just below 0.3 in Figure 9. The corresponding predicted rupture time at 100°C is 43 000 ± 9 000 years, which is again less than the specified safe life even if a life of 100 000 years is considered as a requirement (note however that the foreseen temperature is much less already after some 1 000 years if not earlier). This new prediction is based on the Wilshire rupture model, an apparent activation energy of 90 ± 3 kJ/mol, and allows an uncertainty of ±2.5% in the ultimate tensile stress at temperature, and ±2°C in temperature. The predicted life fraction consumed during the first 10 000 years with the temperature profile presented by Raiko [2] is at 50 MPa less than 1%. The predicted life is lower than those obtained earlier. It should be noted that much of the predicted shortening is due to the optimised apparent activation energy being reduced from about 104 kJ/mol (i.e. that for expected self-diffusion of copper) to 90 kJ/mol.

References

1. Auerkari, P., Rantala, J., Salonen, J., Laukkanen, A., Holmström, S. & Kinnunen, T. Effect of defects on low temperature creep of OFP copper. 2nd International ECCC Conference, Creep & Fracture in High Temperature Components – Design & Life Assessment. Dübendorf, Switzerland, April 21−23, 2009.

2. Raiko, H. Disposal canister for spent nuclear fuel – design report. Posiva Report 2005-2. ISBN 951-652-134-7.

3. Rantala, J., Auerkari, P., Holdsworth, S. R. & Hurst, R. C. The LICON approach to life management. In: BALTICA VII. Life Management and Maintenance for Power Plants. Veivo, Juha & Auerkari, Pertti (Eds.). Espoo: VTT, 2007. VTT Symposium 247, Vol. 2. Pp. 222–234.

4. Mendes Martins, V. & Holdsworth, S. R. The LICON methodology for predicting the long term service behaviour of new steels. Materials at High Temperatures, Vol. 19 (2002) 2, pp. 99–103.

5. Holmström, S. Engineering tools for robust creep modeling. Espoo: VTT, 2010. 94 p. + app. 53 p. VTT Publications 728. ISBN 978-951-38-7378-3.

Localization of plastic deformation in copper canisters for spent nuclear fuel

Kati Savolainen, Tapio Saukkonen and Hannu Hänninen
Aalto University School of Science and Technology
Espoo, Finland

Abstract

In Finland and Sweden the spent nuclear fuel will be deposited in a deep repository in copper corrosion barrier canisters surrounding cast iron inserts. The 50 mm thick copper canisters will we sealed using either electron beam welding (EB) or friction stir welding (FSW) to join the tubes and the lids/bottoms. The canisters will deform in the repository conditions, e.g., due to the hydrostatic pressure. The deformation will localize to different discontinuities, such as defects and microstructural heterogeneity.

This study compared the localization of plastic deformation in EB and FSW welds as well as in the base materials (both forged and extruded) using optical strain measurement methods. The results show that in the base materials the deformation occurs very uniformly over the entire gauge length. In FSW welds the deformation localizes in the weld at a line of entrapped oxide particles. In EB welds the deformation localizes to the large grains in the middle of the weld or at the steep grain size gradient between the weld and the tube material. Tensile strength is lowest in the EB welds (175 MPa as compared to 200 MPa or higher for the other samples). Elongation to fracture of the FSW welds is similar to those of the base materials, but for the EB welds it is significantly lower (appr. 40% compared to 65%).

1. Introduction

Finland and Sweden have decided that the spent nuclear fuel will be encapsulated and deposited into long-term repositories. The spent nuclear fuel will be placed in cast iron inserts surrounded by copper corrosion barrier canisters. The 50 mm thick copper canisters consist of an extruded tubular body and forged lid and bottom parts. The canisters will be sealed using either electron beam welding (EB) or friction stir welding (FSW) to join the tubes and the lids/bottoms. Plastic deformation caused by the repository conditions, such as hydrostatic pressure and bentonite swelling, will not be distributed evenly around the canister, but instead it will concentrate to certain locations. Microstructural defects, geometric discontinuities, as well as microstructural heterogeneity and residual stresses of the welds, in particular, localize plastic deformation.

The aim of this study was to determine where the plastic deformation localizes in the different parts of the copper canister. Samples of the extruded and forged base materials as well as EB and FSW welds transverse to the welding direction were tensile tested. An optical strain measurement system comprising of a CCD camera and a PC with imaging software was used to measure and analyze the deformation of the samples during tensile testing. The system records successive images of the sample surface and constructs the deformation field using advanced cross correlation algorithms. Many have shown the usefulness of the OIC/DIC method in determining the mechanical properties of the welds [1].

The amount of residual plastic strain is known to have an effect on different long-term materials properties. For instance, effect of prestrain (dislocation density) on creep of copper has been shown [2]. In austenitic AISI 304 stainless steel the amount of cold work exceeding 20% is known to result in initiation of the stress corrosion cracking [3]. Thus, when wanting to ascertain and evaluate the integrity of the copper canister it is very important to know the material properties even in very small localized areas. Electron backscatter diffraction (EBSD) and electron microscopy have in recent years proved to be a promising method to study the plastic strain and other material properties in localized areas. However, due to time constraint when wanting to map large areas, it is beneficial to be able to concentrate only on critical areas. The different regions of a weld are typically exhibiting large variations of residual plastic strain and various discontinuities in the material properties. The optical strain measurement using large test samples containing the whole weld area is an ideal method to detect the critical areas, which can later be studied with electron microscopy in detail.

Different manufacturing and welding methods result in different microstructures. Forged and extruded base materials have a small grain size. FSW is a solid state welding method, where the resulting microstructure has a small, equiaxed grain size, similar to those of the base materials. Properties of the FSWelds have been reported to be very close to those of the base materials [4]. EB is a fusion welding method where a high-energy electron beam locally heats the material to a high temperature. The resulting microstructure has a very coarse grain size.

2. Methods

The base materials of the forged lids and extruded tubes were slightly different depending on the manufacturing method (Table 1). Therefore, the base materials of the welds were different. Due to their similarity and restrictions in the amount of available material, optical strain measurements were made only with tube material of the EB weld and lid material of the FSW weld. The tensile test samples were electro-discharge machined.

Table 1. Grain sizes and amount of twin boundaries of the total amount of grain boundaries of the base materials.

	Grain size (µm)				**Twins (%)**
	Horizontal		**Vertical**		
	Disregarding twins	**Including twins**	**Disregarding twins**	**Including twins**	
Tube (EB)	63	28	44	19	58
Tube (FSW)	75	32	76	35	60
Lid (EB)	70	39	52	30	30
Lid (FSW)	61	29	62	31	53

Tensile testing was performed by MTS 810 material test system at a constant rate of 0.02 mm/s using flat tensile test samples. Gauge length was 40 mm, width 35 mm, and thickness 5 mm. Welds were located at the centre of the gauge length. Images for optical strain measurement were obtained at a rate of 0.3 Hz during tensile testing. Deformation fields were determined using StrainMaster optical strain measurement system by LaVision. Sample preparation for EBSD was made using SiC grinding papers, diamond polishing up to 1 µm, and electrolytic

polishing. Zeiss Ultra 55 FEG-SEM and Channel5 acquisition and analysis software by HKL Technologies were used in SEM and EBSD studies. For macroscopic studies the samples were etched using 50%/50% solution of distilled water and nitric acid for 60 s.

3. Results and Discussion

Figure 1 shows a macrograph of the transverse section of an FSW weld. Figure 2 shows a macrograph of the transverse section of an EB weld. Figure 3 shows a longitudinal section of an EB weld exhibiting its very large grain size.

Figure 1. Macrograph of the transverse section of an FSWeld. Tube material is on the right side and lid material on the left side. Different zones of the weld can be clearly seen. Fracture location is marked with a black line. Thickness of the joint is 50 mm.

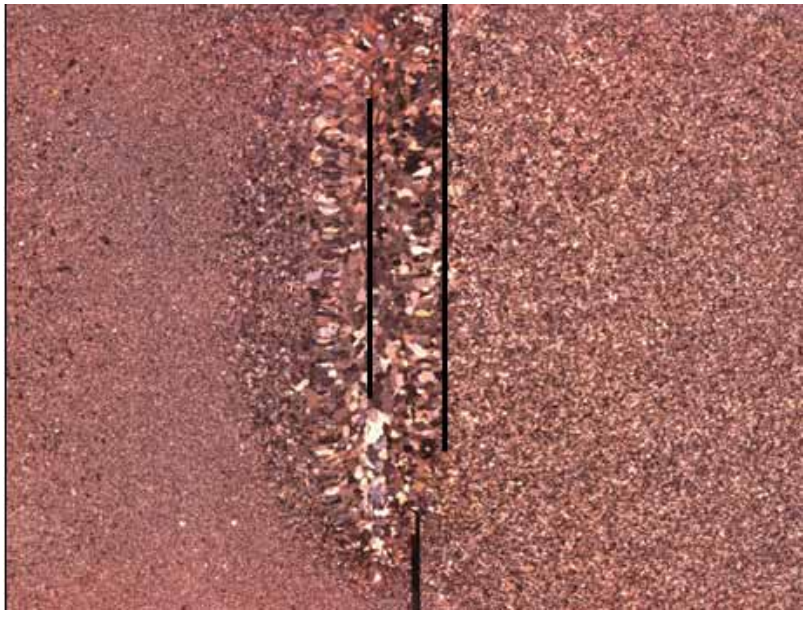

Figure 2. Macrograph of the transverse section of an EB weld. Tube material is on the left side and lid material on the right side. The large grain size of the weld can be clearly seen. Fracture locations are marked with black lines. Thickness of the joint is 50 mm.

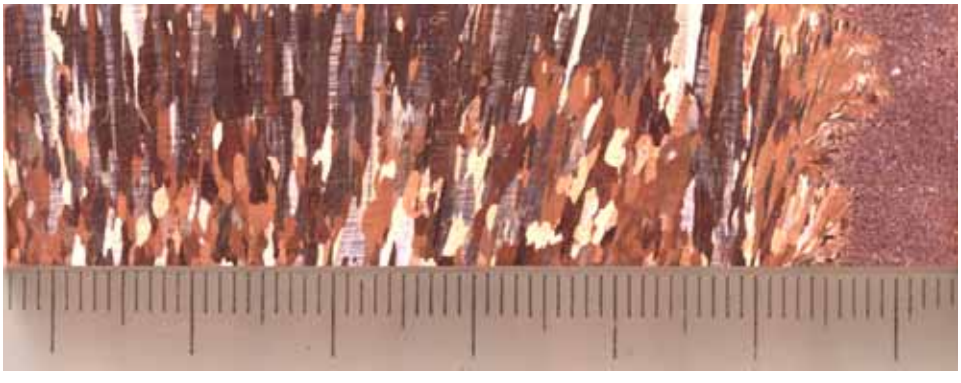

Figure 3. Macrograph of the longitudinal section of an EB weld. Top of the weld is on the left side and bottom on the right side. Tube material can be seen on the right side. The very large longitudinal grain size of the weld can be clearly seen. The scale is a ruler with 1 mm divisions.

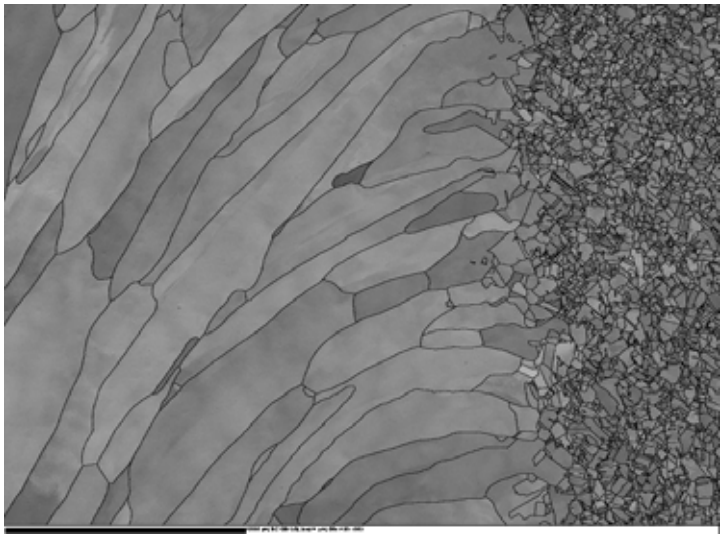

Figure 4. Top view of an EB weld. Large grain size can be clearly seen. Base material is on the right. Length of the scale bar is 2000 µm.

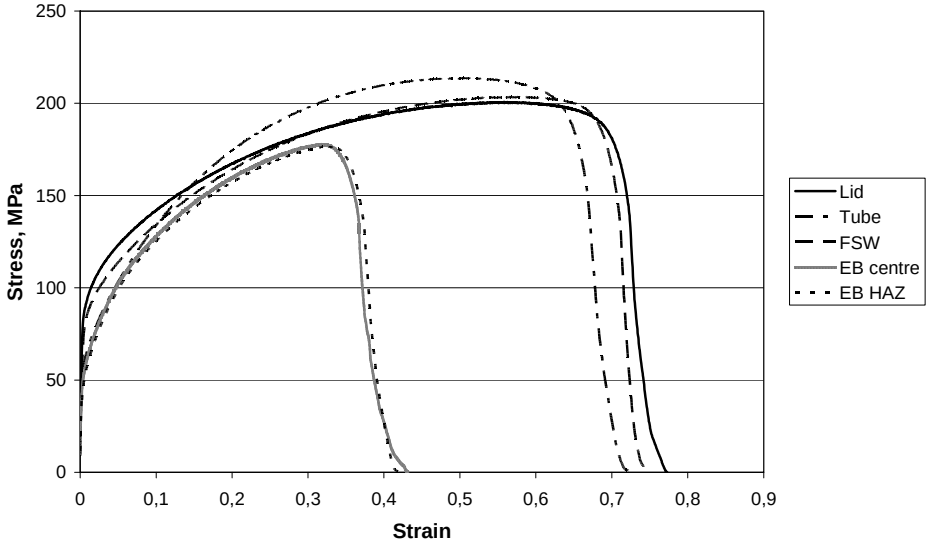

Figure 5. Stress-strain curves of each test sample. It can be seen that the tensile strength of the EB weld is low compared to that of the other samples, 175 MPa as compared to 200 MPa or higher of the other samples.

Figure 5 shows a stress-strain curve for each test sample. It can be seen that the tensile strength of the EB weld is lower than that of the other samples. Tensile strength of the EB weld is 175 MPa while the other samples have a tensile strength of 200 MPa or higher. The extruded tube material has the highest tensile strength of 210 MPa. It can also be seen that the elongation to fracture of the EB weld is significantly lower compared to the other materials. Yield strength was 75 MPa for the tube material and EB weld, 95 MPa for the FSW weld, and 105 MPa for the lid material.

Uniform, local, and total strains of the samples can be seen in Table 2. Elongation to fracture is similar with base materials and the FSW welds. However, for the EB weld it is reduced to almost half compared to the other materials. The reduction of local strain with the EB weld is even more marked than that of the uniform strain. Table 2 shows also strains at the gauge length measured by LaVision. The results differ from those obtained by the displacement measurement. The discrepancy is most likely due to elongation occurring over the entire sample, not merely at the gauge length.

Table 2. Uniform, local, and total strains of the samples as well as the results obtained by LaVision.

	Uniform strain	**Local strain**	**Total strain**	**LaVision**
Tube	0.50	0.23	0.73	0.65
Lid	0.56	0.21	0.77	0.66
FSW	0.55	0.18	0.73	0.61
EBcentre	0.32	0.11	0.43	0.40
EBhaz	0.32	0.10	0.42	0.38

Figures 6–9 show the results of the optical strain measurements at the point of fracture. All images have the same scale for strain (0–3.5). All samples exhibit similar uniform elongation with the exception of the EB weld. In EB weld the extruded tube material is elongated much more than the forged lid material.

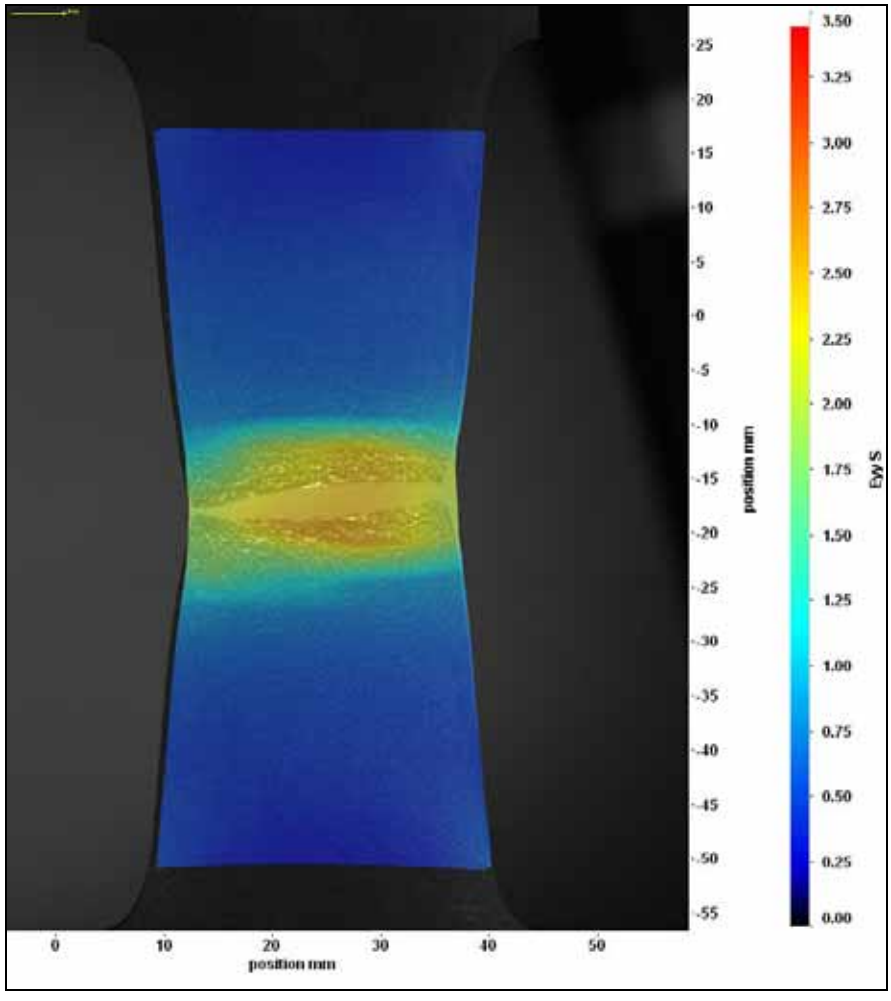

Figure 6. Strain map of lid material.

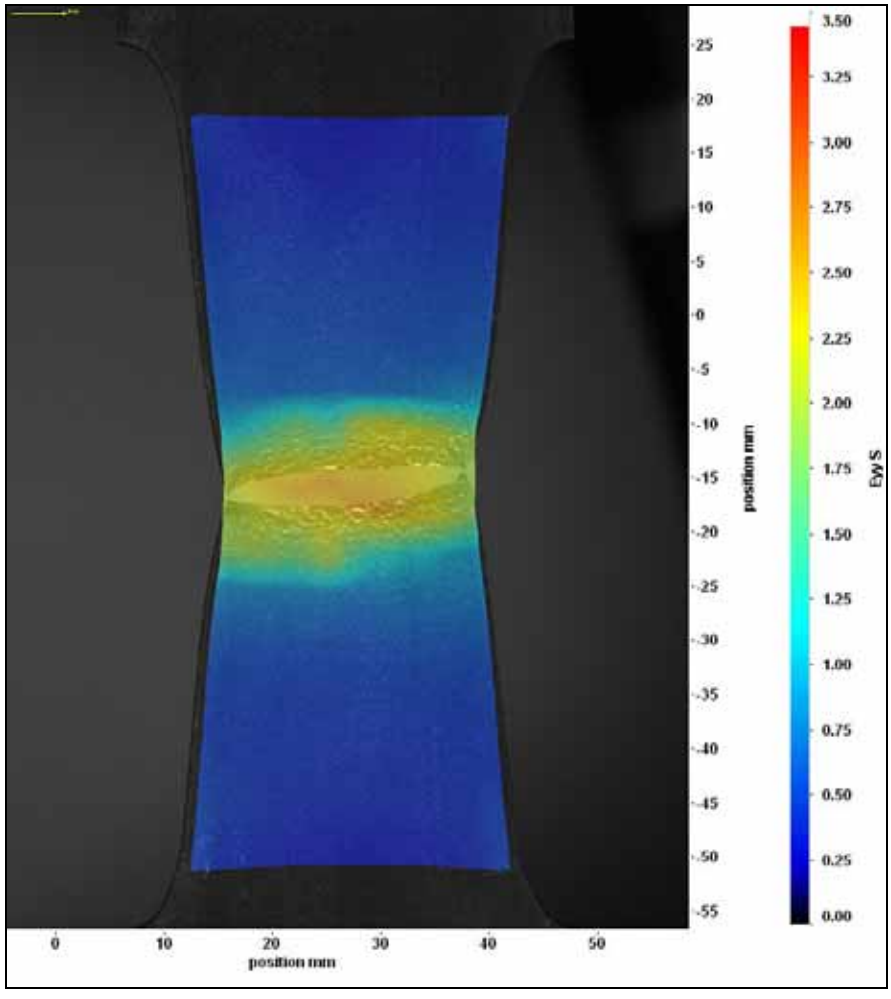

Figure 7. Strain map of tube material.

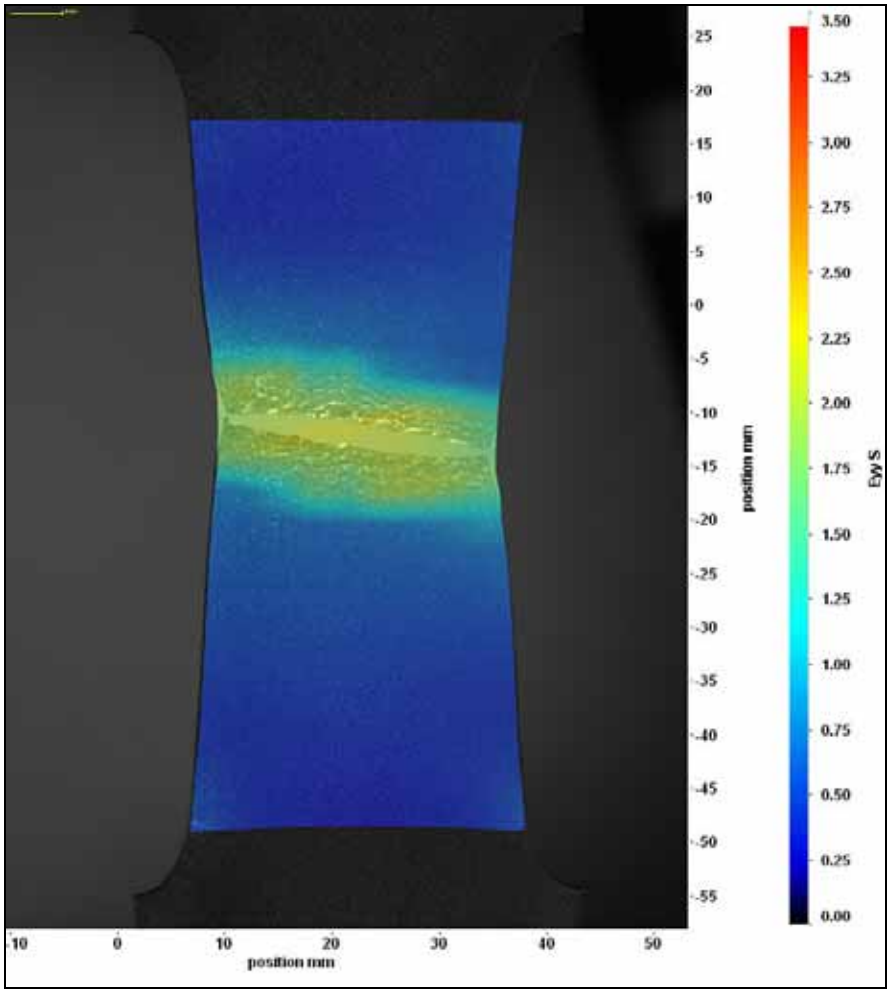

Figure 8. Strain map of an FSWeld. Lid material is on the top and tube material on the bottom. The fracture occurs in the weld closer to the lid material along a line of entrapped oxide particles.

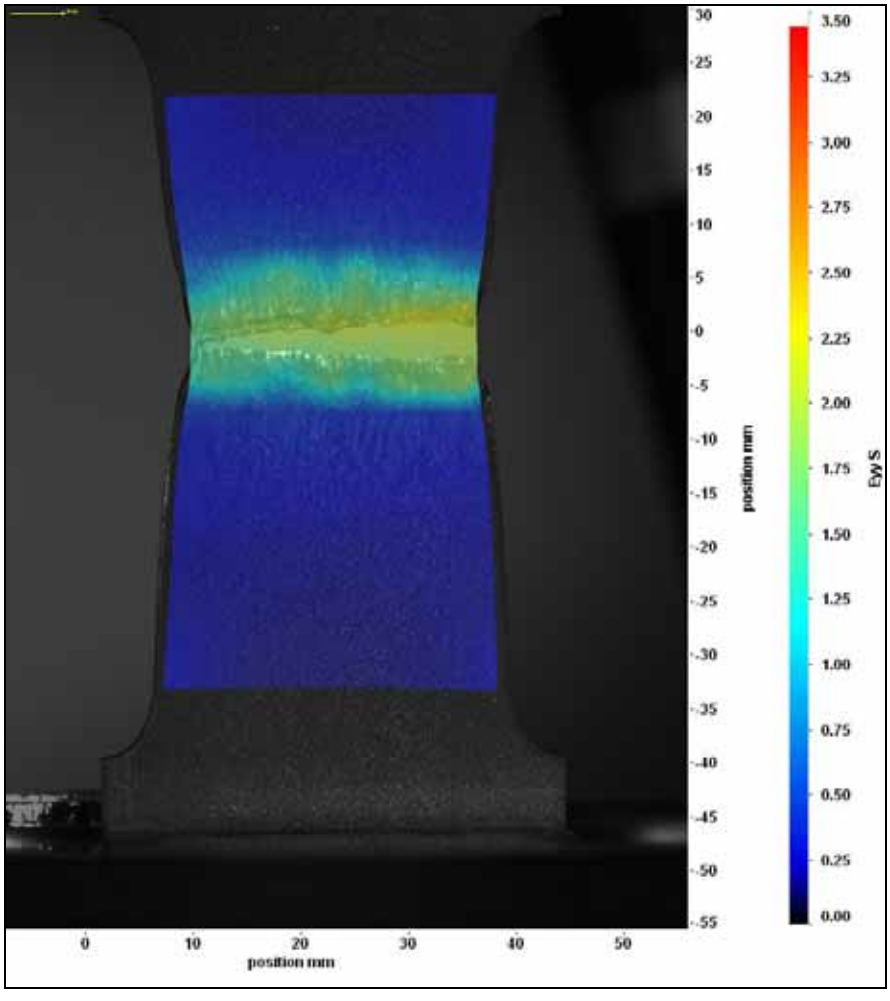

Figure 9. Strain map of an EB weld which fractured at the centre of the weld. Lid material is on the top and tube material on the bottom. Deformation localizes to the middle of the weld with large grain size. It can also be seen that the extruded tube material is elongated much more than the forged lid material.

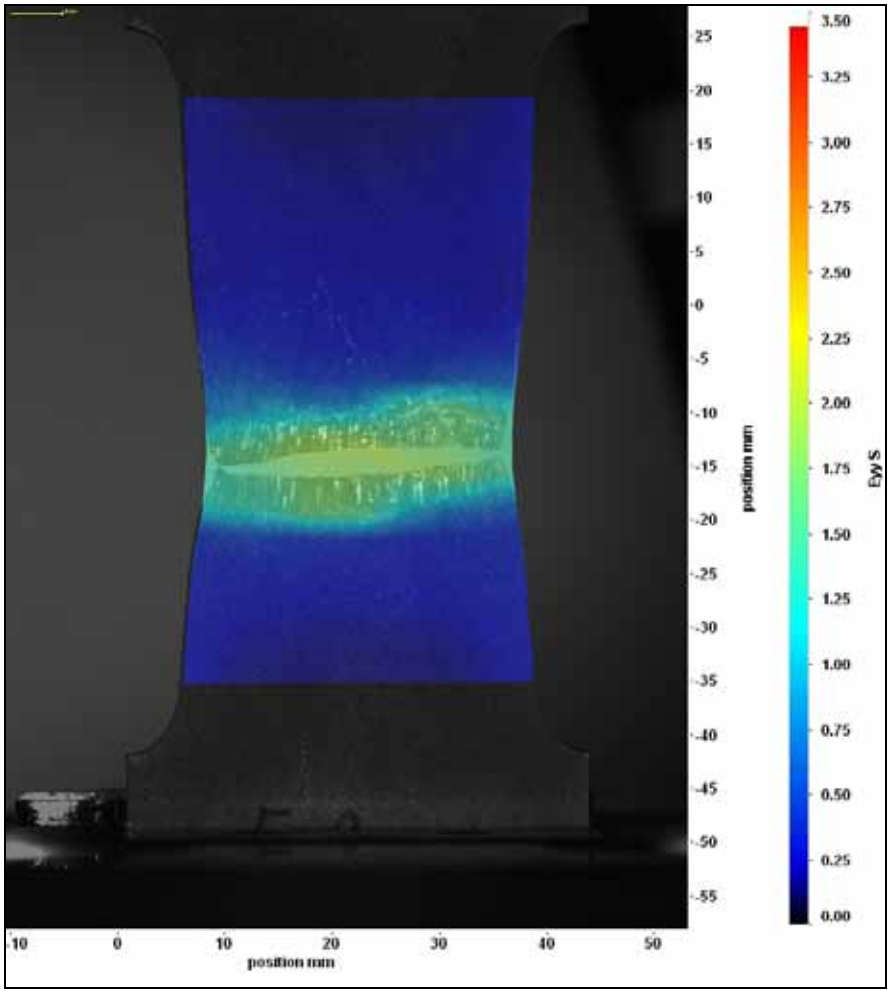

Figure 10. Strain map of an EB weld which fractured at the HAZ. Tube material is on the top and lid material on the bottom. Deformation localizes to the HAZ. It can also be seen that the extruded tube material is elongated much more than the forged lid material.

Figure 11 shows an EBSD map of the root of an FSWeld. Part of the original joint line can be seen on the upper left corner of the image. Weld material is on the top and forged lid material is on the bottom. The smooth transition from the base material to the weld can be seen. Figure 12 shows an EBSD map of the root of the EB weld in transverse direction. The grain size gradient between the base material and the weld is steep, which is even more clearly seen in Figure 4.

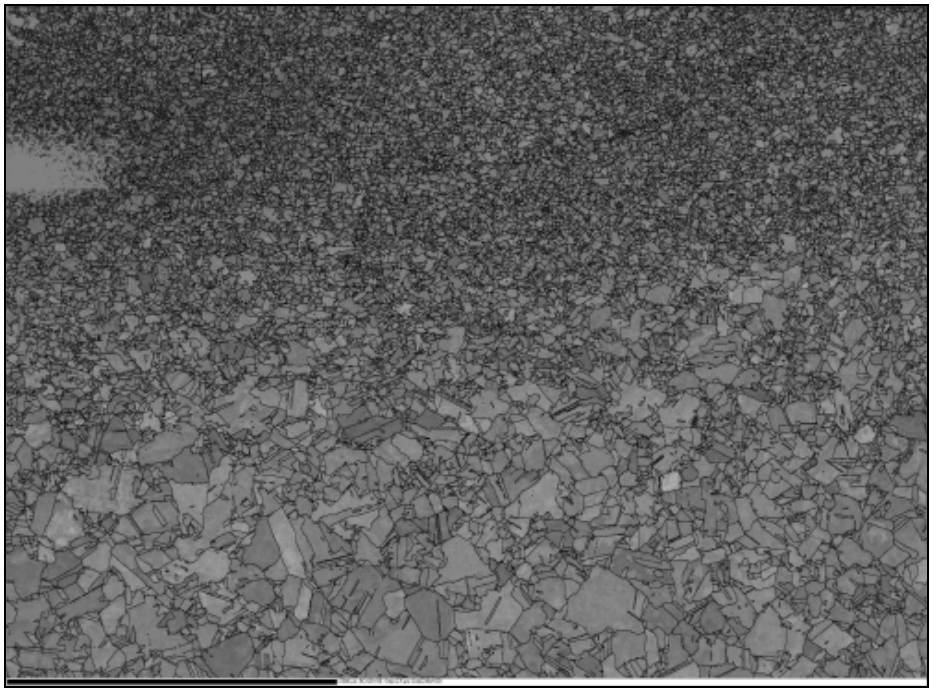

Figure 11. An EBSD map of the root of an FSWeld in transverse direction. Part of the original joint line can be seen on the upper left corner. The weld is on the top and forged lid material on the bottom. The transition from the weld to the base material is smooth. Length of the scale bar is 2000 µm.

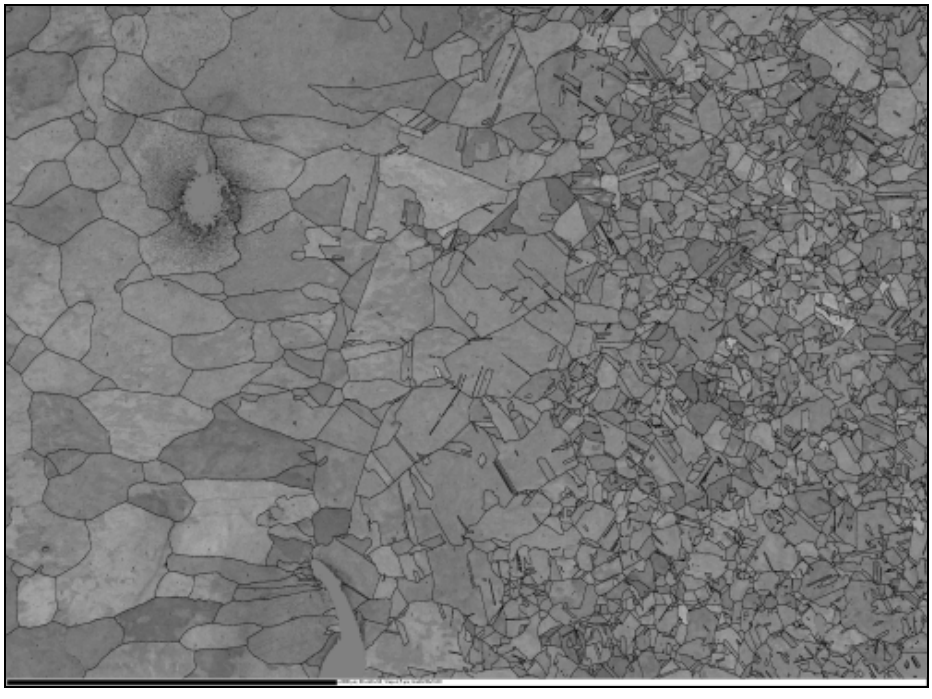

Figure 12. An EBSD map of the root of an EB weld in transverse direction. Part of the original joint line can be seen at the bottom, left from the centre. The weld is on the left and forged lid material on the right. The transition from the weld to the base material is abrupt and in the longitudinal direction the grain size gradient is even more pronounced. A weld defect (void) can be seen on the upper left corner. Length of the scale bar is 2000 µm.

4. Conclusions

Based on the results obtained in this study it can be concluded that deformation occurred quite uniformly in all the samples except for the EB weld. In EB welds the deformation localizes mainly to the large grains in the middle of the weld. It was also noticed that in EB welds the extruded tube material is elongated more than the forged lid material. The tensile strength for EB weld was lower than that for the other materials, 175 MPa and 200 MPa or higher, respectively. Elongation to fracture was similar in the base materials and the FSW welds, but considerably lower in the EB welds (appr. 40% compared to 65%).

It needs to be noted that the strain rates used in this study are high compared to the real strain rates during the 100 000 years in the repository. The actual

strain rates are comparable to those of creep. The strain localization at extremely low strain rates combined with elevated temperatures will be significantly higher than that presented in this study, and this will be carefully studied in the future.

Acknowledgements

The authors wish to thank SKB for FSW welds, Posiva for EB welds, and Kim Widell for help in tensile testing and optical strain measurement.

References

1. Lockwood, W. D. & Reynolds, A. P. Simulation of the global response of a friction stir weld using local constitutive behavior. Materials Science and Engineering, 2003. Vol. A:339, pp. 35–42.

2. Wilshire, B. & Palmer, C. J. Strain accumulation during dislocation creep of prestrained copper. Materials Science and Engineering, 2004. Vol. A:387–389, pp. 716–718.

3. Ehrnstèn, U., Aaltonen, P., Nenonen, P., Hänninen, H., Jansson, C. & Angeliu, T. Intergranular cracking of AISI 316NG stainless steel in BWR environment. 10th Symposium on Environmental Degradation of Materials in Nuclear Power Systems – Water Reactors. Nevada, USA, 5–9 August 2001. 10 p.

4. Cederqvist, L. FSW to seal 50 mm thick copper canisters – a weld that lasts for 100 000 years. 5th International Friction Stir Welding Conference. Metz, France, 14–16 September 2004. 6 p.

Creep properties of phosphorus alloyed oxygen free copper under multiaxial stress state

Rui Wu[1], Rolf Sandström[1,2] and Facredin Seitisleam[1]
Swerea KIMAB AB[1]
Dept. of Materials Science and Engineering, KTH[2]
Stockholm, Sweden

Abstract

Creep tests have been carried out at 75°C using double notch specimens with notch acuities of 0.5, 2, 5, and 18.8, respectively. The creep lifetime for notched specimens is considerably longer than that for the smooth one at a given net section stress, indicating that the investigated Cu-OFP is notch insensitive (notch strengthening). The creep lifetime is notch acuity dependent. The sharper the notch, the longer the creep lifetime is. The creep deformation is to a significant extent concentrated to the region around the notches. Both axial and radial strains on the failed notch are several times larger than those on the unbroken one. Transgranular failure is predominant, independent of stress, rupture time, and notch acuity. To interpret the testing results, finite element computations have been performed using fundamental constitutive equations. The FEM-modelling could represent the creep strain versus time curves for the notched specimens in a satisfactory way. From the FEM-computations a stationary creep stress could be assessed. For a given stationary creep stress, the rupture time can be estimated from the corresponding uniaxial data. This relation can be used to estimate the rupture time for components exposed to creep.

1. Introduction

Phosphorus alloyed oxygen free copper (Cu-OFP) copper canisters are planned to be used for spent nuclear fuel in the Swedish nuclear waste programme. In the repository the copper material will be deformed by creep at temperatures up to about 100°C. To ensure the integrity of the canisters against creep deformation, the copper material must have sufficient creep ductility under the multiaxial stress state that appears at critical positions. Failure mechanism, mode and fracture ductility are found to be affected by the stress state [1–4]. Components under a high state of multiaxial stress can fail prematurely due to the inhibition of deformation and enhancement in fracture processes [1].

One established and convenient method of introducing a state of multiaxial stress into laboratory specimens is to subject circumferentially notched bars to an axial tensile stress [5]. Such notched bar specimens are relatively inexpensive to manufacture and can be tested in the same machine used to collect standard uniaxial data. In addition, various states of stress in terms of ratio between maximum principal stress and effective stress can be obtained and simulated by changing the notch profile [6].

In design when cracks are encountered, the simplest way is to estimate the average stress on the remaining section, the net section stress, and compare it with the design stress. A more sophisticated procedure is to use elastic-plastic FEM-modelling assuming a perfectly plastic material, yielding at different artificial stress levels. The minimum yield stress (effective stress) that can support the external load, the reference stress, can be compared with the design stress. An even more advanced approach is to include a creep calculation in the FEM-model. The resulting (stationary effective) creep stresses can be related to the design stress. In the present paper all three methods will be analysed for notched specimens.

By using notched bar creep specimens, the other purposes of the present project are to study the creep lifetime and ductility of OFP-copper under multiaxial stress state, to compare creep behaviour under multiaxial stress state with that under uniaxial stress state, and to examine creep damage development.

2. Material and experiments

2.1 Material

A forged lid in as-hot worked soft condition made of pure, oxygen-free copper doped with about 50 ppm phosphorus (Cu-OFP) is used in this study. The lid is provided by Svensk Kärnbränslehantering AB (Swedish Nuclear Fuel and Waste Management Company, SKB).

Mixed grain size is observed in the forged lid, see Figure 1. The average grain sizes adjacent to the centre and to the outside are 85 μm and 156 μm, respectively, see also Figure 1. The hardness (HV2), which is a mean value of three measurements, is 78.

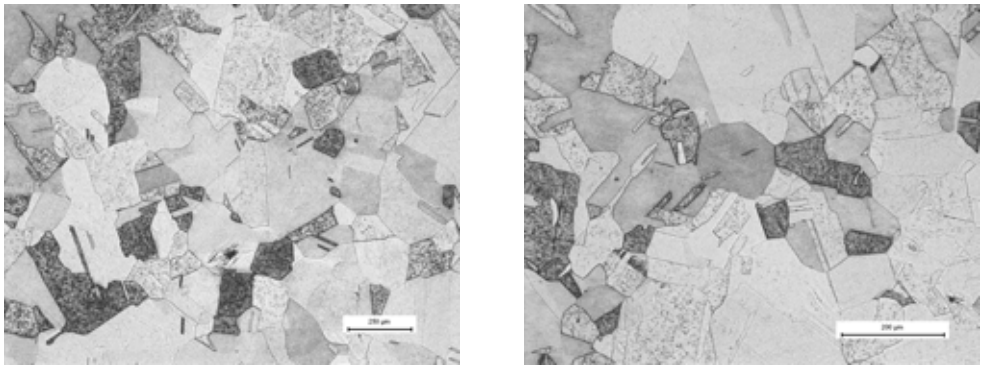

(a) (b)

Figure 1. Grain size distribution in the forged lid (noting different scales). (a) Adjacent to the centre and (b) adjacent to the outside.

2.2 Creep specimen

Two notches are introduced on a cylindrical creep specimen with threaded ends having a diameter of 8 mm in the gauge length and a total gauge length of about 51 mm, see Figure 2. The fracture is expected to take place in one of the two notches, while the other unbroken one should represent the circumstances close to rupture, facilitating the creep damage investigation.

Four different notch acuities are chosen. The notch acuity, a/R, is set to be equal to 0.5, 2, 5 and 18.8, respectively. The parameter a is the radius of the specimen

at the base of the notch position, and R the notch root radius. As an example, the cylindrical, double notched creep specimen with a notch acuity a/R = 0.5 is shown in Figure 2. According to the definition of the notch acuity a/R, the larger the a/R value, the sharper the notch.

The ratio of b/a is set to $\sqrt{2}$. The parameter b is the gross radius of the specimen, see also Figure 2. The dimension of the specimen corresponds to that recommended in the code of practice for notched bar testing [5].

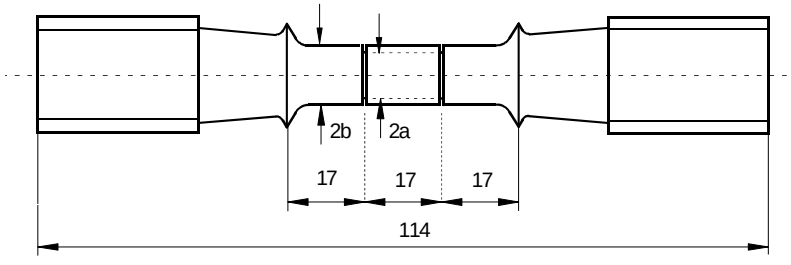

(a)

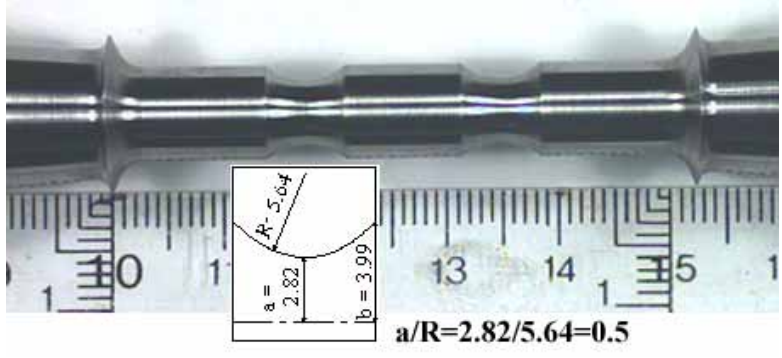

(b)

Figure 2. Double notched cylindrical creep specimen. a) dimension, and b) a specimen having notch acuity a/R = 0.5 prior to test.

2.3 Creep testing

By using single specimen, constant dead load creep testing machines the cylindrical, double notched creep specimens are isothermally tested at constant temperature of 75°C at different initial net section stresses. The net section stress is the applied axial load divided by the minimum cross section at the notch. Uniaxial

load is axially applied on the specimens with measurement of the displacement over the whole gauge length. The tests are allowed to run to rupture. The tests may however be interrupted if an unreasonable long test duration appears.

2.4 Post test metallography

After creep testing, the failed specimens are longitudinally sectioned in the middle, mounted, ground and polished to 0.25 μm, and finally etched in a solution containing 40 g CrO_3, 7.5 g NH_4Cl, 50 ml H_2SO_4, 50 ml HNO_3 and 1 900 ml H_2O. Creep cavitation investigation is then carried out on the etched metallographic samples using light optical microscope (LOM).

3. Results

3.1 Creep tests

As an example, creep strain as a function of time at a/R = 0.5 is exhibited in Figure 3. Creep strain accounts for overall deformation within the gauge length since it is impossible to just measure the axial strain within the notch, which is not uniform either. From Figure 3 it is seen that the primary, secondary and tertiary creep are obvious for the ruptured tests. Creep strain at rupture is larger for the blunt notch (a/R = 0.5) than for the sharper notches.

Creep lifetime in terms of interrupted time and time to rupture is plotted as a function of net section stress in a double logarithmic scale in Figure 4. The creep lifetime under uniaxial stress condition is also included for comparison [7]. It can be seen that

1. the creep lifetime under multiaxial stress state for a given notch acuity increases linearly with decreasing net section stress.
2. the creep lifetime under multiaxial stress state is longer than under uniaxial stress state, indicating notch strengthening (or in another word notch insensitivity). The notch strengthening factor in time is, for instance, greater than 70 at 180 MPa for the bluntest notch (a/R = 0.5).
3. the sharper the notch, the longer the creep lifetime is. At higher net section stresses, the sharpest notch (a/R = 18.8) has a lifetime of about 10^4 times longer than that for the bluntest notch (a/R = 0.5).

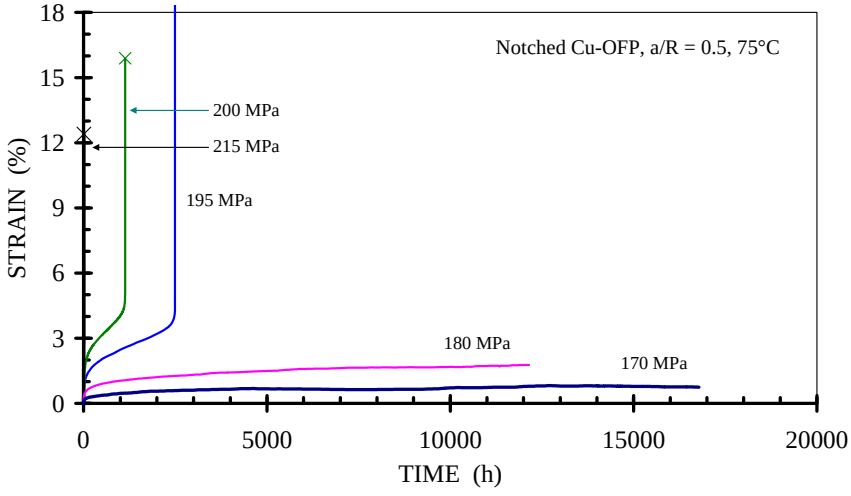

Figure 3. Creep strain as a function of time for specimens having a notch acuity of 0.5 at 75°C. Two tests at 170 and 180 MPa are interrupted.

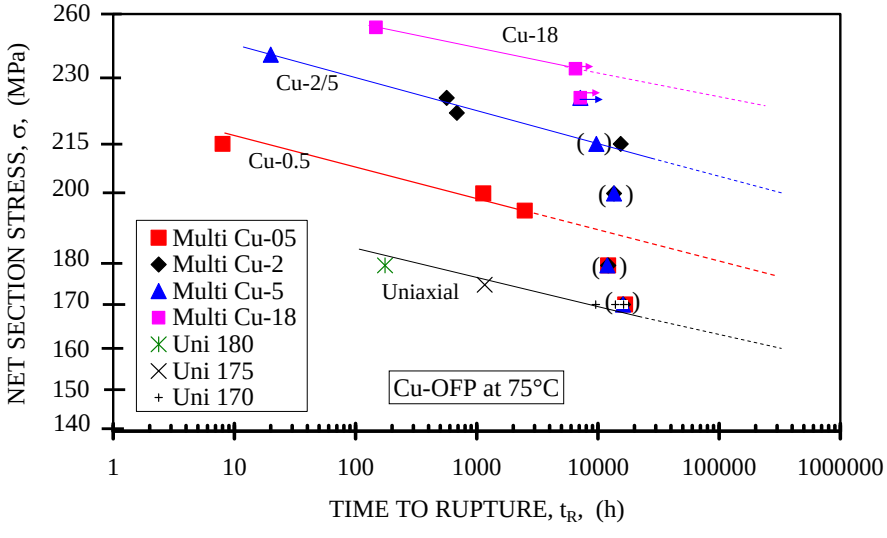

Figure 4. Creep lifetime under multiaxial stress state (multi) as a function of net section stress for notched Cu-OFP at 75°C. Notch acuities are 0.5, 2, 5 and 18. Running tests are indicated by arrows, interrupted tests are in brackets. Creep lifetime under uniaxial stress state (uni) using smooth specimen is included for comparison.

3.2 Deformation of notch

Notch dimensions for all the ruptured tests before and after creep test have been measured on both notches, failed and unbroken, see Figure 5. The same measurements have also been carried out for all the interrupted tests. Considerable creep deformation has occurred on both notches during creep test. This is even more pronounced on the failed notches. The local axial strain within the notch, ε_a, represents the notch width increase. The local radial strain within the notch, ε_r, represents the reduction of area. For the same notch acuity at the same test condition on the failed notch, ε_a and ε_r are usually more than 3 times larger than those on the unbroken one. This indicates an uneven deformation on different notches. ε_a on the failed notch increases with increasing notch acuity. For the bluntest notch (a/R = 0.5), ε_a is about 60%. For the sharpest notch (a/R = 18.8), ε_a can be as high as 780%. The ε_r on the all failed notch seems to be similar, approximately 80%, independent of notch acuity.

Unequal deformations in terms of ε_a and ε_r on two different notches are also found for interrupted tests. Although only minor differences in ε_a and ε_r are sometimes observed between the two notches after long term testing, differences in both ε_a and ε_r do exist.

Plotting ε_r against ε_a see Fig 6, it is clear that ε_r approximately increases linearly with increasing ε_a. This linear relation is notch acuity dependent and can be expressed as:

$$\varepsilon_r = a + b\varepsilon_a \qquad (1)$$

In fact, a can be taken as zero. The notch acuity dependency, described by the slope b, is illustrated in Figure 6. ε_r increases faster than ε_a, if $b > 1$. This is the case for blunt notch, i.e. a/R = 0.5. Otherwise, ε_r increases slower than ε_a, if $b < 1$. This is true for sharper notches, i.e. $a/R \geq 2$.

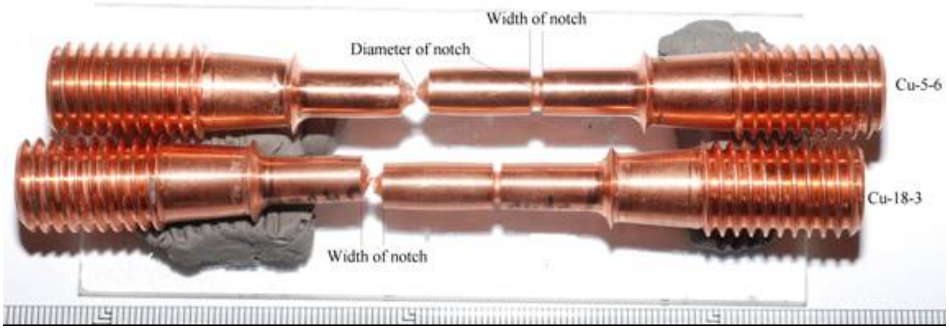

Figure 5. Width and diameter of notches after creep test for two failed creep specimens.

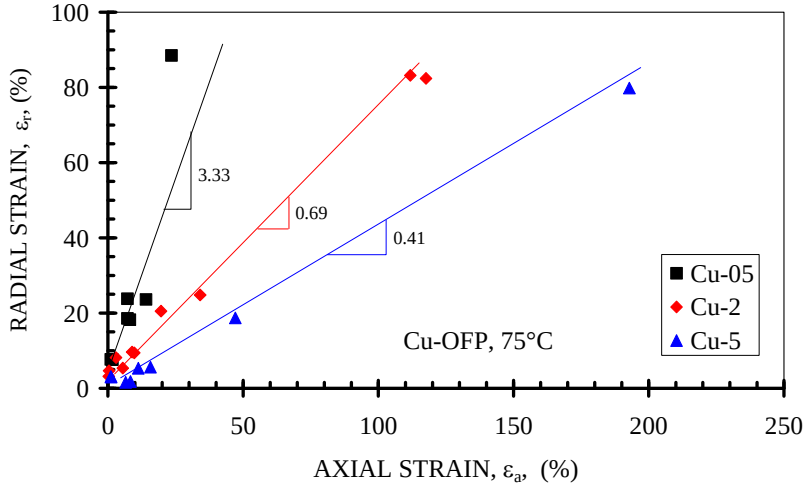

Figure 6. Local axial strain within the notch, ε_a, as a function of local radial strain within the notch, ε_r. The values of ε_a and ε_r are taken from both interrupted and ruptured tests at 75°C. Both notches are taken into account.

3.3 Post test metallography

Transgranular failure is predominant, insensitive to stress, rupture time, or notch acuity. Adjacent to fracture, elongated grains along the stress direction and separate pores and cavities are observed to a small extent, see Figure 7. On the unbroken notch, there is no creep damage visible for the bluntest notch (a/R = 0.5). For the sharper notch (a/R > 2), separate cavities are observed to a small extent on the grain boundary on the unbroken notch, see Figure 8. The cavities are usually

found approximately 0.5–1 mm below the outer surface. For the long term testing, intergranular crack is found on the unbroken notch.

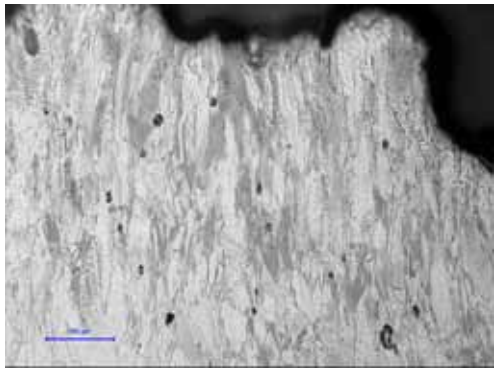

Figure 7. *a*/*R* = 2, 215 MPa, failed after 15 417 hrs. LOM images showing elongated grains and few pores and cavities near fracture.

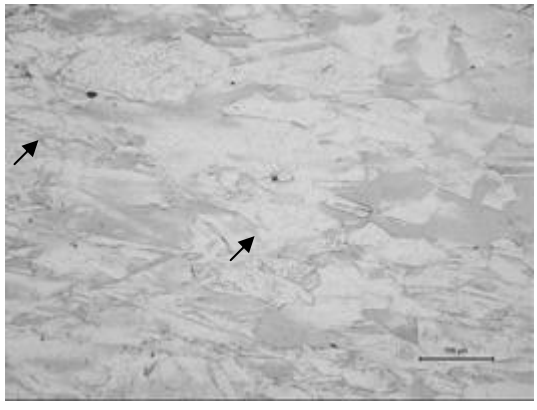

Figure 8. *a*/*R* = 5, 245 MPa, failed after 20 hrs. LOM images showing unbroken notch. Few separate cavities at grain boundaries, indicated by arrow.

4. FEM Simulations

4.1 Constitutive equation

The results of the notched bar creep tests have been studied with the aid of FEM simulations. The principles followed in the FEM analysis are described in [8–10].

Large deformations have been taken into account. A fundamental equation for stationary creep in pure copper is used as a basis for the constitutive equation [11]

$$\dot{\varepsilon}_{OFP} = \frac{2bc_L}{m}\frac{D_{s0}b\tau_L}{k_BT}\left(\frac{\sigma}{\alpha Gb}\right)^3 e^{\frac{\sigma b^3}{k_BT}} e^{-\frac{Q}{RT}\left[1-(\frac{\sigma}{\sigma_{i\max}})^2\right]} / f_P = h(\sigma) \quad (2)$$

where $\dot{\varepsilon}_{OFP}$ is the creep strain rate of Cu-OFP, σ the applied stress and T the temperature. b is burgers vector, m the Taylor factor, k_B Boltzmann's constant, G the shear modulus, τ_L the dislocation line tension, D_{S0} the coefficient for self diffusion, Q the activation energy for self diffusion, R the gas constant, c_L a strain hardening constant, α a constant, $\sigma_{i\max}$ the maximum back stress, and f_P a factor that takes into account the influence of phosphorus. An abbreviation $h(\sigma)$ is introduced for the expression in (2).

For the primary creep model a recently developed fundamental model is used. This is in turn derived from a fundamental model for tensile and compressive flow [12].

$$\sigma = \sigma_y + (\sigma_{creep} - \sigma_y)(1 - e^{-\omega\varepsilon}) \quad (3)$$

where σ_y is the yield strength, and σ_{creep} the stress giving the same creep rate as in the tensile test. For a given strain rate and temperature, σ_{creep} is obtained from (2). Also the yield strength is temperature and strain rate dependent [12]. ω is a fixed constant related to the core radius of the dislocations. Combining eqns. (2) and (3) gives the creep rate.

$$\frac{d\varepsilon_c}{dt} = h(\sigma_y e^{-\varepsilon} + \frac{\sigma - \sigma_y e^{-\varepsilon}}{1 - e^{-\omega\varepsilon}}) \quad (4)$$

Eqn. (4) has been used successfully to represent uniaxial creep curves for Cu-OFP in the temperature interval 75 to 250 ºC [13]. The models (2), (3), and (4) are referred to as fundamental. The reason is that they are based on fundamental physical principles and that no fitting parameters are involved. Using Odqvist's equation, (4) can be transferred to multiaxial stress states

$$\frac{d\boldsymbol{\varepsilon}_c}{dt} = \frac{3}{2}\frac{d\varepsilon_c^{eff}}{dt}\frac{\boldsymbol{\sigma}'}{\sigma_{eff}} \quad (5)$$

where $\boldsymbol{\varepsilon}_c$ is the creep strain tensor, σ_{eff} the effective (von Mises) stress and $\boldsymbol{\sigma}'$ the stress deviator tensor. The effective creep strain rate is given by

$$\frac{d\varepsilon_c^{eff}}{dt} = h(\sigma_y e^{-\varepsilon} + \frac{\sigma_{eff} - \sigma_y e^{-\varepsilon}}{1 - e^{-\omega\varepsilon}}) \qquad (6)$$

Eqn. (5) is applied FEM creep analysis below. To determine the direct effect when the specimens are loaded, elasto-plastic analysis was applied. Eqn. (3) was used to describe the stress strain curve.

4.2 Creep curves

In the FEM analysis of the notched bars, the cylinder symmetry is taken into account. The geometry of the specimens is given in Figure 2. On loading there is a pronounced stress concentration at the notch. This is exemplified in Figures 9a and 10a. The stress distributions in Figures 9a and 10a have been determined with elasto-plastic analysis.

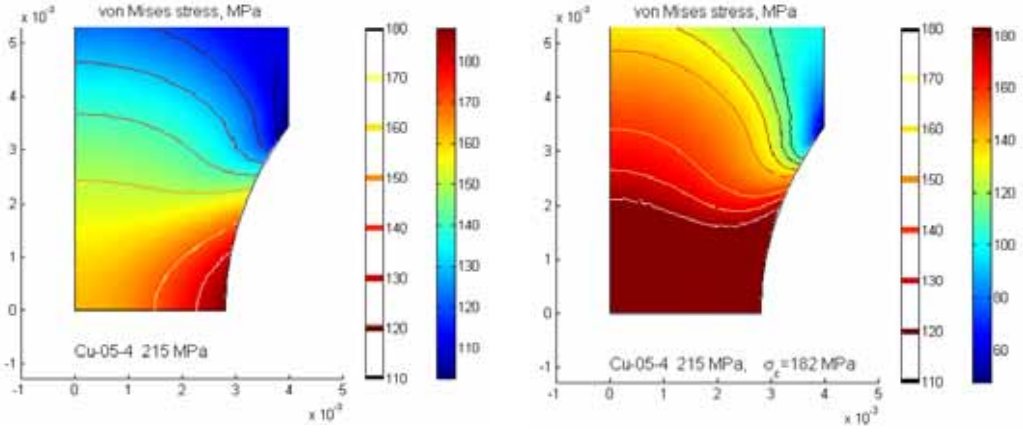

a) b)

Figure 9. von Mises stress distribution for specimen Cu-05-4 with an acuity of 0.5 and a net section stress of 215 MPa. The radial and axial coordinates r and z are on the axes with origin at the centre of the notch. a) Directly after loading, b) after a stationary creep stress σ_C = 182 MPa has been reached.

This type of stress distribution gives rise to inhomogeneous creep. Outside the notch there will hardly be any creep deformation. In the notches the creep rate would be very high if these local areas could be deformed independently. Since this is not possible, stress relaxation will take place and the remainder of the section will take a higher load. Eventually stress redistribution occurs and in a band across the specimen the effective stress becomes almost constant. This is illustrated in Figures 9b and 10b. This process is typically fast and appears after about $t_R/100$, where t_R is the rupture time.

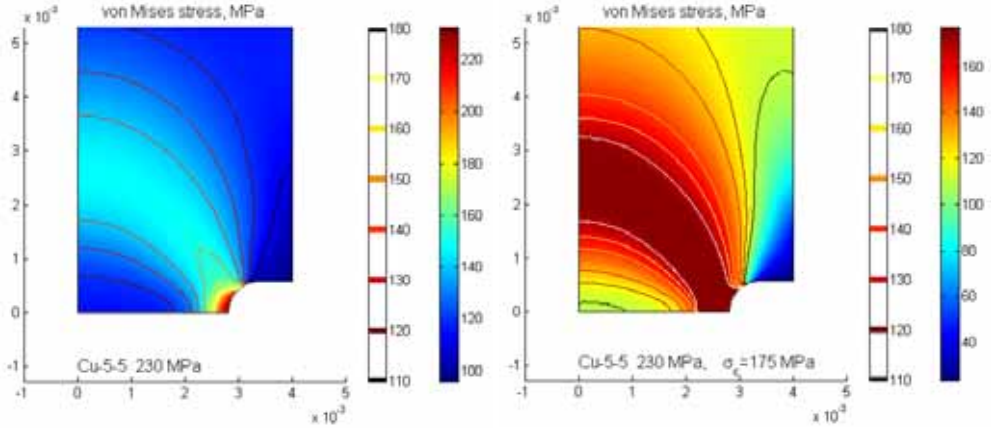

Figure 10. von Mises stress distribution for specimen Cu-5-5 with a notch acuity of 5 and a net section stress of 230 MPa. The radial and axial coordinates r and z are on the axes with origin at the centre of the notch. a) Directly after loading, b) after a stationary creep stress σ_C = 175 MPa has been reached.

For specimens with the acuity 0.5, the band with the constant stress lies across the centre of the notch, see Figure 9b. On the other hand, for the specimens with acuities of 2, 5 and 18, the band takes almost a spherical form, see Figure 10b. In both situations the band is fairly wide. When this stationary situation is reached, the specimens are free to creep in the axial direction. It should be noticed that the width of the band in the axial direction is fairly constant, which helps the creep deformation.

The model results are compared to the experimental creep strain data for two specimens in Figure 11. In the model only primary and secondary creep are taken into account, so the tertiary creep observed is not covered. The model predicts creep strains of the right order in spite of the absence of fitting parameters.

In the specimens with acuity of 18.8, the notch is quite sharp. Its radius is only 0.15 mm. In spite of this, the creep model can reproduce the experimental creep strain data quite well (not shown).

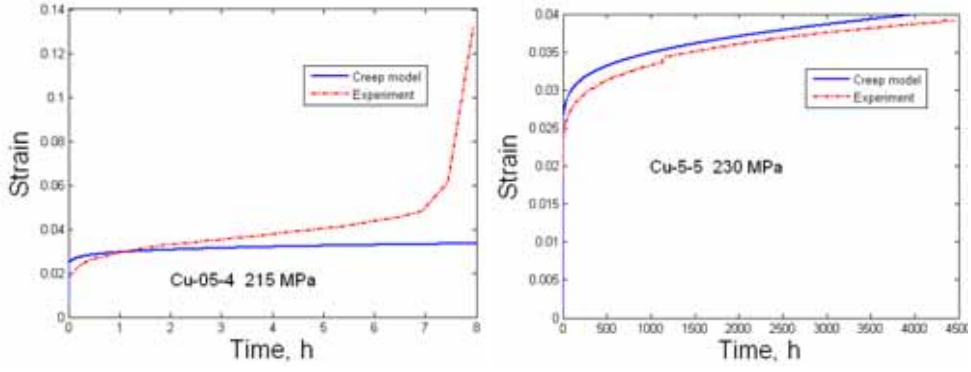

Figure 11. Creep strain versus time for one specimen with a notch acuity of 0.5 one with an acuity of 5. The model in eqn. (5) is compared to experimental data. The specimen designation and net section stress are given in the Figures.

4.3 Creep rupture

In the previous section it was demonstrated that the creep model (5) could represent the creep strain versus time curves in a satisfactory manner. Since tertiary creep is not included in the model, it cannot be used to predict rupture. Instead the stationary creep stresses σ_C will be used. σ_C is the stationary effective stress that is reached after the initial redistribution of stresses, see Figures 9b and 10b. The creep exponent of Cu-OFP is about 65 at 75°C. This high creep exponent implies that the creep rate is approximately constant for a constant σ_c.

σ_C is compared with uniaxial creep rupture data in Figure 12. The uniaxial data are for forged and extruded Cu-OFP at 75 ºC [7]. The values for notched bars are grouped in two categories. For specimens with notch acuity of 0.5, a homogeneous stress distribution is obtained at the centre of the notch. This is referred to as waist deformation, see Figure 9b. For the higher acuities 2, 5, and 18.8 the constant stress appears in a spherical band, see Figure 10b. This is referred as to band deformation.

In the case of band deformation, the stationary stresses σ_C fall approximately on the band for the uniaxial data in Figure 12. In this case if σ_C is inserted in the

uniaxial creep rupture curve, an approximate time to rupture is obtained. Since σ_C lies slightly above the uniaxial curve, this approach should be conservative.

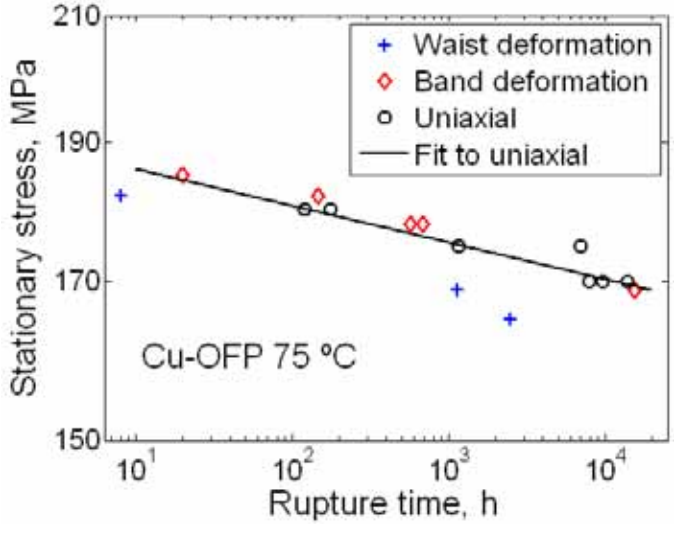

Figure 12. Creep stress versus rupture time. The experiments are uniaxial data for Cu-OFP at 75 ºC [7]. For notched bar specimens the stationary stress σ_c is given as function of rupture time. Waist deformation represents notch acuity of 0.5, and band deformation notch acuities of 2, 5, and 18.8.

In the case of waist deformation, σ_C lies 3 to 5% below the uniaxial curve. With the type of stress distribution in Figure 9b, the creep deformation is strongly concentrated to the centre of the notch. This will give rise to necking and early plastic collapse of the specimen. This is believed to be the reason for the lower rupture stresses.

5. Discussion

Due to difficulty in measuring axial strain just within the notch during creep test and non-uniform deformation over the notch and the specimen, the overall axial strain measured within the gauge length of 51 mm is used to present behaviour of deformation versus time, see Figure 3. The local strain in the notch is of course much larger than the average overall strain. The significance of Figure 3 is however to show the primary, secondary and tertiary creep in relation to stress and notch acuity.

As expected, significant deformation takes place within the notches, e.g. the ratio between ε_a and the overall axial strain can be as high as 200 for the sharpest notch (a/R = 18.8) at 255 MPa. Comparing to the unbroken notch, both ε_a and ε_r are several times larger on the failed notch. This implies that the notches may deform unevenly. The linear relation between ε_a and ε_r, see Figure 6, makes it possible to estimate ε_r if ε_a is known, or vice versa. It is also noted that the relation is notch acuity dependent. The sharper the notch, the faster ε_a increases.

An important result in the present investigation is that the tested Cu-OFP material is insensitive to notches at 75°C, see Figure 4. This is the case for all the studied notch acuities. In fact, the creep lifetime under multiaxial stress state is longer than that under uniaxial stress state, indicating notch strengthening. The notch strengthening factor in time is greater than 70 at the net section stress of 180 MPa for the bluntest notch (a/R = 0.5). Notch strengthening has been observed in some other studies [14–16].

Notch strengthening may be affected by ductility. The studied Cu-OFP is quite ductile. Under uniaxial stress state, the creep strain at failure is around 50% [7]. Even higher strain has been locally obtained under multiaxial stress state, see Figure 6. Considerable plastic deformation will change notch dimension, or notch acuity, which in turn alters the stress state. Actually, notch dimension/acuity starts to change from uploading. The overall axial strain at full load increases with increasing net section stress. At net section stresses greater than 180 MPa, the overall axial strain at full load exceeds in most cases 0.5%, implying occurrence of plastic deformation. Supposing the local axial strain within the notch is much larger than the overall one, notch dimension/acuity, and thereby stress state and stress concentration factor, may have altered at full load, as the creep test begins.

In the creep investigation, the net section stress gives quite a conservative estimate of the lifetime if compared with a uniaxial creep rupture curve. But this result can still be used in design to give a first estimate of safety when a crack is present. A more accurate estimate is obtained if elastic plastic FEM-modelling is performed for a perfect plastic material. The resulting reference stress can be compared to the uniaxial creep rupture data. This estimate is not fully conservative. Some of the rupture stresses are found up to 5% below the uniaxial rupture line. A still more accurate approach is to include creep in the FEM-model. A prerequisite is that precise constitutive equations are available. For the investigated creep specimens the largest creep stresses can be found in a

homogenous band around the notches, which can be used to predict the rupture time if it is combined with uniaxial data.

6. Conclusions

The influence of multiaxial stresses on creep properties of Cu-OFP at 75°C has been studied by using double notch specimens with notch acuities of 0.5, 2, 5, and 18.8, respectively. The following conclusions can be drawn

1. The creep lifetime under multiaxial stress state is longer than that under uniaxial stress state, indicating notch strengthening at given net section stresses. The notch strengthening factor in time is in the range 100 to 10 000.
2. Significant deformation takes place within the notch. The ratio between local axial strain within notch and overall axial strain within gauge length can be as high as 200, implying a strong underestimation of local deformation by the overall axial strain.
3, Transgranular failure is predominant, independent of stress, rupture time, and notch acuity. Adjacent to fracture, elongated grains along the stress direction, few separate pores and cavities are often visible. On the unbroken notch, fewer separate cavities have been observed in several cases.
4. Using a fundamental creep model without fitting parameters, it has been possible to represent the creep strain curves for the notched specimens quite well. This is the case in spite of the very large difference in lifetime in comparison to uniaxial specimens at given net section stresses.
5. In the FEM-modelling of the creep deformation a stationary stress state was soon obtained. The highest stresses appeared in a band of constant stress around the notch. This constant stationary creep stress is close to the reference stress. For the blunter notch this band was at the centre of the notches, whereas for the sharper notches the band had a spherical form. In the band the main part of the creep deformation takes place.
6. To predict the rupture time, the stationary creep stress using FEM-modelling should be used together with uniaxial creep data.

Acknowledgement

The financial support from the Swedish Nuclear Fuel and Waste Management Co (SKB) is greatly acknowledged. The SKB is also thanked for providing the test material.

References

1. Dyson, B. F. & Loveday, M. S. Creep fracture in Nimonic 80A under triaxial tensile stressing, Proc. Creep in Structures, IUTAM Symp. Pergamon Press, Oxford, 1981. Pp. 406–421.

2. Loveday, M. S. & Dyson, B. F. Creep deformation and cavitation damage in Nimonic 80A under triaxial tensile stressing. Proc. ICM 3, Vol. 2, Cambridge, 1979. Pp. 213–222.

3. Hayhurst, D. R. & Webster, G. A. An overview on studies of stress state effects during creep of circumferentially notched bars. Techniques for multiaxial creep testing. Eds. Gooch D. J. and How I. M. Elsevier Applied Science, 1986, Chapter 9. Pp. 137–143.

4. Hayhurst, D. R. & Henderson, J. T. Creep stress redistribution in notched bars. Int. J. Mech. Sci., 1977. Vol. 19, pp. 133–146.

5. Webster, G. A., Aplin, P. F., Cane, B. J., Dyson, B. F. & Loveday, M. S. A code of practice for notched car creep rupture testing: procedures and interpretations of data for design. Harmonisation of Testing Practice for High Temperature Materials, Eds. Loveday M. S. and Gibbons T. B. London, Elsevier Applied Science, 1992. Pp. 295–330.

6. Al-Faddagh, K., Webster, G. A. & Dyson, B. F. The influence of stress on the creep failure of 2¼Cr, 1Mo steel. Mechanical Behaviour of Materials IV. Eds. Carlsson J. and Ohlsson N. G. Oxford, 1984. Pp. 289–295.

7. Andersson, H. C. M., Seitisleam, F. & Sandström, R. Creep testing and creep loading experiments on friction stir welds in copper at 75°C. Stockholm, Sweden, Svensk Kärnbränslehantering AB, 2007. Report TR-07-08. http://www.skb.se.

8. Jin, L.-Z. & Sandström, R. Creep of copper canisters in power-law breakdown. Computational Materials Science, 2008. Vol. 43, pp. 403–416.

9. Jin, L.-Z. & Sandström, R. Non-stationary creep simulation with a modified Armstrong-Frederick relation applied to copper canisters. Computational Materials Science, 2009. Vol. 46, pp. 339–346.

10. Jin, L-Z. & Sandström, R. Modified Armstrong-Frederick relation for handling back stresses in FEM computations. Proceedings 2nd International ECCC Conference. Creep & Fracture in High Temperature Components – Design & Life Assessment issues, Dübendorf, Switzerland. I. A. Shibli & S. R. Holdworth (Eds.). 2009. Pp. 836–847.

11. Sandström, R. & Andersson, H. C. M. Creep in phosphorus alloyed copper during power-law breakdown. Journal of Nuclear Materials, 2008. Vol. 372, pp. 76–88.

12. Sandström, R., Hallgren, J. & Burman, G. Stress strain flow curves for Cu-OFP. SKB Report R09-14, 2009.

13. Andersson-Östling, H. C. M. & Sandström, R. Survey of creep properties of copper intended for nuclear waste disposal. SKB-Report, 2010. http://www.skb.se.

14. Storesund, J., Tada, N. & Sandström, R. Notch sensitivity of creep failure below the limit temperature. Swedish Institute for Metals Research, Report IM-2961, December, 1992.

15. Browne, R. J., Flewitt, P. E. J., Lonsdale, D., Shammas, M. & Soo, J. N. Multiaxial creep of fine grained 0.5Cr-0.5Mo-0.25V and coarse grained 1Cr-0.5Mo steels. Materials Science and Technology, 1991. Vol. 7, August, pp. 707–717.

16. Wu, R., Seitisleam, F. & Sandström, R. Creep crack growth in a high strength low alloy steel at 360°C. Proc. Int. Conf. Creep and Fracture of Engineering Materials and Structures. Tsukuba City, Japan, 1–5 November, 1999. Pp. 139–146.

Corrosion issues in relation to copper canisters for disposal of spent nuclear fuel

Timo Saario
VTT Technical Research Centre of Finland
Espoo, Finland

Abstract

Spent nuclear fuel in Finland and Sweden will be disposed in deposition holes excavated in granitic bedrock at a depth of about 400 to 500 m. The release of activated products is prevented by a multi-barrier concept. A copper canister with 50 mm wall thickness will be the main corrosion shield, expected to last unperforated for over 100 000 years.

There are several different corrosion mechanisms that in principle may threaten the integrity of the copper canister. Likewise, there are several different scenarios which may expose the copper canister to these corrosion phenomena. During the years, most of the corrosion related concerns have been satisfactorily dealt with, leaving a few to be further researched.

This paper gives an overview of the corrosion related issues with regard to the integrity of the copper canister, as well as the main approaches developed by the share holders to ensure the integrity for the duration needed. A more detailed description of the few remaining ongoing corrosion related research items is also included.

1. Introduction

In the present Finnish and Swedish design spent nuclear fuel is packed in a canister made of spheroidal graphite cast iron. The cast iron canister has an outer shield made of copper. The copper shield is responsible for the corrosion protection of the canister. The design thickness of the wall of the copper shield is

currently 50 mm, and this sets a limit for the maximum corrosion allowance of copper in the disposal conditions. The design life, a minimum 100,000+ years, sets challenges for the prediction of the longevity of the corrosion resistance of the copper shield.

The repository will go through an oxic period during the operational phase (as the tunnels remain open to air), as well as for some 30 … 300 years after the closure until all entrapped oxygen has been consumed. The rest of the repository life is considered to be anoxic. The temperature of the canister surface will go through a maximum of T = 90°C in the early years and then cool down slowly.

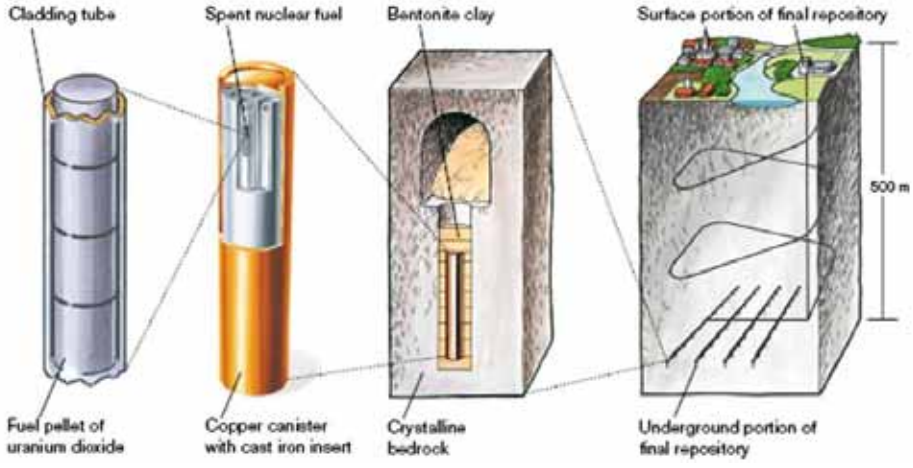

Figure 1. The concept of spent fuel storage.

The copper canister, Figure 1, is surrounded by a buffer, presumably bentonite clay, which will act as a diffusion barrier, slowing down both the movement of reactants towards the canister surface and reaction products away from the canister surface. As long as the bentonite layer is intact, it will effectively hinder the corrosion processes. However, there are at least two mechanisms which may degrade bentonite locally, namely piping and bentonite erosion. Piping occurs locally during operational phase of the repository, immediately after deposition, and is caused by the formation of hydraulically conductive channels within the bedrock due to the high groundwater pressure gradients in the open repository. The flowing dilute water may cause local erosion of bentonite. Bentonite erosion may also occur locally as dilute groundwaters penetrate to the disposal vault for extended periods of time when glacial conditions prevail.

There are several different corrosion mechanisms that may threaten the longevity of the canister, including general corrosion, pitting corrosion, stress corrosion cracking and corrosion assisted creep. In the following, the approaches chosen to deal with these mechanisms and the related scenarios will be shortly described.

2. General corrosion

General corrosion of copper will occur in the repository, both during the oxic and anoxic period. The maximum extent of general corrosion can be rather reliably estimated based on the storage of main reactants, i.e. oxygen during the oxic period and sulphide during the anoxic period. This is called a mass balance calculation. A more advanced method is based on analysis of the rate determining step in the corrosion process, which has been found to be the transport of Cu(II) away from the canister surface. The estimates show [1] that at maximum, general corrosion would consume only a few millimetres of the thickness of the copper canister, and thus would not be able to penetrate the canister wall during the design period.

Recently, a new corrosion mechanism of copper has been proposed, involving oxidation of copper by water under anoxic conditions. Szakálos et al. [2] have proposed that copper reacts with water under anoxic conditions producing a copper hydroxide film, and that a major part of the hydrogen liberated in the process enters copper, possibly making it mechanically brittle. The BRITE-expert group for SSM, in their evaluation [3] of the scientific publication of Szakálos et al. stated that while it is not possible to exclude such a process based on thermodynamics they believe that it is very unlikely that the process has been dominant in nature (e.g., as attested to by the existence and persistence of native copper deposits) or that it will be significant under the conditions that are expected to occur in a spent fuel repository of the type being proposed by SKB. The corrosion rates estimated by the BRITE group, based on the data presented by Szakálos et al., would be insignificant.

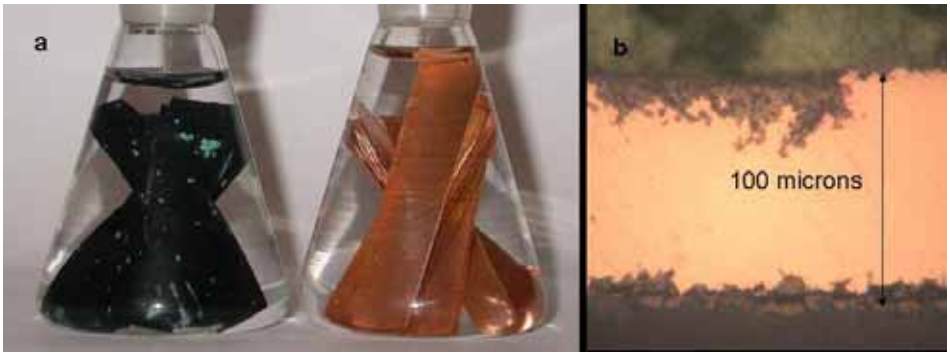

Figure 2. Results from Hultquist et al. [4]. Copper coupons exposed to distilled water; (a) in a vessel with sealing made of Pd-foil allowing hydrogen to escape (left) and in a vessel with sealing made of Pt-foil (right), (b) cross-section of the foil (a, left) showing an irregular corrosion product layer.

There is an ongoing debate on this issue at the moment. Szakálos et al. have proposed that the corrosion rate evaluation by the BRITE group is misleading and too low by orders of magnitude, since it is based on the hydrogen evolution rate, and since most of the hydrogen would enter the copper metal. In their second publication Hultquist et al. [4] show results from a 15 year exposure test, where copper has been exposed to ion pure water. In their test set up, one flask was sealed with a Pd-foil enabling hydrogen to escape (Pd is permeable to hydrogen) and thus any reaction producing hydrogen could proceed in this container. In Figure 2, reproduced from [4], the copper foils exposed to distilled water in a flask with a Pd-seal show a greenish corrosion product, whereas the foils exposed similarly in a flask with a Pt-seal have a metallic appearance with no apparent surface film.

In their paper Hultquist et al. report that "originally the water volume was equal in the flasks in beginning of the exposure". As the original volume was 50 cm^3, the volume of water in the left hand side flask can be estimated to have reduced by more than 1 cm^3. The loss of water (and oxygen) in moles then becomes ΔV_{H2O} = 0.056 mol at minimum, which translates to 0.028 mol of $Cu(OH)_2$ (Szakálos et al. are actually proposing that the corrosion product is of the form H_xCuO_y, but as there are no data on such species we use here $Cu(OH)_2$ as a close enough substitute). Taking the exposed area of 85 cm^2, and estimating the average oxide thickness from Figure 2 at about 10 microns results in a volume of the oxide at V = 0.085 cm^3. The molar volume of $Cu(OH)_2$ is V_m = 29 cm^3/mol, therefore the amount of oxide on the copper foil surfaces in the left hand flask is

about $n = V/V_m = 0.0029$ mol. This corresponds only to about 10% of the oxygen in the missing water volume. Another way to arrive at the same conclusion is to estimate how much copper has reacted, again based on cross-section in Figure 2. Normally the volume of oxides and hydroxides is roughly twice that of the original reacted metal (e.g. $\rho = 3.368$ g/cm^3 for $Cu(OH)_2$), so the approximate mass of copper reacted becomes 0.38 g, using $\rho_{Cu} = 8.92$ gcm^{-3}. With the molar mass of copper $M = 63.54$ gmol^{-1} this corresponds to about 0.006 M of copper, again roughly a factor five to ten less than the consumed oxygen in the missing water. Based on this rough calculation it is clear that most part of the water must have leaked out from the flask, indicating that the sealing has not been functioning properly. Thus, a likely explanation to the presence of the oxide coverage in this case is that because of the leakage path, air has leaked in resulting in normal aerobic corrosion of copper.

It is clear that there are quite a lot of uncertainties in the publications supporting the hypothesis put forward by Szakálos et al. [2], and therefore further evidence is needed before any decisive conclusions can be made. At present, at least two independent research projects are being conducted to investigate the plausibility of the hypothesis and possible consequences thereof.

3. Pitting corrosion

Pitting corrosion is a form of localised corrosion, where a local area becomes more anodic than the surrounding area and thus dissolution occurs more rapidly in this local area, generating a pit. Severity of pitting can in general be described by the so-called pitting factor PF, i.e. the ratio of maximum pit depth to that of general corrosion. Oxygen (in principle any oxidising agent) is considered a pre-requisite for pit propagation. A decrease in dissolved oxygen concentration (because of the limited amount of air/O_2 available in the repository) would result in less Cu dissolution and an increase in the pit pH, both of would eventually tend to cause the pit to stop propagating. In the latest published analysis of the copper canister case [1], using pitting factors to assess the depth of localized corrosion (realistic PF = 2, conservative PF = 5), the predicted depth of localized corrosion remains at less than 2 mm.

4. Corrosion assisted creep

Creep (slow deformation) of the copper canister does occur in the repository. When resaturation takes place, bentonite swelling forces the copper canister to yield until it becomes supported by the inner cast iron canister. Also, in case of a sudden shear movement (e.g. as a result of an earth quake) some of the canisters may be affected and would accommodate part of the remaining stress by creep. In early days, with the oxygen free copper, Cu-OF) some data sets showed what was then called brittle creep fracture, i.e. creep ductility of clearly less than 10%. Addition of small amount of phosphorus (40 … 60 ppm) resulted in CuOFP with superior creep properties, and disappearance of the brittle creep fracture phenomena. The remaining question which may need an answer is, with the very long time in question (possibly tens of years for bentonite swelling), will the brittle creep phenomena appear again or not. To answer this question convincingly, either reliable micromechanical modelling approaches or long term creep tests are possibly needed.

Creep is a mechanical degradation phenomenon, which may be enhanced by corrosion processes. The data sets used for safety analyses regarding creep of copper canisters have been measured in laboratory air, not in corrosive environment representative that of the repository. Creep tests of CuOFP under conditions representative of the early oxic period are ongoing to answer this question.

5. Stress corrosion cracking

Stress corrosion cracking (SCC) is a failure mechanism which has the potential capacity of damaging all the canisters in a relatively short time. Thus, approaches have been developed to exclude the possibility of SCC.

5.1 Stress corrosion cracking under oxic conditions

The main SCC agents for CuOFP known to exist in the repository and to be produced by bacterial activity are ammonia, acetate and nitrite. The approach chosen by the operators (SKB and Posiva) is to prove that the necessary ingredients for SCC to occur, i.e. high enough stress, high enough potential and high enough concentration of the aggressive species do not co-exist ever in the repository. This is called the decision tree –method (or fault tree –method). The method has shown to be promising and there seems to be some consensus at the

moment that SCC under oxic conditions would not threaten the integrity of the copper canisters in the repository. If one were to look for the weakest link in the argumentation it may the microbe models used to predict the evolution of the microbe populations in time, as to the knowledge of the author they have not been calibrated by any set of experiments.

5.2 Stress corrosion cracking due to sulphides under anoxic conditions

In 2007 a new Japanese research showed that also sulphides can cause SCC in pure copper under anoxic high chloride water conditions [4]. Sulphides may come to contact with the copper canister surface through three different processes: 1) transport via groundwater flow, 2) production at the bentonite/rock interface via sulphate reducing bacteria (SRB) and further transport and 3) through SRB activity within bentonite (pyrite reduction). In the groundwater sulphide concentrations are typically relatively low, 1–3 mg/l. The maximum value that can be formed through SRB activity at the bentonite/rock interface can be high (in the range 400 to 500 mg/l), causing a high diffusion gradient through the bentonite. The sulphide concentration that forms because of SRB activity within bentonite is known to some extent as a function of bentonite density. According to experimental findings sulphides may form within the bentonite even in fully compacted bentonite [5]. In scenarios where the density of bentonite locally decreases (e.g. early piping, bentonite erosion by glacial melt waters) the access of sulphide to the copper surface will be much easier.

A relatively large effort is ongoing to experimentally determine whether CuOFP base material is susceptible to SCC in presence of sulphides when exposed to a representative anoxic groundwater. Furthermore, if the material is susceptible, what would be the minimum concentration of sulphide needed for SCC to occur (within 0 to 100 mg/l concentration range). Within the same effort, also a diffusion model is being developed allowing the three above described different scenarios to be considered.

6. Summary

Since the introduction of the prevailing methodology for disposal of spent nuclear fuel in Sweden and Finland, a remarkable effort has been made to investigate the possible degrading effects of different corrosion phenomena on

the main technical radioactivity release barrier, the copper canister. Some remaining questions still exist, which need clarification.

In the general corrosion field, the recent hypothesis of copper being corroded by water under anoxic conditions needs further investigation, and research on this topic is being currently carried out. Corrosion assisted creep as well as the possibility of brittle creep fracture of CuOFP, are also subjects where current research efforts are on-going. Stress corrosion cracking of CuOFP caused by sulphides under anoxic conditions is a new mechanism which should, and is being researched e.g. within the national nuclear waste disposal programs.

References

1. King, F., Ahonen, L., Taxén, C., Vuorinen, U. & Werme, L. Copper corrosion under expected conditions in a deep geologic repository. SKB TR-01-23, 2001.

2. Szakálos, P., Hultquist, G. & Wikmark, G. Corrosion of copper by water. Electrochemical and Solid-State Letters 2007, 10 (11) C63-C67.

3. Apted, M., Bennett, D. & Saario, T. A review of evidence for corrosion of copper by water. SSM Report 2009:30.

4. Hultquist, G., Szakálos, P., Graham, M. J., Sproule, G. I. & Wikmark, G. Detection of hydrogen in corrosion of copper in pure water. 17th ICC 2008, Paper 3884. NACE 2009.

5. Taniguchi, N. & Kawasaki, M. Influence of sulphide concentration on the corrosion behaviour of pure copper in synthetic sea water. 3rd Int. Workshop on Long-term Prediction of Corrosion Damage in Nuclear Waste Systems. Pennsylvania State University, May 14–18, 2007.

6. Pedersen, K. Presentation at SACNUC-workshop. Brussels, Belgium, October 21–23, 2008.

Flaw detection trial using virtual ultrasonic testing

Matti Sarkimo
VTT Technical Research Centre of Finland
Espoo, Finland

Abstract

This report presents features of ultrasonic simulation and aspects to be considered in virtual inspection trials. A simulation trial implementation and results are reported, with main purpose to test different features of the selected simulation software in creation and analysis of a virtual detectability trial.

A series of simulations was conducted using simple test block geometry that included notch shaped flaws with varying depths. To make the case realistic, significant structural noise and moderate attenuation were added to the simulation using the material properties settings. The simulation was run using different probe frequency values and crystal dimensions to produce variation in the flaw detectability.

The simulated ultrasonic inspection data was analyzed using analysis tools of the used software. The signal-to-noise ratios and locations of the detected indications were characterized and detectability dependence on the notch height was assessed. Also, study about signal-to-noise ratios measured from the detected indications was performed.

1. Introduction

When ultrasonic inspection technique is developed for a specific component there is often a need for practical trials. One wants to test the performance of the inspection system and the available parameter choices to achieve the best

outcome. In the qualification process there are often also official requirements for practical test trials.

The production of the real test blocks is usually expensive and time consuming. Also the number of the defects that can be introduced in the test block is often quite limited. Ultrasonic inspection simulations using computers offer a possibility to create virtual test blocks that can be applied to imitate practical trials. The component and flaw properties (e.g. material, geometry, noise level, defect size, defect location and defect orientation) or inspection parameters (e.g. inspection technique, and probe characteristics) can be varied very flexibly and quickly.

Inspection of a virtual test block means running simulation using similar scan pattern as the real inspection. The simulation computation can take from minutes to several hours or even days depending of the complexity of the case. The result will be data files including similar information as real inspection result files. Using the simulation result files it is possible to create the typical A-, B-, C- and D-scan views for the analysis of the inspection data. Thus it is possible to interpret the results of a virtual inspection in a quite similar way as in the case of a real inspection.

This report gives some general information about ultrasonic part of the Civa simulation program (developed by CEA, Commissariat à l'Énergie Atomique) to show some of the possibilities to apply virtual test blocks and inspections. Several simulations (virtual inspections) were run to produce result files which could then be used for analysis trials. According to the analysis results it could clearly be measured that flaw detectability was depending on the size of the flaw and on the other hand also on the probe properties.

2. Brief review of some Civa simulation options

Civa provides a number of component geometries and possibility to define the material properties to produce a realistic component for the simulation. The ultrasonic probe design and characteristics have a wide variety of options. During the simulation the data sampling and probe movement on the component surface can imitate a mechanized inspection.

2.1 Geometry of components

The standard choices for component geometry in Civa (version 9) are: plane, cylinder, cone, sphere, elbow and nozzle. In addition to the standard geometries component geometry can be created using two-dimensional CAD tool (2D CAD) or imported as a 3D CAD model in STEP or IGES format.

However there are some limitations in the use of the various component geometries in different simulation applications. All computations are not necessarily available in all of the geometries and also the scanning movement may be difficult or impossible to accomplish in some geometries using the current program version.

In the following only the simple component geometries are briefly discussed.

2.1.1 Plane

The plane is the simplest component geometry for simulations. The component is rectangular and its dimensions can be freely chosen. A plane component with a scan pattern on its surface is shown in Figure 1. Different flaws can be introduced in the component by defining their shape, size, orientation and location coordinates. The locations of the flaws are defined using component coordinate system.

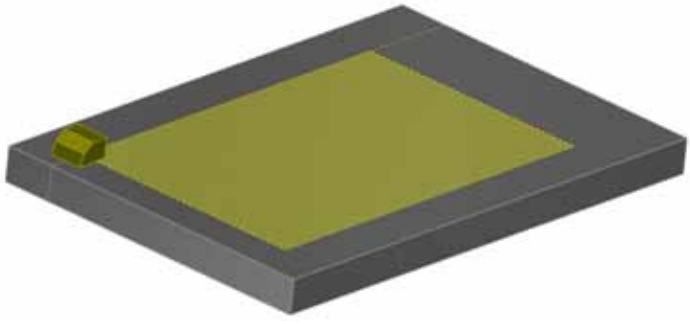

Figure 1. A rectangular component with plane geometry and scan pattern drawn on it.

2.1.2 Cylinder

Using the component definition option “Cylinder” simple cylindrical or tube formed components can be designed. Different scanning patterns are possible.

The flaws can accurately be positioned using component coordinate system. On the other hand the positioning of indications in the data analysis phase is not very convenient and straight forward in the current version (version 9) of the program.

If for example a tube also includes a weld the component should be designed using 2D CAD extension included in the program. Using this option it is possible to define different volumes where material properties may differ. Thus for example the weld and base material can have different attenuation and noise properties. When using this CAD option it is also possible to visualize weld geometry and influence to the location of the origin of the coordinate system, see Figure 2.

Figure 2. Weld inspection design in 2D CAD module and a scan pattern for the inspection simulation.

2.2 Material properties

The two basic material properties, sound velocity and density, must always be defined because they are taken into account in each computation. In the usual cases these values can be obtained from a list available to Civa program. In addition to these basic parameters also attenuation and structural noise of the material can be included into computation using quite simple definitions.

The attenuation is defined as a frequency depending parameter using either exponential or polynomial attenuation law. The definition is first made in a table format and then the attenuation frequency dependency can be reviewed as a curve, see Figure 3.

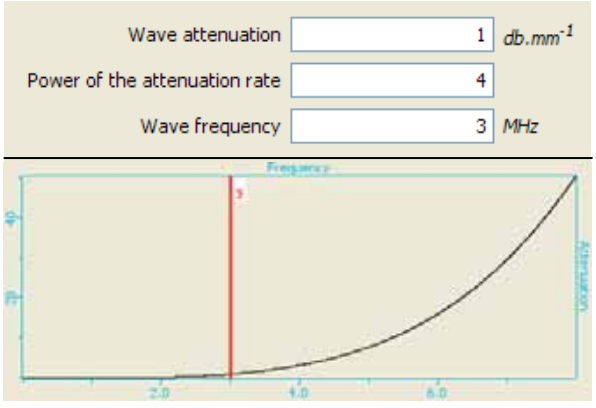

Figure 3. Definition of the attenuation using exponential attenuation law. The table for typing of parameters (top) and the visualization of the frequency dependency (bottom).

The structural noise is modelled using diffracting points randomly positioned in the material. The user has to define the density of these points and also reflectivity amplitude of points. The reflectivity is a zero-mean Gaussian distribution having a standard deviation which is given by the operator.

Civa also provides a possibility to model more complicated material structures e.g. anisotropic welds or multilayer materials. In these cases more material property parameters (for example crystal structure and crystal orientation) must be known and be given for the computation.

2.3 Probe

Civa includes quite extensive possibilities to define different types of probes that are applied in the simulations. The choices include contact, immersion and various phased array probes. The element size and shape as well as the wedge geometry can be exactly defined and also visualized, see Figure 4. The user can set the probe centre frequency and bandwidth. There is a wide variety of possibilities concerning phased array probe design and many options are available to create delay laws.

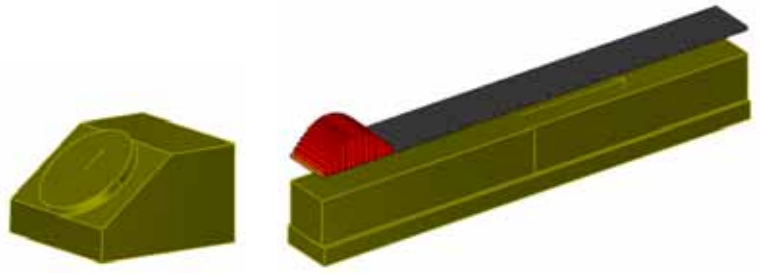

Figure 4. Conventional single crystal probe with an angle wedge and a 128 element phased array probe with a flat wedge designed in Civa. The delay law visualization is presented using red columns.

2.4 Flaws

The typical list of the flaw shapes that can be inserted in the components is: planar rectangular or semi elliptical notch, spherical void, side-drilled hole, flat-bottomed or hemispherical-bottomed hole, planar CAD defect, multifaceted type planar defect, plain cylinder and ellipsoidal inclusion. Some examples of the flaw geometries are shown in Figure 5. The flaw geometries are typically "empty". The spherical, cylindrical and ellipsoidal shapes can be filled by an isotropic material referring to inclusions.

The dimensions, location and orientation of the flaws can be chosen freely which makes the design and variation of the virtual test pieces very convenient.

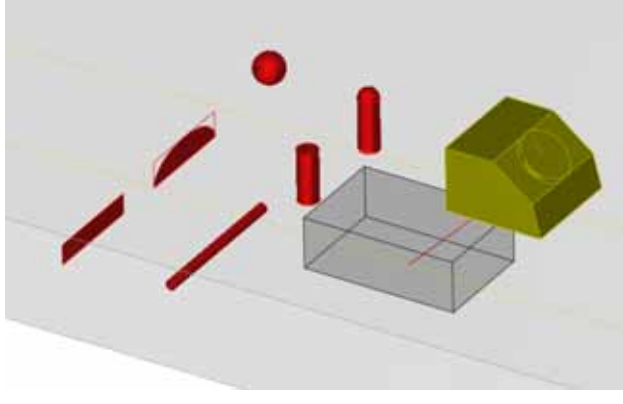

Figure 5. Some examples of flaw shapes in a planar test component.

2.5 Computation

Concerning the computation there are several options to be chosen how the simulation will be performed. For example back wall echoes, corner echoes, surface echoes, mode conversion, shadowing effects etc. can be taken into account if desired. The choice of options available depends to some extent on the applied component geometry and other simulation parameters.

Civa allows the user to specify which flaw scattering model is applied in the computation concerning the ultrasonic beam interaction with flaws. There are three models available and Civa manual states concerning their validity [1]:

- Kirchhoff: Valid for the most of the cases, e.g. specular reflection over planar or volumetric defects. Also corner echo over planar or volumetric defects is computed correctly. There are limitations in computation of tip diffraction signals. Computation of the tip diffraction signals is valid only for the time-of-flight not for the amplitude. The probes (transmitter and receiver) have to be on the “same side” of the defect plane and thus most of the standard cases of TOFD (time-of-flight diffraction) applications are not valid.
- GTD (Geometrical Theory of Diffraction): This interaction model is able to predict echoes diffracted by the edges of planar flaws. Thus it is applicable for TOFD case computations. GTD model is not valid near the specular reflection.
- Born: The flaws filled by an elastic medium and embedded in an other elastic medium can in Civa 9 be modelled using Born approximation.

3. Detectability exercise using a virtual test block

To test the simulation possibilities in assessment of flaw detectability a virtual test block was designed and then scanned using different probe designs. Finally the data files of inspection simulations were analyzed applying a few procedure-like rules.

3.1 Test block

The virtual test sample applied was a rectangular flat block with dimensions 200 x 300 x 20 mm, see Figure 6. The material of the block was stainless steel.

To make the inspection more challenging and realistic some noise and attenuation was defined using the material properties parameters. The noise parameters applied were: density 0.2 pts/mm^3 and amplitude 60 S.I. (in the first simulation 50 S.I). The attenuation was defined according to exponential attenuation law having value of 0.025 dB/mm at 2 MHz and 0.2 dB/mm at 4 MHz for both longitudinal and transversal wave modes.

Several defects were set on the surface opposite to the scanning surface. Some pretest trials were performed varying different defect parameters (height, length, tilt angle and skew angle). Finally it was decided to vary only the height (depth) of the defects to see better the effect of one certain parameter on the detectabilility. The shape, orientation and length of the defects were kept same for all defects. The flaws were semi-elliptical notches with length of 10 mm.

Based on the pretest results the defect height between 0.5–1.0 mm was seen interesting considering detectability. Thus this range was applied and randomized when choosing the defect heights. When the above presented material and defect parameters were applied it was obvious that some defects could not be distinguished among the noise signals with the probe specifications applied in the pretests. Thus it would depend on the inspection technique and probe characteristics how successful the inspection would be.

The general view of the virtual inspection in the simulation program is shown in Figure 6. The test block can be changed opaque and thus it is possible to hide the defects. However any program user is able to turn the test block transparent and view the defects and also access the defect definition information.

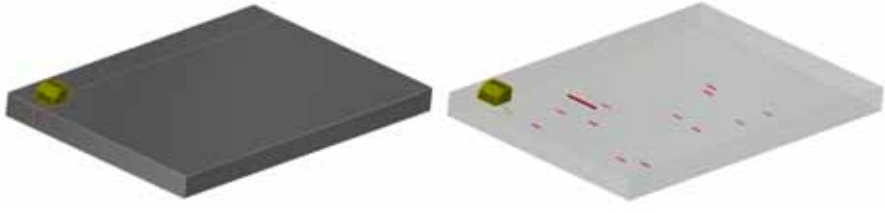

Figure 6. Virtual test block (opaque) and the probe at the scan start position (left). Locations of the defects on the block back surface when the block is made transparent.

An exact top view of the locations of the notches (D2–D13) and the side-drilled hole (D1) is shown in Figure 7. The positions for the defects were randomized in the area that was chosen to be scanned.

One side drilled hole (∅ 2 mm) was also positioned in the block at the depth of 15 mm for calibration purposes. All the flaw size and positioning information is given in Table 1.

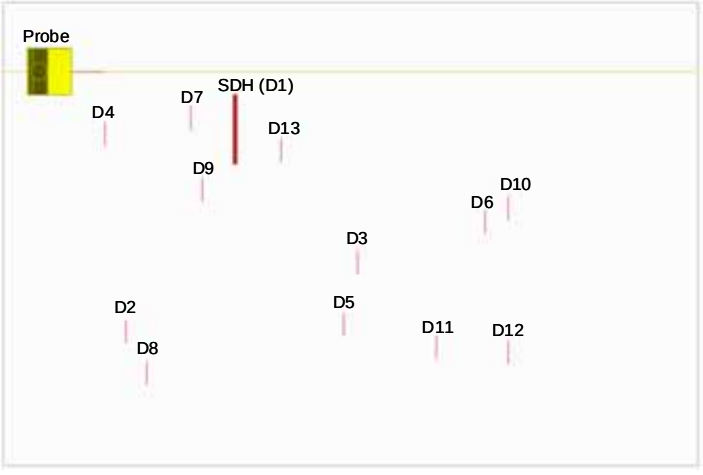

Figure 7. Locations of the semi-elliptical notches (D2 - D12) and side-drilled hole (D1) in the block (top view). Also probe is shown in its scan start position.

Table 1. Flaw dimensions and positions.

ID	Type	Length (mm)	Height (mm)	X (mm)	Y (mm)
D1	SDH	30	2	100	55
D2	Semi-ell.	10	0.8	53	142
D3	Semi-ell.	10	0.6	153	112
D4	Semi-ell.	10	0.8	44	57
D5	Semi-ell.	10	0.8	147	139
D6	Semi-ell.	10	0.9	208	95
D7	Semi-ell.	10	0.6	81	50
D8	Semi-ell.	10	0.9	62	160
D9	Semi-ell.	10	1	86	81
D10	Semi-ell.	10	0.9	218	89
D11	Semi-ell.	10	0.5	187	149
D12	Semi-ell.	10	0.5	218	151
D13	Semi-ell.	10	0.5	120	64

3.2 Scanning

Data was “acquired” using a simulation computation. In this simulation the data was “sampled” using 1 mm steps in scan direction and using 2 mm steps in index direction (step between scan lines).

The simulation runs (“scans”) were made using several different probe types varying their frequency and crystal size. The applied probes were “created” rather freely and the parameters are not directly equivalent with any existing probe. The applied probe designs in the 12 simulations made are given in Table 2. The purpose was to find out if some clear differences could be seen between the performances of the probes.

Table 2. Probe designs applied in the simulations.

Case ID	Frequency (MHz)	Element shape	Element/ aperture size (mm)	Focus depth (mm)
Simulation 1	4	Circumferential	10	None
Simulation 2	4	Circumferential	10	None
Simulation 3	4	Circumferential	8 mm	None
Simulation 4	4	Phased-array	20x17	20
Simulation 5	4	Circumferential	12	None
Simulation 6	4	Circumferential	6	None
Simulation 7	1	Circumferential	12	None
Simulation 8	2.5	Circumferential	12	None
Simulation 9	1	Rectangular	20x22	None
Simulation 10	2	Rectangular	8x8	None
Simulation 11	4	Rectangular	8x9	None
Simulation 12	2	Rectangular	20x22	None

After simulation computation the result was available as A-, B-, C- and D- scan presentations which are typical presentations of mechanical ultrasonic inspection data.

3.3 Data analysis

The simulation result files are very much similar to those that can be obtained from real ultrasonic inspections thus similar analyzing methods as for the measurement data can be applied. To make the analysis somehow consistent a few principles were decided before starting work forming a short and simple “procedure” including the following issues:

The detection target was set quite strictly:

- flaws are open to the back wall
- flaws are perpendicular to scan axis, skew angle 0°
- flaws are perpendicular to block back wall, tilt angle 0°
- flaw height is 0.5–1.0 mm
- flaw length is 10 mm

To identify relevant indication following detection criteria was set:

- signal-to-noise ratio ≥ 6 dB
- indication visible at least in two scan lines

Measurement of indication amplitude and boundaries:

- amplitude measurement in Civa: use A-scan with “envelope”.
- indication boundary measurement using – 6 dB drop technique.

The analysis was performed by same person who had set up the simulations. All simulations were run as batches and analyses were made separately after considerable time period without checking the real flaw positions at that time. Only when all indications considered being flaws were recorded the findings were compared to the real flaw positions.

The analysis was made using A-, B- and C-scan views. The maximum amplitude value and location coordinates in all three directions were measured for each indications considered relevant. Also the simulation noise level was measured.

4. Results of the simulation trial

In the Figure 8 below is shown C-scan view as an example of the simulation results. This figure shows a result where indications from all defects are clearly visible and can be easily distinguished from the material noise.

In the Figure 9 four C-scan views from different simulations are shown. In these figures the background noise is adjusted to same level to visualise the differences of the defect detectability when various ultrasonic probe characteristics are applied in the simulations.

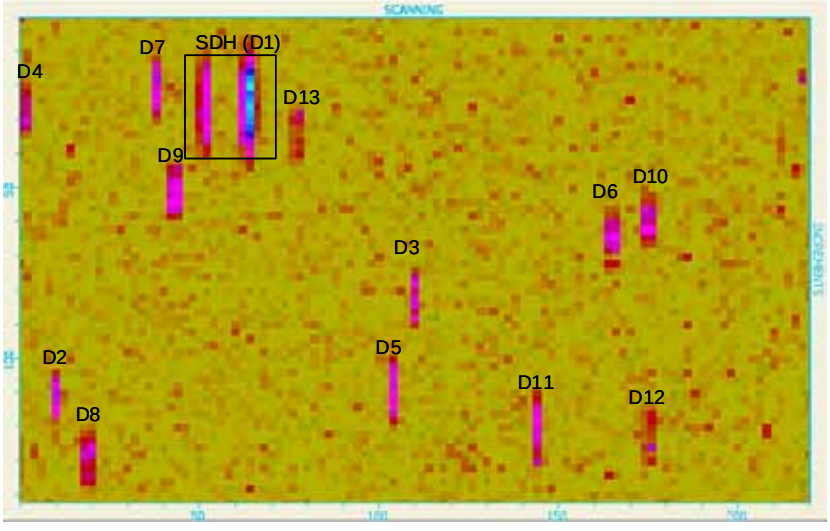

Figure 8. C-scan result when a phased-array probe with focus at the back wall depth was applied in one of the simulations (simulation ID: Sim4). Defect identification codes marked at corresponding indication pattern.

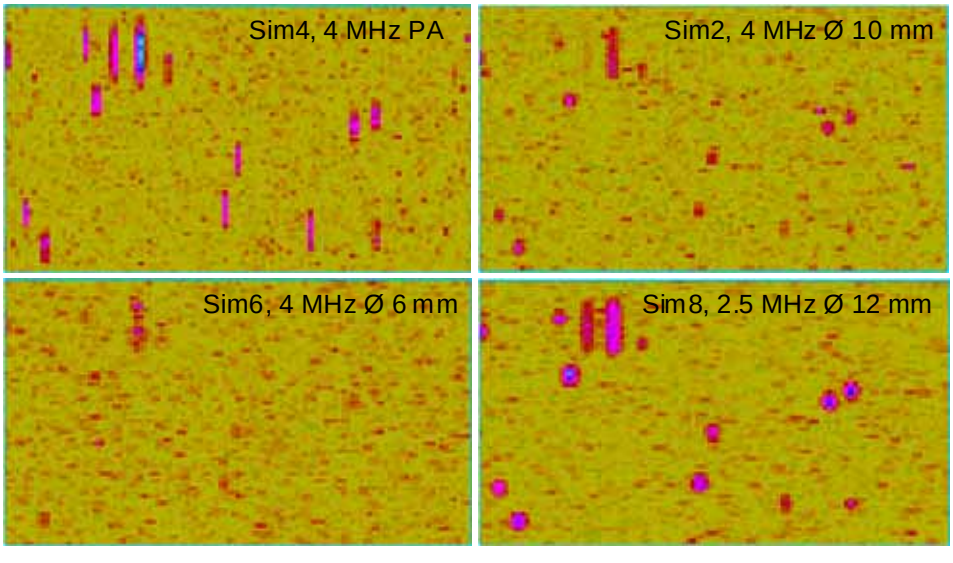

Figure 9. Some C-scan views from different simulations, the probe characteristics are given in the figures. The background noise was adjusted at the same level.

Altogether 12 simulations were analyzed. The search of indications was based in the first place on the high amplitudes, but signal dynamics and repetition in adjacent scan lines were also examined. Thus also many indication signals below the acceptable S/N ratio were identified (breaking the rule that S/N ratio should be ≥ 6 dB) and measured. The S/N ratios of all indications that could be detected somehow reasonably are given in Table 3.

Table 3. S/N ratios (dB) of detected indications.

Simul. ID	Probe characteristics	Defect ID / height (mm)											
		D9 1	D8 0.9	D6 0.9	D10 0.9	D2 0.8	D5 0.8	D4 0.8	D7 0.6	D3 0.6	D11 0.5	D12 0.5	D13 0.5
Sim1	4 MHz, crystal diam. 10 mm	8.5	8.2	8.2	7.4	8	6.5	5.7	5	3.9	5.4		4.2
Sim2	4 MHz, crystal diam. 10 mm	7.5	6.8	6.1	6.2	5.4		5.6					
Sim3	4 MHz, crystal diam. 8 mm	6.1	6.2	5.9	6.5	5.1	5.1						
Sim4	4 MHz, PA FD = 20 mm	8.2	6.9	7.3	7.7	9.2	8.8	6.4	9.1	8.6	7.4	6.1	5.1
Sim5	4 MHz, crystal diam. 12 mm	8.7	7.5	7.1	7.9	5.4	6.6	9.2	3.5	4.7	5.3	5.2	
Sim6	4 MHz, crystal diam. 6 mm	3.9	2.8	3									
Sim7	1 MHz, crystal diam. 12 mm	11.6	9.6	9.9	11.1	7.4	8.2	9.3	5				
Sim8	2.5 MHz, crystal diam. 12 mm	12.1	10.8	10.9	11.2	8.8	9.9	10.6	9.4	7.1	5.6	6.6	
Sim9	1 MHz, crystal 20 x 22 mm	10.2	9.2	8.8	9.5	7.7	7.9	7.9					
Sim10	2 MHz, crystal 8 x 9 mm	12	11	11.1	10.8	10.4	10.3	9.3	6	7.7	7.5		
Sim11	4 MHz, crystal 8 x 9 mm	6.4	5.6	7.4	6	7	5.9	5.4	3.5	4.5	4.4		
Sim12	2 MHz, crystal 20 x 22 mm	6.7	7.2	7.9	6.9	5.5	6.4	7.5					

The result concerning detection of the notches is shown below in Table 4. In the column “detection all” the total number of the detected notches is given regardless of the S/N ratio. According to the “analysis procedure” the S/N ratio should have been ≥ 6 dB in case of acceptable detection. When taking into account this rule the number of detected defects is considerably lower as can been seen in the “Detection S/N ≥ 6 dB” column of Table 4. The high noise level in some simulations caused two false calls during the data analysis phase.

Table 4. Number of detected flaws in different simulations with and without the rule S/N ≥ 6 dB. Also false calls occurred during analysis are given.

Simulation ID	Applied probe characteristics	Detection all number	Detection S/N ≥ 6 dB number	Detecton all %	Detection S/N ≥ 6 dB %	False calls
Sim1	4 MHz, crystal diam. 10 mm	11	6	92	50	-
Sim2	4 MHz, crystal diam. 10 mm	6	4	50	33	1
Sim3	4 MHz, crystal diam. 8 mm	6	3	50	25	-
Sim4	4 MHz, PA FD = 20 mm	12	11	100	92	-
Sim5	4 MHz, crystal diam. 12 mm	11	6	92	50	-
Sim6	4 MHz, crystal diam. 6 mm	3	0	25	0	-
Sim7	1 MHz, crystal diam. 12 mm	8	7	67	58	-
Sim8	2.5 MHz, crystal diam. 12 mm	11	10	92	83	-
Sim9	1 MHz, crystal 20 x 22 mm	7	7	58	58	-
Sim10	2 MHz, crystal 8 x 9 mm	9	9	75	75	-
Sim11	4 MHz, crystal 8 x 9 mm	10	4	83	33	1
Sim12	2 MHz, crystal 20 x 22 mm	7	6	58	50	-

5. Discussion

5.1 Analysis process

The data files produced by simulation can be seen quite realistic from the data analysis point of view. The analysis process of the data in Civa program is similar to the analysis of real data files acquired using ultrasonic equipment. Thus simulations could well be used as training material for data analysis of ultrasonic inspection when Civa is used as the analysis program.

In the simulation the level and location of noise can be controlled and defined to resemble some known real inspection case. Also the attenuation can be set according to the inspection situation to make the simulation realistic. Both of these can be set by material zone or zones to imitate for example the variation of material properties in base and weld material.

In this simulation exercise the data analysis was made by the “creator” of the virtual test block. Anyway the location of the defects and the depth variation was randomized. Also the simulations were run as batches and finally analyzed after some weeks without checking the defect information. In that sense some level of “blind testing” could be achieved. Also the application of predefined rules in the detection process made the analysis more or less independent of the analyst.

It would be useful to apply real blind analysis in such cases where POD (probability of detection) assessments are made using simulation result files.

This would require different persons for final defect setup/simulation runs and analysis phase. Also it would be a desired feature of the simulation program that the defect information could be completely hidden from the analyst. So far such a feature is not available.

5.2 Detectability

In the simulations only certain narrow defect depth interval from 0.5 mm to 1.0 mm was applied. This defect size range was considered to cause reasonable variation in detectability of the applied notches.

Table below shows how well the notches with different depths were detected with and without the 6 dB S/N ratio requirement. It must be noticed that the result is summary achieved using different probe characteristics, some showing very good and some poor performance. In this case one could state that detection of 1 mm notch was reliable using nearly “any probe design”.

Table 5. The detection rate of the notches with different depths.

Notch depth (mm)	**1**	**0.9**	**0.8**	**0.6**	**0.5**
No. of detection possibilities	12	36	36	24	36
Detected all	12	35	31	13	11
Detected all (%)	100	97	86	54	31
Detected with S/N ≥ 6 dB	11	31	22	6	4
Detected with S/N ≥ 6 dB (%)	92	86	61	25	11

The corresponding detection rate curves using the data of Table 5 are shown in Figure 10.

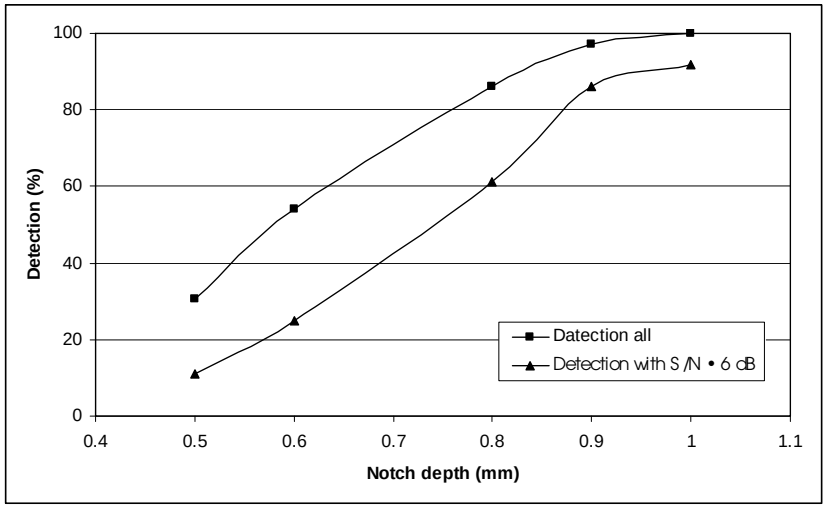

Figure 10. Percentage of detected notches versus notch depth.

Figure 11 shows how the defects were detected at different S/N ratio levels. Here the S/N ratio is the average of all hits made of a certain notch. In this trial the number of defects and hits per defect is low and cannot produce statistically reliable results. However, running simulations repeatedly with same settings more data could be generated to achieve also statistically meaningful results, as noise is randomized in every single simulation.

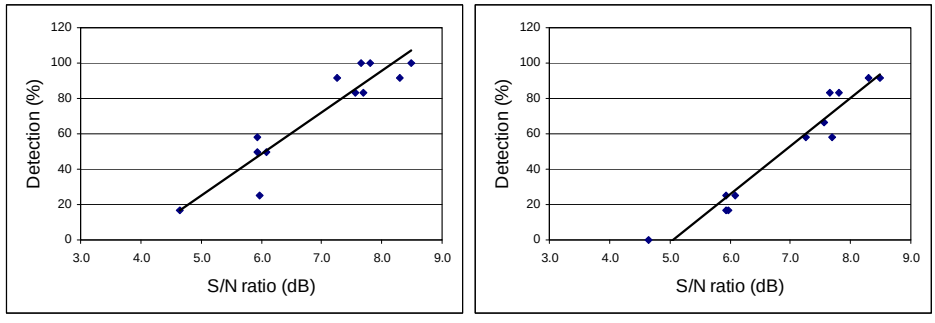

Figure 11. Percentage of detected notches versus S/N ratio. Left using detection with all S/N ratios and right with S/N ratio ≥ 6 dB.

6. Conclusions

The simulation examples show that quite realistic “inspection” data files could be produced using the simulation program. By using noise and attenuation controls it is possible to hide the flaws in the virtual test block. Thus the indications arising from the flaw are not obvious, and useful challenges can be created for the data analysis.

For imitation of an existing inspection case it would be necessary to match a simulation with a real inspection. This would require measurement of the existing noise level in a representative test block. After that the noise level and appearance should be adjusted and tested through trials in the simulation to find the equivalent level.

The simulation data and analysis result seem to provide material that could be used in POD assessments. It is obvious that the starting point of POD definition should be based on data from real experimental measurements. But because the amount of experimental data is often limited, addition of data and extension of parameter limits could be made using simulations.

Some other interesting possibilities to apply virtual test blocks would be personnel training of both on inspection techniques and data analysis. It could also be possible to organize personnel qualification on data analysis applying data files from simulations.

Concerning serious data generation for POD assessment and personnel qualifications there would be a requirement for blind tests (data analysis). This could be organized quite easily if in the simulation result files the flaw information could be hidden or completely removed.

The advantage of the application of virtual test blocks is production of virtual inspection data at low costs. Even if simulation computations can take hours or days a computer can work by it self after the parameters are set. There is a great freedom and flexibility to change and vary defect and component parameters. The changes of inspection techniques and probe characteristics are also possible very easily.

Reference

1. Civa 9 User Manual. CEA (Commissariat à l’Énergie Atomique) 2008.

Ultrasonic inspection of nodular cast iron insert edge distance using curved linear PA-probe

Aarne Lipponen, Jorma Pitkänen* and Matti Sarkimo
VTT Technical Research Centre of Finland
Espoo, Finland
*Posiva Oy, Eurajoki, Finland

Abstract

Nuclear fuel disposal canisters consist of a copper tube and a cast iron insert. The copper tube is designed for corrosion protection. The design and use of the nodular cast iron insert is based on strength and fracture mechanic aspects and it is the load carrying part of the structure. The preliminary acceptance criteria for the cast iron insert are under study.

There are several aspects in accepting the inspection results of nodular cast iron insert for use. One aspect among others is the position of the edge which is nearest to surface. In an earlier study this was stated to have a tolerance of edge position ±5 mm. There have been studies both on eccentricity and the real position of the nearest edge tolerances.

To determine the edge position, different ultrasonic techniques were tested using a curved linear PA-probe. To evaluate whether the distance variation is within the tolerance limit, the real geometrical nominal distance must be computed. Because the tolerances of the cast iron insert and its internal geometry can give a large variation in the edge position, these must be carefully evaluated.

The applied ultrasonic system is a 128 element phased array equipment. The used probe is curved and adjusted to curvature of the cast iron insert. The curved probe was designed to inspect the edge of the channel with one long axial line scanning. During line scanning the phased array probe does at the same time

electronical scanning. To optimize this electronic scanning, three different ultrasonic techniques were used.

This evaluation of edge distance was tested in four inspections of real size cast iron inserts. It was seen that the variation of the edge position is about 1 to 12 mm in radial direction (straightness) and in circumferential direction about 2 to 8 mm (twist) in range of about 4 m.

1. Manufacturing of cast iron insert

Nuclear fuel disposal canisters consist of the copper tube, the insert and the lids, see Figure 1. The insert is made of nodular graphite cast iron in one piece.

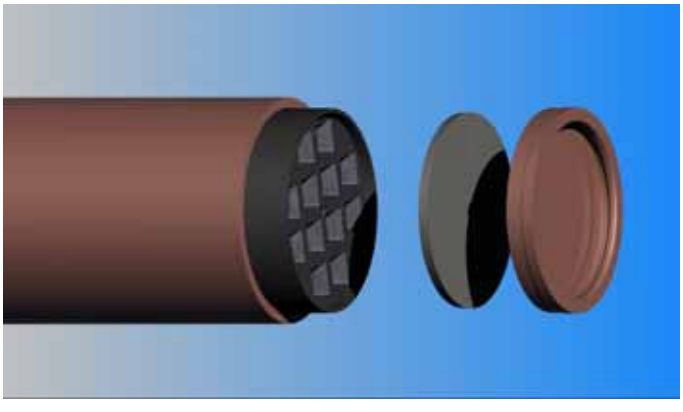

Figure 1. BWR-canister components, from the left: copper cylinder, iron insert, steel lid and copper lid [1].

The material of cast iron insert must meet the grade EN-GJS-400-15J requirements regarding mechanical properties. The machining tolerance of ±0.5 mm for 1 m diameter cylindrical products is typically achieved at length of 4–5 m with “good manufacturing practice” [1]. The diameter for the insert is 949+0.5/-0 mm.

The insert includes the steel profile cassette made of square steel tubes. The design of the cassette depends on the spent fuel characteristics of BWR, VVER and EPR fuel. In the Figure 2 the BWR type cassette can be seen in as-welded condition. The root of the weld is ground and the seam is also inspected by ultrasonic testing in the manufacturing stage.

Figure 2. Welded steel cassette.

As a special request the outer corner radius for the square tubes will be controlled. The radius shall be in accordance with EN 10219 for square tubular products 2.5×T, when the thickness is 6 to 10 mm. This value is to be controlled because the radius has a remarkable effect on the stress concentration that, in turn, has an effect on the load bearing capacity of the insert.

The straightness of the square tubes is controlled before welding with a gauge and a string wire. After assemblage the steel rack form the straightness is controlled again. The channels are gauged successfully with the 156 mm gauge, see Figure 3. After casting the channels are gauged with 152 mm gauge.

The bottom end flatness and perpendicularity is controlled. The allowable inaccuracy is 2 mm. The square profiles are welded together with pieces of flat steel bars.

Figure 3. Control of the straightness of the square tubes with a gauge, BWR type cassette. After welding (upper) and after casting (lower) [2, 4].

The size and shape of the various types of canisters will be kept as similar as possible for standardization, manufacturing and operational reasons. All canister types have the same outer diameter, and the lid design with the shoulder for the gripping device is identical. This is useful in manufacturing and handling operations and minimizes the need of special tools and equipment. The length of canisters is different for different types of fuel, see Figure 4. The channels in the insert have some clearance to assure the installation of fuel assemblies without friction drag or risk of jamming when using the fuel handling machine in the encapsulation station.

Figure 4. Disposal canister for the spent fuel from the Loviisa 1–2 (VVER-440), Olkiluoto 1–2 (BWR) and Olkiluoto 3 (EPR) reactors (from left to right). All versions of the canister have the same outer diameter of 1.050 m and heights of 3.6 m, 4.8 m, and 5.25 m (from left to right) [1].

The channels in the insert are designed to be so wide that the alignment and dimensions are sufficient directly in the casting process. The nominal width of the square channel is 20 mm more than the nominal width of the fuel assemblies. This tolerance allows reasonable casting related inaccuracies in the shape of the channels. In addition the spent fuel assemblies, specially the BWR type, can be in some cases curved. The largest measured deviation in straightness in full length of a BWR flow channel is 9 mm at TVO. The actual width and straightness requirement of the BWR insert channels is controlled after casting with a straight jig with a section of dimension of 156 mm. These tolerances are calculated to allow free installation of even slightly curved fuel assemblies.

The insert is cast in a foundry and no separate thermal treatment is needed. The channels for fuel assemblies are formed to the cast body by setting an equivalent steel structure into the mould. The prefabricated structure is welded together from steel tubes with strict dimensional tolerances. After casting the block is cleaned up, cut into the right length and the outer surface will be machined. The nodular graphite cast iron block is non-destructively tested before and after machining. In addition the dimensions and machined surfaces will be tested.

The machining tolerance of ±0.5 mm in the diameter of cylindrical products with a typical diameter of 1 m and length of 4 to 5 m is achieved typically with "good manufacturing practice". The nominal inside diameter of the copper tube and the outer diameter of the insert has a nominal difference of 2 mm, which corresponds to a nominal 1 mm radial gap between the cylinders. This is needed due to the fact that the machining of the inside of the large soft copper tube cylinder cannot possibly be made to tighter tolerances. An actual difference of 3 mm in the diameters is acceptable according to creep analysis in [9]. This allowance will guarantee a freely sliding installation of the insert into the copper tube.

The final manufacturing of the insert shall fulfill the requirement of the specifications that are described for all dimensions, shapes, material mechanical properties and metallurgical structure of the cast material and the non-destructive testing is used to inspect for manufacturing defects and to verify compliance to the geometrical requirements.

2. Fracture mechanics aspects in edge distance

The planned disposal depth is about 420 m below ground surface in the bedrock. The insert is the load carrying part of the canister structure. The basic dimensioning calculations are performed for normal operating conditions and in some upset conditions. The basic mechanical design load for the canister is 45MPa external pressure. The design load consists of the hydrostatic pressure of the groundwater, the swelling pressure of the bentonite buffer around the canister and of the pressure of glaciation of 2 to 3 km [3]. The cast iron insert is checked in design pressure load cases to have a reasonable margin (safety factor 2) in general membrane stresses when comparing to the material design strength (yield strength) in the design temperature. Secondly, the structure is checked in postulated upset load conditions (5 cm rock shear through the canister position) to have a reasonable margin against failure.

The finite element based stress analysis can take into account the actual geometry of the insert. The finite element code EPFM3D was used for the pressure load calculations. The code is developed for materially non-linear problems, fracture mechanics and creep in VTT.

The finite element model used in the strength analysis of the cast iron insert is shown in Figure 5.

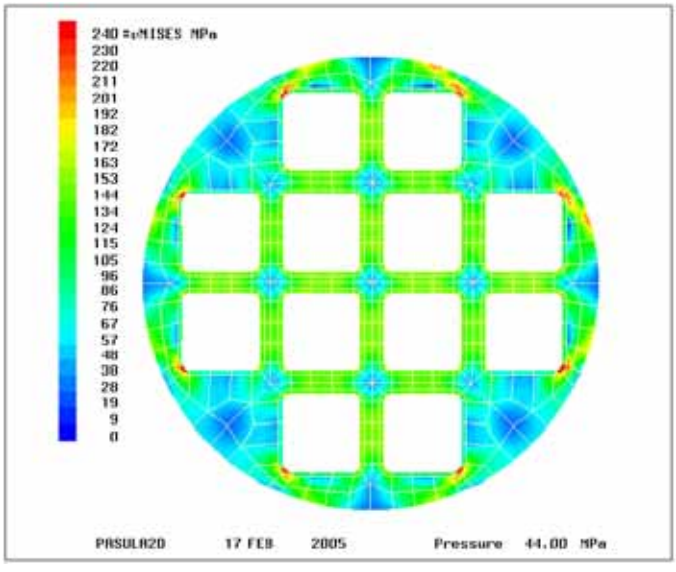

Figure 5. The finite element mesh of the full transverse section of the insert for BWR-type fuel.

In the model the deformations and von Mises stress distribution with design pressure is shown. The eccentricity is 5 mm to upward right direction at an angle of 45 degrees and the copper layer is omitted for conservatism. In the model the square steel profiles (channels) with loose contact against the cast body is included, because they have a strong effect on the collapse load. The results of the numerical stress analysis show that the stiffening and load bearing effects of the internal bulkheads in the iron insert are very pronounced.

There are several important aspects in accepting the inspection results of nodular cast iron insert for use. One aspect among others is the position of the channel edge which is nearest to the insert surface.

Eccentricity of the insert has a strong effect on the collapse load of the canister according to the strength analysis [6]. Eccentricity, which here means the inaccuracy in the polar symmetry of the channels for the fuel elements in the

inserts, is set to a maximum limit of 5 mm after machining. Due to stress concentration, the outer corner radius of the square steel tubes in the BWR insert is specified to be 15–25 mm [1].

Fracture mechanical calculations have been made in Sweden also concerning the semi-elliptical surface defects. Dimension calculations have been made with the design pressure and with short time incident loads corresponding e.g. 5 cm rock shear. Used safety factor was 2 in J_{2mm} value. The defects were located in the axial and radial directions. The dimensioning calculated acceptable defect size of semi-elliptical surface defects (ASME reference defects, semi-elliptical, c/a=3) was 4.5 mm in depth and 27.0 mm in length in circumferential direction.

Non-destructive testing (visual and ultrasonic) is used to inspect manufacturing, machining and handling related defects, such as pores, inclusions, etc in the insert. The geometrical requirements, minimum edge distance, allowable eccentricity and allowable defect size which are related to the strength and fracture resistant analyses can also be verified with the ultrasonic inspection. The strength and fracture resistance analyses are the basis of the ultrasonic inspection requirements, see Figure 6.

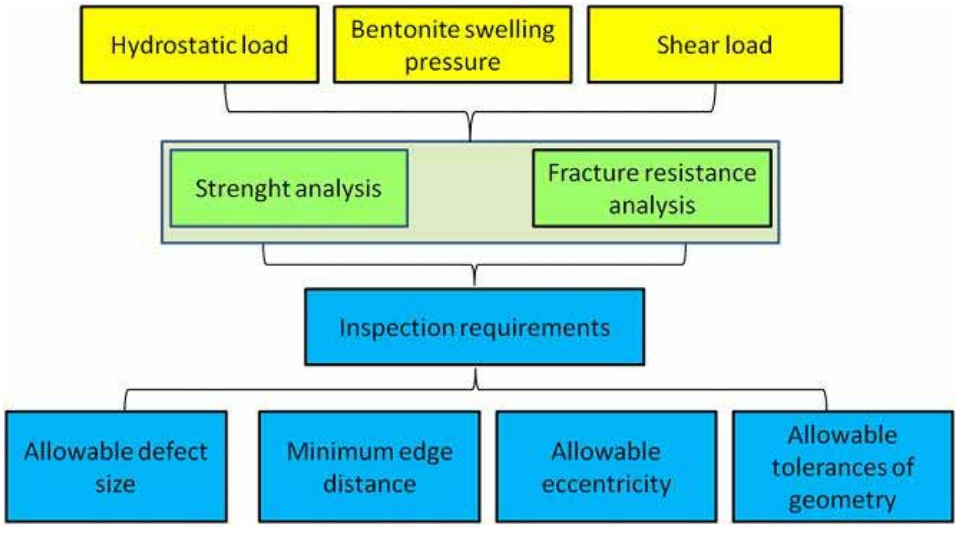

Figure 6. The connection of NDT inspection requirements to loading conditions of insert.

3. Nominal determination of the edge distance

The actual width and straightness requirement of the insert channels will be controlled after casting with a gauge. This will assure the installation of fuel assemblies into the channels without friction drag or risk of jamming.

The eccentricity will influence the strength of the insert. The location of the nearest channel edge can be measured with ultrasonic inspection techniques. The straightness of the outer 8 channels can be evaluated and the eccentricity can be calculated based on the inspection, Figure 8.

To evaluate if the distance variation is within the tolerance limit the real geometrical nominal distance must be computed. Because the tolerances of the cast iron insert internal geometry can give a large variation in edge position, these must be carefully evaluated, Figure 7.

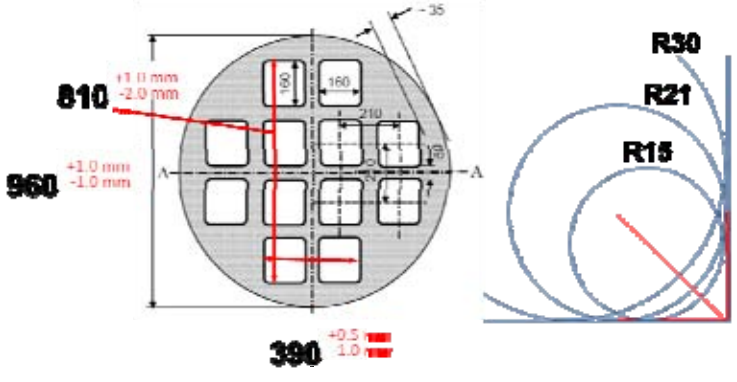

Figure 7. Geometrical information from the insert (BWR – OL1/OL2).

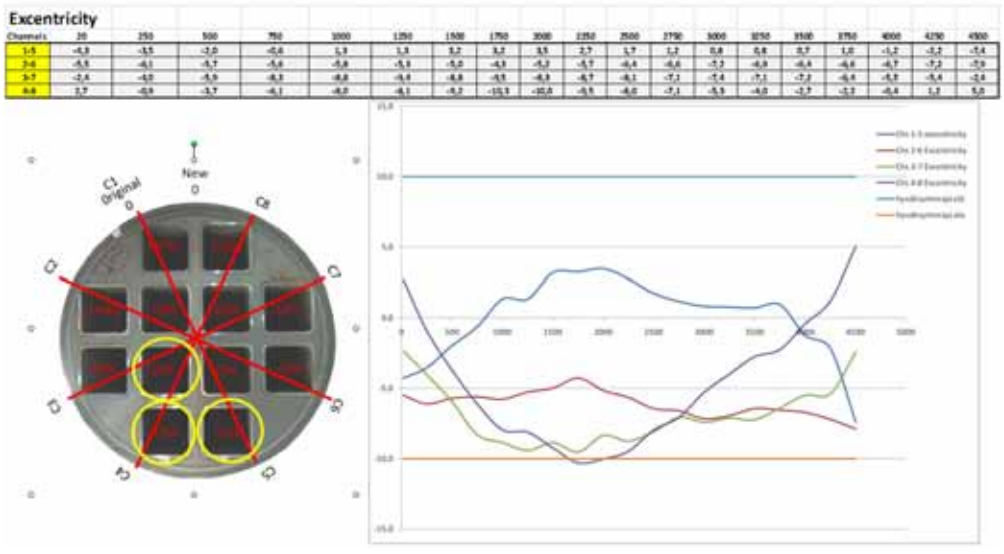

Figure 8. Eccentricity of insert I65 according the ultrasonic testing.

4. Ultrasonic measurement techniques for edge distance

To determine the edge position, different ultrasonic techniques were tested using curved linear PA-probe. The ultrasonic system was a 128 element phased array equipment. The used probe is curved and adjusted to curvature of the cast iron insert. The curved probe is designed in order to inspect the edge of the channel with one long axial scanning. During the mechanical linear scan the phased array probe does at the same time the transverse electronic scanning. To optimize this electronic scanning, three different types of techniques were used [7, 8].

The principle of the measurement of the edge distance is presented in Figure 9. The ultrasonic signal received from the corner area of the channel also reveals how the square steel tube is bonded to the cast iron material.

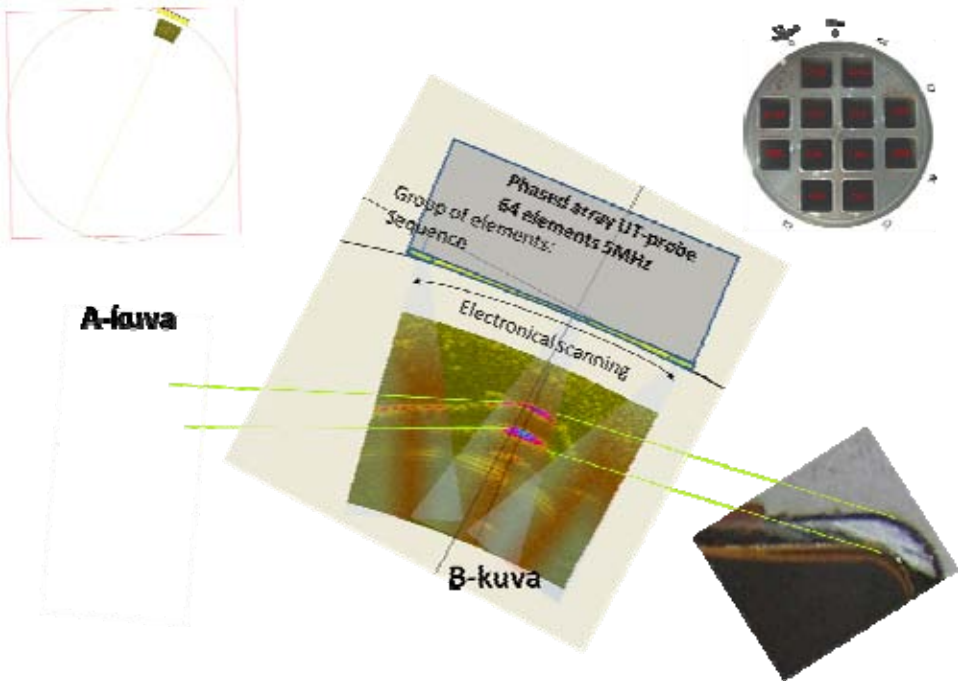

Figure 9. Principle for measurement for distance from outer surface to nearest corner of the fuel channel.

The tested inserts were full-size BWR inserts with 12 channels, Figure 10.

Figure 10. Machined BWR insert [2, 4].

4.1 Equipment and scanning system

One insert has 8 channel corners near to the surface to be measured, see Figure 11. The nominal material thickness between the nearest channel corner and the outside surface is about 35 mm.

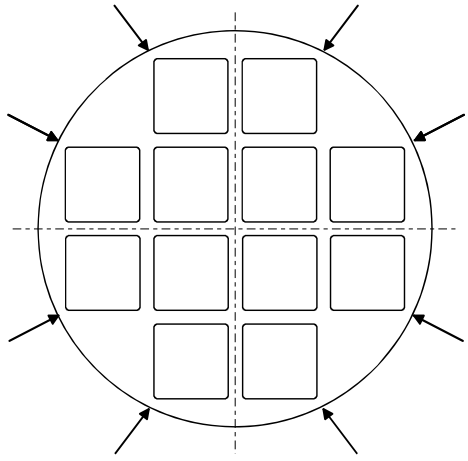

Figure 11. Cross-section of an insert having 12 channels. The locations of the nearest channel corners to the surface are shown with arrows.

The ultrasonic probe was linear phased array transducer having 128 elements. The element size is 0.85 × 13 mm and element spacing 0.15 mm. The centre frequency of the probe is 5 MHz. The probe has concave radius of 480 mm to fit the insert outer surface, Figure 12. The probe was moved mechanically along the insert surface using SKB's Rotator scanner. The component can be rotated and simultaneously the probe holder assembly can be moved in the component axial direction, Figure 12.

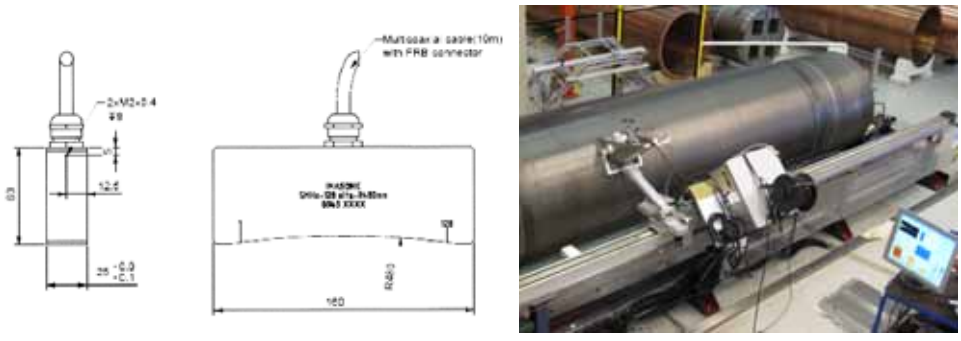

Figure 12. Phased array ultrasonic probe with curved design (left). SKB's Rotator (right).

To ensure the good and steady acoustic contact between the probe and the component a "local" immersion technique was used. The probe was attached in the holder inside a tub that can be filled with water, see Figure 13.

Figure 13. Probe holder design. Probe mounting inside immersion tub (left) and immersion tub filled with water when scanning (right).

The insert channel corners were scanned with the probe in the vertical position along the entire length of the channel, Figure 14. The probe middle was centered at channel corner. After scanning of one corner, the insert was turned to centre the probe at the next corner. Data of all 8 channel corners of one insert were recorded in one acquisition file.

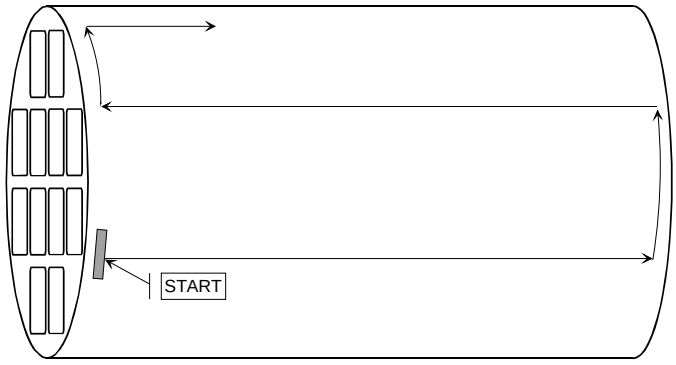

Figure 14. The principle of the probe movement path on the insert surface.

4.2 Ultrasonic techniques and analyzing principles

Application of the phased array probe made it possible to use different techniques during data acquisition. Four techniques were applied to compare the test performance. These techniques are described as follows:

1. Linear scan along the probe using 20 elements and one element step. The sound beam angle is 0° and focus is set at 35 mm depth.
2. Transmission using 8 elements in the centre of the probe without any focusing (null delay law); in reception the probe length is scanned using 20 elements / one element step and using 0° angle / 35 mm focusing depth.
3. Transmission using all (128) elements of the probe without any focusing (null delay law); In reception the probe length is scanned using 20 elements / one element step and using 0° angle / 35 mm focusing depth.
4. Transmission using sector scanning (angles 45°, 49°, 53°, 57°, 61° and 65°) applying 16 elements at the end of the probe. In reception the centre region of probe is scanned with 16 elements in 13 steps applying 0° angle / 35 mm focusing depth. Two salvoes are formed, one for shooting with positive angles from one end of the transducer and the other for shooting with negative angle values from the other probe end.

The scans were started with the probe centre 120 mm from the insert end (applied as zero position of the scans). Similarly at the end the scanning was stopped about 120 mm before the component corner to maintain the water in the local immersion tank.

The applied scan speeds were 50–70 mm/s. In axial direction the data was acquired using 7 mm step size.

The analyses of acquired data were made using Civa software. With this program the so called C-scans (top view), B-scans (side view) and D-scans (end view) could be drawn and the location of echoes originating from channel corners measured.

Figure 15 shows the top view of the channel corner echo along the insert length. In this presentation the circumferential position of the channel corner in the circumferential direction can be approximately seen. Figure 16 shows the end view of the channel corner echo. In this end view also the shape of the corner can be seen and thus its location in the circumferential direction can be determined quite accurately.

Figure 17 shows the side view of the channel corner echo along the insert length. Here the variations of the corner in the radial direction can be seen. The measurement of the corner position in relation to the insert outer surface can be performed using this view together with the end view.

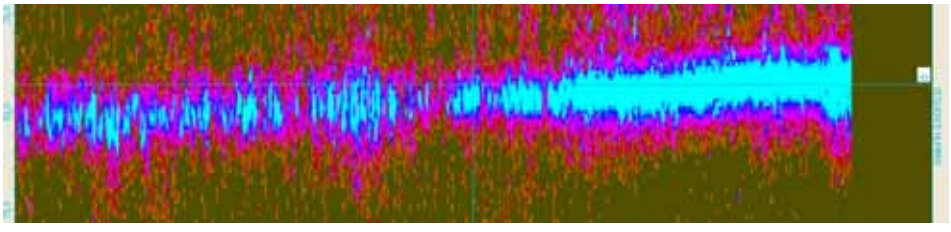

Figure 15. C-scan (top view) showing corner echo location along the insert length in circumferential direction.

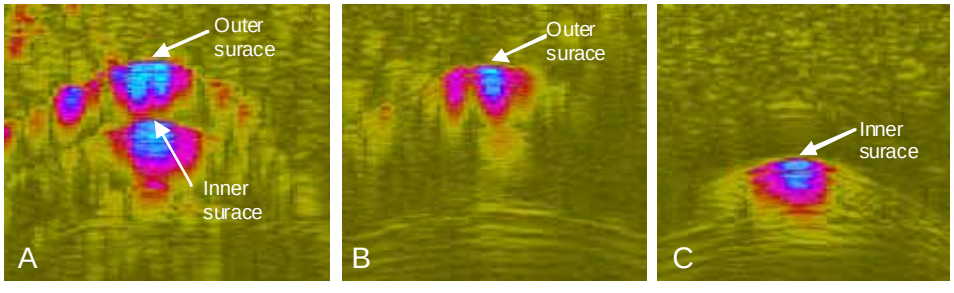

Figure 16. D-scan (end view) showing corner echo location in circumferential direction. Depending on the channel bonding quality at certain cross-section location either outer channel outer surface echo or inner surface echo or both of them are visible.

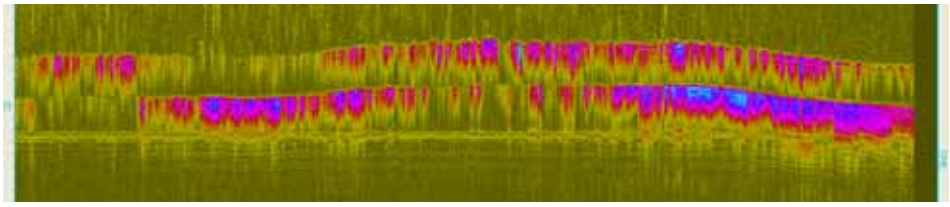

Figure 17. B-scan (side view) showing corner echo location along the insert length in radial direction. Two echo lines originating from inner and outer surface of the channel can be seen.

The echo location changes in radial and circumferential direction were measured from the data sets acquired using three different ultrasonic techniques (phased array delay laws).

The ultrasonic signal received from the corner area also reveals how well the channel steel plate is bonded to the cast iron material. If only the echo originating from the channel outer surface is visible the bonding is weak and the ultrasound is not able to cross the interface. On the other hand if the echo from inner surface is visible and the outer surface echo disappears or is very weak it can be concluded that ultrasound is penetrating through the interface because of good bonding. Figure 16 shows examples of different echo alternatives.

5. Experiences of measurement

All the eight outmost channel corners of the inserts were scanned and data was recorded using the four ultrasonic techniques explained above. In the analysis phase the data from three of the four techniques could be successfully visualized and changes of the channel corner position could be measured. The technique number 4 including several ultrasound shots with varying angle could not be visualized and measured in a meaningful way.

The maximum and minimum values of the channel positions in radial and circumferential directions were measured. The differences between maximum and minimum were calculated to have variation values for each channel corner. Table 1 and Table 2 show the measured differences of the channels in axial and circumferential directions.

Table 1. Measured variations in channel corner positions of insert I52 using different ultrasonic techniques.

	Radial variation				Circumferential variation			
Channel corner positon (°)	Techn 1 (mm)	Techn 2 (mm)	Tecn 3 (mm)	Average (mm)	Techn 1 (mm)	Techn 2 (mm)	Tecn 3 (mm)	Average (mm)
25	4.6	4.3	4.5	4.5	2	2	2	2.0
67	4.8	5.7	5.2	5.2	3	2	2	2.3
115	3.2	3.4	4.0	3.6	6	3	7	5.3
158	5.5	4.9	5.0	5.1	4	2	4	3.3
205	9.2	9.9	9.5	9.5	6	4	5	5.0
247	7.6	8.0	7.6	7.7	8	5	7	6.7
295	5.9	6.2	6.5	6.2	9	7	8	8.0
337	0.4	1.3	0.9	0.9	6	5	5	5.3

Table 2. Measured variations in channel corner positions of insert I64 using different ultrasonic techniques.

	Radial variation				Circumferential variation			
Channel corner positon (°)	Techn 1 (mm)	Techn 2 (mm)	Techn 3 (mm)	Average (mm)	Techn 1 (mm)	Techn 2 (mm)	Tecn 3 (mm)	Average (mm)
23	5.9	5.8	6.5	6.1	5	3	3	3.7
65	8.1	8.4	8.3	8.3	4	4	5	4.3
112	7.2	6.9	7.1	7.1	5	4	6	5.0
153	5.9	6.7	6.2	6.3	7	5	7	6.3
202	4.4	5.0	4.8	4.7	7	6	9	7.3
244	4.5	4.0	5.0	4.5	6	5	8	6.3
292	5.1	6.2	6.8	6.0	3	3	6	4.0
335	5.9	5.9	6.0	6.0	5	3	7	5.0

Figure 18 and Figure 19 below show variation of the channel corner position in graphical format.

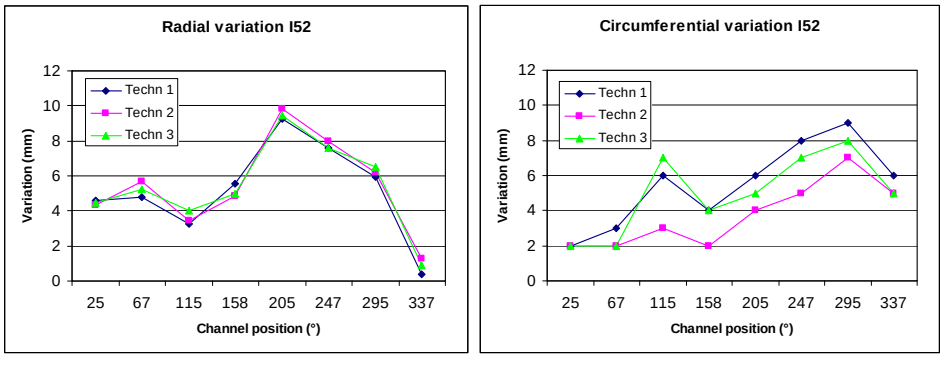

Figure 18. Radial and circumferential variation of channel corner positions of the insert I52.

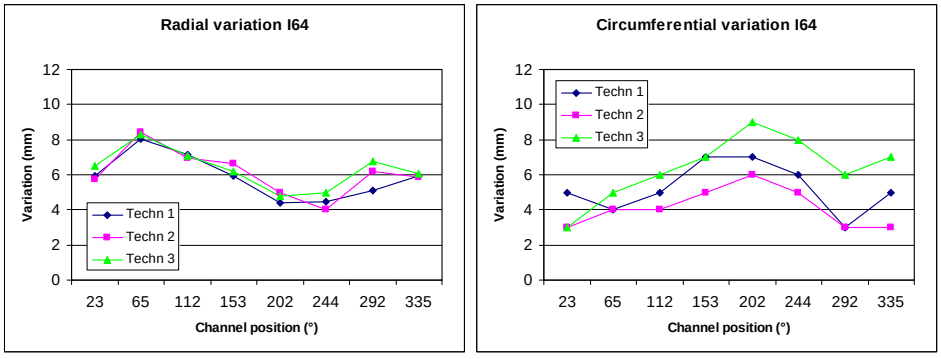

Figure 19. Radial and circumferential variation of channel corner positions of the insert I64.

6. Summary and conclusions

The measurement of the channel corner in radial direction is based directly on the flight time of the ultrasound between the transducer and corner. Therefore quite accurate results can be expected. The results also showed that using different ultrasound techniques very similar results can be achieved.

In the circumferential direction the channel corner position location is based on the positioning of the echo received from the outmost corner of the channel. The identification of the echo to be used and measurement of its position is somewhat less accurate operation than the radial position measurement. Also the readings of the echo position can be obtained in this direction only in one millimeter steps (= step size of the electronic scanning of the phased array probe). The measurement results also showed much larger variation in this direction when considering the different ultrasonic techniques.

When studying the D-scan views, it seems that the technique 1 is reproducing best the corner echo shape. The curved echo shape helps the definition accuracy of the corner centre. Thus this technique would probably be the most suitable for the measurement also in the circumferential direction.

The results could not be compared with the real values of the channel corner positions because such physical values were not available. Therefore the comparison of the different techniques is not a quite straightforward task. In radial direction the results are nearly equal and thus any of the techniques could be used. The technique 1 (zero angle electronic scanning) is simple and physically easy to interpret and thus preferable.

The measurement trial showed that the nearest channel corners of the inserts can be scanned fast and efficiently using a curved phased array ultrasonic probe. Various inspection techniques (phased array delay laws) are possible producing quite comparable results. However the zero angle scanning along the probe seems to work well and produce acceptable results for assessing the corner position both in radial and circumferential direction.

Some experiments to determine the real accuracy of the measurement could be considered. Also the modelling of the possible ultrasonic techniques could give some useful information for the final choice and inspection planning.

Using the top and side views of ultrasonic results it is possible to assess the straightness of the channels and measure the distance between cannel corner and outer surface of the insert. The received echo patterns and their locations also give information about the bonding (welding) between the channel steel wall and the surrounding nodular cast iron.

References

1. Raiko, H. 2005. Test Manufacture of the Canister Insert I35. Posiva Oy. Working Report 2005-53.

2. Raiko, H. 2005. Disposal Canister for Spent Nuclear Fuel. Posiva Oy. Design Report 2005-02.

3. Sarkimo, M. & Pitkänen, J. Phased Array Inspection of Insert Edge Distance (I52 and I64) Using Curved Phased Array. Posiva Oy. Working Report 2009-94 (to be published).

4. Nolvi, L. Manufacture of Disposal Canisters. Posiva Oy. Posiva Report 2009-03.

5. SKB, 2009. Design premises for a SKB-3V repository based on results from the safety assessment SR-Can and some subsequent analyses. Technical Report TR-09-22.

6. Martin, O., Nilsson, K. F. & Nikola, J. 2009. Numerical simulation of plastic collapse of copper-cast iron canister for spent nuclear fuel. Engineering Failure Analysis 16 (2009) 225-241. Institute for Energy, DG-JRC Petten, The Netherlands.

7. Pitkänen, J. Inspection of Disposal Canister Components. Posiva Report (to be published).

8. Pitkänen, J., Sarkimo, M. & Lonne, S. 2007. Modelling of Ultrasonic Testing for Inspection of Nodular Cast Iron Insert. 6th International Conference on NDE in Relation to Structural integrity for Nuclear and Pressurized Components, Budapest 12−14 October. 12 p.

9. Knuutila, A. 2001. Long-term creep of nuclear fuel disposal canister shroud. Posiva Oy, Working Report 2001-13.

Surface and near surface defect detection in thick copper EB-welds using eddy current testing

Jorma Pitkänen and Aarne Lipponen*
Posiva Oy, Eurajoki, Finland
*VTT Technical Research Centre of Finland
Espoo, Finland

Abstract

The surface inspection of thick copper electron beam (EB) welds plays an important role in the acceptance of nuclear fuel disposal. The main reasons to inspect these components are related to potential manufacturing and handling defects. In this work the data acquisition software, visualising tools for eddy current (EC) measurements and eddy current sensors were developed for detection of unwanted defects. The eddy current equipment was manufactured by IZFP and the visualising software in active co-operation with Posiva and IZFP for the inspections. The inspection procedure was produced during the development of the inspection techniques. The inspection method development aims to qualify the method for surface and near surface defect detection and sizing according to ENIQ [1]. The study includes technical justification to be carried out, and compilation of a defect catalogue and experience from measurements within the Posiva's research on issues related to manufacturing.

The depth of penetration in copper components in eddy current testing is rather small. To detect surface breaking defects the eddy current inspection is a good solution. A simple approach was adopted using two techniques:

- higher frequency was used to detect surface defects and to determine the dimensions of the defects except depth

- lower frequency was used to detect defects having a ligament and for sizing of deeper surface breaking defects.

The higher frequency was 30 kHz and the lower frequency was 200 Hz. The higher frequency probes were absolute bobbing coils and lower frequency probes combined transmitter – several receiver coils. To evaluate both methods, calibration blocks were manufactured by FNS for weld inspections [2]. These calibration specimens mainly consisted of electron discharge machined notches and holes of varying shapes, lengths and diameters in the range of 1 mm to 20 mm of depth. Also one copper lid specimen with 152 defects was manufactured and used for evaluation of weld inspection.

Several copper welds have been measured to assess the performance of the eddy current inspection for detection of surface defects. Some metallographic studies to identify the origin of the indications will also conducted, and the results will be reported later in conjunction of the eddy current measurements. The results show the capability of the developed eddy current measurements to detect and size surface defects to 10 mm depth and as well as to see indications having ligament up to 5 mm. This seems reasonable according to the results of EC-modeling.

1. Introduction

Eddy current testing (ET) is a widely applied nondestructive inspection method for the tube and pipe industry. ET equipment is simple to install and operate, and it can provide a much needed monitoring facility at moderate cost. Eddy current testing can be applied to both ferrous and non ferrous metals at different stages of the manufacturing process and also to thickness measurement of coatings on electrically conductive materials.

The purpose of eddy current inspection is to find defects in different materials and also possibly to provide information from changes in material properties. The ability to quantitatively determine the location and shape of any defect or internal structure within materials is important for both evaluation of copper component surface and near surface defects and characteristics of material.

The surface inspection of the copper lid weld plays an important role in the acceptance of nuclear fuel disposal. The grain size in copper and detectability of near surface defects by the phased array techniques limit at the moment the ultrasonic inspection of the copper welds [4]. There are three reasons for

inspection: welding, machining and handling defects. In all these three cases there is possibility for different types of defects.

For the EB-weld inspection, the data acquisition software, visualizing tools for eddy current measurements and eddy current sensors were developed for detection of unwanted defects. The eddy current equipment was manufactured by IZFP in Germany, and the visualizing software in active co-operation with Posiva and IZFP for the inspections. The inspection procedure was produced during the development of the inspection techniques. The aim of the inspection method development is to qualify the method for surface and near surface defect detection and sizing according to ENIQ, in order to show the inspection capability [1]. At the moment the study on technical justification is going on. At the same time a defect catalogue will also be collated, as well as the experience from measurements of Posiva's research welds. The detectability of defects will be studied in different projects on the probability of detection (POD) [2, 3].

2. Welding of copper

Two different welding methods are used for this type of thick copper welds: EBW – Electron Beam Welding and FSW – Friction Stir Welding. Both types of welds can show their characteristic defects (Table 1). The detectable defects set requirements to inspection techniques, because specific and postulated defects are used to plan non-destructive inspections.

Table 1. Defect types in copper welds made by electron beam (EBW) and friction stir welding (FSW).

Defects types	
EBW	FSW
Internal root defects	Joint like hooking
Gas porosity	Pores
Excess of penetration	Lack of penetration
Cavities	Voids
Gun discharge defects	Faying surface flaw
Run out	Tool trace material
Welding stresses	Entrapped oxide

In electron beam welding, gases will be emitted during melting, setting specific requirements for the welding process details [11]. Emitted gases can cause welding porosity, and for precaution deoxidizers must be used. The welding process can be controlled over a very wide range of parameters. The electron beam is tightly focused and the total heat input is much lower than that of any arc welding process. As a result, the effect of welding on the surrounding material is minimal, and the heat-affected zone is narrow. Possible distortion is slight and the work piece cools rapidly.

In EB welding, metal joining is by the heat generated in the bombardment by a high-velocity electron beam. At a typical accelerating voltage of 150 kV for welding, electrons can reach a speed of above 10^8 m/s, or about two-thirds of the speed of light. Electrons impinge the surfaces to be joined and nearly all of their kinetic energy is transformed into heat. Figure 1 (left) shows the principles of EB-welding equipment, where the electron beam will be controlled and directed with the help of a magnetic field produced by annular winding. Heat vaporizes the base metal and allows the electron beam to penetrate until the specified depth is achieved. Electron beam produces a keyhole in the material, which is filled as the beam passes by. Figure 1 (right) shows the phases of the keyhole formation according to [11]. Some of the defect types can be seen in Figure 2 [5].

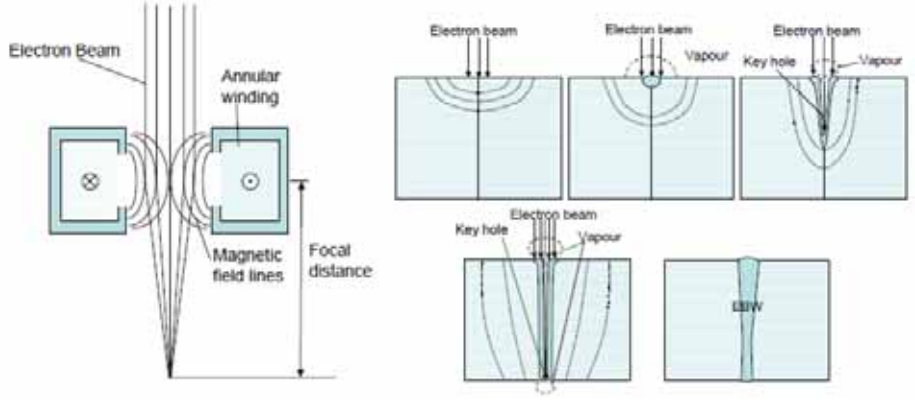

Figure 1. Principle of keyhole formation in electron beam welding.

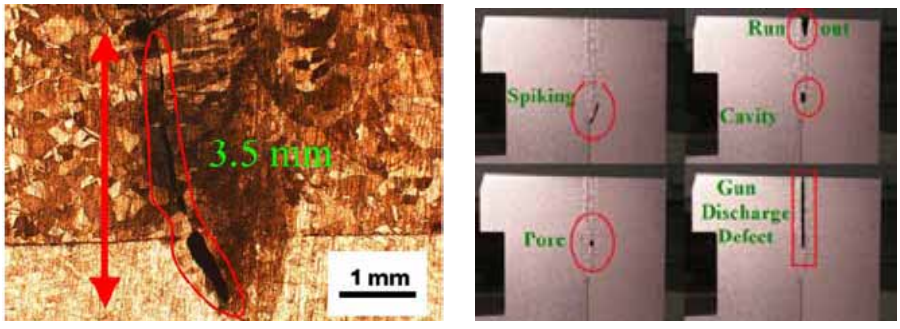

Figure 2. A root defect in copper EB-weld (left) and different defect types in a EB-weld (right).

Friction stir welding (FSW) is a rather new welding technique and it is mainly used for welding of aluminium components. Friction stir welding was applied successfully to thick (50 mm) copper components in co-operation with TWI and SKB. In this kind of thick copper components a pilot hole has to be drilled to make the plunge sequence possible without probe fracture [3]. Friction stir welding is a solid state joining method where the temperature is approximately 70–95% of the melting temperature of the base material [10]. FSW produces welds with fine grain equiaxed microstructure and minimises or eliminates defects due to liquid state. FSW is performed with either converted milling machines or specially designed and made FSW/FSP machines. Typical parameters to control in FS-Welding are shown in Figure 3.

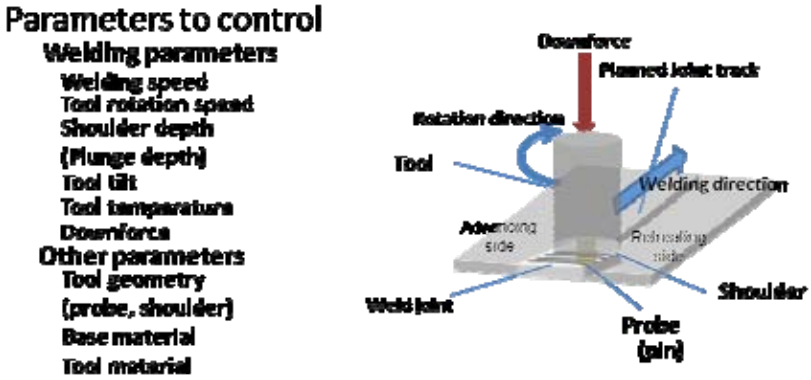

Figure 3. Principle of FS-welding and typical parameters to control.

The typical defects of FSW/FSP differ from those detected in welds made by fusion welding methods, even though friction stir welding method tries to

minimise the formation of defects. The possible defect types in friction stir weld are, [8, 9] (see Figure 4):

- Pores and clustered porosity
- Voids
- Entrapped oxide particles and oxide inclusions
- Tool trace material
- Incomplete penetration
- Joint like hooking
- Faying surface flaw.

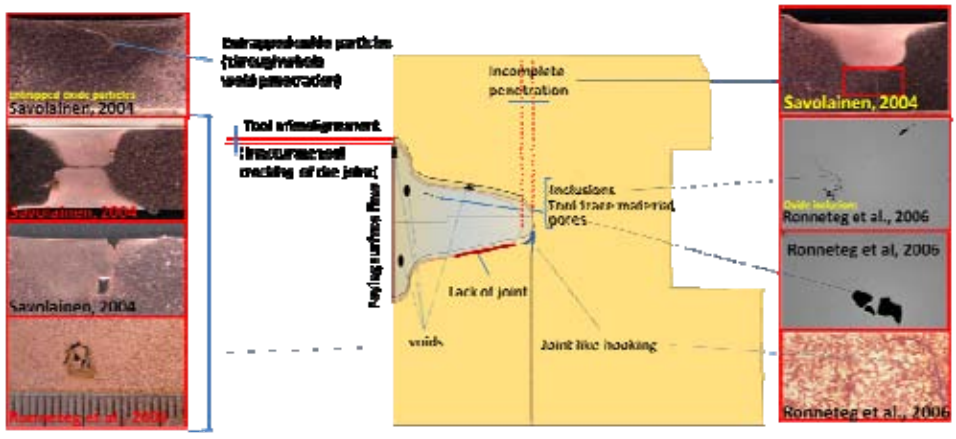

Figure 4. Possible defect types in friction stir welding and found defects in metallographic studies.

3. Eddy current inspection for defect detection

The structure of the used equipment and the principles of the inspection techniques will be discussed in detail in the following. These inspection techniques are also described in [2, 6, 7].

3.1 Eddy current equipment and inspection system

The 32 channel eddy current device is based on two inspECT® eddy current boards. Each board can multiplex up to 16 frequency channels. With the external multiplexer box on board it can drive 16 probes. Frequency and probe multiplexing can be mixed to get multi-frequency data of a sensor array with just

one scan. The device has a two axis coordinate interface for scanning with manipulators. Data connection to the PC is over ethernet with no need of a realtime operating system because the data is buffered in the device and synchronised with the coordinates.

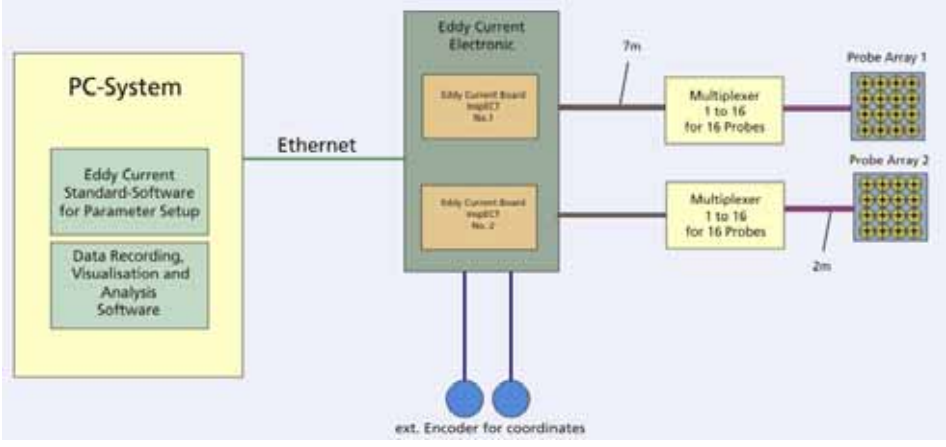

Figure 5. Block diagram of the 32 channel ET-device.

Technical data of the inspECT® board are following:

Digital

- DUAL DSP Core (SHARC for real-time data processing, BLACKFIN for communication)
- Firmware, flashing (updating) via Ethernet
- 8 Opto-decoupled real-time outputs / 8 Opto-decoupled real-time inputs
- 8 Multiplexer-trigger outputs to control the sensor multiplexer

Analog

- Dual-NCO for test frequencies ranging from 100 Hz to 10 MHz
- Sensor driver (Ri = 50 Ω), 2.2 Vss at 50 Ω
- Sensor input 50Ω, alternative differential input at 1 kΩ
- 10–50 dB HF gain with overload control
- Demodulation and anti-aliasing filter
- 2 x 16-Bit Analog to Digital Converters, 200 kHz sampling rate.

The software package inspECT® is a combination of a multi channel data acquisition system and a powerful C-Scan analysing software which makes it easy to analyse the recorded data and produce indication reports. The inspection is monitored by a laptop shown in the Figure 6 and measurement will be carried out by 2 different probe types – high frequency probe using frequency of 30 kHz and low frequency probe using frequency of 200 Hz. Both probes are shown in Figure 6. For copper inspection low frequency probe was suggested by [12]. This eddy current coil was using several receivers (4) and the transmitter was in the middle of the coil system with a frequency of 2 kHz in the measurements.

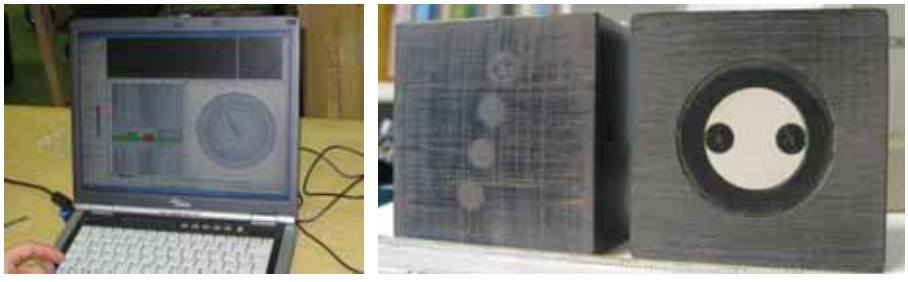

Figure 6. Laptop controlling the eddy current inspection (left) and inspection coils – high frequency coils (4 separate absolute coils) and low frequency differential coil consisting of one transmitter coil and 2 receiver coils (right).

Eddy current testing is affected by electrical conductivity and permeability of the material. These strongly influence the penetration depth of the eddy current density. This depth can be estimated using the simple equation in Figure 7. The frequency of the coil has a similar effect as conductivity and permeability. The frequency of the coil is restricted by the resonance frequency of the coil, and the applied frequency should be clearly less than the resonance frequency. The standard depth of penetration is often given by the curves shown for different metals in Figure 7 to quickly provide the estimated usable range for inspection. At the effective depth of penetration about 5% of the original (surface) eddy current density is available.

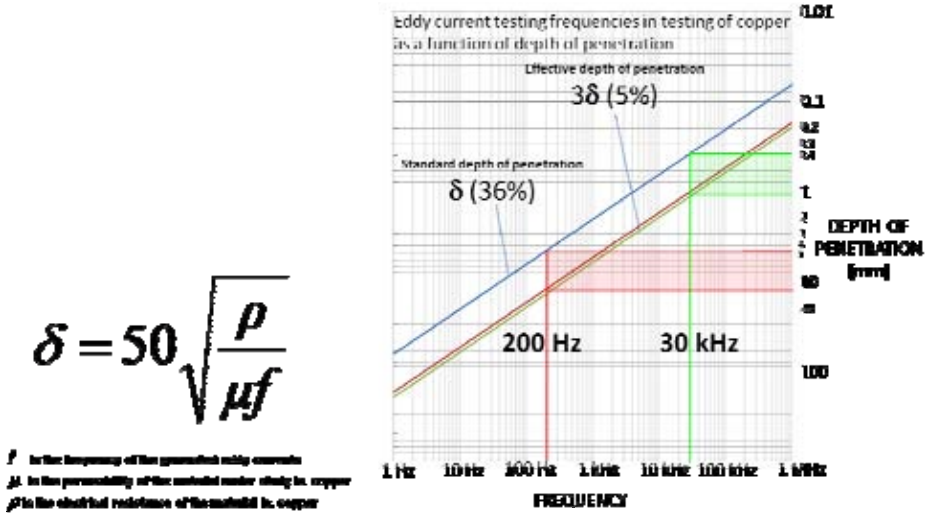

$$\delta = 50\sqrt{\frac{\rho}{\mu f}}$$

Figure 7. The depth of penetration in eddy current testing of copper.

EC density modeling for the high frequency probe (bobbing coil) is shown in Figure 8 and the used frequency has been typically in copper measurements 30 kHz, for high frequency the depth of penetration is about 0.5 mm. The applied coils are identical “absolute” pancake coils that are not shielded. Each coil has the internal reference coil. The coils are sensitive to crack-like and volumetric defects, and the sensitivity is independent of the orientation of the defects. The distance between the neighboring coils is 2.5 mm. The maximum sensitivity drop for circumferential crack-like defects between the coils and scans is 4 dB. To avoid wear and respective changes in sensitivity, the coil heads should not be in contact with the canister surface during examination. The applied distance between the probe head and the surface is 0.25 mm. The coils should be locked onto the probe head, to prevent the changes in the distance between the coils and the surface to be examined..The coil is manufactured in IZFP-FHG in Germany. The eddy current surface inspection is carried out using absolute method. A four-coil array probe has been applied to weld inspection. The width of the active area of the array is 10 mm. Each coil is connected to the respective channel of eddy current unit. The depth of penetration of current density generated by the coils was computed and was shown to be about 1 mm as a maximum, Figure 8.

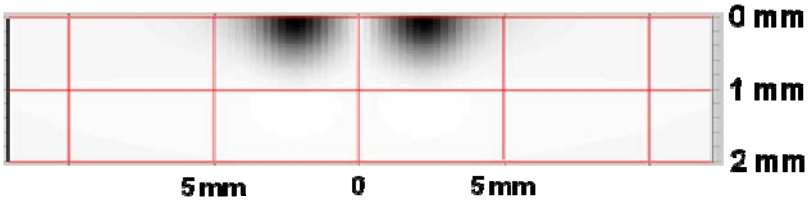

Figure 8. Eddy current density modeling the of the high frequency coil for copper weld inspection.

In the inspection of EB-weld, deep needle type of volumetric defects were found and for this type of defects low frequency probe was developed. In copper EB-weld inspections the used frequency was chosen to be 200 Hz. The low frequency differential coil consists of one transmitter coil and 2 receiver coils, as seen on the right side of Figure 6. According to modelling of the current density, the depth of penetration was computed to be slightly less than 15 mm by the transmitter and in the receiver coils a bit over 10 mm. The modeling software Civa was used also to optimize current density distribution in copper as shown in Figure 9. The area for detection is about 40 mm. The distribution could be lowered to 30 mm with the help of extra ferrite around the transmitter coil, and the sensitivity was increased about 5 dB.

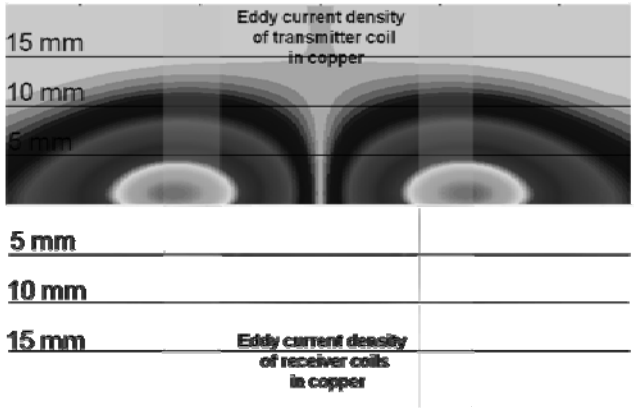

Figure 9. The modeled eddy current density for the low frequency probe.

3.2 Eddy current techniques and analyzing principles

The eddy current testing procedure for copper weld is a combination of high frequency and low frequency probe measurements. In the preliminary weld inspection low frequency measurements were applied in two directions called 0° and 90° inspection directions. In the weld inspections the surface and near surface areas were inspected up to a depth of about 10 mm. Surface breaking defects until 10 mm can be detected and sized, and a defect with a ligament of about 5 mm can also be detected. The inspection area is shown in Figure 10. The detectability of defects will be studied further in separate projects.

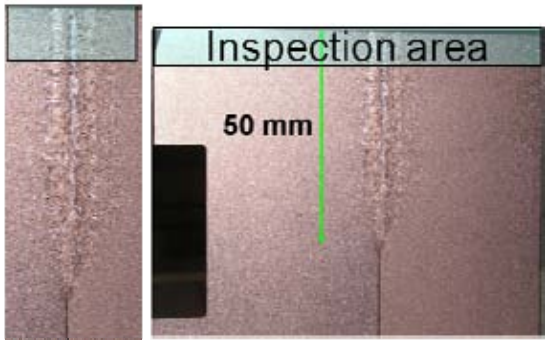

Figure 10. Inspection area of eddy current inspection.

Figure 11. C-scans and selected indication in polar coordinate presentation of EB-weld using low (left) and high (right) frequency coils.

The lid specimen is used as a reference specimen for ET of the weld. Figure 11 shows the ET results of one real size EB weld. So far about 20 real size EB welds and two friction stir welds have been inspected with eddy current testing. The welds may contain subsurface defects. Subsurface defects can be distinguished from other defects, as the range of low frequency coils is up to the

depth of 5 mm, while the ability of high frequency coils to detect defects is limited to 0.5 mm. By combining the above information, characterization and sizing of the defects is relatively simple. The indications of the four screw holes are clearly seen in the C-scans of Figure 11. The surface areas of the indications obtained using high frequency coils are rather small compared to those by low frequency coils. The final evaluation of these indications will be conducted after the evaluation software has been completed.

Data analysis can be divided into defect detection and defect sizing. In eddy current inspection it must be assured that the quality of inspection data meets the requirements of the inspection procedure. In data sizing it must be checked that the signals are not saturated and that the right sensitivity level has been used.

In defect detection the registration limit is important. The registration limit is fixed to level of reference defects. The amplitude of 1 mm deep notch is applied, with registration level of -12 dB from the reference defect. Equipment noise level is about 180 digits, when the indication of a 1 mm deep notch corresponds to 20 557 digits and that of a 2 mm deep notch corresponds to 27 348 digits, see Figure 12. The reference defect is 1 mm deep notch and the signal noise ratio is thus about 41 dB. In the plate weld measurement the signal to noise ratio was about 35 to 38 dB, see Figure 12, so that detectability is considered to be very good. This is not the same as real noise that is affected by the surface roughness and probeholder lifting movement. The registration level is near the real signal to noise ratio. This can be improved by making surface roughness and probeholder movement smaller. In every measurement the indications are compared to the reference defect. The verification of defect indications is under study.

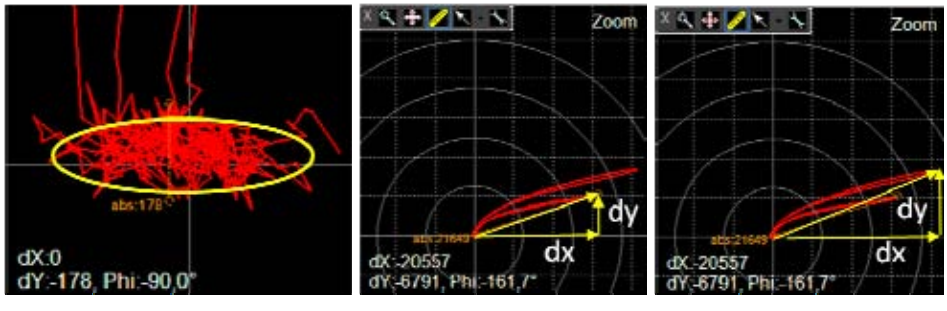

Figure 12. Eddy current noise level and indication from reference defects in copper weld inspection.

In defect sizing the dimensions of the detected indications will be given. This information is a part of the comparison of the inspection results against the acceptance criteria. The eddy current indications of known reference defects with different depths show in the polar coordinate presentation how the angle of indications reveals the depth of the defects. The inaccuracy of depth sizing will be studied. As seen in Figure 13, the indications will saturate at the depth of approximately 10 mm for surface breaking defects. This means that it is possible to estimate the depths of the indications up to 10 mm, and after that the reliability clearly decreases. It is also possible to distinguish between volumetric and planar type of defects. These two types of defects have their own defect depth sizing curves. It is therefore important first to evaluate the type of indication and its surface area to improve the accuracy in sizing.

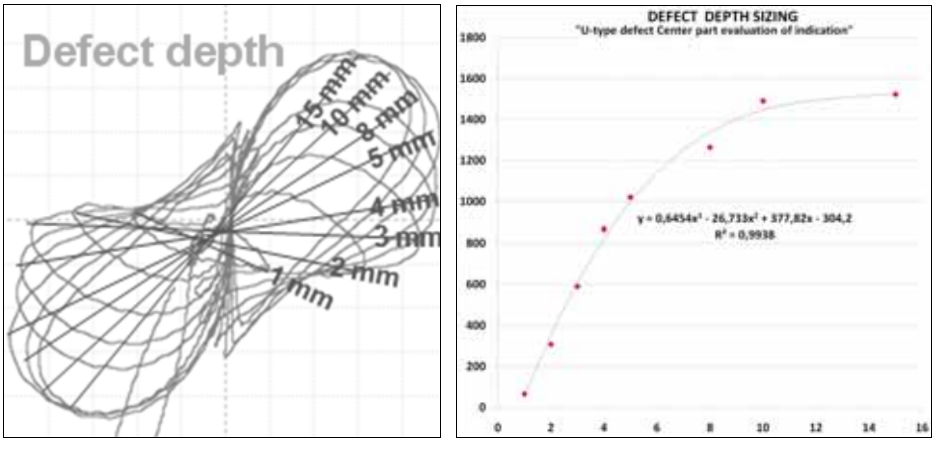

Figure 13. Reference defect depth variations from U-type of defect shows variation in amplitude and angle in polar coordinate presentation for low frequency coils on the left and sizing curve show saturation after 10 mm depth on the right.

The welding process and machining after welding can also produce defects that do not open to the surface, which means that there is a ligament between the defect and component surface. If this ligament is not too thick, the defects can be detected in the eddy current testing. As shown in Figure 14 the defect having ligament up to 5 mm was still detectable. The ligament thickness can be evaluated from the angle of the indications. The evaluation scheme of eddy current signals is shown in Figure 15.

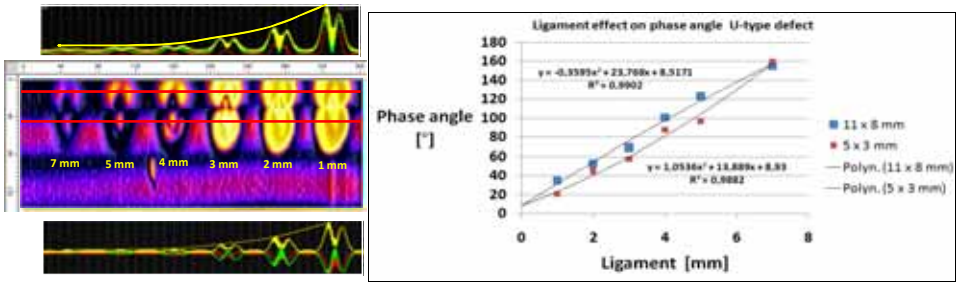

Figure 14. Effect of ligament to angle of indications: C-scan and amplitude scans (left) and dependency of the angle of indications on the ligament size (right).

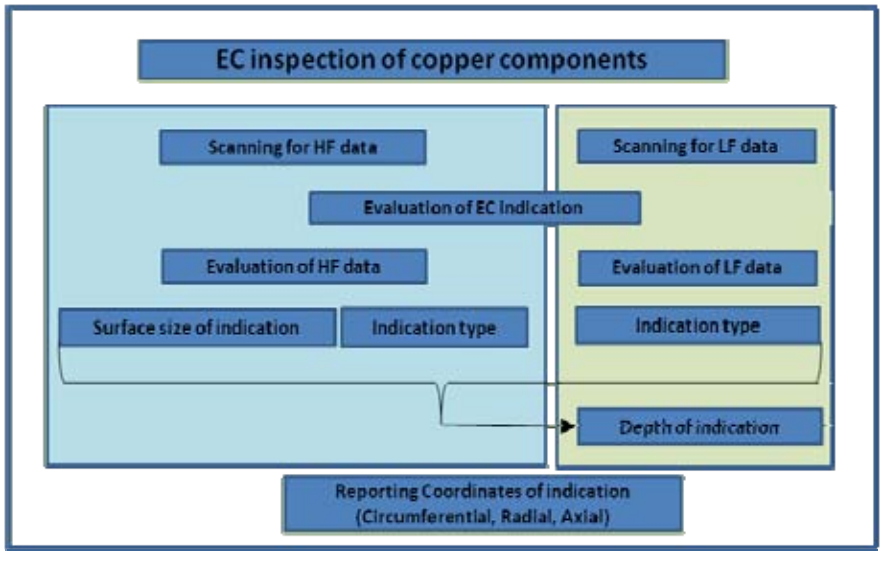

Figure 15. Evaluation scheme for eddy current signals.

4. Summary and conclusions

In this study the eddy current method has been succesfully applied to inspection of welds of copper. The inspections are based on two techniques, low and high frequency eddy current testing.

All studies are based on large scale measurements of reference specimens. Huge amount of testing has been carried out with real size components similar to

those in production and encapsulation plant. About 30 welds have been inspected, mainly including electron beam (EB) welds but also some friction stir welds. The developed low frequency probe will be optimised for higher depths of dectection, with on-going metallographic verification for detected indications in 12 real size EB-welds.

Preliminary inspection procedures have been developed for eddy current testing of copper, and the work carried out will support the qualification of the inspection method according to the ENIQ and Finnish practice in qualification. All necessary documentation and preparation will be carried out for qualifications.

The detectability of defects will be studied in separate projects together with BAM in Germany, in order to produce POD curves for inspections of copper welds.

References

1. ENIQ, 1998. Technical Justification, Pre-trials. ENIQ Report 10 EUR 18114 EN. November 1998. 132 p.

2. Paussu, R. & Pitkänen, J. 2009. Reference Specimens of Copper Components and EB Weld for Qualification and Performance Demonstration Purposes. International Conference on NDE in Relation to Structural integrity for Nuclear and Pressurized Components. Yokohama, 12−14 May 2009. 9 p.

3. Pavlovic, M., Takahashi, K., Müller, C. & Pitkänen, J. 2009. The Total Reliability of NDT Methods for Inspection of the EB Weld of the Copper Canister used for a Long term Storage of Spent Nuclear Fuel. 7th International conference on NDE in Relation to Structural integrity for Nuclear and Pressurized Components. Yokohama, 12−14 May 2009. 5 p.

4. Pitkänen, J., Arnold, W. & Hirsekorn, S. 2007a. The Effect of Grain Size on the Defect Detectability in Copper Components in Ultrasonic Testing. 6th International Conference on NDE in Relation to Structural integrity for Nuclear and Pressurized Components. Budapest, 12−14 October 2007. 14 p.

5. Pitkänen, J., Salonen, J., Sandlin, S. & Ronneteg, U. 2007b. Defect Detectability in EB-welded Copper Disposal Canister with 9 MeV Accelerator. 6th International Conference on NDE in Relation to Structural Integrity for Nuclear and Pressurized Components. Budapest, 12−14 October 2007. 14 p.

6. Pitkänen, J., Lipponen, A., Lahdenperä K. & Kiselmann, I. 2009. The Eddy Current Inspection for Detection of Surface and Near Surface Defects in Copper Components and Copper EB-Weld. 7th International Conference on NDE in Relation to Structural integrity for Nuclear and Pressurized Components. Yokohama 12–14 May 2009. 13 p.

7. Pitkänen, J. Inspection of bottom and lid welds for disposal canisters. Posiva Oy, Posiva Report. (To be published.)

8. Ronneteg, U., Cederqvist, L., Ryden H., Öberg, T. & Müller, C. 2006. Reliability in sealing of canister for spent nuclear fuel. SKB Report R-06-26. 121 p.

9. Savolainen, K. 2004. Friction Stir Weldability of Copper Alloys. Helsinki University of Technology, Laboratory of Engineering Materials. M.Sc. Thesis. 115 p + app. 3 p.

10. Savolainen, K. 2008. Friction stir welding and processing of copper. Helsinki University of Technology, Laboratory of Engineering Materials. Licentiate's Thesis. 82 p.

11. Schultz, H. 1993. Electron Beam Welding. Abington Publishing, Great Britain. 240 p. ISBN 1-85573-034-0.

12. Uchanin, V., Mook G. & Stepinski, T. 2003. The Investigation of Deep Penetrating High Resolution EC Probes For Subsurface Flaw Detection and Sizing. NDT.net – February 2003, Vol. 8, No. 2.

Creep in generation IV nuclear applications

Laura Rissanen
VTT Technical Research Centre of Finland
Espoo, Finland

Abstract

Nuclear power has an important role in fulfilling the world's growing energy needs and reducing the carbon dioxide emission. Six new, innovative nuclear energy systems have been identified and selected for further development by the international Generation Four International Forum (GIF). These generation four (Gen IV) nuclear energy systems include a variety of reactor, energy conversion and fuel cycle technologies. The successful development and deployment of these largely depend on the performance and reliability of the available structural materials. These potential materials need to sustain their mechanical properties up to high temperatures, high neutron doses and corrosive environments of the new or enhanced types of coolants. Current knowledge on material properties, material-coolant interaction and especially material degradation processes in these new environments are limited. This paper gives an overview of the Gen IV material issues with special emphasis on European design of supercritical light water reactor concept high performance light water reactor (HPLWR). The challenges for the structural materials and the components most likely to suffer from creep and creep-irradiation are highlighted. Some results from relatively short term creep testing in supercritical water are presented for AISI 316NG, 347H and 1.4970 steels. The 1.4970 steel was superior in creep and oxidation resistance.

1. Introduction

Current forecasts indicate that the world's energy need will double by 2050. To mitigating climate change the world has to simultaneously halve the carbon dioxide emissions from the 2000 level [1]. For this purpose nuclear power can provide a potentially significant addition as an energy resource in the absence of alternative technologies with less environmental impact. The Gen IV nuclear reactors will be designed for higher service temperature working conditions than any of the existing reactor types. Table 1 shows comparison of Gen IV nuclear energy systems in relation to the new Gen III nuclear power (Olkiluoto-3, OL3) plant being built in Finland. The operating parameters of the Gen IV systems are nominal, estimates and based on reference plants.

Table 1. Comparison of the foreseen out put and efficiencies of Olkiluoto-3 (Gen III) and Gen IV nuclear reactor units.

Reactor	Thermal output (MWth)	Net electric output (MWe)	Efficiency improvement ratio when OL3 = 1 (net efficiency)	First prototype estimated to be in operation	Number of plants to cover OL3 el. output
OL3 (Gen III)	4 300	1 600	1 (37%)	2 012	1
High Performance Light Water Reactor (HPLWR)	2 300	1 000	1.2 (44%)	2 025	1.6
Very High Temperature Reactor (VHTR)	600	300	1.4 (50%)	2 020	5.3
Sodium-cooled Fast reactor (SFR)	1 500	600 (pool-type)	1.1 (40%)	2 020	2.7
Gas-cooled Fast Reactor (GFR)	1 200	600	1.3 (48%)	2 025	2.7
Lead-cooled Fast Reactor (LFR)	2 900	1 200	1.1 (42%)	2 025	1.3
Molten Salt Reactor (MSR)	2 100	1 000	1.3 (47%)	2 031	1.6

The largest efficiency improvement is expected for the VHTR technology. The first Generation IV reactors are foreseen to be available for commercial use around 2030 at the earliest.

The design lifetime of Gen IV reactors will be up to 60 years. Temperatures up to 1 000°C and high pressures with simultaneous radiation load bring forth new challenges in the materials technology. In these conditions creep will be an active damage mechanism and high temperature properties will become limiting for load bearing structures. Also, retaining dimensional stability under combined mechanical loads, irradiation and corrosive environments will be challenging at high temperatures.

The main objective of the "HPLWR Phase 2" project, part of the GIF research activities on supercritical water-cooled reactors, was to tackle the critical material issues and the technical feasibility of the HPLWR concept [2]. The experimental results presented here are a part of the VTT contribution. The other project partners were NRI, CEA, Areva and JRC-IE. The design parameters for the reference HPLWR unit are presented in Table 2.

Table 2. Reactor design parameters for HPLWR [2].

High Pressure Light Water Reactor (HPLWR) design parameters	
Gross power	1 000 MWe
System pressure	25 MPa
Core coolant mass flow rate	≈ 1160 kg/s
Core inlet temperature Core outlet temperature	280°C 500°C
Cladding temperature	≈ 620°C
Active core height	4 200 mm
Fuel pin outer diameter	8 mm
Fuel pitch	9.5 mm
Fuel assembly shape	hexagonal or square
Reactor pressure vessel total height	13 000 mm
Reactor pressure vessel inner diameter	3 380 mm

The HPLWR concept is based on a reactor pressure vessel similar to a pressurized water reactor (PWR), increasing the design pressure to 25 MPa. The HPLWR has a direct once through steam cycle including high, intermediate and low pressure turbines. The general reactor schematic is presented in Figure 1.

The design core outlet temperature is planned to be 500°C, giving a net cycle efficiency of 44%.

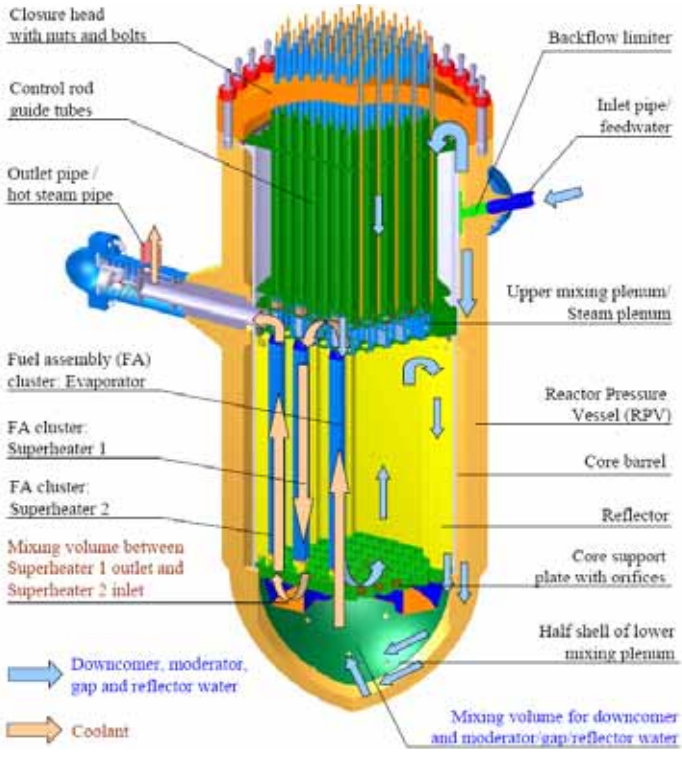

Figure 1. Reactor pressure vessel design for HPLWR [2].

The key advantages of this concept is the more compact design, reduced capital cost, and high thermal efficiency, with many of the safety features of the Gen II/III LWRs streamlined over time.

2. Materials and methods

The effect of supercritical water (SCW) atmosphere on the candidate materials for the HPLWR was studied through oxidation testing (in SCW) and creep testing in both inert (helium) and SCW. The creep testing was done on reference and test materials showing oxidation resistance in the initial exposure testing. The performed tests were mainly constant load creep tests but also one test series of slow strain rate tests (SSRT) were conducted for determination of the upper limits stress values [6].

2.1 SCW environment

In supercritical conditions water is in a single-phase fluid state, reached when the temperature and pressure pass the critical point of 22.1 MPa and 374°C. The current boiling water reactors (BWR) and pressurized water reactors (PWR) operate well below this point (Figure 2) [3]. Above the critical point the fluid cannot be liquefied by increasing the pressure or vaporized by increasing the temperature. Above the critical point high enthalpy coolant can be generated improving the thermal performance of the plant cycle. The proposed operation of supercritical plant would not fall below the critical point in the cycle.

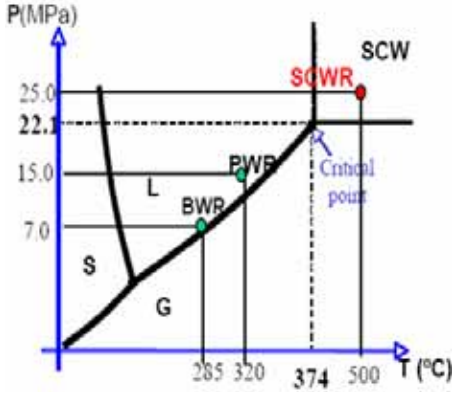

Figure 2. Pressure-temperature regime of super critical water-cooled reactor (SCWR) operation compared to that of current boiling water reactors (BWR) and pressurized water reactors (PWR) [3].

2.2 Test materials

The candidate materials for SCWR systems are ferritic–martensitic steels, austenitic stainless steels, nickel-based alloys and oxide dispersion strengthened alloys. The ferritic–martensitic steels generally have the best resistance to stress corrosion cracking, and excellent tensile properties, but tend to suffer from oxidation. Austenitic stainless steels and nickel-based alloys have better oxidation resistance but are more susceptible to stress corrosion cracking. The creep resistance of these materials is good for the temperature range intended. Nickel-based alloys suffer loss of high temperature ductility due to irradiation effects and swelling effects increase with increasing neutron dose. The oxide

dispersion strengthened (ODS) materials have exceptional resistance to creep and oxidation. The draw-back with these alloys is complicated manufacturing process and there are presently no manufacturers producing larger quantities of ODS materials. Another unsolved problem is the joinability by welding. Refractory metals such as niobium, tantalum, molybdenum, tungsten and vanadium can withstand temperatures up to 3400°C, but suffer from poor oxidation resistance coupled with low temperature radiation embrittlement, making them unsuitable for Gen IV reactor applications [4, 5].

In this work selected test materials were the austenitic stainless steels 316NG (LN), X10NiCrMoTiB15-15 (1.4970) and TP347H. The chemical compositions of the studied alloys (wt-%) are shown in Table 3.

Table 3. Chemical compositions of tested austenitic stainless steels.

	C	**Si**	**Mn**	**S**	**P**	**Cr**	**Ni**	**Mo**
316NG	0.014	0.42	0.80	0.001	0.032	16.6	11.3	2.11
1.4970	0.095	0.53	1.68	0.001	0.007	15.0	15.3	1.18
347H	0.048	0.29	1.84	0.013	0.026	17.6	10.7	
	Cu	**Al**	**W**	**V**	**Ti**	**Co**	**Nb**	**Fe**
316NG	0.23	0.007	0.02	0.04	0.004	0.07	0.01	bal.
1.4970	0.02	0.05	<0.01	0.02	0.45	0.03		bal.
347H							0.56	bal.

The basic mechanical properties for these steels at room temperature, 500°C and 650°C are presented in Table 4.

Table 4. Basic mechanical properties of the tested alloys.

		316NG		**347H**			**1.4970**	
Temperature		RT	500°C	RT	500°C	650°C	RT	650°C
Tensile strength	MPa	620	430	640	435	360	650	400
Elongation	%	55	-	45	34	26	20	22
Yield strength	MPa	280	128	255	145	165	600	320

The creep testing in the SCW environment was conducted with small tensile specimens. The specimen geometry and dimensions are shown in Figure 3.

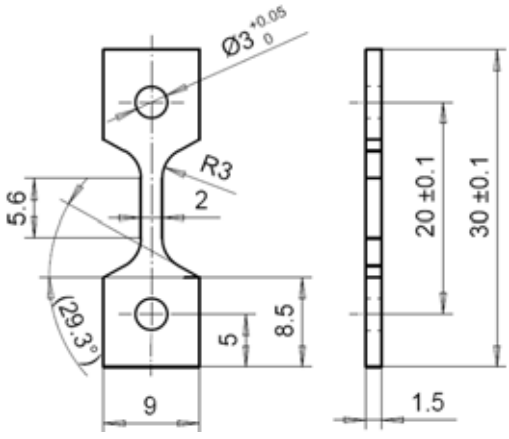

Figure 3. Specimen dimensions [6].

The specimens were machined into 30 mm long plate type specimens with a gauge section of 2.0 by 1.5 mm. Before the tests the surface of the gauge length was polished to 320 grit level.

2.3 Testing in SCW

The specimens were tested in the VTT supercritical autoclave presented in Figure 4.

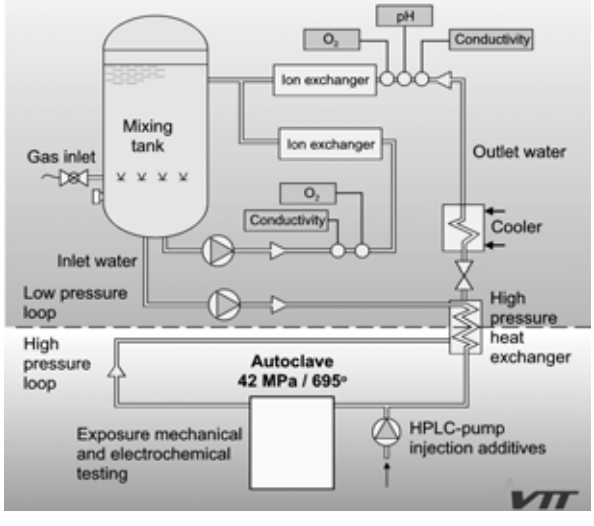

Figure 4. A schematic presentation of the SCW autoclave system of VTT. The system consists of low and high pressure water recirculation loops in addition to the materials testing autoclave [7].

The high pressure recirculation water loop consists of a high pressure pump, a heat exchanger and a preheater. The water returning from the autoclave flows through the heat exchanger and a cooler. The maximum working temperature and pressure of the system is 700°C and 42 MPa, respectively. The maximum flow rate of the high pressure loop is about 85 ml/min.

The load measurement and control is performed using a 2 kN load cell and a step-motor control. Load, pressure, and temperature are continuously monitored and controlled during testing.

Constant load creep tests were performed on austenitic stainless steels AISI 316NG, 347H and 1.4970 in SCW (25 MPa) and helium (1 atm) at 650°C. The duration of one test was limited to a maximum of 400 h. The SCW test solution was deionized water with inlet water conductivity < 0.1 μS/cm and water flow rate of 2–3 ml/min. The dissolved oxygen content was 1 ppm. Suitable test stresses were determined from the initial slow strain rate tests. More detailed description of the slow strain rate test results is presented in Penttilä et al. [6]. The target was to reach a total strain of around 1% in the testing time (~ 400 h). The stress levels selected for the creep testing were selected at 45% and 65% of the material tensile strength.

The effect of the environment was studied through comparing the developing (primary – secondary) creep strain rates from identically loaded tests in SCW and inert atmosphere. The loading cycle consisted of rapid loading to test stress when the test environment had stabilized. The test pressure and temperature were kept constant and the displacement (strain) of the specimen was monitored by LVDTs and the step motor control signal.

After creep testing the specimens were studied using scanning electron microscope (SEM) and energy dispersive spectroscopy (EDS) to assess the effect of oxidation on the test stress (net area reduction).

3. Results

The strain rates were determined from strain vs. time data. An example of the acquired raw data for 347H steel in SCW and helium at 650°C is shown in Figure 5.

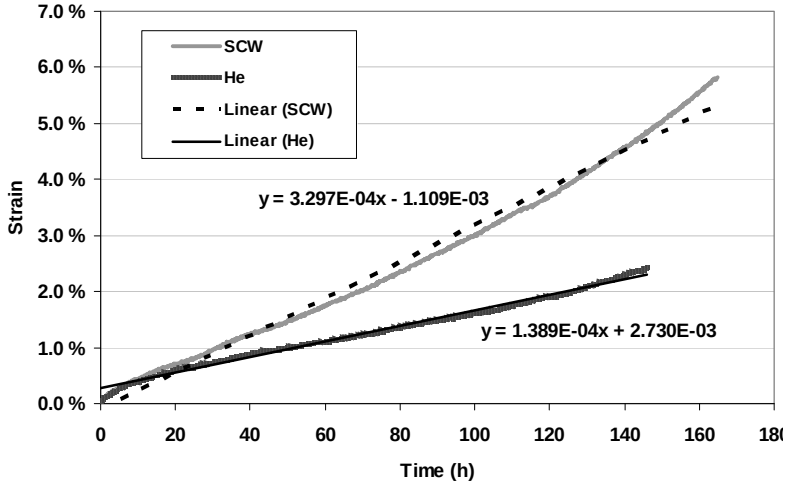

Figure 5. Strain vs. time curves for 347H steel tested in supercritical water and helium at 650°C. The stress is 215 MPa [8].

It was shown that linear regression fits for the accumulated strain as a function of time gave adequate presentations of creep strain rate for environment comparison purpose.

A summary on the creep test results is shown in Table 5. Nominal stress is calculated from the nominal load and specimen net area. Strain is calculated from the displacement control signal acquired from the step motor since the LVDT signal showed more noise. The accuracy of the variables that were kept constant, i.e. temperature and load, were determined from the measured data. The standard deviation of the temperature over the testing time was less than ±2°C. The total strains are reported at the maximum test time. The targeted strain-rate was 1% in two weeks.

Table 5. Summary of the creep tests at 650°C [8].

Material	Test environment	σ	ε_{tmax}	t_{max}	$t_{\dot{\varepsilon}}$	$\varepsilon_{c\dot{\varepsilon}}$	$\dot{\varepsilon}_{prim}$
		MPa	%	h	h	%	1/h
316NG	SCW	90 ± 0.7%	0.28	190	90	0.21	3.64E-06
		130 ± 0.5%	0.83	240	120	0.43	3.07E-05
	He	90 ± 0.6%	0.18	170	90	0.12	2.27E-06
		130 ± 0.4%	0.36	240	120	0.18	1.25E-05
347	SCW	149 ± 0.3%	0.45	170	85	0.32	1.68E-05
		215 ±0.4%	5.82	165	90	2.79	3.30E-04
	He	149 ± 0.3%	0.42	170	80	0.31	1.42E-05
		215 ± 0.2%	2.42	145	85	1.41	1.39E-04
1.4970	SCW	200 ± 0.4%	0.62	170	90	0.58	2.19E-05
		250 ± 0.3%	0.41	170	95	0.24	1.49E-05
	He	200 ± 0.4%	0.65	170	80	0.43	2.53E-05
		250 ± 0.2%	0.40	170	80	0.21	1.73E-05

The large differences in strain rates between materials are due to different creep response at the test stresses at equal normalised stress ratios (σ/σ_{UTS}). For 316NG and 1.4970 steels the creep response was clearly in the primary stage and for 347H the exposure time was sufficient to progress to secondary creep. A clear difference in the behaviour of 316NG and 347H steels between He and SCW environment were observed. The strain rates were 1.5−2.5 times higher in SCW than in helium. For 1.4970 steel no environment dependent difference in the creep behaviour was observed. Comparison of the primary to secondary strain rates in SCW and in helium is presented in Figure 6. A summary of the strain rate results is presented in Table 6.

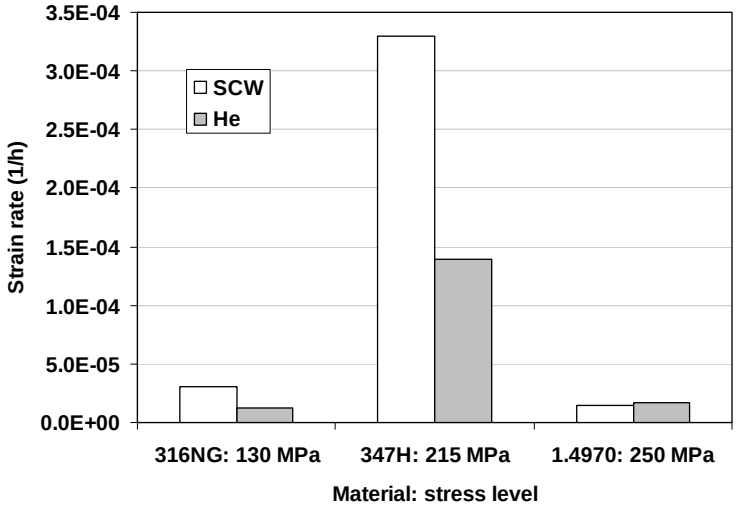

Figure 6. Strain rate comparison for 316NG, 347H and 1.4970 in SCW and inert helium conditions at 650°C [8].

Table 6. Summary of the strain rate comparison for the studied alloys at 650°C [8].

Material	Stress	Strain rate ratio SCW/He
316NG	130 MPa	1.6
316NG	90 MPa	2.5
347H	149 MPa	1.2
347H	215 MPa	2.4
1.4970	200 MPa	≈ 1
1.4970	250 MPa	≈ 1

After the tests the specimens' microstructure and formed oxide layers were determined with SEM. 1.4970 steel seemed to be superior also in oxidation resistance. However, due to short exposure times, the oxide layers showed no impact on the nominal stress levels of any of the materials. The performed constant load creep tests were rather short (testing for creep properties usually > 1 000 h). To verify these results, the test matrix should contain repeated test and include longer tests.

4. Discussion

The general requirements for structural materials at the high temperatures of Gen IV systems are: resistance against thermal and irradiation creep, fatigue, oxidation, coolant interaction and the combination of these. The manufacturing, weldability and maintenance issues are of course also important in the materials selection process.

The materials to be utilized for the initial design suggestions of any Gen IV reactor concept should have a reasonable set of pedigree, long term experience of high temperature service and only need targeted qualification tests to their special needs. For all Gen IV designs, significant materials property data must be obtained to license the future reactor designs. Long time creep testing in material-coolant interaction, testing the combination of creep, irradiation and oxidation resistance of candidate materials and testing new materials as well as modelling are of utmost importance for securing their long term performance of up to 60 years.

Evaluating basic physical and mechanical properties of several candidate in-core and out-of-core materials gives a cross-cutting opportunity that addresses several of the Gen IV concepts. For instance the coolant outlet temperature of the six concepts of Table 1 exceed that of any current design by at least 190°C, and in some cases, by over 600°C. The fast spectrum concepts will result in radiation damage doses to core internals that exceed those in current light water reactors by as much as a factor of 10. For the combination of higher operating temperature and higher radiation damage dose there is little or no commercial plant experience. Above 600ºC, thermal mechanisms, rather than irradiation–induced mechanisms may be dominating. There is indicative results claiming that the radiation damage may be increasingly annealed away at temperatures exceeding the homologous temperature (T/T_m) of 0.6. However, the temperature dependency of irradiation creep is very complicated and more studies of thermal and irradiation creep interaction are needed.

In the field of materials modelling, an important hurdle would be the improvement of tools and methods for determining the microstructural evolution under irradiation (and thermal ageing). The data needed for verification require extensive experimental programs and new testing facilities. It is however clear that material testing (laboratory scale) has to happen in conditions that mimic the real ones and the behaviour in operation then has to be assessed based on extrapolation exercises. Experiment and theory must be regarded and used as

complementary coupled tools. The research community should actively promote and utilize the existing communication links between the actors and stakeholders in the nuclear materials field to effectively shortcut the identification and qualification of materials for the future nuclear systems in the short time period hoped for [9].

For a critical evaluation of the above experimental results, the test matrix, equipment and environment must be taken into account. Firstly, the creep tests were rather short. In design related creep studies, the tests must be much longer, and to reliably determine the overall effect of supercritical water, the test duration and the stress level applied should be adequate to reach minimum strain rate or rupture. In the present work the strain rates were determined at different stages of creep, but for 316NG and 1.4970 steels the minimum strain rate was not reached and the environment comparison is based on primary creep only. For 1.4970 steel no effect of the environment was seen, and the stresses were clearly below yield, and for this material also the rolling direction may have an effect on the strain rate. For statistical reasons and to avoid false conclusions, the test matrix should contain repeated tests. For the test equipment modifications are planned to improve the quality of the strain data. For instance fluctuations in the room temperature should not be visible in the strain measurements; this effect was most likely due to the fact that the displacement measurement was done from the loading bar outside the SCW environment. Displacement should of course be measured directly from the specimen. Improvements have been scheduled to utilise the VTT pneumatic bellows technology in the SCW autoclave.

5. Conclusions

The materials issues are critical in developing new energy concepts with high operating temperatures and especially when neutron flux is involved. Some of the construction material issues in Gen IV development are concept specific, but many are still common to all or most of the concepts. There is much need for developing both materials and testing facilities to meet the Gen IV requirements on time schedules.

In this work three austenitic stainless steels have been tested in supercritical water at 650°C. The test results are considered as initial reference data and as a base for further studies. The tests were conducted in VTT's supercritical water autoclave test facility. The measured strain rates for 316NG and 347H steels were 1.5–2.5 times higher in supercritical water than in inert, helium atmosphere.

For 1.4970 steel no impact on the measured strain-rate was found. The verification of these findings will need longer term and repeated tests. According to SEM observations, oxides were formed on all test materials. However, due to short exposure times, the forming oxide layer had no significant impact on the stress levels. In terms of oxidation, the 1.4970 steel suffered the least in supercritical water. The results suggest that the supercritical water coolant has an impact on creep and that the standard reactor structural materials might not be sufficient for this environment. The SCW testing should also be extended to new candidate materials.

Acknowledgements

The financial support of Academy of Finland project SusEn NETNUC is gratefully acknowledged.

References

1. Helynen, S. et al. Energy conversion technologies. In: Energy Vision 2050. Edita; VTT. Helsinki; Espoo, 2009. Pp. 143–227. ISBN 978-951-37-5595-9.

2. Schulenberg, T. et al. Design status of the high performance light water reactor. Proceedings of 2008 16th Pacific Basin Nuclear Conference (16PBNC). Aomori, Japan, 13–18 October 2008. PaperID: P16P1203.

3. Bellissent-Funel, M.-C. Structure of supercritical water. Journal of Molecular Liquids, 2001. Vol. 90, No. 1–3, pp. 313–322.

4. Murty, K. L. & Charit, I. Structural materials for Gen-IV nuclear reactors: Challenges and opportunities. Journal of Nuclear Materials, 2008. Vol. 383, No. 1–2, pp. 189–195.

5. Rowcliffe, A. F. et al. Perspectives on radiation effects in nickel-base alloys for applications in advanced reactors. Journal of Nuclear Materials, 2009. Vol. 392, No. 2. pp. 341–352.

6. Penttilä, S. et al. Materials studies in EU-HPLWR Phase2 project. Proceedings of Baltica VIII 2010 − International Conference on Life Management and Maintenance for Power Plants. Helsinki–Stockholm−Helsinki, 18−20 May, 2010.

7. Toivonen, A. Testing equipment for the time to failure measurements on irradiated Chooz A core baffle specimens. Espoo: VTT, 2007. VTT Research Report VTT-R-10113-07.

8. Rissanen, L. Creep in Generation IV Nuclear Applications. Espoo: Aalto University, Master's thesis, 2010. 153 p.

9. Heikinheimo, L., Aaltonen, P. & Toivonen, A. Generation IV material issues. Proceedings of Baltica VII − International Conference on Life Management and Maintenance for Power Plants, Vol. 1. Helsinki–Stockholm–Helsinki, 12−14 June, 2007. Espoo: VTT, 2007. VTT Symposium 246. Pp. 212–223.

Application of risk-informed approach to the in-service inspection programme of Unit 1 of Loviisa NPP

Veijo Nikula, Ossi Hietanen and Pentti Kauppinen*
Fortum Ltd., Espoo, Finland
*VTT Technical Research Centre of Finland, Espoo, Finland

Abstract

The pre-service and in-service inspections (ISI) of the primary circuit components and piping of Loviisa NPP (VVER440) have been carried out since the start-up of the plant following the ISI-programme which is based on the requirements presented in the ASME Code Section XI. The latest 10 years' ISI programme was completed in 2007 and the preparation of the new ISI programme for following years was started in 2005. The basis for this new ISI programme is the new YVL-guideline issued in 2003 by the Finnish Radiation and Nuclear Safety Authority STUK. The guideline requires that utilities shall utilize risk-informed methodology when planning new ISI-programmes for safety class 1, 2, 3 and 4 as well as for non nuclear safety class classified piping systems.

The approach applied in drafting the ISI-programme was in principle the same as in ASME XI Supplement R, Method B but the approach was applied for the whole plant. The consequence assessment was based on the results of existing extensive probabilistic safety assessment (PSA) analysis according to the values for Conditional Core Damage Probability (CCDP) and Conditional Large Early Release Probability (CLERP).

The failure assessment was performed on a qualitative basis by a group of Fortum's experts familiar with Loviisa NPP associated materials integrity and in-service activities. The selection of elements for inspection was based on the risk categorization and identified degradation mechanisms of the piping section

in concern. In addition plant specific failure types and experience with their locations were taken into account. The operational history of the plant since 1977 and the experience gained through in-service inspections and maintenance work during the years passed gave valuable additional information for the selection of items to be inspected.

The new approach has brought several new features compared to the existing ISI programme. New systems, system portions and small diameter instrumentation piping of the primary systems were included in the programme.

1. Introduction

Loviisa 1 and 2 VVER 440 units started their operation in 1977 and 1981. Gross electrical power upgrading from original 440 MW to 510 MW was performed in 1996–1997. The original ISI-program for Safety Class 1 and 2 piping and components was based on the rules and guidelines stipulated in ASME Code Section XI.

The new Regulatory Guide in Finland, YVL 3.8 “Nuclear power plant pressure equipment. In-service inspection with non-destructive testing methods” requires that “In the drawing up of inspection programs for Safety Class 1, 2, 3 and 4 piping and Class EYT (nonnuclear) piping as well as in the development of inspection programs for operating plants, risk-informed methods shall be utilized to ascertain the inclusion in the inspection scope of those components posing the highest risk.”

Based on this requirement a plan for utilizing the risk informed methodology for Loviisa unit 1 piping was prepared and submitted to STUK for review and approval in 2005. STUK accepted the plan in 2006 and the preparation of the new risk-informed ISI-programme was started by the utility. STUK accepted new Risk-Informed In-Service Inspection program in 2009.

2. The new ISI programme, approach

The risk-informed selection process as described in ASME XI Supplement R, Method B was chosen as a basic approach for the new ISI program [1].

The plan for the new inspection program started from the following premises:

- The scope of the risk-informed inspection program evaluation will cover the whole plant, not only Safety Class 1 and 2 piping as the existing ASME ISI program.

- System risk assessments will be based on the existing extensive PSA model and the failure consequences to other systems are considered as they are taken into account in the PSA model.
- As selection criteria for the consequence assessment and classification of the systems (categorization/segmentation) Conditional Core Damage Probability (CCDP) and Conditional Large Early Release Probability (CLERP) will be used.
- Failure assessments will be performed on the qualitative basis by the panel of the company experts familiar with Loviisa NPP associated materials integrity and in-service activities.
- Risk informed inspection program will be focused on the piping only.

Methodology for determining the Risk Categories of the segments and segment portions is presented schematically in Figure 1.

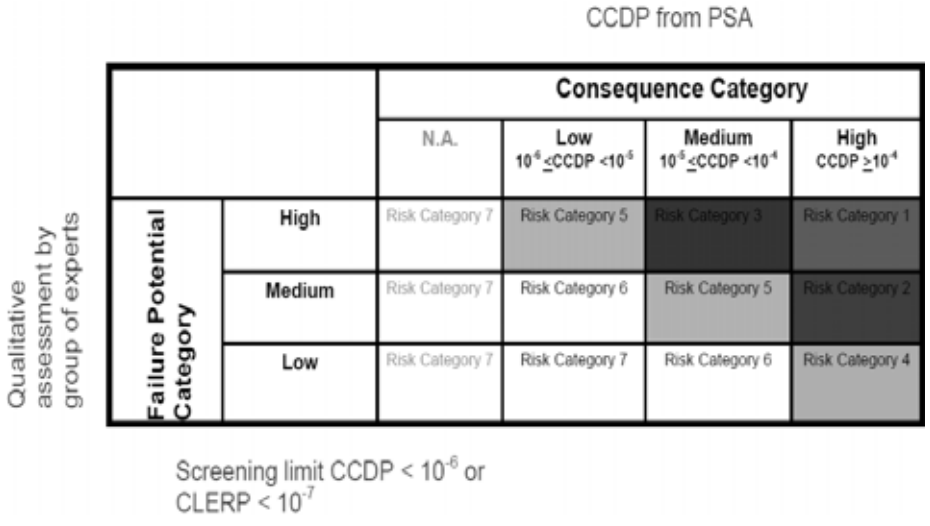

Figure 1. Risk categorization applied for unit 1 of Loviisa NPP.

3. Consequence categorization

A detailed consequence and failure assessment of all piping segments of the plant would need an unreasonable large amount of work. The first screening and selection of the piping segments was made on the basis of the existing PSA, which covers internal and external events and full, low and non power states.

The PSA was judged to be comprehensive and detailed enough for this work, because the consequences of different kinds of leakages have been studied in the flood and internal event PSA. The flood PSA covers leakages that submerge equipment in large areas causing an initiating event and also failing safety components that would be needed in case of such an initiating event. The internal event PSA covers small leakages and water and steam jets causing locally wet single electric equipment.

The work was focused on such systems and piping segments where failures can cause core damage with a probability larger than 10^{-6} or a large early release with a probability larger than 10^{-7}. The other systems and piping have only minor effect on the core damage risk and were screened out. The ratio between these probabilities was selected to be 10 because such a ratio has been used in other safety related decision making at the plant.

Piping within a system is grouped into segments of common failure consequences for consequence categorisation. Then CCDP, on the condition that the piping segment is leaking, is estimated on the basis of the most important leakage size, which is not necessarily a complete rupture of the pipe. Indirect effects of the leak are taken into account. If the leakage cause an initiating event its CCDP is immediately apparent from the PSA results.

If the leakage does not cause an initiating event, but it degrades or fails a system essential to plant safety, the CCDP is estimated from

$$CCDP = 1 - \exp(-CCDF \cdot t),$$

where,

CCDF = Conditional Core Damage Frequency, i.e. the frequency of challenge or the frequency of initiating events that require the system operation,

t = the exposure time that the pipe failure or its consequences can exist. It is the time the system would be unavailable before the plant is changed to a different mode in which the failed system's function is no longer required, the failure is recovered, or other compensatory action is taken.

If the pipe failure can cause both an initiating event and loss of safety important components needed in another initiating event, those effects are added together. CLERP is estimated in the same way.

Pipe segments that exceed the screening level of CCDP = 10^{-6} or CLERP = 10^{-7} are divided into three categories on the basis of their CCDP or CLERP values:

Low: $1 \cdot 10^{-6} \leq$ CCDP $< 1 \cdot 10^{-5}$,
Medium: $1 \cdot 10^{-5} \leq$ CCDP $< 1 \cdot 10^{-4}$ and
High: CCDP $\geq 1 \cdot 10^{-4}$.

The high limit value was selected to be the same as in the ASME XI Supplement R, as stipulated by STUK in its review of the methodology. The CLERP limits are one order of magnitude lower than the CCDP limits. All those pipe segments that have not been screened out are further studied for failure potential categorization.

4. Failure potential categorization

It was decided that failure potential categorization will be performed on the qualitative basis due to the fact that there were not yet available reliable tools, like SRMs (Structural Reliable Model), for all the potential failure mechanisms that currently affect nuclear power plants. On the other hand, there were long operation histories from both units, experiences with failures from own plant and other VVER-plants and experience with similar work during many years related to PLIM (Plant Life Management).

For determination of the potential failure mechanisms at Loviisa Unit 1 systems of the plant were divided in three parts:

- structures and components in contact with primary coolant
- secondary circuit systems
- seawater cooled systems.

The potential failure mechanisms for the systems in contact with primary and secondary water are presented in Figures 2 and 3.

In the seawater systems failure mechanisms vary depending on piping materials and coatings applied. A usage factor is used as a classification parameter in case fatigue analysis has been performed. Fatigue analysis is not, however, performed for the most of the systems.

Cyclic temperature changes due to thermal cycling and striping are used as a qualitative classification parameter for thermal fatigue. Mechanical fatigue including vibrations is also considered. Other possible cyclic loadings are evaluated case by case.

If the validity of the LBB concept can be justified, it is allowed to lower the determined failure classification. In this case the reliability of existing leak detection system should be considered.

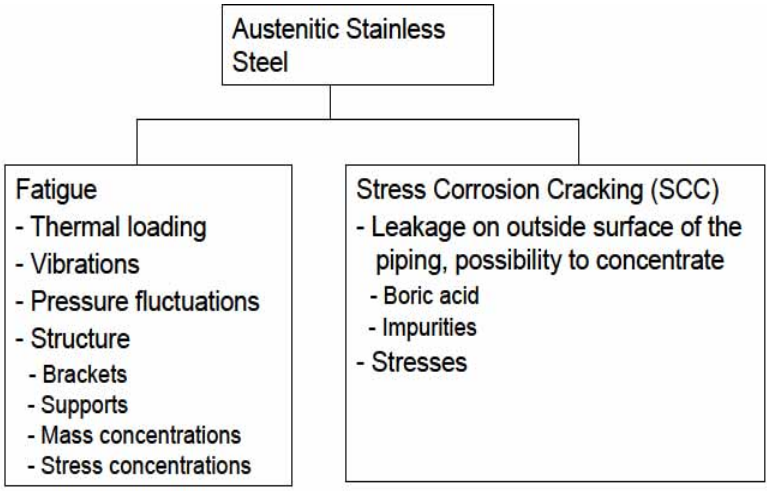

Figure 2. Potential failure mechanisms for the piping and components in contact with primary water.

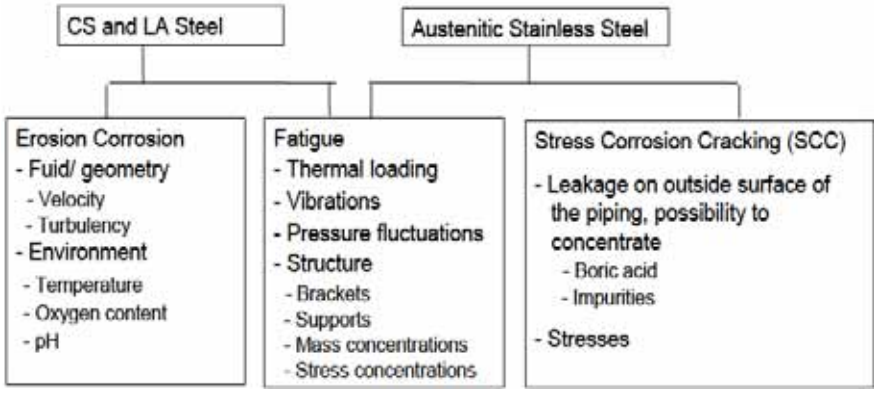

Figure 3. Potential failure mechanisms for the piping and components in contact with secondary water.

The most important secondary systems at Unit 1 have been modelled on the computer software predicting wall thinning of the piping. Predicted wall thinning is used as a failure classification criterion for the systems modelled.

Parameters affecting erosion corrosion like pH, temperature, geometry and material are used as classification criteria for those systems which are not modelled.

SCC is considered to be a potential failure mechanism only in case of leakage or wetting of the outside surface of the piping.

5. Comparison of the new risk informed ISI program with the previous deterministic program

The new Risk Informed approach has brought several new features compared to the existing ISI program. New aspects can be seen in the scope of new program:

- Many totally new systems and new portions of the systems of the existing program are included.
- Small diameter instrumentation piping of the primary systems to be inspected.
- Consequence differences of parallel redundant safety system and system portions can often be discovered (mostly due to fire and flood).

The new Risk Informed ISI program includes a wide range of different inspection objects with different degradation mechanisms and inspection targets. This is managed by separate programs.

- The systems with postulated cracking failures are included into Risk Informed ISI program. The inspection system (procedure, personnel, equipment) shall be qualified according to safety guide YVL 3.8.
- The systems with erosion corrosion, corrosion and outside surface failures are included in the piping condition monitoring program. The Inspection Company shall hold an EN accreditation and NDE examiners shall be qualified to level 2 of EN 473.
- The systems with possible impact of outside failures and leakages (typically small size piping) are included into the “walk down” program of the power plant with typical VT-2 and VT-3 visual examination.

6. NDE aspects to be considered in the risk-informed ISI programme

Changing the in-service inspection program of a nuclear power plant after 30 years of operation is not a straightforward task but several factors affecting the program have to be separately considered.

For the new inspection items that are included in the new programme no formal pre-service inspection has been made. Even though several manufacturing inspections have been made years ago the inspection technique has been different and is not comparable with today's technique. In practice the first inservice inspection is now at the same time the preservice inspection. If necessary, the old inspection data can be reviewed from the archives but this is not made routinely.

In some cases the inspection technique is changing based on the detailed assessment of possible failure mechanisms. Therefore the applicability of old inspection procedures has to be assessed case by case. In this connection the accessibility of the inspection item, its geometry, surface condition etc. have to be reassessed.

After 30 years' operation the radiation level in the inspection environment is known and can be taken into account when planning the practical performance of inspections. In some cases mechanization of inspection may be necessary due to the high dose-rate or some other restrictions.

7. Experience gained in the inservice inspections carried out in 2008−2009

The new RI-ISI-programme has been applied in the inservice inspections carried out at Loviisa NPP unit 1 in 2008 and 2009. So far no remarkable change has been noticed in the overall performance of ISI but some observations can be made.

It is worth mentioning that the current program covers the whole plant, not only the systems classified in safety-classes 1 and 2. This has caused some problems due to the fact that acceptance criteria for components belonging to safety classes 3 and 4 are not presented in the ASME Code. Thus other criteria had to be defined to specify the acceptable sizes of flaws. On the other hand, so far there are no totally new inspection items but some inspections that are now part of ISI have been performed in the past as a part of normal condition

monitoring. Therefore there has not been any remarkable change in the number of inspections performed during the annual shutdown. Consequently, the total radiation exposure of inspection personnel has not decreased. However, it is foreseen that the doses will be decreasing in the future due to the better focussing and timing of inspections. The most important benefit that is expected from the new RI-ISI-program is the improvement of plant safety when more effort in ISI is placed on inspection items that are most important from the safety point of view.

8. Conclusions

In the in-service inspections of Loviisa NPP unit 1 the deterministic inspection programme based on the requirements presented in the ASME Code Section XI has been applied since the start-up of the reactor in 1977.

In 2008 a new Risk-Informed ISI programme was taken into use. In the preparation of the new ISI-program a lot of work had to be performed by several experts on PSA, NDE, plant design, condition monitoring etc. Finally, the draft programme was thoroughly reviewed and discussed by an expert panel formed by experts of Fortum, TVO and VTT. STUK participated in the work as an observer.

In safety classes 1 and 2 the scope of inspections was not drastically changed from the previous program and the major changes where in safety classes 3 and 4. The total number of annual inspections remained almost the same even though some inspections were in the past not classified as in-service inspections.

It is expected that in future the radiation dose of inspection personnel will be reduced when inspections are better focussed on most important items and less important items are inspected at longer intervals. The main target of changing the ISI program was to improve the safety of the plant. The future will show how well this target has been achieved.

Reference

1. Hietanen, O., Jänkälä, K., Bergroth, N., Paussu, R. & Nikula, V. Risk-informed methodology of new ISI program for unit 1 of Loviisa NPP. 6th International Conference on NDE Relation to Structural Integrity for Nuclear and Pressurized Components. Budapest, 2007.

Probabilistic life assessment of steel components used in power plants

Milan Holický and Jana Marková
Czech Technical University in Prague
Prague, Czech Republic

Abstract

Presented life assessment of steel components used in power plants is based on probabilistic methods of the theory of reliability accepted in the International standards ISO 9324, 13822 and ISO 13823. An example of quick-closing valves in a selected hydroelectric power plant illustrates general principles of the reliability and life assessment of steel components for a given model of corrosion. It appears that the probabilistic methods provide rational background information for assessing remaining working life of the components and planning their regular maintenance. The required target reliability level is a key question that remains still open.

1. Introduction

Probabilistic methods for the assessment of reliability and working life of existing structures are currently of a great interest of experts, and wide range of undertakings. That is why two new international documents (ISO 13822 [1] for the basis of design of existing structures and ISO 13823 [2] for durability design) are based on probabilistic methods. These documents were developed considering the general probabilistic principles of the international standard ISO 2394 [3], the European document EN 1990 [4], documents of CEB [5], RILEM [6], fib [7] and research studies [8, 9, 11, 12].

The new international document ISO 13822 [1] for the basis of design of existing structures is a material independent document that has been already

implemented into the systems of national standards. The document [1] was implemented in the Czech Republic together with developed six National Annexes facilitating operational applications. It is expected that the document will be used for the reliability assessment of various types of existing structures including structural members used in different power plants.

The paper describes general probabilistic methods for the durability assessment of existing components of power-producing facilities and their application on assessment of remaining working life of the quick-closing valves in hydroelectric power plant.

2. General requirements

The reliability requirements for existing structures as well as for new ones may be expressed in terms of the failure probability P_f or reliability index β. The relationship between the both reliability indices may be expressed as

$$\beta = \Phi^{-1}(P_f) \tag{1}$$

where $\Phi(.)$ is a standardised normal distribution function. The following condition is required

$$P_f \leq P_{ft} \text{ or } \beta \geq \beta_t \tag{2}$$

where P_{ft} and β_t are the target values of the failure probability and reliability index given in ISO 13822 [1]. Both quantities the failure probability P_f and reliability index β are equivalent measures of structural reliability. However, the reliability index β is preferably used in common engineering practice as its values are within a comfortable range from 0 to about 6.

The target reliability level which should be used for the verification of existing structures may be based on probabilistic optimization taking into account malfunctioning costs and costs required for increasing the reliability. In general the concept of the probabilistic risks optimisation may be applied. The recommended values of the target reliability index β_t for verification of various limit states given in the document [1] are illustrated in Table 1.

Table 1. Recommended values of the target reliability index β_t according to ISO 13822 [1].

Limit states	**Target reliability index β_t**
Serviceability limit states – irreversible	1.5
Fatigue limit state	
– can be inspected	2.3
– cannot be inspected	3.1
Ultimate limit states with	
– very low failure consequences	2.3
– low failure consequences	3.1
– medium failure consequences	3.8
– high failure consequences	4.3

It should be noted that the target reliability indices depending on the consequences of failure and the relative costs of safe design are provided in ISO 2394 [3].

3. Verification of quick-closing valves

The general requirements for the assessment of structural serviceability were applied for the reliability analysis of many years safely running quick-closing steel valves in selected power-plant. The quick-closing valves were old about 50 years. The probabilistic methods of the theory of structural reliability given in document [1] are applied for the specification of the reliability index β and the failure probability P_f.

It is assumed that the time-dependent depth of corrosion $d_{corr}(t)$ in the steel cover plate of quick-closing valves may be estimated on the basis of the relationship

$$d_{corr}(t) = A\, t^{B} \tag{3}$$

where A and B are the parameters of analytical model, which are considered for parameter A in ranges from 0.03 to 0.13 and for parameter B from 0.6 to 0.7 [12,13]. It may be assumed here for non-uniform corrosion

$$A = 0.06 \text{ mm a } B = 0.7 \tag{4}$$

based on the results of inspection of the actual state of steel quick-closing valves.

Figure 1. Deterioration of a steel cover plate of quick-closing valves.

It is assumed that the steel cover plate of quick-closing valves (old about 50 years) is gradually deteriorating due to non-uniform corrosion with average one-side decrease up to 1 mm and about 30% probability of simultaneous weakening at opposite side of the cover plate. Therefore, the model of corrosion introduced in expression (3) considering parameters in expression (4) leads after 50 years to actual average depth of corrosion of 1.3 mm.

The ultimate limit state is expressed as the difference $\Delta M(t)$ of the time-dependent resistance moment $M_R(t)$ and the bending moment M_E due to the water pressure q:

$$\Delta M(t) = \xi_R b\,(d - 1.33 d_{\mathrm{corr}}(t))^2 f_y/4 - \delta q L^2/12 \qquad (5)$$

The theoretical models of all variables are listed in Table 2. Some of the basic variables entering expression (5) are assumed to be deterministic values denoted DET (steel cover plate of span L, width b, parameter of corrosion B and dynamic enhancement factor δ) while the others are considered as random variables having normal (N) or lognormal (LN) distributions.

The reliability of the steel cover plate decreases in time due to the corrosion leading to reduction of its thickness $d_{corr}(t)$. The value of the target reliability index $\beta(80) = \beta_t = 3.7$ for considered 80 year working life of the cover plate is specified on the basis of required reliability index for a reference period of one year $\beta(1) = 4.7$ given as

$$\Phi(\beta(80)) = (\Phi(\beta(1))^{80} = (\Phi(4.7))^{80} = \Phi(3.7) \quad (6)$$

Table 2. Probabilistic models of basic variables.

Basic variable	**Symbol**	**Distr.**	**Mea μ**	**CoV V**
Yield strength [MPa]	f_y	LN	280	0.08
Plate span [m]	L	DET	0.75	-
Plate thickness [m]	d	N	0.018	0.03
Plate width [m]	b	DET	1	-
Parameter A [mm]	A	N	0.06	0.10
Parameter B	B	DET	0.7	-
Water pressure [kN/m^2]	q	N	157.6	0.1
Dynamic factor	δ	DET	1.3	-
Resistance uncertainty	ξ_R	DET	0.85	-

The probabilistic reliability assessment of the steel cover plate is based on own software tool developed in software Mathcad.

Initial reliability of the cover plate non-affected by corrosion (reliability index $\beta = 5.2$ corresponding to failure probability $P_F = 9.4 \times 10^{-8}$) satisfies the target reliability level for considered reference period of 80 let ($\beta_t = 3.7$). For one-side corrosion of 1 mm and cover plate 53 years old, the reliability index decreases to $\beta = 4$ (failure probability $P_F = 3.6 \times 10^{-5}$), see Figure 2.

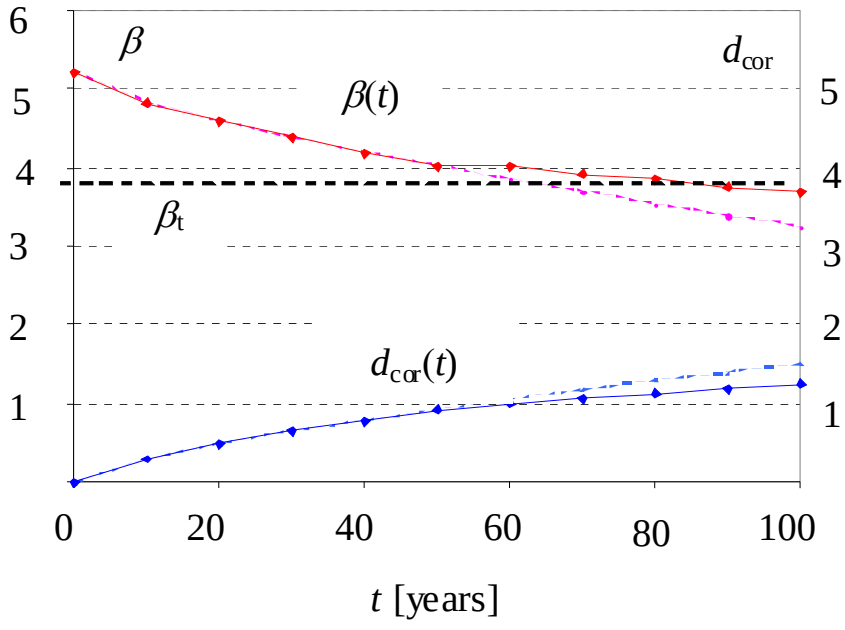

Figure 2. Time-dependent reliability index β(t) and one-side corrosion depth $d_{corr}(t)$.

When a more effective protection level of cover-plate is provided then lower rate of corrosion may be considered (e.g. parameter B = 0.6 only). New estimation of the residual working life is illustrated in Figure 3 leading to extended residual working life from 70 years to 90 years. It appears that the working life of the cover plate may be estimated to approximately 70 years when the reliability index β(t) decreases to 3.7. Thus, the residual working life of a cover plate is considered to be about 20 years.

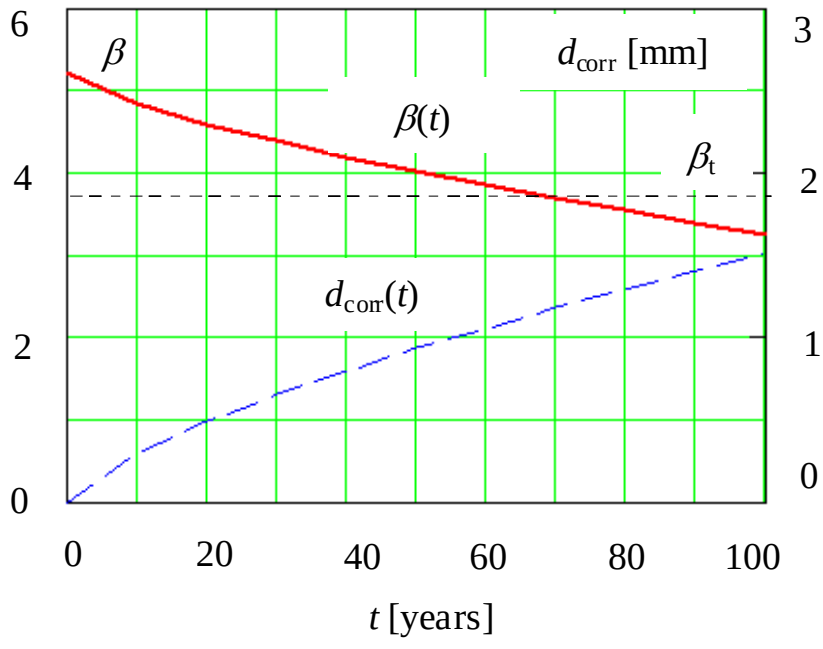

Figure 3. Time-dependent reliability index β(t) and one-side corrosion depth $d_{corr}(t)$ for considered increased maintenance.

4. Concluding remarks

The probabilistic assessment of existing structures provides a rational tool to assess reliability and remaining working life of the components used in power plants. The assessment further enables to plan regular maintenance and to estimate required economic consequences. Presented example of a given quick-closing valve indicates that its residual life-time is about 20 years provided that regular maintenance will be made. Protective layers should be renovated regularly inspected when the reliability index would decrease below the target reliability index 3.7 (estimated to 20 years). A new reliability assessment of cover plates should be made on the basis of updated material characteristic and corrosion models. However, the required target reliability level is a key question that remains still open. In particular cases it can be solved taking into account malfunctioning costs and cost required for increasing reliability of the structural member.

Acknowledgements

Support of the GACR project No. 103/09/0693 Assessment of Safety and Risks is acknowledged.

References

1. ISO 13822, 2001. Bases for design of structures – Assessment of existing structures, ISO, pp. 35.

2. ISO 13823, 2008. General principles on the design of structures for durability, ISO, pp. 39.

3. ISO 2394, 1998. General Principles on reliability for structures, ISO, pp. 73.

4. EN 1990, 2002. Basis of structural design, CEN, pp. 87.

5. CEB Bulletin d'Information No. 238, 1997. New Approach to Durability Design, An example for carbonation induced corrosion, pp. 152.

6. RILEM Report 14. Durability Design of Concrete Structures. Edited by Sarja A. and Vesikari E. Taylor & Francis, 2007, pp. 165.

7. Fib Bulletin 34, 2005. Model Code for Service Life Design.

8. Holický, M. & Marková, J. Design of Structures for Durability. In: Challenges in Transport and Communication, Pardubice, 2006, pp.1063–1068.

9. Holický, M. & Marková, J. Probabilistic Design of Structures for Durability, In: ESREL 07. Taylor & Francis, Balkema, 2007. Pp. 1757–1762.

10. Holický, M. Reliability Analysis for Structural Design, Stellenbosch, 2009, pp. 199. ISBN 978-1-920338-11-4.

11. Frangopol, D. M. & Estes, A. C. System Reliability for Condition Evaluation of Bridges. In: Evaluation of Existing Steel and Composite Bridges, IABSE Workshop, Lausanne, 1997. Pp. 47–56.

12. Val, V. D., Stewart, M. G. & Melchers, R. E. Effects of Reinforcement Corrosion on Reliability of Highway Bridges. Engineering Structures, 1998. Vol. 20, No. 11, pp. 1010–1019.

Risk-informed in-service inspections of nuclear power plants: European activities

Kaisa Simola
VTT Technical Research Centre of Finland
Espoo, Finland

Luca Gandossi
European Commission Joint Research Centre, Institute for Energy
Petten, The Netherlands

Abstract

Risk-informed in-service inspection (RI-ISI) methods aim at enhancing ISI effectiveness by taking into account the risk importance of possible inspection sites. These methods are widely applied in US, but in Europe the situation is different, as there are many regulatory environments implying a variety of ISI codes and standards and national guidelines. The objective of the European Network for Inspection Qualification, ENIQ, is to co-ordinate and to manage at European level expertise and resources for the qualification of non-destructive inspection techniques and procedures primarily for the in-service inspection of nuclear components. ENIQ has established a Task Group on Risk (TGR) to work towards developing best practice for RI-ISI methodologies. TGR has published a European framework document for risk-informed in-service inspection, and the group has been working at producing more detailed recommended practices and discussion documents on several RI-ISI related issues. In addition, TGR has been active in initiating international projects, such as the JRC-OECD/NEA coordinated RI-ISI benchmark exercise (RISMET). This paper describes the activities and publications of TGR to date, and summarises the contents and main results of the RISMET RI-ISI benchmark exercise.

1. Introduction

Risk-informed in-service inspections (RI-ISI) at nuclear power plants aim at rational in-service inspection management by taking into account the results of plant-specific risk analyses in defining the inspection programme and focusing the inspections efforts to the most risk-significant locations. Ideally this could lead to improved safety and availability, reduced doses of radiation and reduced inspection costs.

RI-ISI methods are widely applied in US, where the US Nuclear Regulatory Commission has approved two methodologies as a valid alternative to ASME Section XI [1]. In Europe the situation is traditionally different, as there are as many regulatory environments as there are countries with nuclear power plants in operation, thus implying a variety of ISI codes and standards and national guidelines.

During the last years there has been a growing interest to move towards risk-informed approaches in several European countries. Usually, the US methodologies cannot be adopted as such, since they have been originally developed to the American regulatory environment. Thus, activities are ongoing both to develop own methodologies and to adapt the US methodologies to comply with national requirements. In this framework, European regulators and utilities have established working groups to discuss RI-ISI related issues, to identify common views, and to agree on recommendations and good practices. The Task Group on Risk (TGR) of the European Network for Inspection and Qualification (ENIQ) is a utility driven working group to address these RI-ISI related issues.

First, a brief introduction to RI-ISI at nuclear power plants is given. Second, the activities of the ENIQ TGR are described. Finally, an international RI-ISI benchmarking project is summarised.

2. RI-ISI for nuclear power plants

The purpose of risk-informed in-service inspections (RI-ISI) is to achieve a balanced in-service inspection management by taking into account the results of risk analyses in the definition of the inspection programme. When compared to traditional deterministic ISI programmes, the main difference is the use of plant specific probabilistic safety assessment (PSA) results in determining the risk-importance of components.

When moving from a deterministic ISI programme to a RI-ISI programme, the process typically leads to a proposal with relaxation of inspection of primary circuit and possibly extending the scope of inspections to systems that have earlier been excluded from mandatory inspection programmes. Ideally the optimisation of ISI can lead to improved safety and availability, reduced radiation doses and reduced inspection costs.

A RI-ISI process consists of following main steps:

- Definition of the scope of the RI-ISI programme, collection and analysis of input data
- Identification and evaluation of piping failure consequences
- Identification and evaluation of piping failure potential
- Risk ranking
- Definition of the new inspection programme

These steps are illustrated in Figure 1.

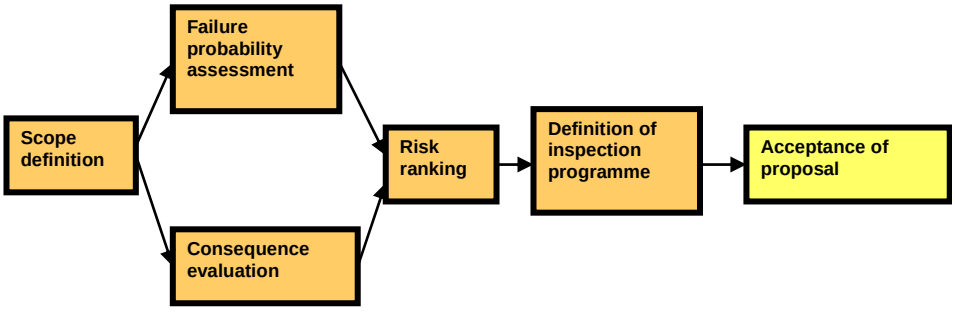

Figure 1. Phases of a RI-ISI process.

When compared to risk-based inspection (RBI) procedures in non-nuclear industry, one could say that the basic steps of the analyses are similar. However, some important differences in nuclear and non-nuclear applications can be pointed out. For instance the consequence measures are different: while in RBI the consequences are measured as fatalities, applications at nuclear power plants use the conditional core damage and large early release of radioactive material as consequence measures. There are also differences in the degradation mechanisms considered.

3. European Network for Inspection and Qualification, Task Group on Risk

The European Network for Inspection and Qualification, ENIQ, was established in 1992 in response to an increasing recognition of the importance of qualification of non-destructive inspection for in-service inspection of nuclear power plants. Driven by European nuclear utilities and managed by the European Commission's Joint Research Centre (JRC) in Petten, the ENIQ network was set up so that the available resources and expertise could be pooled at European level. ENIQ has a Steering Committee consisting of members from EU countries with nuclear plants, and for Switzerland.

In 1996, ENIQ recognised the importance of addressing at European level the issue of optimising inspection strategies on the basis of risk, and a task group was set up with an objective to harmonise the different activities on RI-ISI for nuclear reactor safety and to develop a common European approach to RI-ISI. Currently the ENIQ Task Group on Risk (TGR) has about 20 members representing European nuclear utilities, research organisations and consultants, as well as representatives from the US and Canadian nuclear industry.

In 2005 TGR published the European framework document for risk-informed in-service inspection [2]. The document is intended to serve as guidelines for both developing own RI-ISI approaches and using or adapting already established approaches to European environment taking into account utility-specific characteristics and national regulatory requirements.

The RI-ISI framework document provides general principles on the RI-ISI process, but does not go in details in RI-ISI implementation. After the publication of this document, the TGR has been working on producing more detailed Recommended Practices (RP) and discussion documents on several RI-ISI related issues. In addition, the TGR has initiated two separate projects that required larger resources and involved external participants as well. Because the benchmarking of various RI-ISI methodologies was identified as one of TGR's top priorities, a project was successfully launched in co-operation with JRC and the OECD Nuclear Energy Agency (NEA). Further, a project on the relationship between RI-ISI and inspection qualification was also organised separately and funded by a group of European nuclear power utilities.

3.1 European Framework Document

The European framework document for risk-informed in-service inspection [2] provides guidance for developing and applying RI-ISI methodologies. Whilst providing a consistent European approach for RI-ISI, the framework document allows a certain degree of flexibility in order to account for the range of different utility-specific characteristics and national regulatory requirements which are prevalent in Europe.

Within the terms of advice provided in the framework document it is possible either to develop new approaches to RI-ISI or adapt established approaches for application in a European environment. Both quantitative and semi-quantitative approaches to RI-ISI are addressed, and key principles of RI-ISI are identified. Purely qualitative methods that do not use either Probabilistic Safety Assessment (PSA) to estimate consequences of failure, or any form of structural assessment to determine probability of failure, are not considered.

Risk assessment forms a keystone for any RI-ISI methodology, and advice is provided regarding the assessment of probability of failure, consequences of failure and how these provide the basis for risk characterisation and ranking. Other important aspects of RI-ISI, such as the roles/responsibilities of personnel and the requirements for documentation and archiving of an RI-ISI program are also addressed.

The framework document was developed specifically to address RI-ISI planning in the nuclear industry within Europe, and was envisaged to be primarily applied to piping systems. However, application of the guidance to non-nuclear plant, or to components other than piping (for example the reactor pressure vessel), was not precluded. The scope of the framework document is limited to setting out the general principles which define good practice for RI-ISI in Europe. Other documents providing more detailed advice concerning particular aspects of RI-ISI are also published by TGR. These are described in the following.

3.2 Other documents

TGR has published reports on following topics: The role of ISI within the philosophy of defence-in-depth; The verification and validation of structural reliability models to be used in RI-ISI programs; The use of expert panels in RI-ISI; The applicability of RI-ISI to the reactor pressure vessel; and RI-ISI updating.

3.2.1 Guidelines for the validation and verification structural reliability models

The purpose of a structural reliability model (SRM) is to calculate failure probabilities of piping or other components. These calculations are generally carried out by means of software-based probabilistic fracture mechanics techniques.

To support the application of SRMs in RI-ISI programs, TGR published in 2007 the ENIQ Recommended Practice document "Verification and validation of structural reliability models, and associated software to be used in RI-ISI programmes" [3]. The Recommended Practice document is largely based on earlier work performed as part of the NURBIM project [4], which sought to define best practice methodologies and acceptance criteria for risk-based analysis in Europe.

The document provides guidance regarding various aspects including quality assurance of computer programs, principles and assumptions associated with the modelling, experimental validation, comparison with international industrial data, benchmarking with other SRMs, and the role of expert judgment. The Recommended Practice document concludes that it is essential to verify and validate any SRMs used in the evaluation of failure probabilities for RI-ISI, and in order to achieve this the following criteria should be met:

1. SRM computer programs should be verified. This should be supported by suitable quality assurance documentation.
2. The scope, analytical assumptions and limitations of the modelling capability should be clearly defined.
3. The analytical assumptions should be well grounded and based on theory that is accepted as representative of the situations considered by the SRM.
4. The model should be capable of reproducing the data on which its analytical assumptions are based. Examples should be provided to demonstrate general agreement with available experimental data.
5. SRM results should be validated by comparison with relevant world or field data.

6. A SRM should be benchmarked against other models with similar scope or applicability. The reasons for any significant differences which are identified should be justified.
7. The choice of statistical distributions for input to the SRM should be justified. Sensitivity analyses should be performed to assess the influence of input parameters and choice of statistical distributions.

In addition to the criteria listed above, the importance of regular reviews to update validation of SRM software is emphasised.

3.2.2 Discussion document on defence-in-depth

Defence-in-depth, which may be expressed in simple terms as the provision of several levels of protection against potentially significant faults or failures, is a well established concept in the nuclear industry.

The "ENIQ TGR discussion document on the role of in-service inspection within the philosophy of defence in depth" [5], published in 2007, provides a basis for discussion on how defence-in-depth concepts may be applied within an RI-ISI framework. It is acknowledged that an RI-ISI program should be evaluated to ensure that defence-in-depth is maintained. Several levels of defence-in-depth are identified for consideration within the context of RI-ISI, as follows:

1. Prevention of abnormal operation and failures (conservative, robust design, high-quality performance).
2. Control of abnormal operation and detection of failures (supervision, surveillance).
3. Control of accident within the design basis (engineered safety features/systems and accident management).
4. Control of severe plant conditions, prevention of accident progression and mitigation of the consequences of severe accidents.
5. Mitigation of radiological consequences of significant releases of radioactive materials (offsite emergency response).

The document discusses the role of the RI-ISI program and associated activities, within the entire reactor safety program, with particular focus on the defence-in-depth philosophy for reactor safety. It also addresses the role of ISI within the different levels of defence-in-depth. The potential for an RI-ISI program to

contribute to the control of abnormal operation and detection of failures is identified, as is the potential for PSA to effectively identify shortfalls in other levels of defence-in-depth.

The tools and processes used to determine pipe break frequencies are discussed in some detail, providing a perspective on how pipe break frequency may influence assessment of consequences of failure (expressed in terms of core damage frequency).

The discussion document identifies several defence-in-depth objectives for an RI-ISI program, as follows:

- The RI-ISI program should seek to confirm the validity of pipe breaks frequencies applied the in PSA and Final Safety Analysis reports,
- The RI-ISI program should focus on risk-dominant piping and welds, which are identified through extensive use of PSA studies,
- Defence-in-depth considerations can help to optimise the RI-ISI program, both in economic terms and in terms of doses to workers, for welds identified as high probability and low consequences of failure,
- Based on recorded operating experience, the RI-ISI program should seek to identify new failure mechanisms in piping with very low failure frequencies.

3.2.3 Guidelines on expert panels

The European framework document for risk-informed in-service inspection [2] recommends the use of expert panels to review the selection of safety-significant sites before the inspection program is finalised. However, more detailed guidance is not provided. The development of guidelines for the expert panel process in this area was also recommended by the Nuclear Regulatory Working Group, who explicitly advocates the use of expert panels in its report on the regulatory experience of RI-ISI [6].

In 2008, ENIQ TGR published the Recommended Practice “Guidance on expert panels in RI-ISI” [7]. The report is intended to assist a user involved in a RI-ISI application on how to form, prepare, conduct and document an expert panel whose final goal is making decisions concerning the inclusion or exclusion of sites from the risk-informed inspection program.

The role and composition of an expert panel may vary, and may be an integral part of the RI-ISI team or an independent body. The role of the expert panel will generally be to conduct a systematic review of the risk analyses and to check that the multi-disciplinary information and expertise supporting the decision-making process is well balanced. Particular subjects for review may include failure probability and consequence analyses, or a review of the risk ranking. The guidance provided in the document mainly concentrates on a review of the risk ranking, but notes that a similar approach can also be adopted for reviewing the final selection of inspection sites, periodic re-assessments and the impact of PSA updates on the RI-ISI program.

The report gives recommendations on the composition of an expert panel. Different roles are identified, among which those of (1) the Decision maker; (2) the RI-ISI Project Leader; (3) the Panel Leader; (4) the Technical experts and (5) the Technical secretary. For each role, the RP identifies the main responsibilities.

Guidance is also given regarding the planning and preparation of the expert panel, for instance regarding the training given to the participants, and the conduction of the expert panel sessions. The RP states that decisions taken by the expert panel should be reached by consensus, but if a unanimous decision cannot be reached, the panel should identify the reasons behind the differing opinions, and whenever possible, the panel should take appropriate measures (for instance, obtain additional information, request additional analyses, etc.) to facilitate a convergence of the differing views.

The report emphasises the importance of a thorough record keeping of the panel discussions and the final decisions. In particular those instances when a consensus was not reached, and reasons why, should be well documented.

3.2.4 Discussion document on RI-ISI for reactor pressure vessels

The European In terms of plant safety, the reactor pressure vessel (RPV) is the most critical pressure boundary component in light water reactors. The RPV represents a barrier against fission-product release, supports control rods and vessel internals, provides coolant around the reactor core and directs reactor coolant to the steam generator (in a PWR) or steam to the turbine (in a BWR).

The European framework document for RI-ISI [2] focuses on piping, but it does not exclude its application to the RPV. In 2008, ENIQ TGR published the “Discussion document on the role of in-service inspection of the reactor pressure vessel” [8], which discusses the application of an RI-ISI strategy to the RPV.

There are few known damage mechanisms affecting the RPV, and for many locations there are no identified damage mechanisms. Thus, when considering a structural element of the RPV, such as a weld, it is typically concluded that the consequence of a structural failure are high and the probability of such a failure is low. If an inspection program were to be specified solely on the basis of risk, this may suggest that the RPV should be excluded from an inspection program. However, it is generally the case that stringent inspection requirements are maintained for the RPV due to the potentially high consequences of failure.

The framework document [2] acknowledges the special situation of inspection sites with a high consequence and a low probability of failure and recognises that a problem of confidence can arise if the component's probability of failure is well below the area for which there is any practical experience. It states that any inspection in this area is intended to provide additional confidence in the assessed probability of failure and provides an element of conceptual defence-in-depth.

Based on experience reported in the discussion document, the following conclusions are drawn:

- The consequences of failure of the RPV are high, but the failure probability is low. Accordingly, special consideration should be given when identifying inspection requirements for the RPV. As part of the second level of defence-in-depth, ISI of the RPV should be used where it gives as large a benefit as possible to reduce the risk for rupture or leakage.
- RI-ISI as outlined in the European framework document [2] is applicable for planning and performing in-service inspection of the RPV.
- Experience based on known damage mechanisms, the probability of failure and the capability of in-service inspection to reduce the probability of failure, clearly indicates that inspection effort should be aimed at relatively high-risk locations.

3.2.5 Discussion document on RI-ISI updating

The European framework document on RI-ISI [2] emphasises the process of keeping RI-ISI a living process, i.e. updated, and provides a brief discussion on the concept of living RI-ISI. An effective risk-informed inspection strategy requires the development of a feedback procedure to update the risk ranking

after plant changes are carried out or new relevant information is acquired. Further, the Nuclear Regulatory Working Group document [6] highlights the importance of performance monitoring and updating of a RI-ISI programme. In the US, a document on RI-ISI updating [9] provides several examples of plants having conducted updates to their RI-ISI programs. Based on these considerations, ENIQ TGR has developed a discussion document [10] with the intention of assisting a user involved in a RI-ISI application in how to maintain and update a RI-ISI program.

Risk ranking of piping is the most important of several aspects which may influence the risk-informed selection of inspection targets. Changes in risk importance can basically arise either from a change in the estimate of failure probability or of the consequence of the failure. The main issues having a potential influence on risk ranking are as follows:

- Plant modifications.
- Changes in operating and maintenance procedures.
- Changes in input information for failure probability and consequence evaluation, due to e.g. operating experience.
- Changes in models for failure probability and consequence evaluation.

The document discusses these subjects, as well as some PSA issues, RI-ISI updating cycle and documentation. The document also provides an overview of current ISI updating practices in the majority of EU member states having operating nuclear power plants.

4. International RI-ISI benchmark project

In 2005, the Joint Research Centre of the European Commission together with the Nuclear Energy Agency (NEA) of the OECD launched a project for benchmarking various RI-ISI methodologies, and this RISMET project was officially started in 2006. The objective of the project was to apply various RI-ISI methodologies, as well as the traditional deterministic ISI selection approach, to a set of piping systems in one nuclear power plant. The comparison and evaluation of the results would identify main differences in the approaches and the impact of chosen methodology to the resulting ISI programme.

Four systems from the Swedish Ringhals 4 pressurised water reactor (PWR) unit were selected for the benchmark exercise. Five RI-ISI methodologies and

the deterministic ASME Section XI approach were applied by teams composed of participating organisations having knowledge and experience in one or more RI-ISI methodologies. The results of applications were evaluated by teams composed of generalists and experts in specific areas of a RI-ISI process. Further specific regulatory aspects were considered by a team consisting of representatives of some nuclear regulatory bodies.

4.1 Scope of the benchmark

The benchmark was limited to include four systems at Ringhals 4 PWR unit (R4). Several criteria were identified for selecting systems to be included in the scope:

- All safety classes should be covered
- A variety of degradation mechanisms should be covered
- Good coverage of risk categories should be achieved
- Systems with a significant increase or decrease in the new inspection program (before/after applying RI-ISI) should be included
- Balance between initiating and mitigating systems should be ensured.

The systems selected for the benchmark exercise are presented in Table 1.

Table 1. Systems analysed in the RISMET benchmark.

System	Safety Class	Degradation mechanisms	Risk characteristics
Reactor Coolant System (313)	1	Low cycle fatigue, thermal stratification	High consequences, low failure probability
Residual Heat Removal System (321)	1&2	Vibration fatigue, thermal mixing points, cavitation	Medium consequences, high failure probability
Main Steam System (411)	2&4	Low cycle fatigue, steam hammer	Relatively high consequences, high failure probability
Condensate System (414)	4	Erosion corrosion, low cycle fatigue, thermal stratification, water hammer	Low consequences, high failure probability

For all these systems, Ringhals NPP provided for the application groups the necessary information for analysing the systems, e.g. system and process information and drawings, PSA results, and system operating and design information.

4.2 Applied methodologies

Altogether five RI-ISI approaches were included in the benchmark exercise. These were:

- Swedish regulatory requirements ("SKIFS")
- PWROG methodology
- PWROG methodology adapted to Swedish regulatory requirements ("PWROG Swedish")
- EPRI methodology
- Code Case N-716, EPRI "streamlined RI-ISI".

In addition, the deterministic ASME Section XI ISI selection approach was applied to the selected systems. Whilst it was possible to carry out full SKIFS, PWROG, and PWROG Swedish analyses, it was necessary to incorporate and acknowledge some limitations and assumptions in the application of the EPRI, CC N-716 and ASME Section XI methodologies.

The ISI program of R4 was based on the Swedish regulations, SKIFS [11]. In this approach the probability that degradation occurs in the specific component is described with a qualitative Damage Index. The Consequence Index is a qualitative measure for the probability that the degradation will result in core damage, damage of the reactor containment, release of radioactive material or other damages that may lead to injuries or health hazards. Inspection groups are determined on the basis of these indexes.

The PWROG methodology [12] is a quantitative RI-ISI approach. The failure consequences are evaluated with PSA, and the risk reduction worth (RRW) is used as the main importance measure to evaluate the safety significance of a piping segment. A probabilistic fracture mechanics code and Monte Carlo simulation are used to quantify failure probabilities of piping segments. The numerical output describes the relative estimate of the susceptibility of a piping segment to failure. The final ranking of piping safety significance is conducted by a plant expert panel which combines the PSA and engineering information.

The PWROG Swedish is an adaptation of the PWROG methodology to the Swedish regulatory environment. The approach follows the PWROG methodology in segmentation, failure probability and consequence analyses and initial risk ranking. Here also an expert panel is used to verify the initial risk ranking. In the phase of classifying and selecting inspection sites, the approach follows the Swedish SKIFS principles.

The EPRI methodology [13] is the most widely applied RI-ISI in the nuclear industry. Ping systems are divided into segments based both on the pipe rupture potential and its consequences. Each segment is placed onto the appropriate place on the EPRI Risk Characterization Matrix having three categories for degradation potential and four categories for consequence severity. The failure potential category is determined on the basis of identified degradation mechanism. The consequence category is determined by the conditional core damage probability (CCDP) and the conditional large early release probability (CLERP).

Code Case N-716 [14] is a streamlined process for implementing and maintaining RI-ISI, based upon lessons learned from numerous approved RI-ISI applications. The approach differs from the traditional approaches in two respects. First, the consequence assessment is not required. The consequence assessment has been replaced with a pre-determined set of high safety significant locations (e.g. reactor coolant system, break exclusion area) and a plant-specific assessment of the impact of pressure boundary failure using the plant PSA directly. Second, a partial scope application, which is allowed by previous RI-ISI approaches, is not allowed by Code Case N-716.

ASME Section XI [1] is the most commonly applied approach to define ISI programs, and is based on deterministic rules. The general philosophy of the ASME section XI aims at determining an inspection sample among the ASME classes 1, 2 and 3 piping (following the ASME section III rules). Volumetric non destructive examinations are proposed for ASME classes 1 and 2 whereas class 3 are only submitted to visual examinations. The sampling from classes 1 and 2 is kept well balanced by several requirements which drive the selection process among the overall scope.

4.3 Results of the study

The application results were evaluated by five groups focusing on the following issues: 1) Scope of application; 2) Failure Probability Analyses; 3) Consequence analyses; 4) Risk ranking, classification and selection of segments/sites to be

included in inspection programs; and 5) Regulatory aspects. The evaluation included the identification of differences in the RI-ISI applications, the analysis of the importance of identified differences, and the comparison between RI-ISI and “traditional” inspection programs.

4.3.1 Evaluation of the scope

In the evaluation of the scope of the ISI selection approach, attention was paid especially to the limitations and flexibility of the scope.

The SKIFS and ASME Section XI offer a pre-determined, fixed scope of application. The Code Case N-716 methodology allows only a full scope application. The EPRI and PWROG methodologies offer a range of scopes from very limited to full scope applications. The PWROG Swedish methodology scope of application is in principle the same as the PWROG methodology scope, but only full scope applications have been performed.

Changing the scope of application may impact the results of the RI-ISI programs for the PWROG and PWROG Swedish methodologies since a relative ranking system is utilised. For these methodologies, decreasing the scope of application typically results in an increase the number of inspections in the remaining systems. Changing the scope of application in the EPRI methodology does not impact the results within any given system or in the total program, because an absolute ranking process is used.

4.3.2 Evaluation of failure probability analyses

The objective of this evaluation group’s work was to contrast-and-compare the different technical approaches to pipe failure probability analysis that were used by the application groups. The evaluation addressed e.g. the explicit consideration of industry experience and plant-specific operating experience, quantitative assessment of pipe failure probability, structural failure mode(s) modelled, and verification and validation of methodology.

With some exceptions, a comparison of the EPRI and PWROG methodologies points to similar ranges of failure probabilities. The PWROG methodology appears to be more resource intensive than any of the other RI-ISI methodologies that are included in the RISMET scope of work. Respective topical report and implementation guidelines address the role and importance of service experience data in ensuring realistic results and as input to future RI-ISI program updates.

Within the scope of the PWROG Sweden application the explicit roles of the plant-specific and industry wide service experience data could not be assessed, however.

4.3.3 Evaluation of failure consequence analyses

The evaluation group reviewed the characteristics of various approaches concerning consequence analyses. Also conservatism and uncertainties in the PSA model were addressed.

The result from SKIFS methodology and the ASME method are independent of the PSA, and they include only safety classified piping systems. In the Code Case N-716 methodology, the consequence assessment is replaced with a pre-determined set of high safety significant (HSS) locations. Additionally, the PSA is used directly as a complementary measure to identify other welds as HSS.

A conclusion of the consequence assessment is that the PSA model should have a high degree of realism in those areas that are of importance for the risk evaluation. Conservatism, uncertainties or other weaknesses in the PSA may affect the risk ranking in RI-ISI methodologies. A check should be performed to avoid excessive conservatism in the PSA analyses. The assumptions made about the success criteria for the different initiating events, about safe condition (end state) for transients and about crediting operator actions are important.

4.3.4 Analysis of risk ranking and site selection

The main tasks of this evaluation group were to identify and analyse the differences in the process of risk ranking and inspection site selection, and in the results. The results were compared both qualitatively and quantitatively.

It was noted that all risk-informed approaches would result in significantly fewer inspections in the Reactor Coolant System than the ASME XI application. For the results of the Residual Heat Removal System, there are some significant differences in the ISI scope between the risk-informed applications, even if there is large agreement on the low safety significance of most of the segments. The SKIFS and CC N716 applications would result in only few inspections. In other applications, inspection needs are mainly driven by the high consequences. For the Main Steam System, there is generally a good accordance of the low safety significance of most of the segments.

In the Condensate System the main degradation mechanism is the flow accelerated corrosion (FAC). In practice FAC is excluded from the RI-ISI process in US, and the analysis only points to the plant's augmented programme which should be in line with the existing regulations. The system was however analysed in the Ringhals RI-ISI project, and some FAC susceptible piping is included in the Swedish regulatory ISI program.

4.3.5 Regulatory aspects

National nuclear safety authorities participating in the RI-ISI benchmark brought up regulatory aspects. Specific issues addressed in their evaluation were the scope of application, expert panels, inspection effectiveness and inspection intervals, and living RI-ISI programme.

Several issues for future research efforts were identified. In relation to the failure probability assessment, there is a need for consistent criteria to determine when a potential for a certain damage mechanism occurs; leak detection issues need further considerations; and more efforts should be devoted to further develop probabilistic models which better correlate to service experience data. Regarding the consequence assessment, it is noted that there are no detailed guidelines for how PSA analyses should be designed for the application of risk-informed inspection programmes. More and better information is needed regarding the efficiency of inspection for various NDE methods that are used for risk reduction. In this context it is also important to further explore the role of probabilistic methods to determine inspection intervals.

4.4 Conclusions of the benchmark

The variety in the scope of the benchmarked systems regarding the safety class, potential degradation mechanisms and pipe break consequences ensured a good coverage of issues for a comparative study. The risk-informed methodologies have some significant differences, and result in slightly different risk ranking and selection of inspection sites. However, the risk impact of these differences seems to be small.

Risk-informed applications that base the consequence assessment on a plant specific PSA model have the capability of identifying risk important inspection locations that might otherwise be ignored. This is a clear benefit of the RI-ISI approaches, especially in full scope applications where also other than highest

safety class systems are considered. Reduction of inspections in primary circuit can be justified, and thus radiation doses can be significantly reduced. The economical benefit for the plant of moving to a RI-ISI depends on the present ISI scope, rules and regulations.

The effectiveness of the ISI program depends on the choice of inspected elements, the inspection capability and ISI intervals. The benchmark was focused on the ranking and selection of ISI sites at segments level, and excluded the exact choice of welds or other sites to be inspected, the inspection methods and intervals. Thus it is impossible to judge how close the final selection of inspection locations would have been between applications, and whether the methodology would have had an impact on ISI method selection.

5. Conclusions

RI-ISI methodologies are well established in the USA, and in recent years have increasingly been applied in the European nuclear power generation industry. In Europe, different regulatory attitudes exist and therefore the approach towards risk-informed regulation in general (and correspondingly towards risk-informed in-service inspection) is very varied.

The ENIQ Task Group Risk has contributed to the development of best practices for the application of RI-ISI in European nuclear power plants. After publishing the European Framework Document for RI-ISI in 2005, ENIQ TGR has published a number of supporting documents giving more detailed guidance on some issues related to the RI-ISI process. In addition TGR has been active in international RI-ISI projects, including a RI-ISI benchmarking exercise coordinated by the European Commission's JRC and the OECD/NEA.

The RISMET RI-ISI benchmark shows that risk-informed methodologies have some significant differences, and they can result in slightly different results, but the risk impact of these differences seems to be small. The RI-ISI approaches can identify safety important piping segments that are ignored by approaches not using PSA. The results of the RISMET benchmark improve the knowledge on differences in approaches and their impact on plant safety, and promote the use of risk-informed ISI. The final report of the RISMET benchmark will be published in 2010.

References

1. ASME Boiler and Pressure Vessel Code, Section XI: Rules for In-service Inspection of Nuclear Power Plant Components, American Society of Mechanical Engineers, 2001.

2. Chapman, O. J. V., Gandossi, L., Mengolini, A., Simola, K., Eyre, T. & Walker, A. E. (Eds.). European framework document for risk informed in-service inspection. ENIQ Report No. 23, JRC-Petten, EUR 21581/EN, 2005.

3. Cueto-Felgueroso, C., Simola, K. & Gandossi, L. ENIQ Recommended Practice 9: Verification and validation of structural reliability models and associated software to be used in risk-informed in-service inspection programmes. ENIQ Report No. 30, EUR Report 22228EN, 2007.

4. Schulz, H., Schimpfke, T., Brickstad, B., Chapman, V., Shepherd, B., Kelly, S., Olsson, S., Wintle, J., Muhammed, A. & Simola, K. Final report of the Nuclear Risk-Based Inspection Methodology for passive components (NURBIM) project, 2004.

5. Hultqvist, G. ENIQ TGR discussion document on the role of in-service inspection within the philosophy of defence in depth. ENIQ Report No. 29, EUR Report 22230 EN, 2007.

6. Report on the regulatory experience of risk-informed in-service inspection of nuclear power plant components and common views. Final Report, EUR 21320/EN, 2004.

7. Simola, K., Gandossi, L., Mengolini, A., Cueto-Felgueroso, C. & Leijon, A. ENIQ Recommended Practice 11: Guidance on expert panels in RI-ISI. ENIQ Report No. 34, EUR Report 22234EN, 2008.

8. Lötman, J. ENIQ TGR discussion document on the role of in-service inspection of the reactor pressure vessel. ENIQ Report No. 35, EUR Report 23419 EN, 2008.

9. Living Program Guidance to Maintain Risk-informed In-service Inspection Programs for Nuclear Plant Piping Systems, NEI 04-05.

10. Simola, K. & Gandossi, L. ENIQ TGR discussion document – Updating of risk-informed in-service inspection programmes. ENIQ Report No. 37, EUR 23929 EN, 2010.

11. The Swedish Nuclear Power Inspectorate's regulations concerning structural components in nuclear installations. SKIFS 1994:1. SKI, Stockholm, Sweden, 1994.

12. Westinghouse Energy Systems, Westinghouse Owners Group Application of Risk-informed Methods to Piping Inservice Inspection Topical Report, WCAP-14572. Revision 1-NP-A, Pittsburgh (PA), February 1999.

13. Electric Power Research Institute. Revised Risk-Informed Inservice Inspection Procedure, TR-112657, Revision B-A, Palo Alto (CA), December 1999.

14. American Society of Mechanical Engineers. Alternative Piping Classification and Examination Requirements. ASME Section XI Division 1, Code Case N-716. New York (NY), April 2006.

Practical application of risk based management in thermal power plant

Christopher Smith and Sarinova Simandjuntak
European Technology Development Ltd.
Leatherhead, Surrey, United Kingdom

Abstract

The paper provides the audience with an insight into the practical application of risk based management at a thermal power station. The paper includes data collection, methodologies to identify and determine the potential impact of risks resulting in the recommendations of practical solutions in order to reduce/eliminate risk within the plants management structure and boiler units. Identification of the risks, potential impact and recommendations for risk reduction within the management structure has been shown to be achievable by reviewing the data collected and comparing the findings with industrial best practices/guidelines such as statutory environmental regulations, knowledge of industry experts and published literature. Implementation risk assessment within the boiler units has been successfully carried out by reviewing the components history, condition assessment, operating conditions/parameters, knowledge of industry experts and compliance with industry guidelines such as the safety of pressure systems ACOP (approved code of practice).

The risks have been evaluated to give an output in terms of compliance risk scores using a risk based management template which was developed for ETD's RBM Procedure known as ''RISKFIT''. The ranking of the risk scores has been represented in a spider chart.

1. Introduction

The operation of a power plant at high temperatures and pressures carries potentially many risks. The degree of risks associated with operation is defined as a product of the impact or consequence of a failure event and the likelihood or probability of the failure event occurring. This is a simple statement, which is well recognised. However, one of the difficulties in managing risk is in establishing objective and consistent methods for determining the probability and consequences of failure events.

Numerous methods for dealing with risk have been developed within a variety of different industries. In relation to engineering or technical risk the nuclear industry in the 1970's and 1980's was very active in this area but now the petrochemical and refining industries are advancing their risk based assessment procedures [1]. These procedures allow the level of risk to be determined according to a detailed methodology. Whilst these methodologies are to a certain extent transferable there is no specific procedure applicable to thermal power plant, although general guidance is available such as in the ASME [2] and in the RIMAP (Europe) procedures [3].

Through the 1990's developments, particularly in the field of Risk Based Inspection, occurred in Europe [4, 5] and in the US but the procedures are still complex and somewhat fragmented rather than a comprehensive system for application. The recent changes within the Electricity industry has led to increased global competition which in turn has resulted in the need to improve the cost efficiency of the maintenance and inspection functions without compromising safety or availability. A recent European survey [6] highlighted a high level of interest from power plant operators in risk informed methods.

ETD has been involved in discussions with the members of Japan-Korea grouping on risk based management for power plant. ETD was also involved in similar discussions with the USA and European group members and as a consequence of this and its consulting experience worldwide in this field the company has developed its very own risk based approach to include Risk Based Maintenance and Inspection (RBMI). ETD's this Procedure and Software for thermal power plant is known as **'Riskfit'**. The procedure is structured such that quantitative failure consequences can be evaluated using generic representations, for example, by defining the value of failures and impacts as low, medium or high. Within 'Riskfit', there are models which look at how the plant risk is being managed in terms of management programmes, how well these programs are

being implemented and then it looks at the component condition in detail. The models were constructed by means of benchmarking i.e. comparing against best practices in the risk management of the thermal power plant. The final stage of this process is the detailed review of the value, in risk terms, and cost of the activities/tasks that are carried out during overhauls. The objective would be to prioritise the maintenance and inspection with respect to the criticality of the components. Discussion of ‘‘Riskfit’’ procedure is given in the next section. ‘‘Riskfit’’ has been found to be a flexible, easy to use, yet a robust system to perform risk assessment in power plant.

The objective of this paper is to demonstrate the findings of risk based assessment from the management programme level and implementation programme level which are the first and the second stages of ‘‘Riskfit’’ RBMI procedure. The focus of this paper is the plant management structure and implementation of plant maintenance and inspection with regards to boiler units.

2. ETD ‘‘Riskfit’’ procedure

The main objective of ‘‘Riskfit’’ is to allow a framework to identify and measure the risk areas and thereby allow optimised focussing of available resources. As such it is a management tool. It is important to recognise that identification of risks does not necessarily require a substantial financial or resource commitment rather, a simplified system has been developed that readily highlights and ranks risk areas for attention. It will ultimately allow a means of choosing what level of risk a station will operate under without compromising the safety and reliability of the plant.

‘‘Riskfit’’ essentially comprises a systematic approach for optimising plant operation, maintenance, and integrity management processes by focusing on appropriate level of maintenance resources (both financial and staff) and management effort at the highest risk areas of plant. The principle aim is to be able to prioritise the areas of highest risk in order to make informed decisions as to the funding and resource commitments.

Conceptually this procedure involves a “Risk Waterfall” where the level of detailed information about the plant and its condition increases and the accuracy and focus of the assessment improve with depth of the process i.e. the process initially starts at a high level with the identification of general risk areas. This involves examining how well the plant is managed in terms of technical and other programs and is carried out by comparison with good/best practice

attributes (or lack of attributes) of the program for each area. The output is a numerical indication of the level of risk in different plant areas. This is followed by a more detailed evaluation of the degree of risk by assessing how effectively the technical programmes are implemented and an estimate of the probable condition of specific components. Finally the maintenance activities to be performed on the component at the next shutdown are examined in terms of their risk based value and the cost of the activity to prioritize on a value cost basis. This allows elimination of the low value tasks and hence saving the costs associated with these tasks.

‘‘RISKFIT’’ involves four basic levels as follows:

A) Management Programme Level Risk Assessment:

This, as the name suggests primarily identifies management programme deficiencies in terms of risk. This is derived by assessing the attributes that are present in each management program from the pilot plant against best practice template. Each attribute is weighted for significance. The impact of an attribute or rather its omission from the management program is also classified together with a timescale factor. This latter factor effectively yields a higher risk score for attributes that will cause problems in the short term as opposed to over the longer term. An example of a Management Program Attribute scoring table is presented in Figure 1. On completion of a program assessment the output is in terms of a percentage rating. A high percentage score indicates missing positive attributes hence the risk is high. A typical output represented in a spider chart from the Program Risk Assessment is shown in Figure 1.

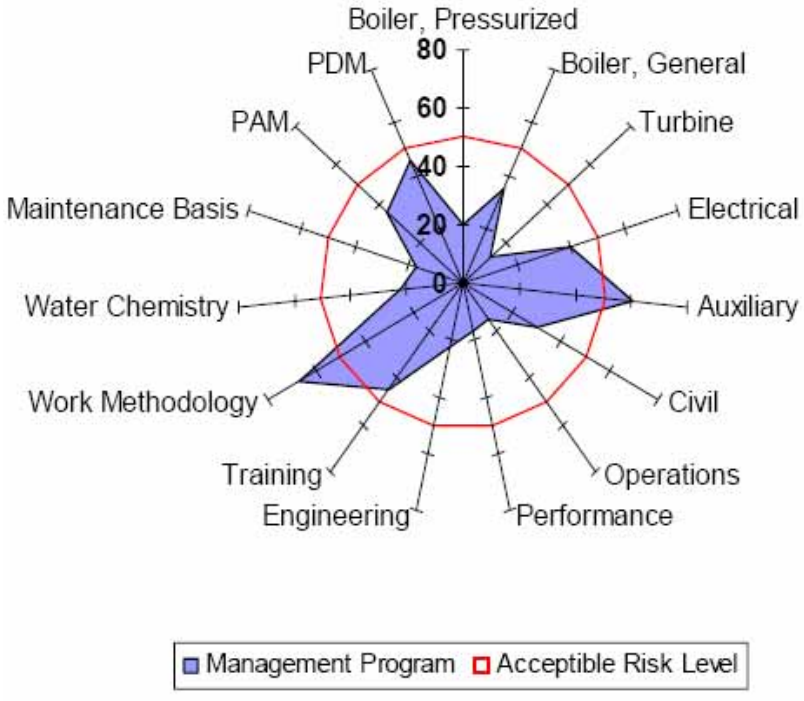

Figure 1. Example of Program attributes assessment output showing high scores (high risk) in Management Programs for Work Methodology and for Auxiliary equipment.

B) Implementation Risk Assessment

This is aimed at highlighting where there is inadequate application of the management programs. This involves what is essentially a compliance audit. This is in effect a series of questions aimed at identifying if any aspect of any of the management programs is not being carried out. Simply if a procedure is not being implemented the risk is higher than if it was. Note this is once again based on best practice rather than against the incumbent management programs. Several different management programs can be related to a single component therefore at this stage the focus has moved to specific plant components, hence the questions are component based. An example of a typical compliance "audit" is shown in Figure 2. This is combined with a generic failure event consequence and likelihood table to yield an overall Implementation Risk Score. The risk scoring output will again be represented in a spider chart similar to the one shown in Figure 1.

Query	Response	Compliance Factor
Is inspection policy fully adhered to	Yes	1
Is the inspection programme drawn up by competent person	Yes	1
Is inspection programme fully completed	Yes	1
Are all tube failures recorded	No	0
Are all tube failures subject to root cause analysis	No	0
Are the number of tube failures decreasing	Yes	1
Are tube repairs/replacements always carried out to documented and approved procedures / engineering standards	Yes	1
Are temporary repairs used	Yes	1
Are temporary repairs always subsequently replaced with permanent repairs	Yes	1
Has a remanent life assessment that considers all feasible failure mechanisms been carried out by a competent person	Yes	1
Is the remanent life assessment updated by a competent person after each overhaul	Yes	1
Are historical inspection records available	Yes	1
Are operating steam temperatures monitored	Yes	1
Are metal temperatures monitored	Yes	1
Are significant temperature deviations fed back into life assessment process and inspection plans	Yes	1
Is the internal oxide thickness monitored regularly	Yes	1
ACTUAL TOTAL		14
POSSIBLE TOTAL		16
COMPLIANCE RATIO		**0.875**

Figure 2. Example of Implementation Risk Assessment Audit.

C) Component Risk Assessment

This is aimed at providing a simple and quick method for ranking the most critical components. It uses a classification system for estimating the criticality of a component in terms of the principal influencing factors i.e. age, cycles, temperature, operating environmental conditions, generic design aspects, inspection and the expected conditions. An example of a component specific condition ranking template table is shown such as Table 2. Evaluation against such a table will provide a Component Factor which when combined with the Implementation Score gives the Component Risk. The classification system and indeed most of the factors used to produce the Component Risk can be either generic or can be customised to suite specific situations of plant needs.

	1	2	3	4	5
Age	< 50K Hours	50-90K Hours	90-130K Hours	130-170K Hours	>170K Hours
Cycles	< 200	200-500	500-1000	1000-2000	>20000
Temperature	Constantly below design conditions	Generally at design	Occasionally above design	Frequently above design or poor monitoring	Generally above design/ unknown
Environmental Conditions	Begnin service conditions	Minor corrosion or wastage possible	corrosion or wastage possible	Corrosion or wastage probable	Very aggressive corrosion or wastage / unknown
Generic Design/ Component type	no known design related failures	Very few failures with this design	occasional failures with this design but different operating mode	occasional failures with this design and operating mode	Known design weaknesses - subject to frequent failures
Inspection	Comprehensive inspection within last 4 years	Partial inspection within last 4 years	Comprehensive inspection within last 8 years	Partial inspection within last 8 years	No inspection within last 8 years
Expected Current Condition	Very Good condition	Average condition	Poor condition	Condition Unknown	Very poor condition

Figure 3. example of a generic tubing condition assessment template.

D) Risk Based Task Prioritisation

Task specific value assessment prioritises in risk terms the most critical work. This is performed on a structured basis using a detailed methodology for assessing each task. As would be expected at this stage this evaluation is more involved than for the higher level assessments. In summary, the procedure requires assessing the value of four distinct aspects related to a task. The four elements comprising the Value of a task are:

- The value of the task (this is a function the nature of the task and the information that performing it yields)
- Value of the component on which the task is being performed
- The value of the system to which the component belongs and
- The value of the consequences of failure.

Each of these elements is in turn a function of several parameters e.g. the value of the component on which the task is being performed is determined from such factors as the repair cost, replacement availability and whether there is redundancy for that component. Typically four or five factors are required to determine each element of the value criteria. A similar, but simpler, exercise is then performed to establish the cost of each task.

Such values and costs can be ranked for example from the inspection during outage (after examination of risk exposure, inspection costs are determined as a function of inspection coverage, frequency, technique, procedure and on-line plant monitoring). One of the advantages of prioritisation is the plant owner/ manager can use risk criteria defined during the inspection to determine the interval of outages.

3. Methodology

One European thermal power plant in which this study was recently conducted chose to implement the management programme and implementation risk assessment levels of the ETD's ''Riskfit'' Procedure. The methodology of implementing these programme levels are as follows:

Task 1: Conduct Senior Management Workshop

A 2-day Workshop to provide the client's senior management team with an overview of risk based management process, plant operation, maintenance and inspection during daily plant activities and outage. The workshop is aimed at the different stakeholders in the project in order to agree on the project organisation and its implementation. It is also aimed at capturing key RBMI issues and where the utility as a whole sees its strength and areas that need improvement.

Task 2: Data Collection

This task consists of collecting all necessary information to be used during the project. Data required include:

- Previous outage plans and outage schedules
- Outage work and maintenance history
- Failure history
- Manufacturer's operational and maintenance documentation

- Maintenance and inspection procedures, reports, engineering studies/ projects
- Operation (typical) data e.g. pressure and temperature
- Detailed engineering drawings of all work-scope components
- Safety system information related to the existing protection and mitigation devices.

Note: data requirement is dependent on the type of ''Riskfit'' levels implemented.

Task 3: Management Programme Risk Assessment

A comprehensive review of the technical management programs at the plant. The attributes and metrics of each program assessed relative to an industry best practice program template. Using the procedure outlined above the Management Program Risk will be assessed. Ranking is performed first in terms of risk, and then by way of a corrective cost function to identify the cost prioritised actions/procedural improvements that would mitigate the most risk.

Task 4: Program Implementation Audit

A comprehensive review of how well the existing technical management programs that relate to component integrity are being implemented. This involves interactive discussions with a variety of station staff including operations, maintenance and management personnel as well as review of the plant's current state, documentation, logs etc. associated with operation and maintenance. The aim is to determine the degree of compliance and to ascertain specific reasons why some aspects of the programs may not be fully applied in all situations. It will also provide a benchmark against current best practice including the ACOP (Approved Code of Practice), PSSR (Pressure System Safety Regulation) and Health and Safety regulations.

For Tasks 3 and 4 a **questionnaire** was prepared such that the principal objectives contain management attributes which are represented by positive questions. The responses to the questions have to be a 'Yes' or 'No'. Having a possibility of a 'don't know' answer has lead to the application of Fourier's analysis type solution to evaluate the risk score of each of the principal objectives. The analysis applies the weight factor to the answers, i.e. since the questions are set up in a positive answer manner, if the answer is 'No' or 'Don't

know', the weight factor is less. In other words, the *higher the risk scores obtained, the lower the risks are* [8].

Task 5: Program Implementation Risk Calculation

Risk calculation involved compliance audit on components (not program) and the criticality analysis of boiler units. The boiler unit consisted of four boilers set up in a range of system. Included in the assessment were all the pressurised components and their protective devices. Component specific generic failure templates (similar to Figure 3) were generated and customised where appropriate to take account of any specific plant variations. The definitions and scaling factors used for defining the consequences and likelihood criteria are also subject to modification in agreement with any specific Station requirements or conventions. These were then be used in conjunction with the output from Task 3 to give an Implementation Risk Score. Risk mitigating actions were again identified.

4. Results and discussion

4.1 Risk scores

From the Questionnaires distributed, data were collected and analysed. The results are presented in Figure 4 – a spider chart showing the principal objectives with their associated risk scores. Due to the scatter in data obtained from the questionnaire, the *acceptable risk scores* were evaluated using the probabilistic (Monte-Carlo simulation) method [7], also to calculate the optimum answers which are assessed relative to industry best practice programme.

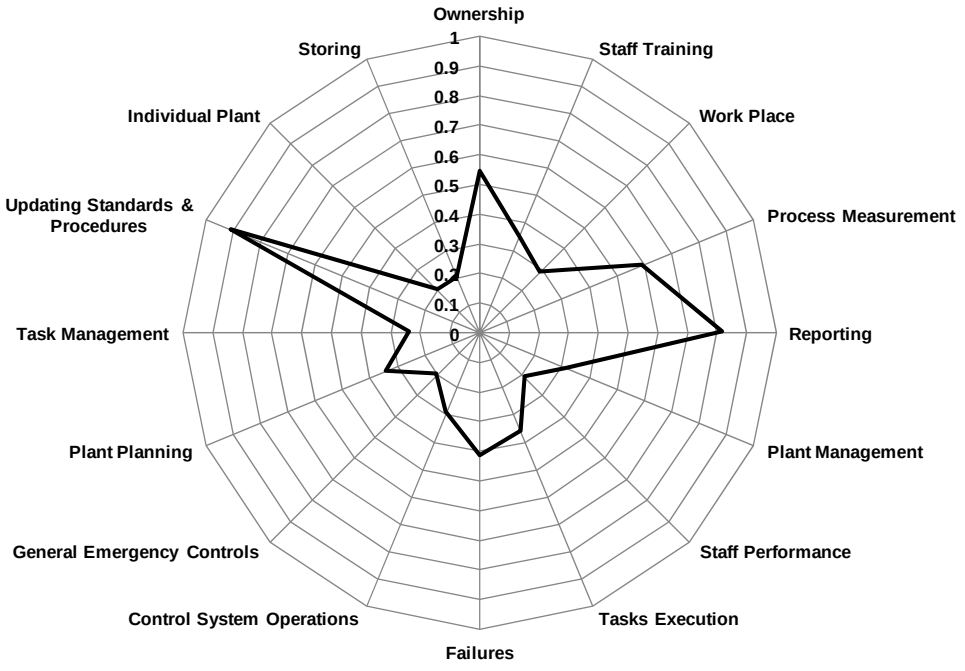

Higher the risk score, higher the risk

Figure 4. Management Programme Risk Assessment from Questionnaires.

‘‘Riskfit’’ ETD RBM procedure has been utilised to identify risks, rank risk areas and once identified highlight these specific areas for management attention. Some of these areas are Ownership, Process Measurement, Reporting and Updating Standards & Procedures. The results suggested that the management of Updating Standards & Procedures followed by reporting were the highest risk contributors assessed in this particular management programme level. However, from the questionnaire, the interviews and the workshop, there were apparent differences in the understanding/knowledge on the management objectives and their implementation in the organisation. This indicates that there might be a communication problem. The position and responsibility of an employee in the management levels could lead to the culture of ‘need to know’ basis. From the interviews, ETD established that many of the employees were also not fully aware of the plant (management) objectives.

Many of the managers/supervisors are also responsible for the control over the quality of maintenance and inspection works, contractors, or other general tasks performed on-site (such as during process measurement and storing). From the

organisational structure it is apparent that there is currently no special Quality Assurance role, therefore there are potentially higher risks in the management related to standards of maintenance / inspection / modifications, i.e. engineering work quality in general. This includes quality assurance of the contractors work.

4.2 Boilers risk assessment

The plant boiler units investigated have recently undergone an overhaul. The risk assessment work was carried out in August 2009. During the February 2009 outage, many of the components have been replaced or modified, including the roller grate, the mesh in the water cooling tower, and the superheater tubing (applying refractory materials on some areas of the tubing to reduce corrosion and erosion).

Nevertheless, the owner would like to perform boilers risk assessment to assess the risks from the implementation of maintenance & inspection of the boiler units against best practice/directives/regulations as example is shown in Table 1. Table 1 represents an example of the compliance of the plant to the ACOP. ETD analysed the compliance of all pressure parts and their protective devices to ACOP and PSSR. Although detailed component condition risk assessments were not conducted, implementation risks were calculated by taking into account the past and present service and condition histories, the maintenance & inspection programs, and the failure history and its consequence (in the last 5 years). Since risk (R) is the product of the probability of failure (P) and the consequence of failure (C), Table 3 refers to the risk score calculations of the boilers and their attributes. The final results are presented in the spider diagram in Figure 5; none of the attributes presented a high degree of risk; the safety valves, roller grate, economiser, main ring pipes, common system and common duct dampers presented a medium degree of risk.

Table 1. Compliance of the plant to the ACOP.

ACOP Requirement	**Conformance**	**Recommendation**
Where substantial modifications or repairs (including extensions or additions) are to be carried out which might increase the risk of system failure, the user should consult a person who is competent to advise before work begins.	The decision to make a modification to the system is made by the plants engineering manager. There is no other competent group or persons assigned to verify the proposed modification or for consultation.	The plants owners / management should consider the formation of a quality assurance (QA) department consisting of competent individuals or team to assess the quality and impact of modifications and maintenance activities.

Table 2. Boiler risk assessment scoring.

Probability (P):	**Consequence (C):**	**Risk (R):**
1. Not likely to happen 2. Not likely but possible 3. Likely to happen 4. More likely to happen 5. More than likely to happen	1. Delay the process 2. Stop the process 3. Stop the process/ Break down 4. Stop the process/personal injury/ break down 5. Stop the process/loss of lives/Major break downs	Risk = P X C 1–8 Low Risk 9–15 Medium Risk 16–25 High Risk

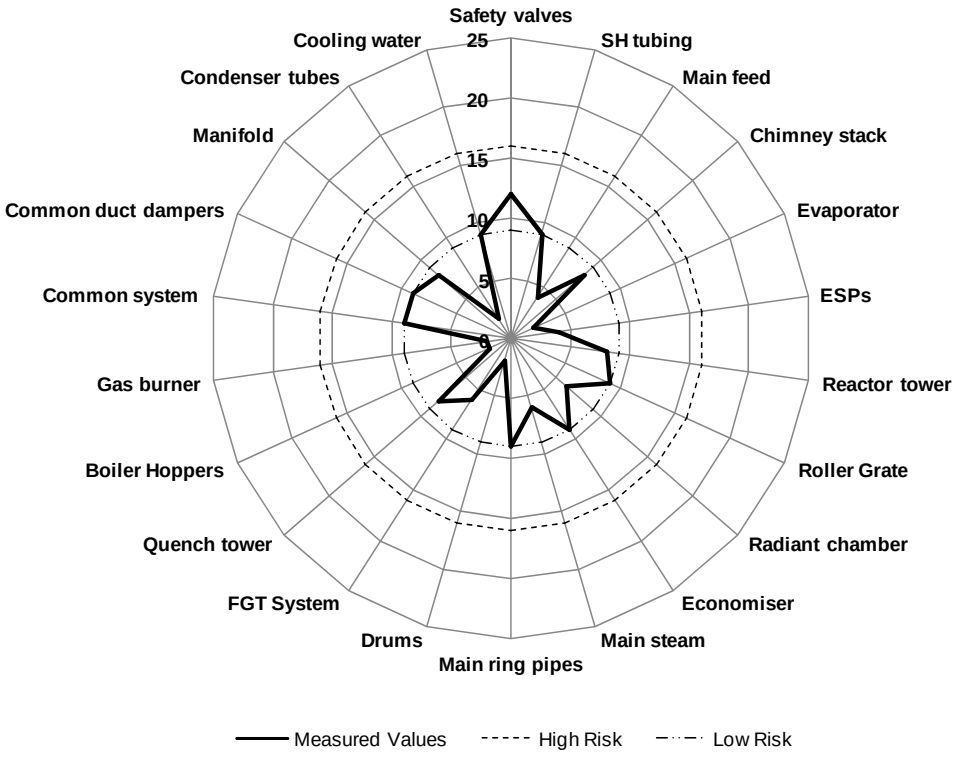

Higher the risk score, higher the risk

Figure 5. Implementation Programme Risk Assessment of Boilers and their attributes.

5. Conclusions

- ‘‘Riskfit’’ ETD RBM procedure for power plants has been utilised to identify risks, rank risk areas and once identified highlight these specific areas for management attention. One particular example of its application in a European power plant is described here.
- Some of these areas are Ownership, Process Measurement, Reporting and Updating Standards & Procedures.
- When identifying risks at the management programme level, it has been established that the plant is lacking in its communication which results in different or no understanding of management objectives between individual employees.

- There was no pooling of resources for engineering standards and procedures which leads to cultural and cognitive problems such as in performing task and reporting. From the organisational structure it is apparent that there is currently no special Quality Assurance role, therefore there are potentially higher risks in the management related to standards of maintenance / inspection / modifications, i.e. engineering work quality in general.

- In general the plant complied with the best practice guidelines/regulations (ACOP, PSSR). However, due to the lack of role in the quality assurance, in the understanding of engineering standards and reporting, the plant is exposed to the associated risk.

- ETD has performed benchmarking of thermal power plant on the management performance and cost, maintenance and inspection cost and procedures, damage mechanisms and probability of failures resulting in an established database for cost and best practice guidelines which were referred to in this work.

- Database has also been used to determine the best practice guidelines and/or procedures

- Some of the quality assurance role has somewhat been shifted to the contractors which leaves the plant owner / management vulnerable in the event of failure or accidents**.**

References

1. API Publications 580 and 581 on Risk Based Inspection. American Petroleum institute, 1998.

2. ASME, Risk Based Inspection – Development of Guidelines, Vol. 1, General document, CRTD – Vol. 20-1. American Society of Mechanical Engineers, 1991.

3. Standard Data Format for the RBI/RBLM in RIMAP Workbook for Power Plants. RIMAP, Revision Number 1, May 2007.

4. ENIQ recommendations, European Network on Inspection Qualification.

5. PED97/23, Testing and Inspection of Pressure Equipment – European Pressure Equipment Directive.

6. Jovanovic, A. Current European effort to establish risk-based life management for components in the power and process plants. Presented at Baltica V Conference, Porvoo, Finland, 2001.

7. http://www.palisade.com/risk/.

8. ETD Report No. 1119-tp-97, Implementing RBM in Power Generation Plant.

Materials qualification testing for next generation nuclear reactors

Roger Hurst and Peter Hähner
European Commission, JRC Institute for Energy
Petten, The Netherlands

Abstract

The development of next generation, innovative nuclear fission reactors, needed to replace or supplement the current designs of nuclear reactors within the next say 30 years, critically depends on the availability of advanced structural and functional materials systems which must withstand extreme conditions: intense neutron irradiation, high temperatures, and potentially strongly corrosive coolant environments, in combination with complex loading states and cyclic loading histories. The mechanical performance and reliability of those materials depends on the service and off-normal conditions in whichever of the six candidate systems for Generation IV reactors, under the global Generation IV International Forum (GIF) agreement, they will be applied. This paper gives an overview of the suite of six selected reactor systems indicating where research on materials and structural integrity is still needed. Some of these reactor systems have been under study for many years whereas others are relatively new concepts but all still require a major expenditure of effort before they can be considered as realistic contenders. In particular the materials selection and component integrity for service will play a major role in a final successful design. Specific issues include: the endurance and stability with respect to creep, fatigue and fracture mechanics loading, the need for in situ environmental testing versus pre-exposure of materials and advanced structural-functional materials systems for specific applications. Using examples taken from research projects in which the authors' laboratory has participated, the materials qualification high temperature testing for three crucial components, reactor pressure vessel and piping, gas

turbines and heat exchangers is described in some detail. Finally pointers are derived as to not only the scale of the remaining research needs but also the mechanisms which are planned to be followed in Europe, not to mention globally, to obtain the required data and understanding.

1. Introduction

The recognition within Europe and many other countries during the last 10 years that an increase in the share of nuclear generated energy in the total energy mix would be beneficial, if not necessary, for addressing the problems of climate change and security of supply while matching the rapidly increasing global energy requirements is becoming widely accepted. In some countries this has led to a complete reversal of policy decisions while in others the green light has been given to new nuclear build and also to extending the licenses of operating nuclear plants. This nuclear renaissance which involves principally Generation II and III is now taking place in parallel with the initiative to prepare for the introduction of Generation IV reactors which should have been the natural successors to current reactors being introduced no earlier than 2020/2030 and seen as the sustainable systems for generations to come. Fortunately, GEN III reactor development requires limited new research and research capacity appears to be unhindered with reference to the plans set up in 2001/2 for the GEN IV International Forum (GIF). The main aim of GIF is to develop nuclear reactors which show improvement over current reactors with regard to sustainability, safety and reliability, economics and proliferation resistance. In addition the potential for producing process heat as well as electricity is considered as a distinct bonus. A suite of six potential reactor systems are under study as candidates for Generation IV reactors under the global GIF agreement. Some of these have been investigated for many years whereas others are relatively new concepts but all still require a major expenditure of effort before they can be considered as realistic contenders. In particular the materials selection and component integrity for service will play a major role in a final successful design including the availability of advanced structural and functional materials systems which have to withstand potentially extreme conditions compared to current generation reactors: high temperatures, intense neutron irradiation, and strongly corrosive coolant environments, in combination with complex loading states and cyclic loading histories [1–3]. The mechanical performance and reliability of those materials systems have to be assessed considering the actual environments

that the materials are exposed to during service and off-normal conditions. Specific issues include: the endurance and stability with respect to creep, fatigue and fracture mechanics loading, the need for environmental testing versus pre-exposure of materials and advanced structural-functional materials systems for specific applications.

Within Europe many of these issues have been addressed by various research projects co-funded by the EC within the last Euratom Framework Programmes (FP). In fact, a number of results presented in the present paper have been obtained within the European projects HTR-M (FP4), HTR-M1 (FP5) and the ongoing RAPHAEL (FP6) sub-project on VHTR materials, many issues of which are in common with GFR technology. Specific materials issues relating to liquid metal technology for SFR and LFR, as well as the materials requirements in going from pressurised and boiling water to supercritical water conditions as foreseen for the SCWR have been addressed in dedicated European projects such as the High Performance Light Water Reactor (HPLWR) Phase 2 project from which some results are later reported. In FP7, the large scale integrating project GETMAT has been launched to address cross-cutting materials issues, which are common to GEN IV and transmutation systems and, to some extent, also to thermo-nuclear fusion. Major emphasis of this project is on the development and qualification of 9 to 14% Cr ferritic/martensitic steels and their ODS variants for nuclear high temperature applications, including joining and welding technologies, as well as coatings for corrosion and erosion protection in various coolant environments.

Materials issues of next generation nuclear reactor systems are also being addressed by the Sustainable Nuclear Energy Technology Platform (SNE-TP), the European Technology Platform aimed at promoting the research, development and demonstration of European nuclear fission technologies, which was launched in 2007. Apart from developing a long-term vision of the role of nuclear energy, SNE-TP has drafted a Strategic Research Agenda (SRA) addressing the short, medium and long term R&D challenges of the Sustainable Energy Technology Plan with respect to fission technologies. This SRA is not only guiding the current seventh and future Euratom FPs, but is also expected to have an impact on national research programmes associated with future nuclear energy systems.

For the present paper and in order to cover a wide field for materials applications in future reactors for each GEN IV candidate system there will be focus in particular on any elevated temperature creep and fatigue requirements and, where applicable, their interaction with environmental factors. This overview

is followed by a variety of detailed examples of case studies and research carried out in the authors' laboratory in support of GEN IV.

2. Generation IV candidate systems

As a general remark it should first be mentioned that the increased operating temperatures and loads and the additional environmental constraints imposed do not necessarily oblige the immediate implementation of exotic materials or the development of completely new materials. In many cases, materials exist and are used successfully in other, non-nuclear, applications but have to be introduced into nuclear design codes and firstly into the minds of nuclear designers and nuclear engineers and even nuclear materials engineers. Qualification of the selected materials for the particular application is of course another matter and is currently the highest priority. Research can also tell where material improvement is out of reach and, hence, other solutions (e.g. design) are required.

Of the six candidate systems, three are fast reactors involving high energy neutrons and providing the capability of breeding new fissile material useful for enhancing sustainability of the fissile fuel but also capable of incinerating some waste actinides. The other reactors are essentially thermal or epithermal reactors operating at similar neutron energy levels to current reactors where only the epithermal variants can contribute towards actinide management. An overview of the systems' main parameters is shown in Table 1 where it should be added that in addition to electricity generation, the gas reactors are expected to play a prominent role in the generation of process heat. A schematic of all six reactor types is shown in Figure 1, and each is described briefly below.

The Sodium Fast Reactor (SFR) has been under development over the last 20–30 years with several prototypes built and operated, but with low priority compared to GEN II and III reactors. Nevertheless, its promise in actinide management and fuel breeding is such that this reactor has already been selected as the highest priority for early development of a prototype by the European SNE-TP. In this reactor the coolant is liquid sodium which in the second heat exchanger reaches a temperature of 550°C which will then be fed into conventional steam or carbon dioxide driven turbines. As the sodium is essentially at low pressure, the materials selection (ferritic/martensitic/austenitic stainless steels) is based purely on irradiation and corrosion behaviour, with the creep loads being so low so as not to be considered in design.

Table 1. Main parameters associated with the six selected GEN IV systems.

System	Neutron spectrum	Coolant	Outlet Temp. °C	Fuel cycle	Size (MWe)
VHTR (Very high temperature gas reactor)	thermal	helium	> 850 (Lower temps also considered)	open/ closed	250–300
SFR (Sodium-cooled fast reactor)	fast	sodium	550	closed	30–150, 300–500, 1 000–2 000
SCWR/HPLWR (Supercritical water cooled reactor)	thermal/ epithermal	water	510–625	open/ closed	300–700 1 000–1 500
GFR (Gas-cooled fast reactor)	fast	helium	850	closed	1 200
LFR (Lead-cooled fast reactor)	fast	lead	480–800	closed	20–180, 300–1 200, 600–1 000
MSR (Molten salt reactor)	epithermal	fluoride salts	700–800	closed	1 000

The Gas-Cooled Fast Reactor (GFR), probably the most ambitious GIF concept, on the other hand immediately presents structural challenges due to the high pressure helium coolant with an expected outlet temperature of 850°C either directly or indirectly into turbines or indirectly used as process heat. Although ferritic/martensitic steels can be considered for the pressure vessel, for such designs, nickel based alloys and ferritic ODS materials have to be considered from the primary circuit outwards due to their creep and corrosion (helium is never pure) resistance.

The Lead-Cooled Fast Reactor (LFR) comprises designs aimed at outlet temperatures from 550°C up to 850°C where process heat may be of interest for example for hydrogen production. A carbon dioxide heat exchanger and turbines are proposed and all indications are that high creep strength alloys with environmental resistance (lead and CO_2) will be required possibly with coatings.

The Molten Salt Reactor (MSR), currently low in the European GEN IV priorities, operates using molten fluorides as the fuel. With molten salt/molten

salt and molten salt/carbon dioxide heat exchangers the outlet temperature is intended to be around 700–800°C. The low pressures involved would again indicate that component/ molten salt compatibility is to be more important in design than high temperature structural integrity just as for the SFR.

The Supercritical Water Cooled Reactor (SCWR) is basically a higher temperature version of a Light Water Reactor with higher efficiency and economical benefits due to the maintenance of a single phase coolant. The reactor can also be configured with faster spectrum for actinide management. Outlet temperatures are planned for 510°C to 625°C and materials requirements include both the need for corrosion resistance and high temperature strength.

The Very High Temperature Reactor (VHTR), so called as the successor to the HTR, was first designed in the 60's/70's, with prototypes built or under construction in Germany, USA, China, Japan and South Africa. Even the temperature and operating conditions of the HTR for the helium coolant imposes high demands for materials with regard to creep and corrosion resistance but the evolution in the long term to 1 000°C operation desirable for process heat applications, necessitates the introduction of nickel base alloys and ODS alloys for heat exchanger and turbine applications. Even the pressure vessels will have to be constructed of materials not normally foreseen in nuclear reactors.

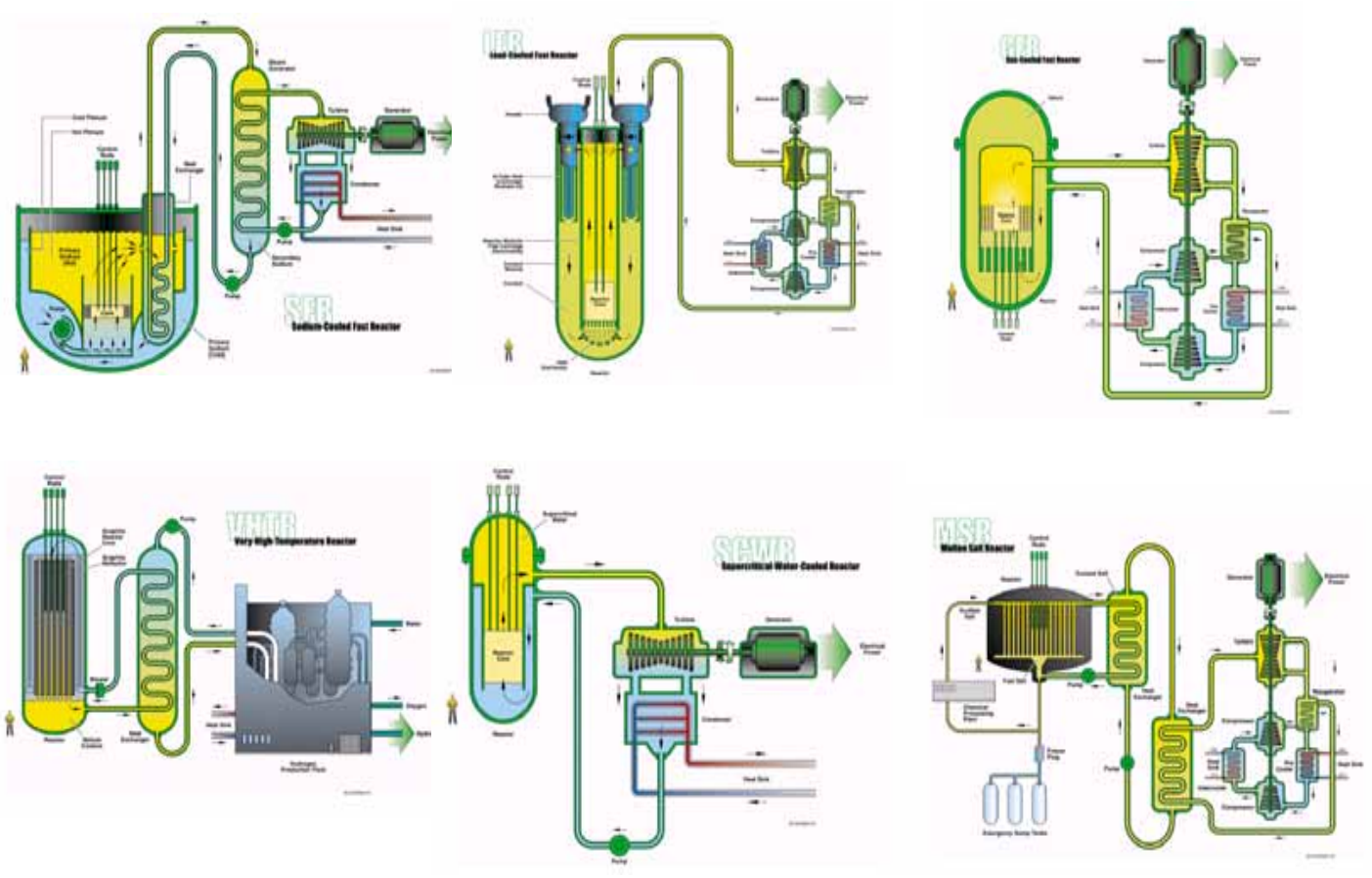

Figure 1. Schematic layout of the six reactor systems.

3. Reactor pressure vessel and piping steels

3.1 Reference creep tests on P91 at lower than conventional design temperatures

For high temperature reactors, the alloy P91 is under strong consideration [4] as the most suitable material for constructing the pressure vessel and piping. In the case of a conventional HTR i.e. not a VHTR the vessel operating temperature may be up to around 450°C with excursions under accident conditions to 550/ 600°C. Very little was known about creep at 450°C as the material has been developed for service at 550°C and above. In fact it had been suggested that negligible or even negative creep might manifest at the lower temperature. In the testing programme the importance of construction weldments had to be taken into account just as for higher temperature operation for conventional power generation plant but also any effect of irradiation damage had to be included. Hence the creep part of the assessment covered base metal, weld and cross-weld specimens at both 450°C and 550°C in irradiated and un-irradiated conditions. At 450°C, it can be seen in Figure 2 that creep results for base metal taken from the longitudinal and transverse sections of a rolled bar (BM-L and BM-T) are similar and in fact the actual creep curves show no tendency towards negligible or negative creep with significant creep rupture strains exceeding 15% up to 15 000 h of life. Earlier data, provided by CEA within the RAPHAEL project, is shown for comparison purposes. In terms of stress rupture strength, both the weld metal and cross weld test specimens are considerably weaker than those manufactured from base metal.

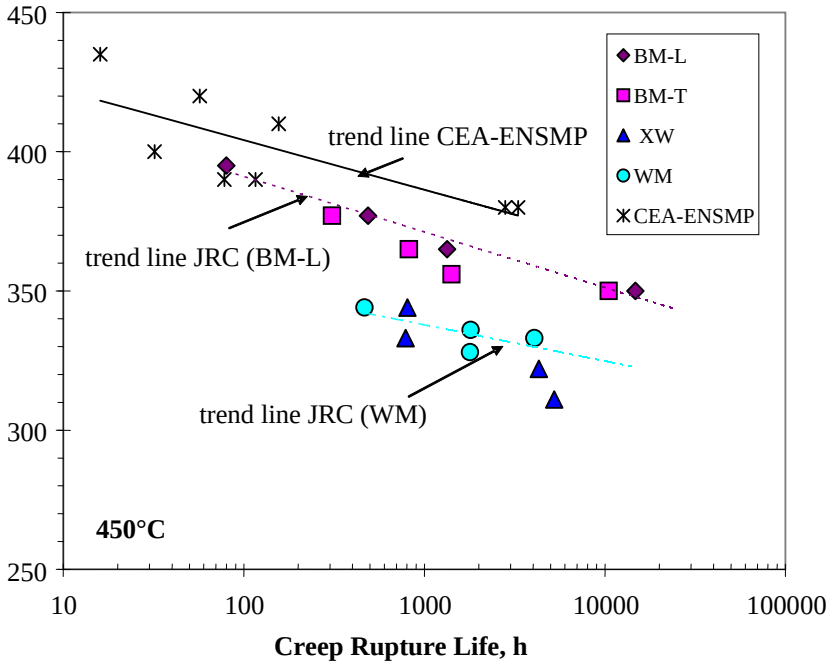

Figure 2. Creep rupture behaviour of welded P91 at 450°C for the base metal (BM, in two directions), for the weld metal (WM) and for cross-weld (XW) specimens.

At this temperature, nearly all cross weld specimens fail in the weld metal due to the high constraint in the narrow HAZ zone and no cavitation being developed in this zone in such short tests. At 550°C on the other hand, long term (> 5 000 h) tests do tend to fail in the HAZ as cavitation can develop in the intercritical zone but again weld metal and cross weld strengths are lower than those for base metal in the two directions indicating that Weld Strength Reduction Factors considerably below 1 should be used in design. Nonetheless no extra factor has to be built in concerning the effect of irradiation as no detrimental reduction in creep strength (Figure 3) was observed for specimens irradiated in the HFR Petten by NRG for an equivalent exposure to reactor pressure vessel end of life conditions.

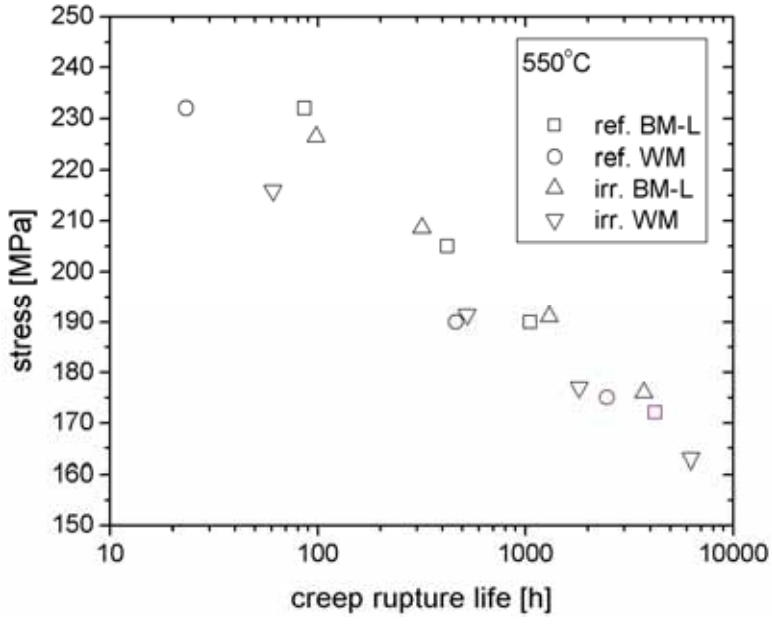

Figure 3. Influence of irradiation on stress rupture creep properties of P91 base metal and weld metal (courtesy NRG).

3.2 Qualification of welded P91 alloys using miniaturized creep and fracture testing

As highlighted above, in many applications but particularly for a pressure vessel, qualification has to be made concerning any fabrication weldments. Determination of behaviour under creep loading using cross-weld specimens can be achieved as shown but the exact interpretation of the results in a form suitable for understanding the integrity of a welded plant component is far from achievable. This is not only due to the constraint in the areas close to the vulnerable zones in a weldment but also to other size related factors and of course the loading direction. In an attempt to find a solution to this problem an alternative route has been followed relying on the testing of discrete areas in the constituent parts of the weldment using miniaturized testing, in this case using the Small Punch (SP) testing method. The SP test method was originally developed for nuclear applications in order to non-invasively test portions of operating components as a means of establishing their possible levels of damage (through irradiation, creep or other causes), in turn, allowing the estimation of

the remaining life of the component. This method has been also of considerable interest to non-nuclear plants particularly those operating at high temperatures such as fossil fuelled power plant and petro-chemical installations. The wide introduction of the method has been hindered by lack of test standardisation and the problems associated with correlating the SP test results with conventional data which the design engineers are acquainted with. Recently a Code of Practice [5] has been prepared under the auspices of the European standardization body, CEN, with the aim of overcoming these difficulties and enhancing the acceptability of the method. The method can also be applied to fracture toughness evaluation but the work reported here is for creep of P91 weldments.

Due to the availability of a welded component, part of which had seen service at 600°C, and conventional creep data for the pipe materials at the same temperature, it was decided to carry out SP tests at the same temperature. A service exposed (SE) P91 pipe has been joined to a new pipe of P91 base metal (BM) with a conventional circumferential weldment. SP test specimens, in the form of discs 8 mm diameter and 0.5 mm thick, were removed by electro-discharge machining from each pipe material, the weld metal (WM) and the heat affected zone (HAZ) in two areas, the coarse grained (CG) close to the weld metal, and the fine grained (FG) material close to the pipe, see Figure 4 [6].

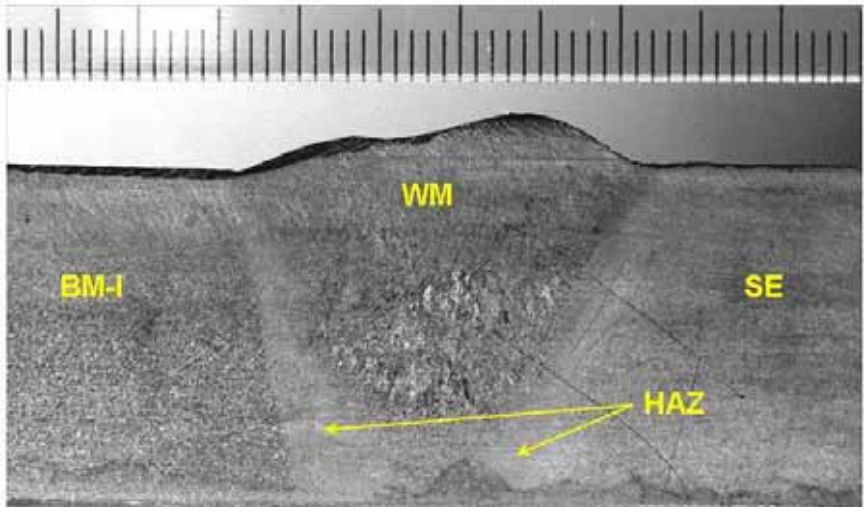

Figure 4. Section of the welded P91 pipe showing SP test piece locations.

The Code of Practice procedures were carefully followed and the load-deflection curves generated for the different disc materials are shown in Figure 5 (left) where for comparison purposes the same load, 250N, was used in each test. The marked difference in response is striking but the shapes of the creep curves are essentially the same as those for conventional creep tests. To compare all results a traditional stress rupture curve had to be derived with the difficult problem of translating the creep load used in the SP test to the specimen stress. The Code proposes a load/stress conversion equation and this was duly used to provide Figure 5 (right) again clearly emphasizing the spread of behaviour encountered for each location.

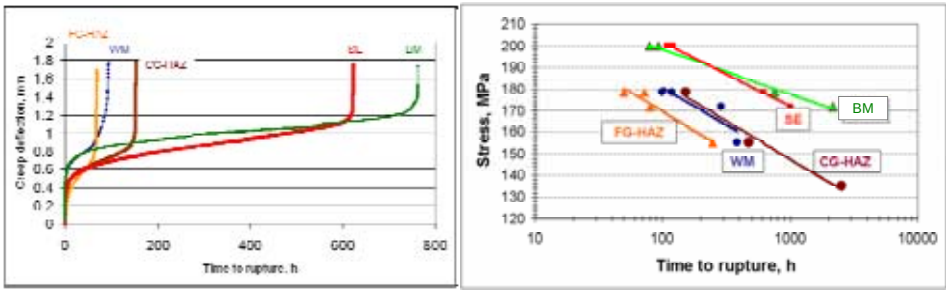

Figure 5. SP testing creep curves (left) and stress rupture results (right) for different constituents of the welded P91 pipe.

Comparison of the creep strengths of the base material pipe (BM) and the service exposed (SE) base materials at 600°C shows similar stress rupture properties in the SP testing just as was the case for conventional creep testing. However the SP tests on weld material and samples taken from the fine and coarse grained HAZ result in much shorter times to rupture than those for the two base materials. While the fine grained HAZ is the weakest weldment zone, the coarse grained HAZ adjacent to the WM reveals similar creep strengths to the WM itself. Interpretation of the data for the different zones allows creep models to be developed which can be introduced into finite element analysis models [6] and eventually integrated to predict the performance of weldments in components. This approach potentially will provide a more robust approach to predicting component behaviour than could ever be gleaned from cross weld testing.

Another potential use of SP testing relevant to the qualification of materials for creep service in GEN IV applications concerns novel material development. For challenging exposure conditions new and possibly exotic materials may

have to be developed. The material manufacture may be only achieved in small quantities which would be insufficient for conventional creep qualification testing. Additionally, if facilities for SP testing of irradiated material were made available then the very small disc sizes used for SP testing would minimize the volume to be irradiated.

4. Mechanical performance assessment of turbine materials for direct cycle gas-cooled reactors

4.1 Blade alloys

Among the six GEN IV concepts, the VHTR and the GFR are gas-cooled reactor systems. While the former is designed for high efficiency and process heat applications, e.g. thermo-chemical hydrogen production, it exhibits a once-through fuel cycle. The GFR, on the other hand, features a fast neutron spectrum and a closed fuel cycle with emphasis on a sustainable use of nuclear fuel and the management of long-lived radioactive waste. Reference concepts of both systems envisage helium coolants with 850°C outlet temperatures and, in the direct Brayton cycle options, helium gas turbines for electricity production. This raises the issue of materials compatibility with the high temperature coolant [7–9].

Specifically, high temperature corrosion problems have to be addressed, since the helium will contain impurities of H_2, H_2O, CH_4, CO, CO_2, O_2, so that the coolant actually represents a multi-component gas environment with mixed oxidants and a certain level of carbon activity. In practice, carbon activity and oxygen partial pressure will depend on a variety of factors. Besides temperature, pressure and flow rates of the coolant, the inventory of the primary circuit, alloy composition and ageing state will play important roles. Accordingly, the materials design has to address dynamic far-from-equilibrium corrosion processes which are affected by the nucleation and growth and the integrity of the corrosion product scales, a meaningful kinetic description of which may be difficult to obtain. In particular, the coolant environment may have a carburising or decarburising effect, depending on the specific composition of the various impurities contained in the helium.

Carburisation and decarburisation of structural materials thus represent critical issues, particularly for the gas turbines of helium cooled reactors with direct

cycle, as well as for the intermediate heat exchangers of an indirect cycle or for process heat applications. The complexity of the corrosion processes and the fact that the corrosion state will depend on the whole operation history of the primary circuit suggest to investigate the potential materials degradation in some limiting cases, such as the heavily carburised or conversely the strongly decarburised state. To address these issues, three turbine materials have been investigated: CM247 and IN792 as candidate blade alloys, and U720 as a disk material.
CM247 and IN792 are directionally solidified Ni-based superalloys with good corrosion and oxidation properties owing to their alumina and chromia forming capability, respectively. To assess the most detrimental effects of specific VHTR or GFR environments with direct cycle the two alloys have been pre-exposed to gaseous atmospheres leading to a heavily carburised state (1 000 h at 950ºC in argon with 2% CH_4) and a decarburised state (1 000 h at 950ºC in Ar with 0.1% H_2 and 0.01% H_2O). For comparison, other test-pieces were creep tested in the as received state (fully solution and aged heat treated for service), while a final batch of CM247 underwent an additional thermal ageing treatment of 1 000 h at 950ºC in pure argon to mimic the thermal effect of the corrosion treatments. For IN792 a variety of ageing treatments in argon were applied.

While the actual blade materials are supposed to operate at temperatures of 850°C with an indicative operating stress level of 160 MPa for a nominal operating period of 60 000 hours, only short and medium term creep tests have been then carried out on the pre-exposed alloys at 850°C at stress levels of 375, 325, 275, and 225 MPa. For both alloys the carburisation treatment produces a densely carburised zone to a depth of approximately 360 μm from the surface and a substantial increase in carbide size also in the bulk of the specimens. The decarburisation process leads to grain growth and grain-reorientation, especially in the zone close to the surface. For the thermally aged state this occurs through the entire specimen.

The carburisation treatment on CM247 and IN792 causes a marked loss of creep strength (Figure 6) accompanied by accelerated creep rate especially for the CM247 with respect to the as-received and the thermally aged conditions, while, interestingly, the rupture ductility remains comparable to that of the as-received condition. On the other hand, the decarburisation treatment was found to have an effect comparable to the thermal ageing, again more for the CM247 where the results in terms of time and elongation to rupture, time to 1% strain, minimum creep rate observed on decarburised specimens do not significantly differ from those obtained on the thermally aged ones.

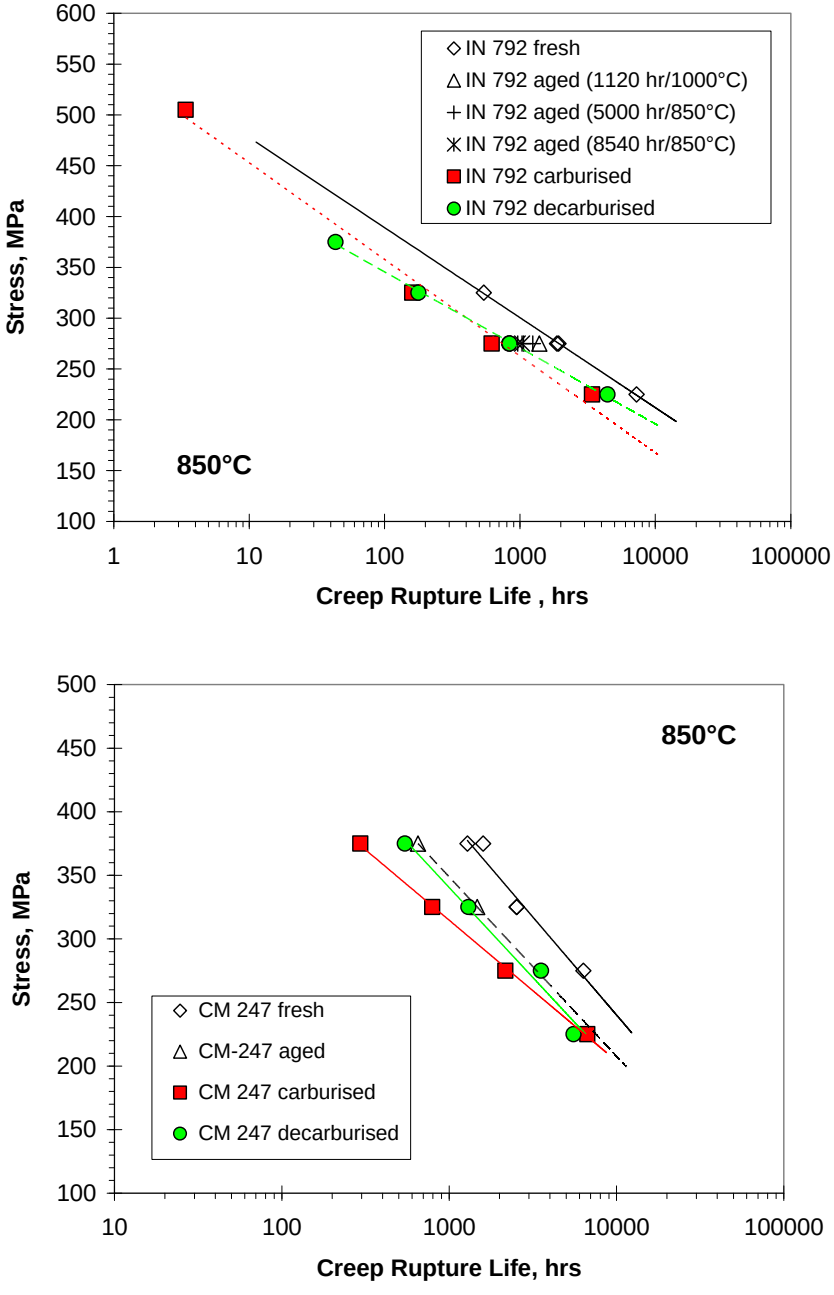

Figure 6. Creep rupture data for IN792 (top) and CM247 (bottom) at 850°C.

In general the difference in performance between the four states reduces with decreasing stress, particularly in the case of CM247. The results of the creep

tests show that the IN792 alloy is less prone to degradation by thermal aging and corrosion (carburisation and decarburisation) as compared to CM247. At the same time, the carburised and the decarburised IN792 exhibit creep damage localisation and necking which is almost absent in the as-received and the thermally aged states.

Over the times tested however, the alloy CM247 shows superior creep performance to IN792 in all four conditions (as-received, thermally aged, carburised, decarburised). Microstructural analysis indicates the creep strength loss and creep rate acceleration to be associated with grain growth and micro-cracking at the interface between matrix and second phase particles, in particular the large carbides found in the carburised state. For both alloys investigated carburisation results in more significant performance degradation than decarburization.

4.2 Disc alloy

As a candidate turbine disc alloy for VHTR and GFR applications, the wrought Ni-base superalloy U720Li [10] has been investigated. This alloy features a low interstitial (Li) content to suppress the formation of deleterious carbide stringers and a Cr content which is low enough to avoid sigma phase precipitation at high temperatures. Besides a sufficient creep resistance, the disc alloy has to be designed to withstand cyclic loads, which is why LCF tests at 650°C have been performed in addition to creep tests at 750°C. Again the potential detrimental effect of carburisation had to be assessed on specimens pre-exposed to the carburising atmosphere as above.

The carburisation pre-treatment on U720Li was found to produce oxide layers of about 50 to 100 μm thickness followed by a densely carburised zone to a depth of approximately 700 μm from the surface. In the bulk of the specimen the pre-treatment acted as a mere thermal aging process leading to recrystallisation, grain growth, annealing twin formation, growth of secondary γ' particles, and dislocation recovery. These processes are largely suppressed in the subsurface zone where carbide nucleation and growth prevent recovery. In particular, a competition between the grain growth and carbide nucleation at grain and twin boundaries has been observed (Figure 7).

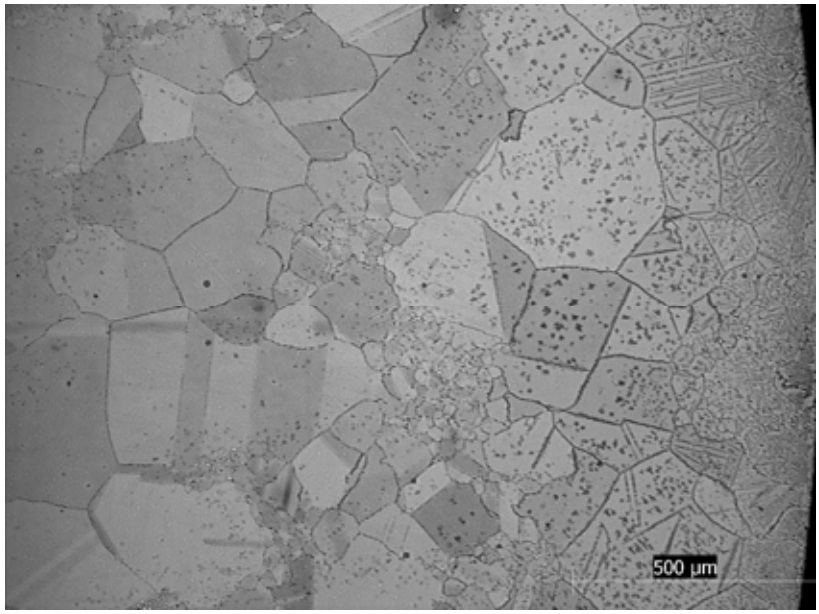

Figure 7. Optical micrograph of carburised U720Li showing grain growth in the bulk (left) and a dense dispersion of carbides within an approx. 700 µm thick surface layer (right).

Creep tests on U720Li have been performed at 750°C in the stress range from 350 to 700 MPa. The results (Figure 8) show that the carburised material exhibits a marked loss of creep strength as compared to the as-received material. This is accompanied by a corresponding increase in minimum creep rate. The Norton coefficient derived from the stress dependence of the minimum creep rate amounts to $n = 12$ over the whole stress range, for both the as-received and the carburised materials. This high value is typical of a γ' particle-dislocations interaction based creep deformation mechanism of high strength superalloys. The creep ductility (in terms of the percentage of elongation at rupture), however, slightly increases in the carburised case. At the same time, a greater reduction of cross-sectional area points at an increased deformation localisation. It is important to note that the creep performance degradation associated with carburisation does not always go hand in hand with a loss in ductility. The loss in creep strength is mainly associated with grain growth, micro-cracking and, most importantly, with the dissolution of tertiary and coarsening of secondary γ' particles. For low creep stresses the predominant damage results from stress accelerated grain boundary oxidation due to oxygen diffusion along grain boundaries. This local oxidation can lead to dissolution of the γ' phase in the

vicinity of cracks. The fracture surfaces of all crept carburised specimens show predominantly ductile features, suggesting intergranular failure mode. As compared to the low creep stresses, the specimens tested at high stress exhibit less alignment of the grains at the fracture surface, while creep damage appears more evident, with several microcracks at the grain boundaries, both in the bulk and at the outer surfaces

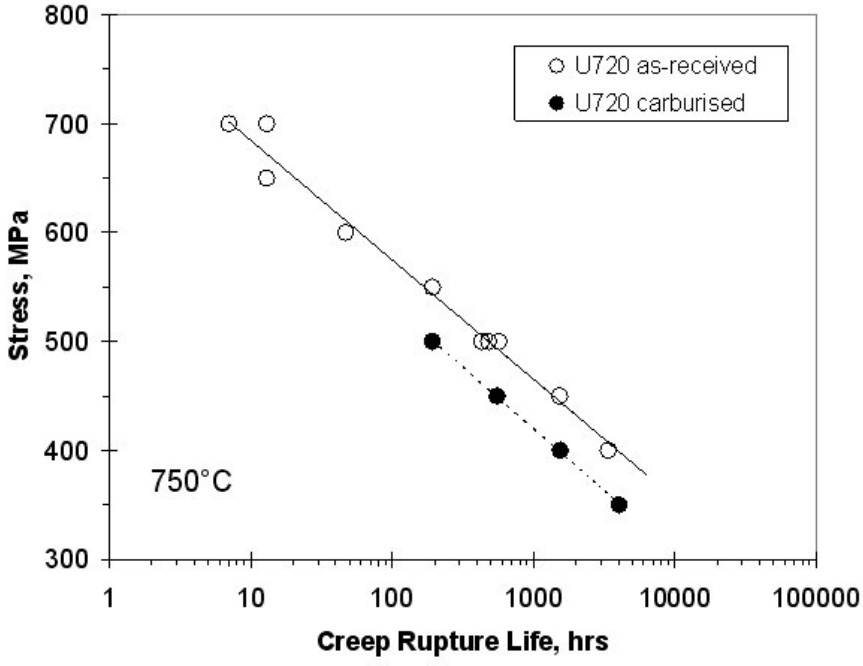

Figure 8. Creep rupture data for U720Li at 750°C, incl. CEA results for the as received state (HTR-M Deliverable 2.10, Rapport Technique DTEN/DL/2005/013 by R. Couturier et al.)

Exactly the same types of pre-treatments as carried out for the blading materials, namely carburizing, decarburising and thermal ageing were carried out on further sets of U720Li specimens prior to low-cycle fatigue (LCF) testing. As, in particular, the carburisation treatment leads to surface damage which may affect LCF crack initiation, specimens were generally re-polished prior to LCF testing, while for comparison some specimens were tested in the as-exposed state with pitting corrosion visible at low magnification on the specimen surface. LCF testing was conducted on a digitally controlled electro-mechanical test rig at a temperature of 650°C achieved by induction heating. All LCF tests were

performed in total strain control, using triangular strain waveforms, a strain ratio of R = 0.05 (always tension), and different maximum total strain values of 0.6%, 0.7%, 0.8%, and 1.0%. The cycle period varied as to maintain a constant strain rate of +/- 0.1%/s for all tests.

The LCF results, in terms of maximum total strain versus number of cycles to failure, presented in Figure 9, reveal the detrimental effect of the carburisation on the LCF performance. This is particularly true at high strain ranges and low numbers of cycles to failure. For a given strain range of 0.95% (i.e. max. strain 1%), the as-received material bears significantly larger stress ranges while LCF lives are still longer. This observation holds irrespective of the surface quality, corrosion pitted, or re-polished. It relates to the bulk yield strengths ($R_{p\ 0.2\%}$) of 880 MPa and 630 MPa observed for the as-received and the carburised states, respectively. At the same time, the embrittling effect of the carburisation treatment seems to lead to appreciable scatter in the number of cycles to failure. The carburisation treatment also changed the LCF failure mode. In the as-received state equiaxed grains and predominantly transcrystalline fractures are observed, whereas the carburised specimens show a more complex fracture structure associated with the strong recrystallisation in the specimen bulk and the dense carbide dispersion close to the surface. Owing to their limited toughness, many cracked carbide particles and cracks extending from fractured carbides are observed in the grain interior as well and on the decorated grain boundaries (Figure 10). Intercrystalline fracture predominates in the outer part of the specimen, while transcrystalline fracture predominates in the bulk.

With $R_{p\ 0.2\%}$ values of 570 MPa, the yield strengths of both the decarburised and the thermally aged states were found to be even lower. Figure 9 shows that the loss in strength which is associated with the coarsening of the microstructure had a strongly detrimental effect on the LCF lives for the larger applied strains (max. total strain of 0.8% and higher), whereas the LCF performance for max. total strains of 0.7 and 0.6% was governed by the presence/absence of carbides: the LCF resistance of the decarburised state remained well below that of the three other states, while the thermally aged state even slightly outperformed the as-received state.

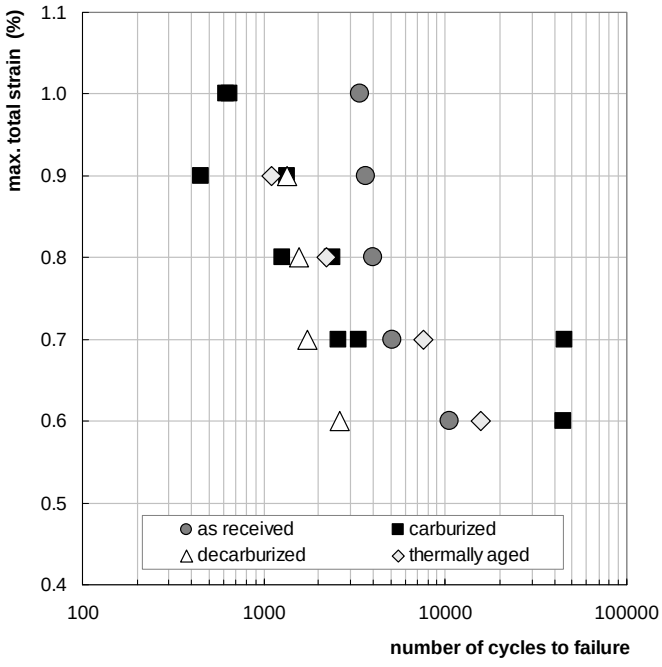

Figure 9. Maximum total strain versus number of cycles to failure of U720Li for LCF tests in strain control at 650°C.

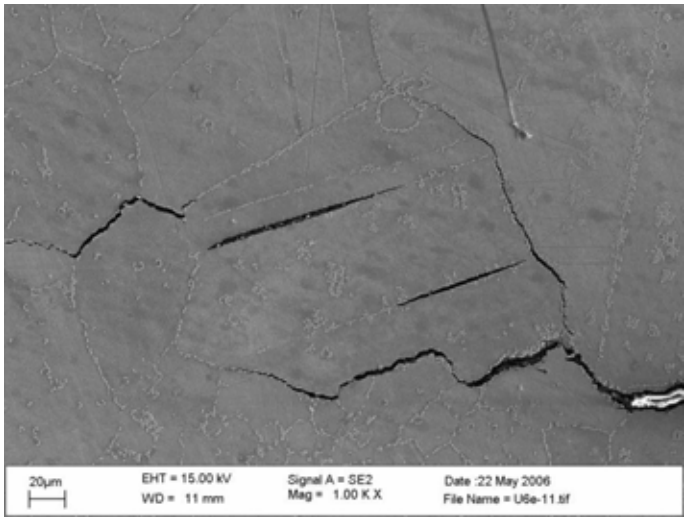

Figure 10. Scanning electron micrograph of carburised LCF tested U720Li showing fatigue cracks extending along carbide decorated grain and twin boundaries.

It is concluded that the materials compatibility with the impurities containing helium coolant deserves further attention, in particular, in a situation where the actual impurity concentrations in the primary circuits of VHTR and GFR reactors are largely unknown, as they will depend on details of the core designs and inventories. The results of the present test campaigns show that, generally speaking, the creep performance of the turbine alloys was significantly reduced by corrosion. It should be mentioned that under strain-controlled LCF conditions, carburised U720Li disk material, for instance, exhibits up to five times shorter lives as compared to the as-received material, albeit the observed stress ranges are lower [11]. As the impure helium applications become more specifically targeted, the effect of coolant environments on the creep and LCF properties will have to be investigated in more detail within future studies.

5. Qualification of ODS steels for high temperature creep service

Oxide Dispersion Strengthened steels have shown promise as candidate heat exchanger materials for operation up to around 1 100°C for more than 20 years. It has been shown that there is little doubt that their oxidation and corrosion resistance will not let them down during extended service in most common environments. Their theoretical creep strengths exceed the requirements for fitness for service by large margins. However the problems of the powder route for manufacture, the potential for major anisotropy and the difficulties of joining, in order to fabricate components, have limited the use of the alloys to no more than a handful of applications. There is a current resurgence of interest in these alloys triggered not only by the GEN IV needs, however this has not been matched by an equivalent manufacturing potential. China and Japan are developing new alloys such as 9Cr ODS but most research results are available for the high chromium ODS steels even though they are hardly any longer manufactured. The JRC work has concentrated on three of these alloys, namely MA 956, ODM 751 and PM 2000 with the original purpose [12] of eventually encouraging the construction of a very high temperature prototype heat exchanger which was unfortunately short lived. Encouraged by manufacturer's data for creep strength of MA 956 derived for sheet material a large creep testing programme was commenced on heat exchanger tubing manufactured from all three alloys. Early results on MA 956 showed a dramatic reduction in strength compared to manufacturer's data when tubes were tested under internal pressure,

thereby subjected to hoop stresses. Immediately the microstructural anisotropy (Figure 11) with some large grains and more importantly very high GAR (Grain Aspect Ratios) could be blamed but nevertheless it was decided to measure also the actual axial/longitudinal strength of the tubes and to this end special specimens were cut out from the tube walls for uniaxial creep testing.

The conclusions of this work are clear from Figure 12 where the inferior creep strengths measured in the tubes' circumferential direction are obvious for all three materials and importantly there was no indication that even the best alloy (PM 2000) would be able to operate for long times when subjected to just 12 MPa in the circumferential direction corresponding to only 25 bar pressure for the dimension of tube tested. Further work [13] showed that even with circumferential notches to the depth of 80% of the wall thickness, failure under internal pressure still took place in the axial direction. All these tests were conducted at 1 100°C which would be very ambitious for VHTR applications and thus there remains some hope. Over the last years it is understood that significant improvements have been achieved through different manufacturing processes including cross rolling of tubes and with this the hoop strengths are likely to increase. Nevertheless for some GEN IV applications even low pressure operation is foreseen and providing the environmental resistance is maintained, application of ODS alloys could follow providing of course that the manufacturing route was commercially available.

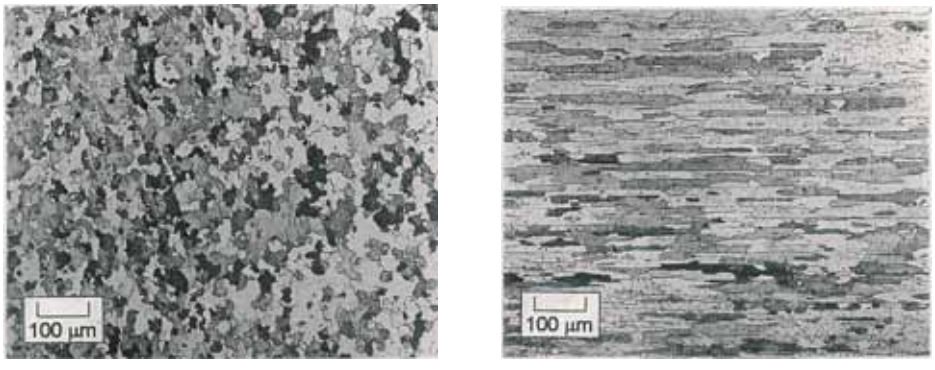

a) transverse b) longitudinal

Figure 11. Microstructural demonstration of anisotropy in MA 956 tubes.

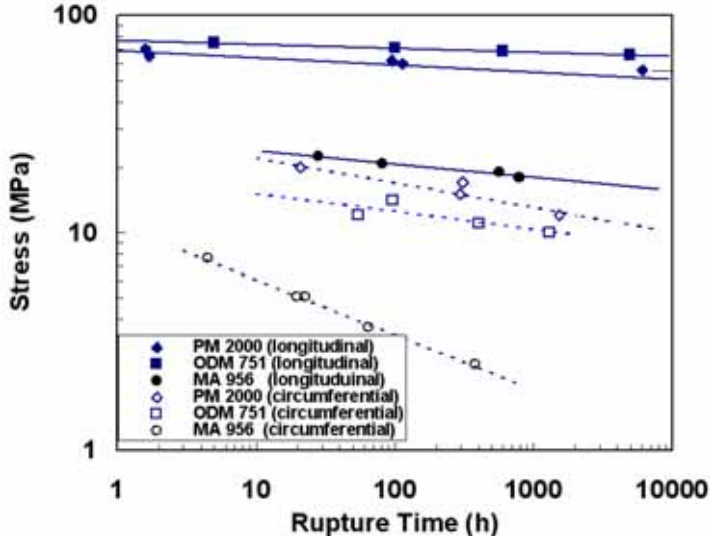

Figure 12. Stress rupture behaviour of three ODS steels, MA956, ODM 751, PM2000 tubes tested at 1 100°C in the circumferential (internal pressure hoop loading) and longitudinal (axial loading) directions.

A further proviso for the introduction of ODS alloys into plant components concerns the experiences related to finding a way to join such materials even to each other. The test procedure chosen for internal pressurization of tubes already introduced the problem of joining as the tubes had to be sealed for the testing. Early attempts to use fusion processes including laser and electron beam welding were unsuccessful due to the dissolution of the strengthening oxide particles. For the above tests only diffusion bonding was found to work satisfactorily but even this was not taken to its limits due to the low pressures which could be employed in the tests. More recently additional routes have been attempted with more success such as inertia welding, plasma assisted diffusion and transient liquid phase bonding. In any creep research programme specifically directed to ODS alloys for GEN IV service both the anisotropy and the joining questions have to be addressed.

6. Study of stress corrosion cracking resistance for components in Super-Critical Water Reactors

Although there is considerable recent experience in understanding the materials resistance to super critical steam coming from fossil fuel fired power plant, apart

from the potentially strong influence of irradiation in the SCWR there is also the question of difference in size, in fact wall thickness, of components (cladding as opposed to boiler tubes) which might be subjected to (stress) corrosion effects. In a corrosion testing programme carried out jointly with VTT [14], it has been shown that (i) austenitic stainless steels exhibit smaller weight gains than ferritic-martensitic or ODS steels, (ii) oxidation rates of austenitic stainless steels increase dramatically above 550^{o}C and (iii) titanium stabilized austenitic stainless steel grades AISI 321 and 1.4970 exhibit lower oxidation rates than the non-stabilized grades AISI 316NG and BGA4.

Stress corrosion cracking (SCC) susceptibility in supercritical water (SCW) was studied for austenitic stainless steel 316L, with the aim to identify the specific failure mechanisms prevailing during slow strain-rate tensile (SSRT) tests in ultra-pure demineralized SCW solution with controlled oxygen content. The SSRT tests were performed using a step-motor controlled loading device in an autoclave at 550^{o}C SCW, under pressures of 250 bar and with oxygen levels at either at 5, 200 or 900 ppb. Besides the strain rate, determined by the crosshead speed, the oxygen content was varied in the series of tests. The specimens SSRT tested to failure were subjected to fractographic analysis, in order to characterize the failure mechanisms.

The cold worked steel shows a propensity to SCC and for most specimens this was indeed observed in that failure was due to transgranular SCC followed by transgranular ductile fracture as shown in Figure 13. In the early stages of this test programme, the ratio of SCC and ductile fracture in the failure process of individual specimens was shown to be affected by the parameters of the SSRT tests. This was particularly clear from the strain rate influence, where slow strain rates increase the sensitivity to SCC, but also the influence of oxygen content on SCC resistance has been confirmed for the highest strain rate. More test results and additional pre-normative research into the validity of the SSRT tests for SCC susceptibility assessment are required before sensitivity maps like the one shown in Figure 14 can be accepted also for implementation in component design procedures.

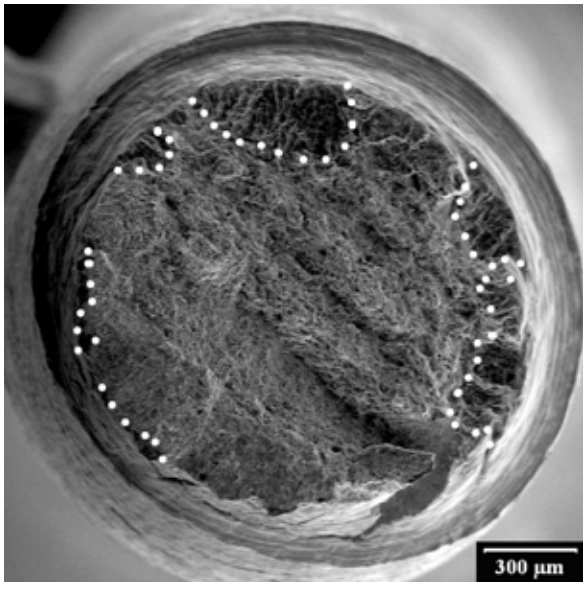

Figure 13. Initiation of failure through transgranular SCC leading to ductile failure.

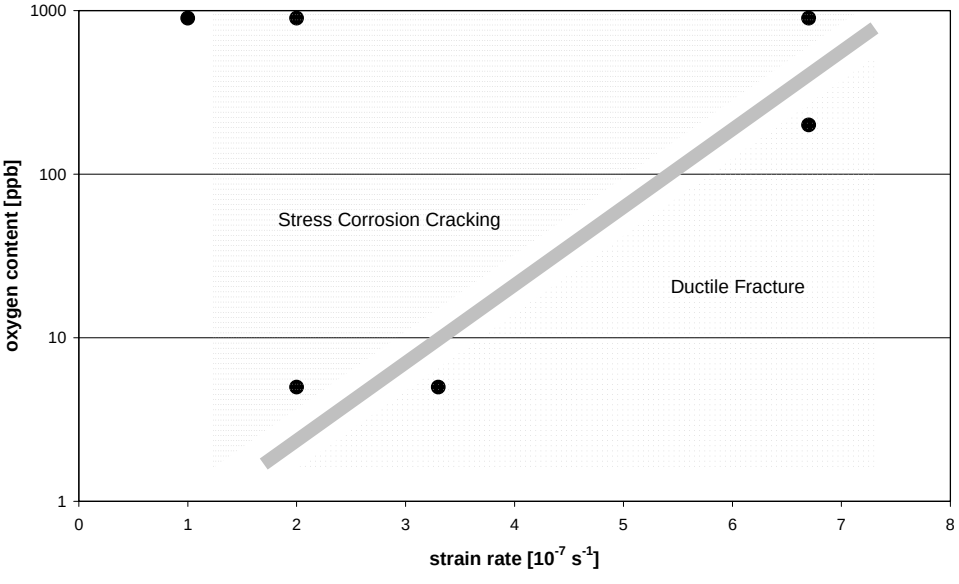

Figure 14. SCC sensitivity map for oxygen content and strain rate.

7. Conclusions

While water-cooled reactors have formed the keystone of 20th century nuclear technology, new coolants (helium gas, liquid metals, supercritical water) are envisaged for the next generation of nuclear systems to be deployed in 2020 and beyond. Also operating temperatures will tend to become higher to increase thermal efficiency and to open up novel industrial process heat applications. At the same time longer operation periods and higher burn-ups are foreseen to ensure economical viability. The combination of increased thermo-mechanical loads, irradiation damage associated with high fluencies and corrosive attack translates into demanding coolant compatibility requirements which have to be met by the construction materials to be deployed in future reactor systems.

The various challenges for construction materials within the six candidate GEN IV concepts have been identified with the emphasis being directed towards those applications where elevated temperature creep is expected to play a prominent role. A series of examples have been detailed where research has been conducted in the authors' laboratory to qualify suitable materials, such as P91, IN792, CM247, U720, 316L stainless steel and various ODS steels for application for GEN IV pressure vessels and piping, for heat exchangers, for gas turbines and for internals.

It can be concluded that there is an urgent need for more research into the qualification of materials for GEN IV service and it is recognised that within Europe, ongoing and new projects guided under the auspices of the European Technology Platform (SNE-TP) are to make valuable contributions whereas globally the GIF cooperation should augment and amplify this effort.

References

Raj, B., Vijayalakshmi, M., Vasudeva Rao, P. R. & Rao, K. B. S. Challenges in materials research for sustainable nuclear energy. MRS Bulletin, 2008. Vol. 33, pp. 327–337.

Murty, K. L. & Charit, I. Structural materials for Gen-IV nuclear reactors: Challenges and opportunities. J. Nucl. Mat., 2008. Vol. 383, pp. 189–195.

Klueh, R. H. & Nelson, A. T. Ferritic/martensitic steels for next generation reactors. J. Nucl. Mat., 2007. Vol. 371, pp. 37–52.

Buckthorpe, D. & Breuil, E. RAPHAEL: Achievements within the VHTR Materials and Components programmes. Proc. of the 4th Int. Topical Meeting on High Temperature Reactor Technology 58122 Sept/Oct, 2008, Washington, D.C., USA.

CEN Workshop Agreement, CWA 15627:2006 E. “Small Punch test Method for Metallic Materials”. Brussels: CEN, 2006.

Blagoeva, D. & Hurst, R. C. Application of the CEN Small Punch Testing Code of Practice to a representative repair welded P91 pipe. Mater. Sci. Eng. A. 2009. (In press.)

Graham, L. W. Corrosion of metallic materials in HTR-helium environments. J. Nucl. Mat., 1990. Vol. 171, pp. 76–83.

Quadakkers, W. J. & Schuster, H. Corrosion of high temperature alloys in the primary circuit helium of high temperature gas cooled reactors – Part II: Experimental results. Werkstoffe und Korrosion, 1985. Vol. 36, pp. 335–347.

Rouillard, F., Cabet C., Wolski K., Pijolat M. Oxide layer formation and stability on a nickel-base alloy in impure helium at high temperature. Oxidation of Metals, 2007. Vol. 68, pp. 133–148.

Dubiez Le-Groff, S., Couturier, R., Guetaz, L. & Burlet, H. Effect of microstructure on the creep behaviour of PM Udimet 720 superalloy – experiments and modelling. Mater. Sci. Eng. A, 2004. Vols. 387–389, pp. 599–603.

Musella, M., Mathis K., Couturier, R. & Hähner, P. (To be published.)

Healy, J. C., Rees, M., Parker, J. D. & Hurst, R. C. The multiaxial creep behaviour of ferritic ODS alloys as candidate materials for high temperature heat exchangers, in: Creep and Fracture of Eng. Mat. & Structures, Eds. J. C. Earthman, F. A. Mohamed. Warrendale PA: TMS, 1997, pp 719–772.

Rees, M., Healy, J. C., Hurst, R. C. & Parker, J. D. Assessment of notched tubular ferritic ODS components subjected to multiaxial creep loading at 1100^{o}C. Int. J. of Fracture, 1996. Vol. 82, pp. 115–129.

Penttilä, S., Toivonen, A., Heikinheimo, L. & Novotny, R. Corrosion studies of candidate materials for European HPLWR. International Congress on Advances in Nuclear Power Plants (ICAPP '08), Anaheim, California, USA, June 8–12, 2008.

Candidate materials performance under Supercritical Water Reactor (SCWR) conditions

Aki Toivonen, Sami Penttilä and Laura Rissanen
VTT Technical Research Centre of Finland
Espoo, Finland

Abstract

The High Performance Light Water Reactor (HPLWR) is working at super-critical pressure (25 MPa) and a core coolant temperature up to 500°C. As an evolutionary step this reactor type follows the development path of modern supercritical coal-fired plants. This paper reviews the results on performance of commercial candidate materials for in-core applications focusing on corrosion, stress corrosion cracking (SCC) and creep issues. General corrosion (oxidation) tests with an inlet oxygen concentration of 125–150 ppb have been performed on several iron and nickel alloys at 300 to 650°C and 25 MPa in supercritical water. Stress corrosion cracking (SCC) susceptibility of selected austenitic stainless steels and a high chromium ODS (Oxide Dispersion Strengthened) alloy were also studied in slow strain rate tests (SSRT) in supercritical water at 500°C and 650°C. Furthermore, constant load creep tests have been performed on selected austenitic steels at 500°C and 650°C in supercritical water (25 MPa, 1 ppm O_2) and in an inert atmosphere (He, pressure 1 atm). Based on the materials studies, the current candidate materials for the core internals are austenitic steels with sufficient oxidation and creep resistance up to 500–550°C. High chromium austenitic steels and ODS alloys steels are considered for the fuel rod cladding due to their oxidation resistance up to 650°C. However, problems with manufacturing and joining of ODS alloys need to be solved. Alloys with high nickel content were not considered for the SCC or creep studies because of the strong effect of Ni on neutronics of the reactor core.

1. Introduction

High Performance Light Water Reactor (HPLWR) uses supercritical water as a cooling medium. In Gen II and III light water reactors, the cooling medium has usually been either sub-critical pure water (Boiling Water Reactor, BWR) or lithiated boric acid-water solution (Pressurized Water Reactor, PWR). The temperature and pressure regimes of BWRs, PWRs and supercritical water reactors (SCWR) are shown in Figure 1.

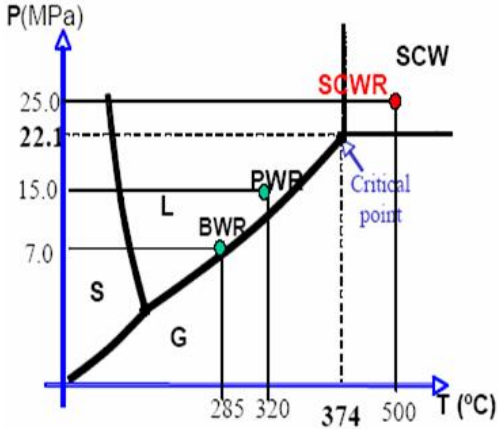

Figure. 1. Operating regime of SCWR/HPLWR compared to Gen II and III LWRs [1].

General corrosion in Gen II and III LWRs is not considered to be a problem in either case, BWR or PWR. A thin, in the range of 1 micrometer, protective film is formed soon on the surface of the construction materials exposed to water at the operating temperatures (270–350°C, depending on the plant type). However, the situation is different at supercritical temperatures and pressures.

The properties of the supercritical water (SCW) are significantly different from those of sub-critical water. SCW resembles a dense gas by its compressibility. At the critical temperature under constant pressure the density, viscosity and solubility of inorganic salts decrease quickly and hydrocarbon solubility increases. A higher steam enthalpy at the turbine inlet reduces the steam mass flow rate needed for equivalent turbine power as in subcritical systems. This lower steam mass flow rate reduces the costs of the overall steam cycle reducing the size of specific components, e.g. condensers and pumps. Even more cost advantages are expected from plant simplifications such as missing

steam separators or primary pumps in case of direct steam cycle at supercritical pressures [2].

However, supercritical water introduces challenges compared to conventional LWRs. Owing to the unique properties of SCW and the extreme operating temperatures and pressures the behaviour of materials in such conditions is one of the main issues to be investigated. The high operating temperature and pressure (280–620°C and 25 MPa, respectively) of HPLWR cause requirements for materials not seen in conventional LWRs. The viability of the SCWRs depends on whether the structural materials of the reactor can withstand the harsh environment for the required time. Candidate materials for structural components are ferritic-martensitic (F/M) steels, including oxide dispersion strengthened (ODS) ones, austenitic stainless steels and Ni-based alloys. Materials generally considered for fuel cladding include chromium alloyed F/M steels and austenitic stainless steels. All the reactor pressure vessel internals components will be designed for periodic replacement so that high neutron fluences (> 20 dpa) will not need to be considered [3].

The results of HPLWR Phase 2 materials studies considering general corrosion, stress corrosion cracking and creep properties of the candidate materials are summarized in this paper.

2. Experimental

The autoclave experiments performed as part of materials studies in HPLWR Phase 2 project included general corrosion tests, stress corrosion cracking tests and creep tests. Initial oxidation/SCC model development was also done as part of the materials work package.

In general corrosion tests, the oxide structures were studied using scanning electron microscope (SEM), energy dispersive spectroscopy (EDS) and X-ray diffraction (XRD). The test matrix included a number of materials from four alloy classes: ferritic/martensitic (F/M) steels, ODS steels, austenitic stainless steels and nickel base alloys. In stress corrosion cracking studies, some of the materials were tested in SCW using slow strain rate tensile tests (SSRT). Creep tests were done in a supercritical autoclave in two atmospheres, in supercritical water and in helium.

2.1 Experimental materials and conditions

The compositions of the studied alloys (Table 1) were measured using optical emission spectroscopy with the exception of Eurofer 97 and Alloy 690 of which the nominal compositions are shown in Table 1.

Table 1. Chemical composition of the tested materials.

	C	Si	Mn	S	P	Cr	Ni	Mo
P91	0.11	0.41	0.43	0.005	0.012	8.3	0.11	0.96
P92	0.08	0.09	0.42	0.006	0.001	8.9	0.02	0.49
ODS(1)	0.021	0.12	0.36	0.007	0.002	9	0.05	0.02
ODS(2)	0.035	0.03	0.4	0.011	0.001	9.2	0.03	0.02
Eurofer97	0.11		0.47			8.9		
PM2000	0.005	0.02	0.08	0.001	0.007	20.1	0.03	0.09
316NG	0.014	0.42	0.8	0.001	0.032	16.6	11.3	2.11
347	0.048	0.29	1.84	0.013	0.026	17.58	10.7	
1.4970	0.095	0.53	1.68	0.001	0.007	15	15.3	1.18
BGA4	0.11	0.49	6.1	0.024	0.02	22.9	15.4	0.14
800H	0.06	0.36	0.67	0.003	0.01	20.5	30.8	0.13
625	0.02	0.07	0.05	0.005	0.001	22.4	bal.	9.1
690	<0.04	<0.5	<0.5	<0.015		28-31	bal.	

	Cu	Al	W	V	Ti	Co	Nb	Fe	Others
P91	0.02	0.01	<0,01	0.23	<0,003	<0,01	0.05	bal.	
P92	<0,01	<0,01	2.1	0.22	<0,01	<0,01	0.05	bal.	
ODS(1)	<0,01	<0,01	1.3	0.21	<0,003	0.01	<0,01	bal.	
ODS(2)	<0,01	<0,01	1.3	0.21	<0,003	0.01	<0,01	bal.	
Eurofer97			1.1	0.2				bal.	0.14 Ta
PM2000	<0,01	5.5	<0,01	0.03	0.43	0.04	0.03	bal.	
316NG	0.23	0.007	0.02	0.04	0.004	0.07	0.01	bal.	
347							0.56	bal.	
1.4970	0.02	0.04	<0,01	0.02	0.45	0.03		bal.	
BGA4	2.7		1.49	0.31			0.61	bal.	
800H	0.06	0.26	<0,01	0.04	0.36	0.09	0.01	bal.	
625	0.03	0.29	0.12	<0,01	0.25	0.06	3.3	2.6	
690						<0.1		7-11	

At VTT, most of the general corrosion test specimens were machined into a coupon form with the dimensions of $25 \times 15 \times 5 \times$ mm. Specimens prepared from BGA4 steel were otherwise similar, but due to the small amount of material available, the sample thickness was smaller, 2 mm. All other samples except for the 1.4970 samples were prepared with the same surface finish, i.e., polished with #1200 SiC paper. Austenitic stainless steel 1.4970 was in the form of thin walled tube used for the fuel cladding in sodium cooled fast breeders. The cladding specimens were cut into 30 mm long tube samples and they had "as delivered" surface finish. The specimens at JRC-IE were either $10 \times 10 \times 3$ or $6 \times 6 \times 3$ mm coupons with the same surface finish as in VTT's coupons.

After the tests the corrosion rate was studied by the weight change of the specimens and oxide thickness measurements using SEM. The specimens were attached to a specimen holder during the exposure. The specimen holder is shown in Figure 2.

Of the original selection of materials for general corrosion tests, PM2000, 316NG, 1.4970, BGA4 and 347H were taken for further stress corrosion cracking studies. The SCC tests were SSRT tests (slow strain rate tensile tests). Samples for the SSRT experiments were electric discharge machined into 30 mm long plate type tensile specimens with a gauge section of 2.0 by 1.5 mm. The specimen geometry and dimensions are shown in Figure 2. Before the tests, the gauge sections of the specimens were polished using standard metallographic techniques.

The test materials for the creep experiments were austenitic stainless steels AISI 316NG, 15Cr15NiTi (1.4970) and TP347H. The tests were performed on similar specimens as the SCC tests.

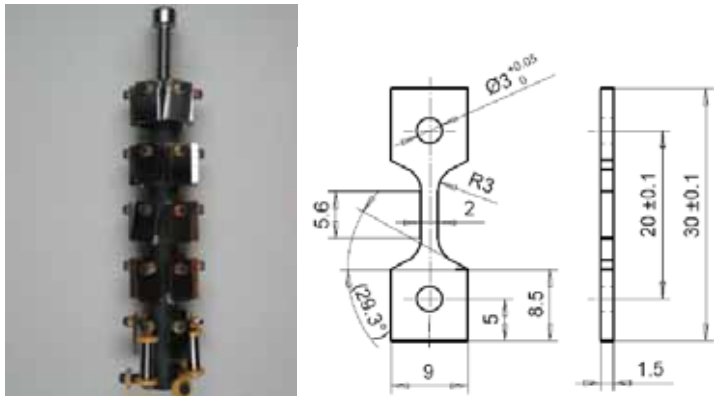

Figure 2. The specimen holder for weight gain test samples (left) and SSRT and creep test specimen with geometry and dimensions (right).

The specimens were exposed to high temperature water in a supercritical autoclave, which was connected to a recirculation water loop, Figure 3. The maximum working temperature and pressure of the system at VTT is 700°C and 42 MPa, respectively. At JRC-IE, the maximum operating temperature is 650°C and pressure 35 MPa. Otherwise the facilities at VTT and JRC-IE are similar. The high pressure loop is pressurised using a diaphragm pump and a back pressure regulator. The maximum flow rate of the high pressure loop is 5 dm^3/h. Slow strain rate tests (SSRT) and creep tests were performed using a step motor controlled loading device.

The weight gain tests (general corrosion tests) were conducted under supercritical and subcritical water conditions over the temperature range of 300°C to 650°C at 25 MPa. The exposure times were up to 1 000 hours. The test solution was demineralized pure water. During the experiment the inlet water conductivity was < 0.1 μS/cm (outlet water conductivity changed from ~0.5–1.0 μS/cm to < 0.2 μS/cm along with increasing exposure time). In normal water chemistry (NWC) the oxygen content was maintained at 0 ppb (JRC-IE), 125 ppb (VTT) or 150 ppb (JRC-IE) and in one exposure done in hydrogen water chemistry (HWC) the hydrogen content was maintained at 30 cc/kg. After the weight gain measurements, the specimens were studied using scanning electron microscope (SEM) in conjunction with energy dispersive spectroscopy (EDS). The structure of the corrosion layers of selected samples were also characterized by X-ray Diffraction (XRD) analysis at JRC-IE. XRD spectra were obtained using Phillips instrument with a PW3830 X-ray generator operated at 40 kV and 50 mA. The X'pert Graphics and identify program was used to identify particular phases using JCPDF database.

Stress corrosion cracking (SCC) susceptibilities of the five selected alloys were studied at 500°C and 650°C under SCW conditions. The samples were strained at a nominal rate of 3×10^{-7} s^{-1}. During the SSRT experiments the inlet water conductivity was below 0.1 μS/cm. The inlet oxygen content was maintained between 100–150 ppb. After SSRT experiments, samples were examined using a scanning electron microscope (SEM) in order to characterize the cracking mode on the fracture and the gauge surfaces. Samples, when needed, were cross-sectioned in order to determine the nature of the cracking mode on the gauge section surfaces.

The possible effect of supercritical water atmosphere on creep of the test materials was studied at temperatures 500°C and 650°C and pressure of 25 MPa. One specimen of each material was tested in an inert helium gas atmosphere at 650°C for reference purpose. The constant load creep tests were carried out at two different stress levels. The stress levels for the creep tests were determined from the slow strain rate tests performed at 500°C and 650°C in SCW. Duration of one test was two weeks because of limited time available for the tests.

3. Results and discussions

3.1 General corrosion test results

Oxidation rate was determined both from weight gain measurements and cross-section samples. The tests were performed mainly in oxygenated water, but a comparison test was also performed in hydrogenated supercritical water. The observed oxidation rates in the hydrogenated water were similar to those in water with 100–150 ppb O_2. Based on those results, the tests were decided to be continued using 100–150 ppb O_2.

At 300°C the weight gains in all materials were too small to be measured and those results are, thus, not further considered. The weight gains of the alloys tested at VTT at 400°C, 500°C and 650°C (exposure time 600 h) are shown in Figure 3.

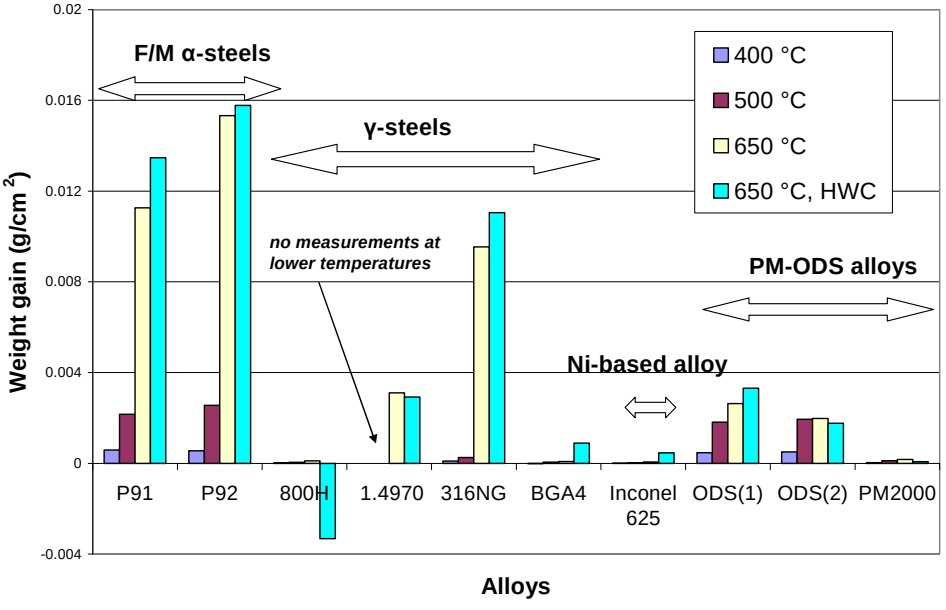

Figure 3. The weight gain test results for tested alloys.

Generally, the tested alloys showed similar trends, i.e., the weight gain was dependent on the test temperature. F/M steels P91 and P92 and 9% Cr ODS steels showed notable weight gains already at 400°C in BWR NWC water. At 500°C, the weight gains were 3–4 times higher than at 400°C in both alloy

classes. However, temperature increase from 500°C to 650°C resulted in a considerable increase in the weight gain in F/M steels, whereas in 9% Cr ODS steels the weight gain did not increase or the increase was minimal. In austenitic stainless steel 316NG, the weight gain was rather small up to 500°C, but at 650°C it was almost as high as in the F/M steels. This indicates that the oxidation mechanism of austenitic stainless steel 316NG changes between those temperatures. The weight gain of the 15%Cr 15%Ni austenitic stainless steel 1.4970 was measured only at 650°C. The measured weight gain was in the same range as in 9% Cr ODS steels, i.e., between that of high chromium or high nickel alloys and austenitic stainless steel 316NG. Similar weight gains as in 1.4970 were seen also in 347 steel. High chromium (20% Cr) and high nickel alloys, i.e., alloys BGA4, 800H, 625 and 690, showed small weight gains at all temperatures.

At 650°C (~30°C above the estimated fuel cladding temperature of ~620°C), the general corrosion rate in austenitic stainless steels, e.g., 316NG, is in the range of a millimetre/year at 25 MPa pressure assuming linear oxide growth. The conventional F/M steels showed even faster oxidation rates at 650°C as expected (1.5 mm/year). Thus stainless steels are generally not suitable candidates for thin walled SCWR internal components if linear growth is assumed.

Austenitic stainless steel 1.4970, which is used for sodium cooled reactors, has sufficient creep strength up to 620°C and acceptable swelling resistance. The general corrosion properties observed within this study are, however, somewhat ambiguous: different oxidation rates were observed in different locations of the samples. This steel requires further studies.

With respect to general corrosion rate, Alloy 800H, Alloy 625, BGA4 steel and 20% Cr ODS steel PM2000 seem to have adequate general corrosion resistance for fuel cladding. However alloys 800H and 625 can be excluded because of high Ni content which cause problems with neutronics. BGA4 steel and 20% Cr ODS steel PM2000 are acceptable for fuel cladding with respect to oxidation rate at 650°C and Ni content. However, it should be noted that F/M steels (like PM2000) with chromium content above ~14% are susceptible to 475°C embrittlement. The properties of BGA4 steel proved to be unacceptable in further SCC studies.

However, during the project surface cold work was observed to improve the oxidation resistance considerably. A tube sample exposed after machining without surface polishing is shown in Figure 4 together with tubes with as-received and also with polished surfaces. The specimens were exposed to

supercritical water at 650°C for 1000 h. It is noticeable that the machined sample (sample #1) has a transparent, very thin, oxide layer. The reason to the slow oxidation of the surface cold worked specimen is assumed to be high defect density in the surface layer resulting in a more homogeneous diffusion than in solution annealed and/or polished surfaces with slow bulk diffusion inside the grains and fast diffusion along the grain boundaries.

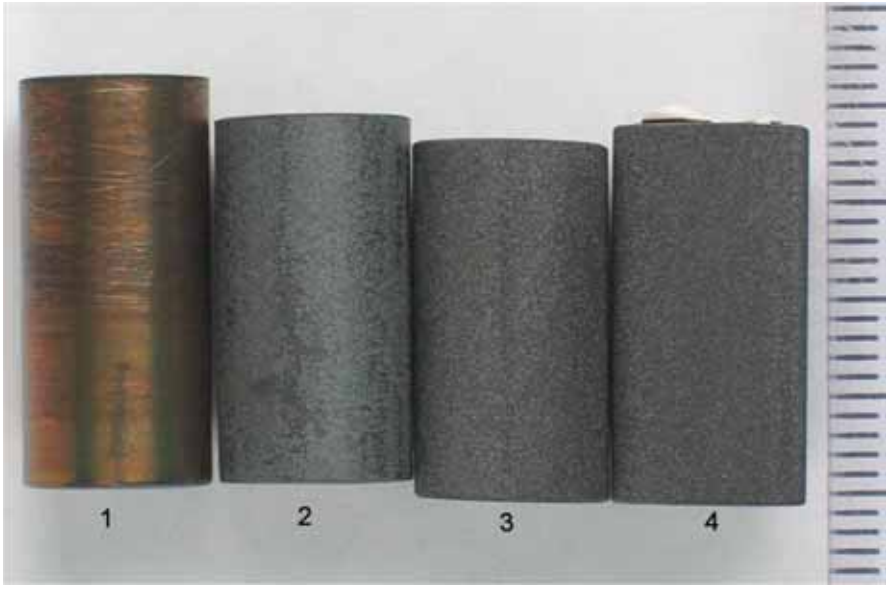

Figure 4. Alloy 316L tube samples after 1000 h exposure under SCW conditions at 650°C: Sample 1) machined with blunt edge hard metal cutting tool, 2) "as received", 3) surface finish after machining with #600 emery paper and 4) with #1200 emery paper.

3.2 Stress corrosion test results

For the thin-walled components in the design of an SCWR, stress corrosion cracking is anticipated to be an important degradation mode that needs to be understood and controlled.

Austenitic alloys, 316NG, 347H, 1.4970 and BGA4, and F/M ODS steel PM2000 were tested in SCW between 100–150 ppb of dissolved oxygen content at temperatures of 500°C and 650ºC. The tests were slow strain rate tensile tests using a strain rate of 3×10^{-7} 1/s. Stress-strain curves of the tested specimens at 500°C and 650°C are shown in Figure 5a and b, respectively. All austenitic

stainless steels exhibited strain hardening at 500°C although the degree of strain hardening of 1.4970 was rather low. The low degree of strain hardening results from cold work done when the component from which the specimen was cut was prepared. Typically all austenitic stainless steels behave in the same way as 1.4970 after cold work. Cold work also decreases the strain to failure, which can be seen in Figure 5a when 1.4970 steel is compared to the other austenitic stainless steels which were in solution annealed condition. The oxide dispersion strengthened steel PM2000 shows two different yielding values because the specimen was loaded using a strain rate of 3×10^{-8} 1/s in the beginning after which the strain rate was changed to 3×10^{-7} 1/s (at about 10% strain). The sudden increase in the stress level when the strain rate was changed indicates that there is a time dependent component present in the stress-strain behaviour, i.e., creep. The PM2000 specimen did not show any considerable strain hardening.

When Figures 5a and b are compared, it is evident that the test temperature has a considerable influence into the stress-strain behaviour of all of the tested alloys. All strength values have decreased considerably as the test temperature has been increased from 500 to 650°C (strain rate was the same, 3×10^{-7} 1/s, in both cases). Especially remarkable decrease has taken place in the yield stress of PM2000, which has decreased to ~1/3. The reason for this decrease is not clear at the moment. The material suppliers' data sheet give a yield strength of ~300 MPa at 600°C and ~200 MPa at 700°C. The decrease in the yield stress was confirmed by performing a second test (interrupted at 17% strain) using the same test parameters, see Figure 5b.

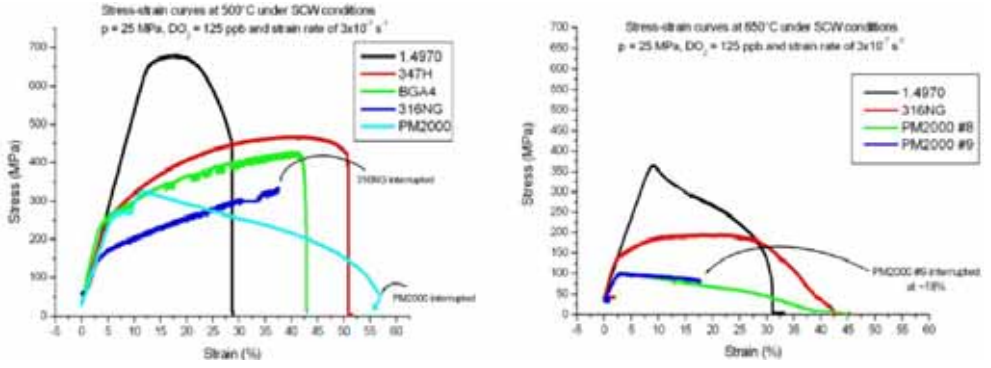

Figure 5. Stress-strain curves for the studied alloys under SCW conditions at a) 500°C and b) 650°C.

Post test SEM studies of the SSRT specimens showed that 347H, 316NG and 1.4970 are possibly slightly susceptible to SCC at 500 and 650°C. No clear SCC was observed on the fracture surfaces, but on side surfaces there were small cracks of which morphology, however, could not be identified except in the case of 316NG (which had both inter and transgranular cracks, IGSCC and TGSCC). Experimental creep resistant steel BGA4 specimen contained a considerable amount of IGSCC both on the fracture surface and the side surfaces after the test at 500°C. Due to the SCC susceptibility, this steel was not tested at 650°C. At 500 and 650°C, PM2000 did not show any susceptibility to SCC at all. Necking occurred until the specimen failed (i.e., the fracture location was almost “knife edge” sharp). However, the observed maximum stresses on PM2000 specimens remained considerably lower than expected based on the material suppliers creep and tensile data.

The tested austenitic stainless steels 1.4970, 347H and 316NG appear to be rather resistant to SCC when compared to the resistance of BGA4. BGA4 had a lot of secondary cracks on the gauge section and clear intergranular cracking on the fracture surface after the SSRT test at 500°C. Because of the SCC susceptibility, no further tests were performed at higher temperature on this alloy. The other tested stainless steels showed no clear SCC susceptibility either at 500 or 650°C. However, the SSRT results on PM2000 are not in line with the creep strength specifications of the ODS alloy. Thus, more studies are needed in the behaviour of high Cr F/M ODS steels in supercritical water.

Also, the main problems of the ODS materials are that they are difficult to weld and expensive. Therefore these materials are recommended to applications where high strength and oxidation resistance are needed, but little additional

joining is required. A possible road for the fuel cladding development, if ODS steels appear not to be a suitable solution, may be coating of austenitic stainless steels or F/M steels.

3.2.1 Modelling of general corrosion and SCC

Corrosion resistance is one of the key requirements for the candidate materials to be used in SCWR and thus necessitates understanding the corrosion mechanisms of alloys at high temperatures and pressures. In order to understand the behaviour of the metal/oxide film/coolant system on a theoretical level, physical-chemical modelling is of utmost importance. At the moment, there are several papers in the open literature considering general corrosion of candidate materials for SCW. Tests have been conducted in a wide range of conditions. However, temperatures used in the experiments have been systematically lower than the estimated peak temperature of the fuel cladding in a supercritical reactor, i.e. ~630°C. Also exposure times in autoclave tests have been usually very short, typically < 1000 h.

The oxidation and SCC modelling based on original approach proved to be difficult. In-situ electric impedance measurements of the oxidation processes were impossible to be performed using electric impedance method. Typically electric impedance method yields information about the ionic processes taking place during oxidation. However, in supercritical water the oxides appear to be electrically conductive which prevents the measurement of ionic processes. A backwards calculation method is proposed for the future studies. This method is based on the measured oxide composition (EDS, GDOES or some other analysis method applicable for the post exposure oxide structure characterization) and diffusion rates of the elements.

The method was used in order to obtain estimates of kinetic and transport parameters for the oxidation of AISI 316L(NG) and F/M steel P91 in SCW conditions. The predictions of the model were compared with the experimentally measured depth profiles of the elements in the oxide. At this point, the types of the defects in the oxides, via which the respective metallic elements are transported through the inner layer of the oxides, are not distinguished. Thus, the reaction rate constant at the alloy/inner layer interface for different elements e.g. for Fe (k_{1Fe}) can be regarded as a sum of the reaction rate constants of oxidation of Fe. On the other hand, the diffusion coefficients D_{Cr}, D_{Fe}, D_{Ni} and D_{Mn} can be regarded as characterising the overall transport of cations through the inner layer.

According to the PDM and MCM models (Point Defect and Mixed Conduction models, respectively) [4, 5] the inner layer growth proceeds via the sequence of reactions involving the generation of normal cation positions and injection of oxygen vacancies at the alloy/film interface, their transport via a diffusion-migration mechanism and subsequent consumption at the film/ electrolyte interface via a reaction with adsorbed water. In parallel to that process, metal cation dissolution through the layer, involving either the generation of cation vacancies at the outer interface, their transport and consumption at the inner interface, or generation, transport and consumption of interstitial cations, respectively, is also expected to occur. Due to the low solubility of the constituent metals in the high-temperature SCW, the dissolved cations are expected to mainly redeposit and form the outer layer, or react directly with water and/or oxygen at the compact layer/water interface to form the outer part of the oxide.

In the case of SCW, in analogy to what has been found in subcritical water at temperatures above 150°C, the large number of defects in the oxide films at high temperatures is not likely to support the high electric field conditions. Depending on the magnitude of the electric field strength the mathematical treatment of the transport process should be carried out in a different way. Thus the low-field approximation of the generalised transport equation given by Fromhold and Cook is used in the present study [6]. The non-stationary transport equation results from the differentiation of the flux with respect to the change of the concentration over time and the following expression for a given component of the film is obtained in the low-field approximation:

$$\frac{\partial y_j}{\partial t} = D\frac{\partial^2 y_j}{\partial x^2} + D\frac{XF\vec{E}}{RT}\frac{\partial y_j}{\partial x} \tag{1}$$

where X is the valence of the ions, F is the Faraday constant, E is the electric field strength, R is the gas constant, and T the absolute temperature. After the exposure of the samples, the location of the metal/film interface in the coupon sample was determined from the experimental profile of the concentration of oxygen obtained by GDOES. After that, the profiles of the mass fractions n_i of main metallic elements (Fe, Cr, Ni, Mn) were normalized to the total metallic content n_{TOT} of the film:

$$y_i = \frac{n_i}{n_{TOT}} \tag{2}$$

and the respective profiles were recalculated with the estimated position of the metal/film interface taken as zero. As a first step of the calculation, the system of equations is solved subject to the initial and boundary conditions using a Crank-Nicholson method in order to obtain the compositional profiles in the inner layer. The problem has been approached as follows: the depth profile of a metallic oxide constituent j = Fe, Cr, Ni and Mn, can be expressed as the dependence of its molar fraction, $y_j = c_j V_{m,MO}$, where c_j is the molar concentration and $V_{m,MO}$ the molar volume of the phase in the layer. It is assumed that the value of the molar volume is the mean molar mass of a spinel oxide which is sufficiently close to Fe_3O_4 because the atomic masses of Cr, Ni and Mn are rather close to that of Fe. The resulting value of $V_{m,MO}$ is then 44.5 cm^3/mol. Certainly this is an oversimplification with regard to the fact that several other phases such as FeO has been reported to form during oxidation of ferritic and ferritic-martensitic alloys in supercritical water [1]. Clearly, the transport parameters of individual constituents would be different in different phases, however, a further complication of the model was judged precarious in view of the lack of systematic studies of the detailed phase composition of the oxides at this stage.

At this stage of the modeling, we do not consider the existence of a transition layer between the bulk alloy and the alloy/oxide interface in which the composition of the underlying alloy is modified, which means that also possible internal oxidation reactions are neglected. In other words, the respective mass fractions at the alloy / film interface are taken as equal to the fractions in the bulk alloy $y_j(x,0) = y_{j,a}$. Albeit admittedly a crude simplification, this assumption facilitates the computations markedly. The introduction of the transition layer at a later stage of this work is, however, conceptually straightforward. The boundary conditions at the film/electrolyte interface are given by the steady-state concentrations of the respective metallic constituents at that interface obtained by the steady-state solution of the transport equations. More detailed description of the equations used in this study (i.e. transient diffusion-migratation equations for each metallic elements and boundary condition equations at both interfaces) are shown in papers [6] and [7].

Figure 6 shows the in-depth concentration of metallic elements as molar fractions normalized to the total amount of metallic elements to exclude the influence of the oxygen profile on their distribution. The calculated depth profiles are shown as solid lines. Based on the depth profiles, the extent of the Cr enrichment in the inner layer on P91 seems to be independent on temperature. Cr

enrichment reflects the preferential oxidation of this element and its slower transport rate through the inner oxide. Nickel is enriched both in the inner layer and at the inner layer/alloy interface, which reflects both its slower oxidation and transport rate through the inner oxide. Contrary to Cr and Ni, Mn is rather strongly enriched in the outer layer of the oxides at all three temperatures. This phenomenon reflects the fact that the transport rate of Mn in the oxide is noticeably higher than that of Cr or Ni. The extent of Cr enrichment in the inner layer on AISI 316L(NG) is in general smaller at 600 and 700°C than at 500°C. The inner oxide at 500 and 700°C is also enriched in Mn. Both Cr and Ni are practically absent in the outer layers on the two materials, which are composed of Fe with a certain amount of Mn. Alternatively, it could be due to the fact that Cr and also Ni are retained in the inner layer due to their slower transport rate in comparison to Fe.

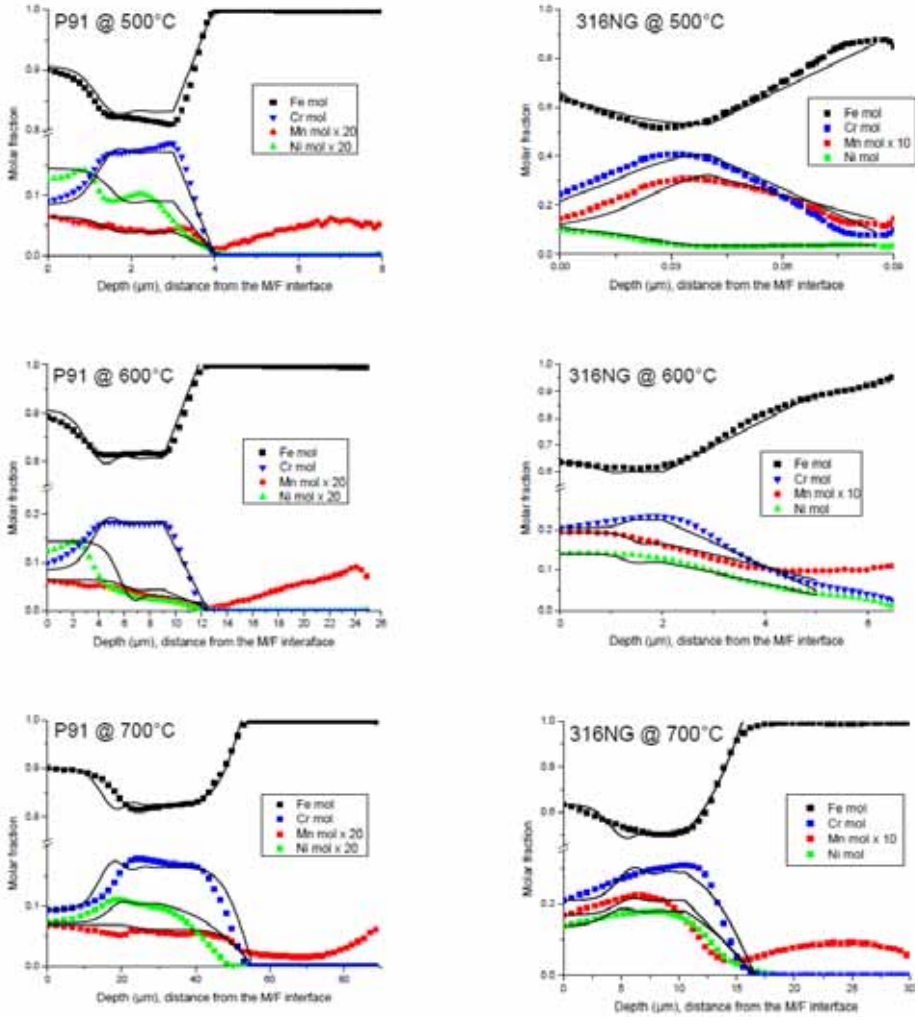

Figure 6. Measured and calculated (solid line) in-depth concentration of metallic elements on oxide films formed on F/M steel P91 (left) and AISI316L(NG) (right) at temperatures of 500°C, 600°C and 700°C after 100 h exposure in SCW as function of distance from the metal film (M/F) interface.

The backward calculation procedure based on MCM appears to be usable in order to estimate the kinetic constants and diffusion coefficients of individual alloying components for oxide films forming processes on F/M steel P91 and AISI 316L(NG) stainless steel in SCW. Thus the described calculation results demonstrate that the proposed framework can serve as a modelling approach to the growth of the oxide films. The apparent next step following this study is to

adopt this calculation procedure to kinetic and transport parameters for long-term experiments in order to test the ability of the proposed approach to predict much thicker oxide layer compositions. Further modifications of the model to allow for the co-existence of different phases in the oxide layers, as well as for internal oxidation processes, are in progress and will be communicated in the near future.

Together the creep and oxidation processes, apparently, contribute to stress corrosion cracking. Thus, a model called selective dissolution - vacancy creep, SDVC, is proposed as an approach to SCC modelling in SCW. This model has been suggested to be applicable also in hydrogenated water [8]. Vacancy injection into the base material, resulting from selective oxidation or dissolution, is expected to take place and to enhance the creep rate at the crack tip. In SCW, the oxidation seems to enhance also the bulk creep rate. This effect is speculated to result from vacancy injection into the bulk metal. The effect of the vacancy generation on the creep rate should be dependent on the oxidation rate/specimen thickness, i.e., in thick walled components this effect is expected to be negligible. However, the stresses ahead of an existing crack tip in a thick walled component are always higher than the bulk stress (in the range of yield stress or higher depending on the stress triaxiality), so based on the suggested model, stress corrosion cracking can take place even at much lower nominal stress levels.

The mechanistic processes in steam, high temperature water and SCW are thought to be the same. The initial model was developed already in the middle of 1990's. The development was virtually stalled until now, as the creep taking place in the crack tip could not be verified experimentally earlier. Bulk metal creep was not observed at Gen III LWR temperatures in stainless steels by creep tests in water at subcritical temperatures. However, the creep tests of HPLWR Phase 2 indicate that the environment indeed enhances the creep rate and the model could be applied in SCW. Next, the model should be developed further so that quantitative predictions can be done for SCC propagation rates.

3.3 Creep test results

The creep tests were done in a supercritical autoclave at the temperatures of 500°C and 650°C and 25 MPa pressure. The testing time for the autoclave tests was limited to max. 500 h. All the materials were tested in two atmospheres, in supercritical water and in helium. The main objective of the creep testing was to answer the question whether the oxidising supercritical water has an effect on

the creep rate. Based on the results, the oxidation enhances the creep rate at least in the primary stage of the creep process in thin walled components.

To equalise the method to determine the strain rates, linear fits were done to the curves. An example of the linearization of 316NG test data is shown in Figure 7. The fits seem to result in applicable average strain rates for comparison purposes. As can be seen in Figure 7, the strain rate in SCW was considerably higher than in He.

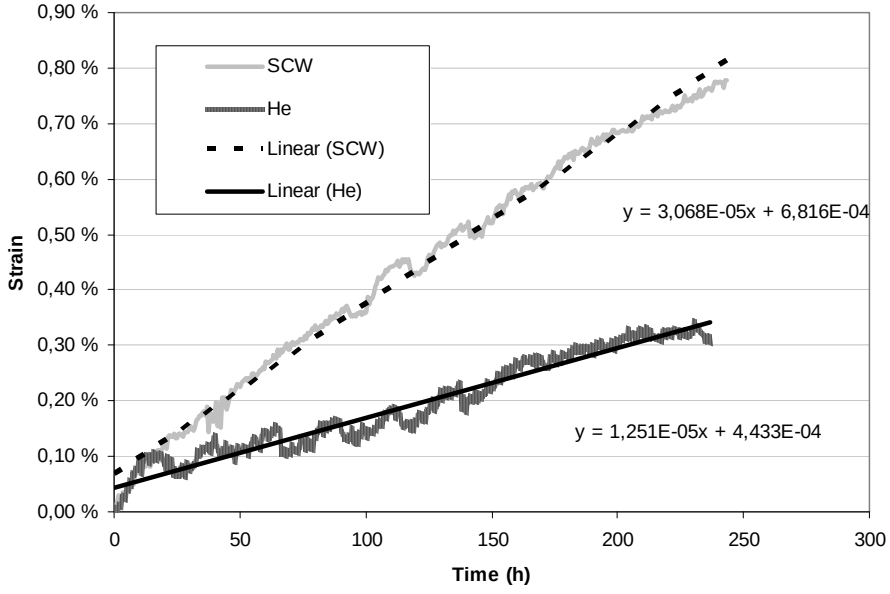

Figure 7. Strain as a function of test duration for 316NG steel both in SCW and He. The test temperature was 650°C and the stress level 130MPa.

The strain rate comparisons for both stress levels at 650°C are collected in Table 2. More detailed description of the creep studies and results are presented by Rissanen [9].

Table 2. Creep strain rate comparison of the test materials loaded to both lower and higher stress levels at 650°C in SCW and He.

650°C	Strain rate SCW/He
316NG: 130 MPa	1.6
316NG: 90 MPa	2.5
347H: 149 MPa	1.2
347H: 215 MPa	2.4
1.4970: 200 MPa	≈ 1
1.4970: 250 MPa	≈ 1

The oxidation process seems to enhance the creep rates, so this should be taken into account in the design phase. However, this is probably the first study where this phenomenon has been observed, so further studies are needed and the phenomenon should be verified independently by another laboratory. There is always the possibility, that the observed phenomenon is a relict of the testing method or the equipment used in the tests.

4. Conclusions

Results of material testing carried out in the frame of HPLWR Phase 2 FP6 project showed that identification of the fuel cladding material operating in supercritical water conditions is one of the most critical issues due to very high surface temperatures foreseen for fuel and its cladding exposed to SCWR conditions (T > 600°C). Currently, there is no commercially available low Ni material licensed for reactor use which would sustain long term exposure in supercritical water at temperatures higher than 600°C. The reason is either poor corrosion and SCC resistance or poor mechanical properties in high temperature environments. ODS steels seem to be the most perspective materials for applications in high temperature supercritical water environment but their commercial production was either stopped (e.g. MA956, MA957 or PM2000) or their development is still under way. Eurofer 97 ODS steel is the only ODS steel licensed for application in nuclear industry, however its general corrosion resistance is not acceptable at temperatures above 500°C under SCW conditions.

A joint European project namely SCWR-FQT (Supercritical Water Reactor – Fuel Qualification Test) will be implemented in the end of year 2010 in a world wide international collaboration with Chinese partners. Thus, continuity for candidate materials research in the near future is seen as an essential part of the

concept study. Materials work package (WP4) of FP7 SCWR-FQT program will focus on evaluation of general corrosion and SCC resistance of three austenitic stainless steels 1.4970, TP347H and 316L, which should be pre-qualified for application as a cladding material for fuel qualification tests in supercritical water conditions. On the basis of the experimental results assessment and calculations, fuel rod mock-up will be designed and manufactured for additional general corrosion test in the experimental supercritical water loop (SCWL) which is available in the Nuclear Research Institute Rez as a result of HPLWR Phase2 project.

References

1. Was, G. S. et al. Corrosion and stress corrosion cracking in supercritical water. Journal of Nuclear Materials, 2007. Vol. 371, No. 1–3, pp. 176–201.

2. Schulenberg, T. & Starflinger, J. Core design concepts for high performance light water reactors. Institute for Nuclear and Energy Technologies, Forschungszentrum Karlsruhe, Germany, 4.6.2007. Pp. 1–17.

3. Buongiorno, J. et al. Supercritical water reactor (SCWR) survey of materials experience and R&D needs to assess viability. INEEL/EXT-03-00693, Revision 1, September 2003. http://www.inl.gov/technicalpublications/Documents/26998 63.pdf.

4. Betova, I. et al. Modelling of the oxide film growth and layer restructuring on stainless steels in LWRs. Materials Science & Technology 2007 Conference and Exhibition, Detroit 2007. Paper 348355.

5. Betova, I. et al. Mixed-conduction model for stainless steel in a high-temperature electrolyte: Estimation of kinetic parameters of inner layer constituents. Journal of The Electrochemical Society, 2008. Vol. 155, No. 2, pp. C81-C92.

6. Bojinov, M. et al. Electrochemical study of the passive behaviour of Ni-Cr alloys in a borate solution – a mixed conduction model approach. Journal of Electroanalytical Chemistry, 2001. Vol. 504, pp. 29–44.

7. Penttilä, S. et al. Characterization of candidate materials in SCWR conditions – estimation of kinetic parameters of individual corrosion layer constituents. ICAPP'10, San Diego, CA, USA, 13–17 June, 2010. Paper #10004.

8. Aaltonen, P. et al. Vacancy-creep model for EAC of metallic materials in high temperature water. Corrosion 96, NACE. Colorado, Denver, USA, 25-28 March 1996. Paper. 81. 12 p.

9. Rissanen, L., Creep in Gen IV nuclear applications, Baltica VIII - Life management and maintenance for power plants, Helsinki–Stockholm–Helsinki, 18–20 May, 2010.

Effect of hydrogenated low temperature water on fracture toughness of nickel-based weld metals

Matias Ahonen*, Ulla Ehrnstén and Hannu Hänninen**
VTT Technical Research Centre of Finland
**Aalto University School of Science and Technology
Espoo, Finland
*Visiting scientist at OECD Halden

Abstract

Nickel-based alloys are susceptible to a form of hydrogen embrittlement, Low Temperature Crack Propagation (LTCP), which can cause severe degradation of the fracture resistance of nickel-based alloys. LTCP may occur in low temperature water, with the highest susceptibility reported at about 55°C, with high stress and slow loading rate in pre-cracked Ni-based materials. Although LTCP has not been reported in commercial reactors, the susceptibility of different alloys is important to establish. As a part of the Finnish Reactor Safety Program, SAFIR 2010, the effect of hydrogenated Pressurized Water Reactor, PWR, primary water on the LTCP susceptibility of nickel-based weld metals of Alloy 182, 82, 152 and 52 was studied performing J-R–tests at a slow displacement rate in simulated low temperature PWR primary water. The results revealed that Alloy 182 is the most susceptible nickel-based weld metal to LTCP. Pure weld metal specimens were substantially more susceptible to LTCP than the dissimilar metal weld specimens. Pre-exposure to high temperature hydrogenated water did not affect remarkably the fracture toughness of any of the test materials.

1. Introduction

Low Temperature Crack Propagation (LTCP) is a hydrogen-induced degradation mechanism that has been observed in laboratory conditions in nickel-based weld metals of Alloy 182/82 and Alloy 152/52 [1–6] and in high strength Alloy X-750 [7]. LTCP may occur in hydrogenated water, at low temperature, with slow loading rate and high stress in pre-cracked Ni-based materials. The phenomenon occurs especially in the temperature range of 50 to 150°C. The decrease in fracture toughness J_{IC} values for Alloys 82 and 52 in 54°C water containing 150 cm^3 H_2/kg H_2O is reported to be an order of magnitude lower compared with results obtained in air tests [2–3]. The effect of hydrogen is discovered through studies [4, 5, 7–8] consistently showing that increasing hydrogen content decreases the fracture toughness of nickel-based materials. However, recently it has also been reported that even at very low hydrogen contents (3–5 cm^3 H_2/kg H_2O) the reduction in fracture toughness is significant [9].

A typical feature of LTCP is a transition in the cracking mechanism from ductile dimple fracture to intergranular (IG) cracking. The microstructure is considered to have a crucial effect on the LTCP susceptibility of nickel-based alloys [9]. During welding small niobium- and titanium-rich carbides form at the grain boundaries, and act as hydrogen traps. In multiple bead welds the recrystallisation in solidified beads causes a decrease in LTCP resistance through localization of deformation in these lower strength recrystallised areas [10].

Most studies have been performed using pure weld metal specimens. The effect of loading rate on LTCP susceptibility in dissimilar metal weld specimens was studied previously at VTT [11]. The specimens were SE(B) type and they were cut off dissimilar metal welds (DMW) of Alloy 182 and 52. The results show, that the fracture toughness of the studied DMW samples was practically unaffected by the environment at high loading rate of 6.7 mm/h. At a slower loading rate, 0.1 mm/h, most Alloy 182 DMW specimens showed typical features of LTCP including interdendritic fracture and significant reduction in fracture toughness. However, the Alloy 52 DMW specimens did not show any signs of LTCP even at the slow (0.1 mm/h) loading rate. Further tests were performed on pure weld metal specimens to compare the LTCP susceptibility of pure and dissimilar metal welded Ni-based weld metals.

2. Methods

The fracture toughness tests were performed using a pneumatic servo-controlled loading device and the crack growth was measured using the potential drop (PD) method. The J-R-curves were calculated according to the standard test method for measurement of fracture toughness ASTM E 1820-01.

2.1 Specimen preparation

The 10 x 10 x 55 mm SE(B) test specimens of pure weld metal of Alloy 182, Alloy 82, Alloy 152 and Alloy 52 were cut from the samples presented in Figure 1. The samples were fabricated by welding multiple beads on crossed steel bars, as presented in Figure 2. The chemical compositions of the weld wires are presented in Table 1 [12]. Welding was carried out manually without post-weld heat treatment. The specimens were cut from the edges of the pure weld metal blocks (Figure 1), as presented in Figure 3. All the specimens were machined, fatigue pre-cracked to nominal 0.5 a/W and 20% side grooved. The microstructures of the materials were characterized using optical microscopy and the fracture surfaces were examined using scanning electron microscopy (SEM).

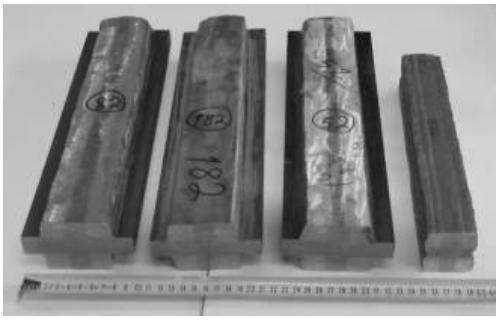

Figure 1. Pure weld metal test blocks of Alloy 82, Alloy 182, Alloy 52 and Alloy 152 (from left to right). [12]

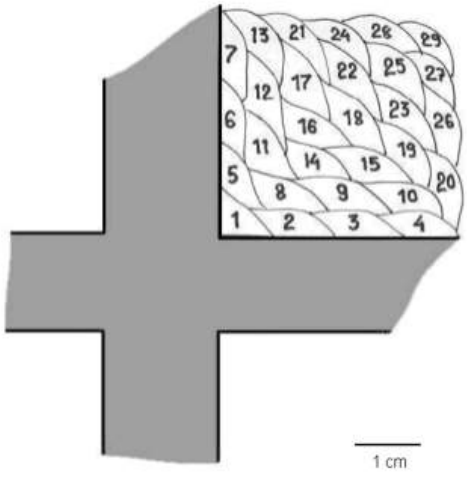

Figure 2. Welding sequence of the pure weld metal test block of Alloy 182. [12]

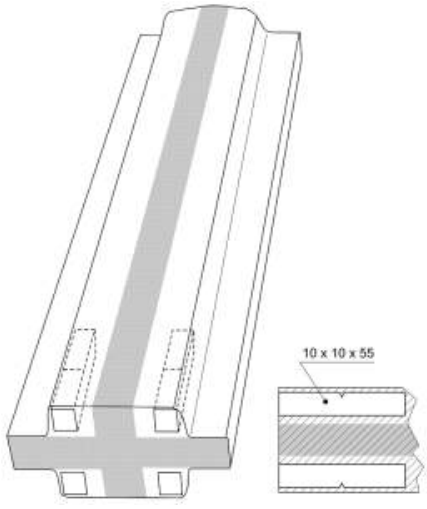

Figure 3. Cutting of the specimens from the pure weld metal test blocks. Dimensions are given in mm.

Table 1. Chemical compositions of the weld filler materials. [12]

	Alloy 182	**Alloy 82**	**Alloy 152**	**Alloy 52**
C	0.03	0.04	0.05	0.03
Si	0.80	0.03	0.04	0.13
Mn	6.50	2.98	4.48	0.24
Cr	6.50	2.98	3.48	0.24
Ni	68.00	72.60	55.20	59.28
Nb	1.80	2.47 (Nb+Ta)	1.54 (Nb+Ta)	<0.02 (Nb+Ta)
Ti	0.10	0.34	0.09	0.51
Fe	6.70	1.00	10.39	9.80
Al	-	-	0.06	0.72

2.2 Environments and Loading

Fracture toughness tests were performed using a pneumatic servo-controlled loading device. The tests were conducted in room temperature air and in an autoclave in hydrogenated water. Air tests were performed at ambient

temperature in order to define the original fracture toughness values for the test materials. The environmental tests were performed at 55°C in water containing boric acid (200 ppm) and lithium hydroxide (2.1 ppm) resulting in pH 7.4. Two target levels of hydrogen concentration were chosen, 100 and 30 cm^3 H_2/kg H_2O. The latter is typical for PWR plants. Temperature of 55°C is the most severe temperature based on the open literature. The effect of pre-exposure at high (operation) temperature was investigated by performing a test series in which the autoclave temperature was elevated to 300°C and maintained for 24 hours prior to testing, and then cooled to the testing temperature 55°C. The hydrogen content in the pre-exposure test series was set to be 100 cm^3 H_2/kg H_2O at the temperature of 55°C.

The test matrix for the J-R-tests is presented in Table 2. The loading rate was 0.1 mm/h in every test series, which corresponds to a test time of approximately 19 hours.

Table 2. Test matrix for the J-R tests comprising totally 16 specimens. The environment was hydrogenated water (T = 55°C) containing boric acid (200 ppm) and lithium hydroxide (2.1 ppm) additions.

Material	Specimens	Air/Environment	Hydrogen content (cm^3 H_2/kg H_2O)	Pre-exposure
Alloy 182	A1	Air	-	
	A2, A3	Environment	100	
	A5-A7	Environment	100	24h, 300 °C
	A8, A9	Environment	30	
Alloy 82	B1	Air	-	
	B2-B4	Environment	100	
	B5-B7	Environment	100	24h, 300 °C
	B8, B9	Environment	30	
Alloy 152	C1	Air	-	
	C2, C3	Environment	100	
	C5-C7	Environment	100	24h, 300 °C
	C8, C9	Environment	30	
Alloy 52	D1	Air	-	
	D2-D4	Environment	100	
	D5-D7	Environment	100	24h, 300 °C
	D8, D9	Environment	30	

3. Results

The J_{IC} values in air could be defined for the weld metals of Alloy 182 and 152, but not for Alloy 82 and 52 due to their high ductility and the restrictions in maximum displacement range of the equipment. The results of the conducted J-R-tests are collated in Figure 4. For some specimens tested in environment, the J_{IC} (or J_Q) value could not be determined, as sufficient crack growth was not achieved. In those cases an arrow above the J_{IC} column indicates, that the J_{IC} value is > 300 kJ/m^2, which is a conservative estimate from the corresponding J-R–curves. A clear decrease in the fracture toughness is observed in most tests. The results will be further examined in the discussion part of this paper.

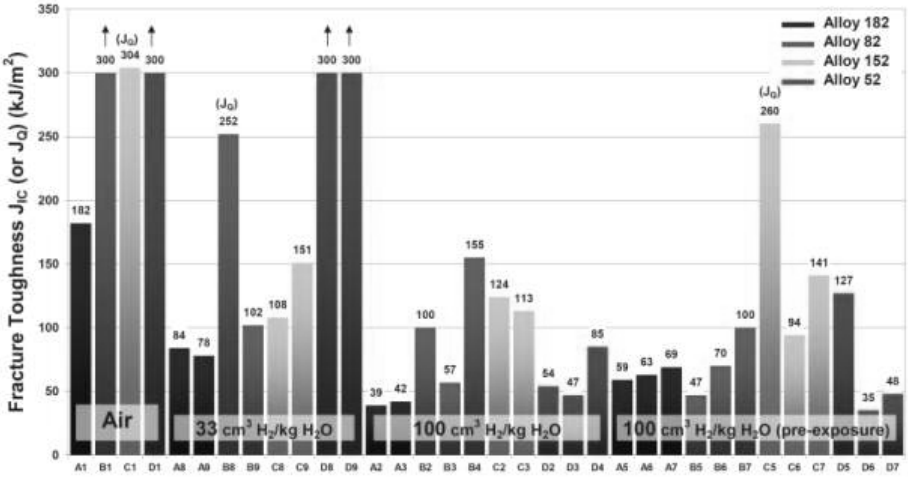

Figure 4. A summary of the J_{IC} (and J_Q) values of all the tested pure weld metal specimens.

The relationship between the cracking mechanism and J_{IC} (or J_Q) values was evaluated in a SEM study. When tested in air, all the studied specimens behaved in a ductile manner. An example is shown in Figure 5. In hydrogenated environment low fracture toughness values corresponded in all investigated alloys to intergranular or interdendritic fracture, as depicted in Figure 6. At higher magnification also very small (diameter 0.1–0.3 µm) carbides were observed on the fracture surface, especially in specimens of Alloy 82. The specimens of Alloy 152 showed the most ductile fracture surface appearance after J-R–tests in hydrogenated water.

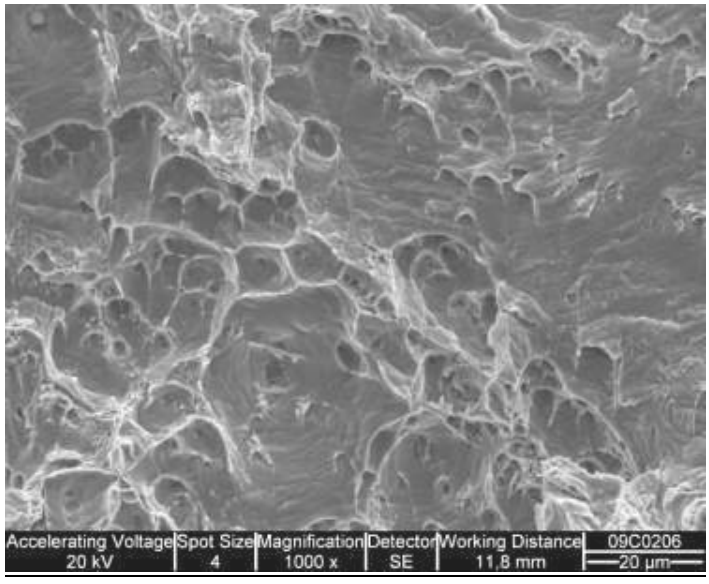

Figure 5. SEM image of the fracture surface of Alloy 82 showing ductile dimple fracture after a J-R test performed in air (specimen B1).

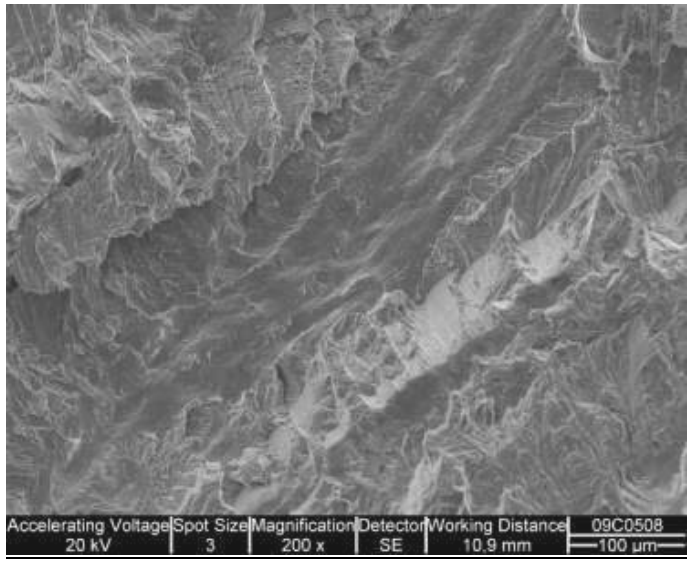

Figure 6. SEM image of the fracture surface of Alloy 82 after a J-R test performed in hydrogenated low temperature water (100 cm^3 H_2/kg H_2O, specimen B3). The fracture surface consists of mainly IG/ID cracking. The areas up left and down right represent fatigue cracking before and after the test, respectively.

4. Discussion

A notable feature in the results obtained from the fracture toughness tests is the scatter in the J_{IC} (or interim fracture toughness J_Q in three cases) values, which is clearly seen in the summarizing Figure 4. A weld metal is always inhomogeneous regarding its composition, morphology and thermal history. Therefore, also the location of a fatigue pre-crack tip with respect to the microstructure affects the shape of the J-R–curve and the J_{IC} value.

4.1 Effect of hydrogen content and pre-exposure

The content of dissolved hydrogen in low temperature water seems to be a crucial parameter of the fracture toughness. All tested alloys exhibit lower average fracture toughness values at the high hydrogen content (100 cm^2 H_2/kg H_2O) than at the low hydrogen content (33 cm^2 H_2/kg H_2O). The difference is most notable for Alloy 52, which seems to be quite immune to LTCP at 33 cm^2 H_2/kg H_2O (J_{IC} > 300 kJ/m^2), but very susceptible at 100 cm^2 H_2/kg H_2O (average J_{IC} = 62 kJ/m^2). This observation is in line with the LTCP literature [4, 5, 9].

The average fracture toughness at hydrogen content 33 cm^2 H_2/kg H_2O is less than half of the value measured in air for Alloy 182 (J_{IC} = 182 → 81 kJ/m^2) and for Alloy 152 (J_{IC} or J_Q = 304 → 130 kJ/m^2). For Alloys 82 and 52, these assessments could not be done, because their exact J_{IC} values in air are unknown (> 300 kJ/m^2). The two results for Alloy 82 at 33 cm^2 H_2/kg H_2O are highly scattered (J_{IC} or J_Q = 252 and 102 kJ/m^2), but the degrading effect of the environment is clear.

In low temperature water containing 100 cm^2 H_2/kg H_2O (without pre-exposure), the lowest J_{IC} values were observed for weld metal Alloy 182 (J_{IC} = 39 and 42 kJ/m^2, 23% of original value). However, the relative decrease of the fracture toughness is assumed to be substantially larger for Alloy 52 (note that the true fracture toughness value in air could not be determined). For both Alloys 152 and 82 the decrease is significant, but their average J_{IC} values still remain over 100 kJ/m^2.

The differences between the results attained with or without pre-exposure are not substantial. The plausible explanations are that the pre-exposure time (24 h) was not long enough, or that the pre-exposure in general does not have a significant effect on the fracture toughness.

4.2 Relationship between the fracture surfaces and J_{IC} values

The general relationship between the presence of IG/ID cracking and low J_{IC} values is obvious. The specimens resulting in the highest fracture toughness values, especially the toughest specimens of Alloy 152, did not exhibit remarkable intergranular cracking, even at hydrogen content 100 cm^2 H_2/kg H_2O. Analogously, the J_{IC} values were low, when the fracture surface consisted mostly of intergranular cracking. This shows that the grain and/or dendrite boundaries have a large effect on LTCP. The grain and dendrite boundary carbides act as hydrogen traps. Further, hydrogen diffuses from the environment into the material at the crack tip. As diffusion is higher along boundaries, this will further increase the hydrogen concentration at the boundaries. If the hydrogen concentration is high enough, cracking will occur along the boundaries rather easily resulting in low fracture resistance values.

4.3 Comparison between dissimilar metal weld and pure weld metal specimens

The J_{IC}/J_Q values obtained from fracture toughness tests performed earlier [11] using dissimilar metal weld specimens are compared with the results of pure weld metals of Alloy 182 and 52 in Figure 7. The J_Q or J_{IC} values in the chart are the average values for each test series.

Based on the results, the dissimilar metal weld specimens seem to have a better LTCP resistance compared to the pure weld metal specimens. The difference is substantial for Alloy 52 specimens. For Alloy 182 the difference is smaller. A possible explanation for the different LTCP behavior between the DMW specimens of Alloy 52 (TU2) and pure Alloy 52 is that the differences in composition affect the LTCP resistance. The nickel content is decreased and the iron content is increased in the DMW due to intermixing during welding. Also other factors, such as the macroscopic and microscopic weld structure, e.g. the orientation of the dendrites in comparison to the cracking/loading direction and the location of the crack tip in the microstructure affect the fracture resistance values.

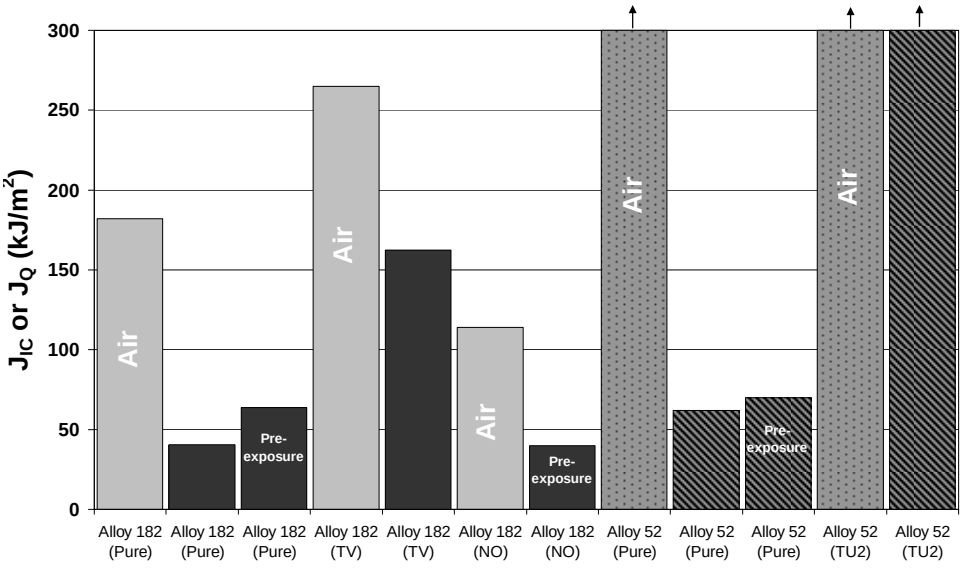

Figure 7. Average fracture toughness values for DMWs and pure weld metals of Alloy 182 and 52 in hydrogenated (100 cm^2 H_2/kg H_2O) water environment (T = 55°C).

5. Conclusions

Based on the obtained results the following conclusions are drawn:

- Hydrogenated water causes significant degradation in the fracture toughness of pure nickel-based weld metals Alloy 182, 82, 152 and 52.
- Alloy 182 is the most susceptible to LTCP.
- Increasing hydrogen content decreases the fracture toughness value.
- The degradation in toughness is assumed to be caused by a hydrogen-induced intergranular cracking mechanism, where the precipitates in the weld metals acting as hydrogen trapping sites play an important role.
- Pure weld metals of Alloy 182 and 52 seem to be more susceptible to LTCP than dissimilar metal welds of Alloy 182 and 52.

References

1. Ahonen, M. Effect of Hydrogenated Low Temperature Water on Fracture Toughness of Nickel-based Weld Metals. Espoo: VTT Technical Research Centre of Finland, 2010. VTT Research Report VTT-R-00474-10. 45 p.

2. Mills, W. J. & Brown, C. M. Fracture Toughness of Alloy 600 and EN82H Weld in Air and Water. Metallurgical and Materials Transactions A, 32A (2001) 5, pp. 1161–1174.

3. Brown, C. M. & Mills, W. J. Fracture Toughness of Alloy 690 and EN52 Welds in Air and Water. Metallurgical and Materials Transactions A, 33A (2002) 6, pp. 1725–1735.

4. McIlree, A., Demma, A., Peng, J. & King, P. J. Effects of Dissolved Hydrogen and Temperature on the Fracture Resistance of Weld Metals 182 and 52 in Simulated PWR Shutdown Environment. Proceedings of the 13th International Symposium on Environmental Degradation of Materials in Nuclear Power Systems – Water Reactors. 2007. Canada: CNS-SNC, 2007.

5. Young, B. A., McIlree, A. & King, P. J. Reduction of Toughness Results for Weld Metal 182 in a PWR Primary Water Environment with Varying Dissolved Hydrogen, Lithium Hydroxide and Boric Acid Concentrations. Proceedings of the 12th International Symposium on Environmental Degradation of Materials in Nuclear Power Systems – Water Reactors. 2005. USA: TMS, 2005.

6. Brown, C. M. & Mills, W. J. Load Path Effects on the Fracture Toughness of Alloy 82H and 52 Welds in Low Temperature Water. Proceedings of the 12th International Symposium on Environmental Degradation of Materials in Nuclear Power Systems – Water Reactors. 2005. USA: TMS, 2005.

7. Mills, W. J., Lebo, M. R. & Kearns, J. J. Hydrogen Embrittlement, Grain Boundary Segregation, and Stress Corrosion Cracking of Alloy X-750 in Low- and High-Temperature Water. Metallurgical and Materials Transactions A, 30 A (1999) 6, pp. 1579–1596.

8. Mills, W. J., Brown, C. M. & Burke, M. G. Effect of Microstructure on Low Temperature Cracking Behavior of EN82H Welds. Proceedings of the 10th International Symposium on Environmental Degradation of Materials in Nuclear Power Systems – Water Reactors. 2001. USA: NACE International, 2002.

9. Herms, E., Raquet, O., De Curières, I. & Joly, P. LTCP of Alloy 182/152 Tested in PWR Primary Water. (To be published.)

10. Young, G. A., Battige, C. K., Lewis, N., Penik, M. A., Kikel, J., Silvia, A.J. & McDonald, C. K. Factors Affecting the Hydrogen Embrittlement Resistance of Ni-Cr-Mn-Nb Welds. 6th International Trends in Welding Research Conference Proceedings. 2002. USA: ASM International, 2003.

11. Ahonen, M. Ympäristön ja muodonmuutosnopeuden vaikutus austeniittisten materiaalien murtumisvastuskäyttäytymiseen. Espoo: Valtion teknillinen tutkimuskeskus, 2008. VTT Tutkimusraportti VTT-R-06182-08. 64 p.

12. Hänninen, H., Brederholm, A., Saukkonen, T., Gripenberg, H., Toivonen, A., Ehrnstén, U. & Aaltonen, P. Hot Cracking and Environment-assisted Cracking Susceptibility of Dissimilar Metal Welds. Espoo: VTT Technical Research Centre of Finland, 2007. VTT Research Notes 2399. 181 p.

13. Richey, E. & Young, G. A. The Effects of Deaerated Water on the Toughness of Nickel-Based Alloys. (To be published.)

Environment-assisted cracking and hot cracking of Ni-base alloy dissimilar metal welds

Pertti Aaltonen, *Hannu Hänninen, *Anssi Brederholm,
Aki Toivonen and Ulla Ehrnstén
VTT Technical Research Centre of Finland
*Aalto University School of Science and Technology,
Faculty of Engineering and Architecture
Espoo, Finland

Abstract

Environment-assisted cracking (EAC) susceptibility of dissimilar metal mock-up welds of Alloy 182 and 82 as well as Alloy 152 and 52 were studied with four-point bending specimens in steam doped with hydrogen, chloride, sulfate and fluoride at 400 °C. The doped steam environment accelerated the crack initiation process and the susceptibility of the studied weld metals to EAC was obtained and ranked.

High susceptibility to crack initiation and growth was observed with Alloy 182 and 82 weld metals, while Alloy 152 and 52 weld metals showed high resistance to crack initiation. No extension of the hot cracks was observed in the doped steam test in any of the studied materials. Fractography of the broken Alloy 182 and 82 samples showed both nickel deposition and presence of NiO in addition to the continuous spinel type Cr-rich oxide film on the fracture surface inside the crack. Fracture path was intergranular in all the studied samples. The same dissimilar metal welds were exposed to Varestraint hot cracking tests and their hot cracking susceptibility was also ranked and determined as a function of the amount of strain. The microstructures of the weld metals were fully

characterized by optical metallography and a modern FE-SEM/EDS system. Hot cracking susceptibility was related to the solidification mechanism and segregation of Nb, Si, P and Mn in the weld metals.

Fractography of the EAC and hot cracks was compared and their characteristic features are demonstrated. Finally, the mechanisms of hot cracking and EAC of nickel-base alloy dissimilar metal welds are identified and discussed.

1. Introduction

The Ni-base alloy dissimilar metal welds in nuclear power plant applications are typically made using Alloy 182 and Alloy 82. Recently, Alloy 52 has been used both in new constructions as well as in repair welding. The trend towards alloys with higher contents of chromium is driven by the observed environment-assisted cracking (EAC) in Alloy 182, and recently also in Alloy 82. One driving force towards the more EAC resistant alloys is also the challenges and costs related to non-destructive examination of dissimilar metal welds.

A limited amount of laboratory EAC test results is available for the new material combinations of dissimilar metal welds of nuclear power plants. A test has been developed to enhance cracking of Ni-base alloys and their weld metals at 400 °C in hydrogenated steam doped with sodium sulphate, fluoride and chloride. According to Staehle and Gorman [1], the initiation time of low potential stress corrosion cracking (LPSCC) follows a monotonic 1/T dependence from hydrogenated steam to water. This suggests that the mechanistic processes in water and steam are the same, at least for pure water. As crack initiation takes very long time (years or decades) in actual LWR water at relevant operating temperatures, the accelerated tests have been conducted at 400°C in steam doped with hydrogen, chloride, sulphate and fluoride.

Several studies have been made to investigate hot cracking susceptibility of filler metals Alloys 82, 182, 52 and 152 and base material Alloy 690, e.g. [2, 3, 4]. Hood & Lin [2] studied hot cracking susceptibility of Ni-base alloy filler metals (Alloys 82, 182, 52 and 152) using the Varestraint and spot-Varestraint tests. The results showed that Alloy 52 exhibited the best resistance to both weld solidification cracking and weld metal liquation cracking, followed by Alloys 82, 152 and 182. Wu & Tsai [3] investigated the hot cracking susceptibility of Alloys 82 and 52 with Alloy 690 by Varestraint tests. Alloy 82 showed greater total crack length (TCL) than Alloy 52. Liquation cracks and ductility dip cracks were found in the heat affected zone (HAZ), but an accurate distinction of the

crack type was difficult. These results indicate that hot cracking susceptibility of Alloy 82 is greater than that of Alloy 52 in Varestraint testing. Recently a Gleeble-based test technique, termed strain-to-fracture (STF), has been developed by Nissley et al. [4] and employed for evaluation of strain-to-fracture of ductility-dip cracking (STF DDC) susceptibility curves for filler metals of Alloys 82 and 52 [5]. The filler metal Alloy 52 was more susceptible to DDC than Alloy 82, which also exhibited heat-to-heat variation in susceptibility. Thus, because of varying observations in various tests there is a major need to rank the Ni-base alloy weld metals for their hot cracking susceptibility and to understand the mechanisms of solidification cracking properly in addition to EAC susceptibility.

2. Materials and experimental methods

Four different dissimilar metal welds were studied using doped steam exposure. The weld geometries contained nickel-base weld metals Alloy 152 (mock-up TU1), 52 (mock-up TU2), both 52 and 152 (mock-up TU3), 182 (mock-up TV1) and of Alloy 182, 82, 152 and 52 pure weld metals simulating weld repairs or overlays, Figure 1 and Table 1. The specimens were $80 \times 15 \times 3$ mm^3 plates cut from the root side of the welds. The specimen dimensions and cutting location are schematically shown in Figure 2 (mock-up TU2 weld as an example). The dissimilar metal weld was in the middle of the specimen with its orientation either transverse (orientation “T”) or parallel (orientation “P”) to the longitudinal axis of the specimen. The specimens were prepared by plane milling from the blocks prepared for Varestraint tests. A smooth mechanical grinding by 600 grit emery paper was performed after milling in order to remove the roughness of the specimen surfaces.

The specimens were bolt-loaded in four-point bend loading. Strain was calculated from the bending radius of a 3 mm thick plate and the nominal target strains for the specimens were 0.35 and 1%. The longest total time of exposure was 2178 h. The specimens were investigated repeatedly after exposure of about 300 h maximum of 5 times using a stereo microscope and liquid penetrant testing. All liquid penetrant indications were further studied using stereo and scanning electron microscopy. Some cracks were opened and specimens were sliced in order to study the crack propagation paths in the microstructure. Some of the specimens were thermally aged in order to simulate long term (~30–50 years) exposure to the operating temperature of 325°C. The ageing was performed

in the same autoclave where the doped steam testing was performed. The ageing temperature was 420°C and the duration was 2000 h. The specimens were protected from oxidation by N_2 gas atmosphere.

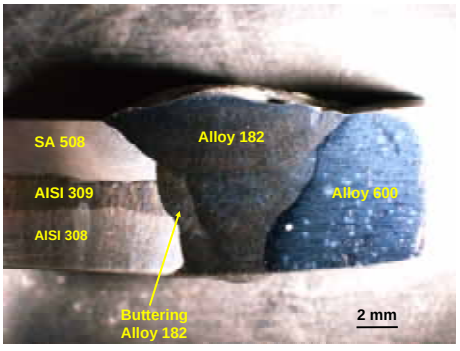

a)

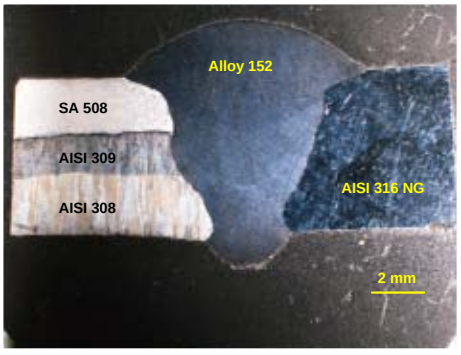

b)

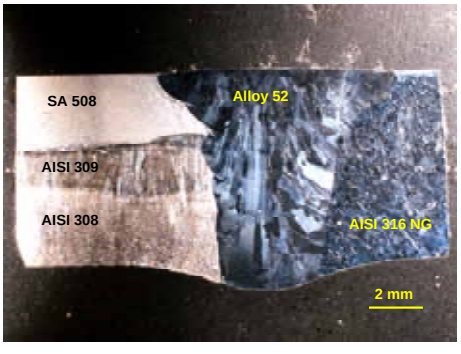

c)

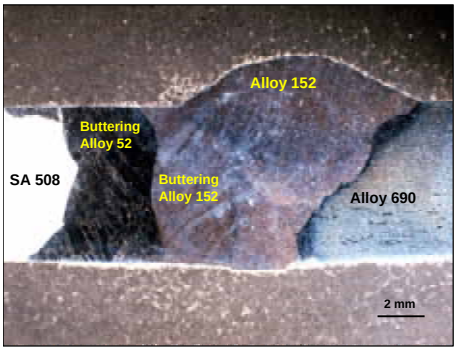

d)

Figure 1. Groove geometry, materials and cross-section of a) mock-up TV1, b) mock-up TU1, c) mock-up TU2 and d) mock-up TU3 dissimilar metal welds.

Hot cracking susceptibility of Ni-base alloy dissimilar metal welds was studied by using the mock-ups shown in Figure 1. The motivation for the study was the needs for repair welding of Alloy 182 welds of safe ends in BWR plants and possible welding problems with new Alloy 152/52 weld metals. Susceptibility to hot cracking was examined by Varestraint tests [8] and weld microstructures were studied by optical and field emission gun scanning electron microscopy (FEG-SEM/EDS). Figure 1 presents the groove geometries, materials and cross-

sections of dissimilar metal welds of Alloys 182, 152 and 52. The clad pressure vessel steel SA 508 side of specimen TV1 (with Alloy 182 buttering) was heat treated at 610°C for 6 h and mock- up TU3 (with Inconel 52 and Inconel 152 buttering) was heat treated at 610°C for 4 h before fusion welding. Whole welded test specimens of mock-ups TU1 and TU2 were heat treated at 610°C for 16 h after fusion welding.

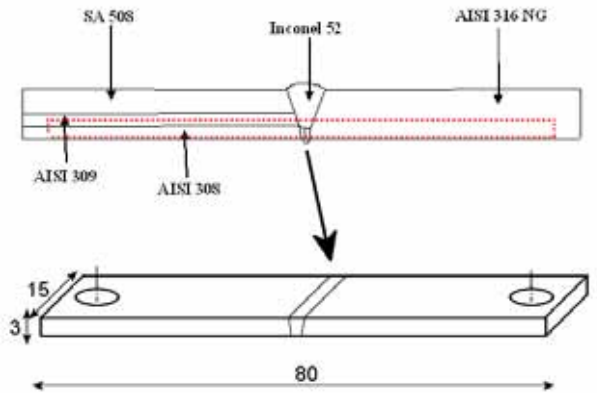

Figure 2. Schematic EAC specimen cutting location (transverse orientation) and specimen dimensions.

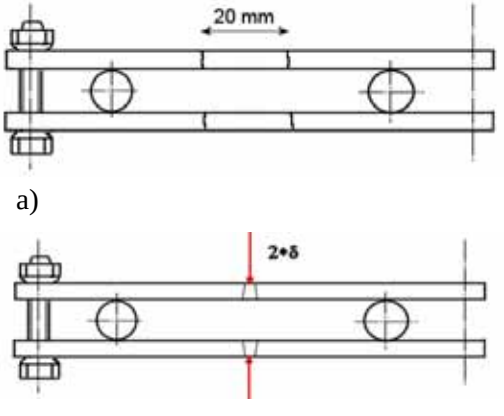

Figure 3. Loading geometry with displacement measurement location indicated by two arrows of (a) pure weld metal and (b) dissimilar weld metal mock-up samples.

Table 1. Chemical compositions of the base materials and filler metals used in the dissimilar metal welds.

	C	Si	Mn	P	S	Cr	Mo	Ni	Nb	N	Ti	Fe	Al	Co	Cu
Base materials															
AISI 316 NG	< 0,03					16,5-18,5	2,5-3	11-14		0,12-0,22					
SA508 (Grade 2)	0,24	0,21	1,38		0,009	0,16	0,54	0,58		0,014			0,015		0,12
Alloy 600	0,07	0,19	0,21	0,007	0,001	16,3		72,86	Nb+Ta 0,10		0,28	9,44	0,229	0,076	0,13
Alloy 690	0,02	0,04	0,16		0,001	29,46		59,82			0,33	9,96	0,2		<0,01
Filler metals															
AISI 308L (OK Band 11.61)	< 0,025	0,4	1,8			20		10							
AISI 309L (OK Band 11.65)	< 0,025	0,4	1,8			24		13							
Alloy 182 (OK 92.26)	0,03	0,8	6,5	0,01	0,003	15,7		68	1,8		0,1	6,7			< 0,01
Alloy 82 (OK Tigrod 19.85)	0,039	0,03	2,98	0,001	0,004	19,94		72,6	Nb+Ta 2,47		0,34	1		0,01	0,01
Alloy 52	0,03	0,13	0,24	<0,001	<0,001	29,2	0,03	59,28	Nb+Ta <0,02		0,51	9,8	0,72	0,009	0,04
Alloy 52M	0,02	0,09	0,8	0,003	0,001	30,06	0,01	59,54	Nb+Ta 0,83		0,224	8,22	0,11	0,027	0,02
Alloy 52MS	0,014	0,12	0,68	0,004	0,0007	29,53	0,02	60,14	0,78		0,19	8,33	0,13	0,008	0,03
Alloy 152	0,048	0,41	3,48	0,003	0,003	28,74	0,01	55,2	Nb+Ta 1,54		0,09	10,39	0,06	<0,005	<0,01
Alloy 152M	0,0293	0,3276	3,247	<0,001	0,0042	28,98	<0,005	57	Nb+Ta 1,533		0,039	8,75	<0,005	0,0119	<0,005

Table 2. Summary of the welding parameters used in the Varestraint tests.

	Current [A]	Voltage [V]	Welding speed [cm/min]	Heat input [kJ/cm]
Mock-up TV1 (Alloy 182)	150	10.5	12	4.7
Mock-up TU1 (Alloy 152)	150	10.5	12	4.7
Mock-up TU2 (Alloy 52)	150	10.5	12	4.7
Mock-up TU3 (Alloy 152)	150	10.5	12	4.7
Alloy 182	250	12.5	12	9.4
Alloy 82	150	10.5	12	4.7
Alloy 82	250	12.5	12	9.4
Alloy 152	150	10.5	12	4.7
Alloy 52	150	10.5	12	4.7

3. Experimental results

3.1 EAC test results

After about 2000 h testing time pure weld metal Alloy 182 and Alloy 82 samples have cracked completely (see Table 3 and examples in Figure 4). First samples were cracked already after first exposure period (240 h). The cracks were in the middle of the welds in pure Alloy 82 and 182 weld metal specimens except for one case in which the cracking took place in the diluted zone of the weld metal ~1–2 mm from the fusion line. In Alloy 182 weld mock-up TV1(specimen No. 32) the crack was also in the middle of the fusion weld (i.e., not in the buttering weld).

Table 3. Test matrix and test results after 2178 h testing.

Number of specimens	Spec. No. / Spec. ID	Weld	Heat treatment	Strain, %	Time to cracking, h
6	1-4 / P182	182 (plain)	-	1,1	750/750/240/750
	5-6 / P182A	182 (plain)	Aged	1,1	750/750
6	7-10 / P82	82 (plain)	-	1,1	240/240/240/240
	11-12 / P82A	82 (plain)	Aged	1,1	750/240
6	13-16 / P152	152 (plain)	-	1,1	-/-/-/-
	17-18 / P152A	152 (plain)	Aged	1,1	-/-
6	19-22 / P52	52 (plain)	-	1,1	-/-/-/-
	23-24 / P52A	52 (plain)	Aged	1,1	-/-
2	25-(26) / TU1A	TU1	Aged	1,1	-/(-)
2	27-28 / TU2A	TU2	Aged	1,1	-/-
2	29-30 / TU3A	TU3	Aged	1,1	990/-
2	(31)-32 / TV1A	TV1	Aged	1,1	(-)/750
1	35 / P182C	182 (plain)	Hot cracked	CMOD ~0.02 mm	-
1	36 / P82C	82 (plain)	Hot cracked	CMOD ~0.02 mm	-
1	37 / P152C	152 (plain)	Hot cracked	CMOD ~0.02 mm	-
1	38 / P52C	52 (plain)	Hot cracked	CMOD ~0.02 mm	-
1	39 / TU1C	TU1	Hot cracked	CMOD ~0.02 mm	-
1	40 / TU2C	TU2	Hot cracked	CMOD ~0.02 mm	-
1	41 / TU3C	TU3	Hot cracked	CMOD ~0.02 mm	-
1	43 / TV1C	TV1	Hot cracked	CMOD ~0.02 mm	-

Aged = thermal ageing at 420°C for 2000 h, represents ~ 50 years at 325°C.

No crack extension was observed in any of the hot cracked specimens after about 2178 h exposure time.

Detailed fractography of broken pure Alloy 182 and 82 specimens showed that the outer surface and fracture surface are covered with an oxide layer. However, on the fracture surface a metallic Ni film forms on the top of the oxide layer and covers almost completely the fracture surface close to the outer surface, Figure 5. In the middle of the fracture surface the formation of NiO was

also observed as small particles growing laterally on the oxide covered surface together with larger Fe-rich spinel oxide particles (Figure 5). Close to the crack tip no metallic Ni or NiO was observed and the fracture surface was covered only by a thin Cr-rich oxide layer.

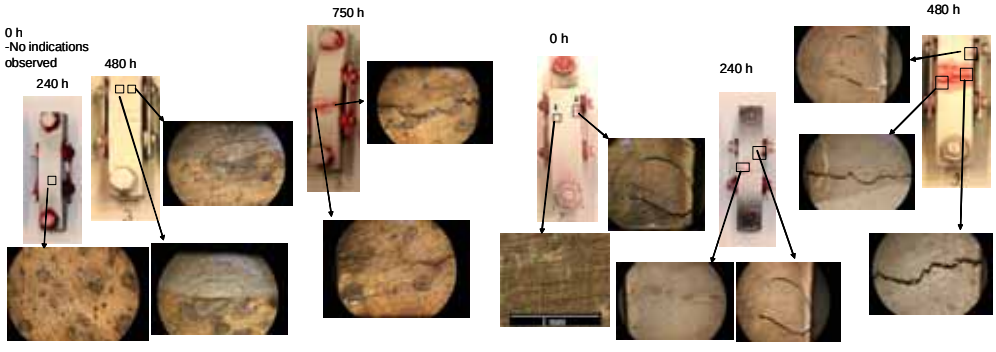

a) b)

Figure 4. Pure Alloy 182 (specimen No. 3) (a) and pure Alloy 82 (specimen No. 9) (b) cracking after various exposure times. Note that neither in Alloy 182 nor Alloy 82 the opened weld defects do not grow further and final fracture takes place in the middle of the specimens.

In order to analyze the thicknesses of the various films forming inside the cracks and on the outer surfaces of the specimens cross-sections of the cracked samples were made. Figure 6 show details of these cross-sections indicating that the metallic Ni film is in the middle of the cracks extending almost up to the crack tip. The metallic Ni deposit in the middle of the crack is surrounded on both sides by a Cr-rich oxide layer which grows into the metal matrix and extends to the crack tip. During the oxide growth nickel diffuses through the Cr-rich oxide film and deposits on the top of the Cr-rich oxide layer as metallic Ni. Typical for Alloy 182 are the Nb-rich phases along the dendrite boundaries. However, the Nb-rich phase does not seem to dissolve quickly in these test conditions as shown in Figure 7. The Nb-rich phases are closely connected to the hot cracking behavior of Nb-alloyed Ni-base alloy weld metals and this observation may explain why hot cracks are not preferably extending during EAC testing.

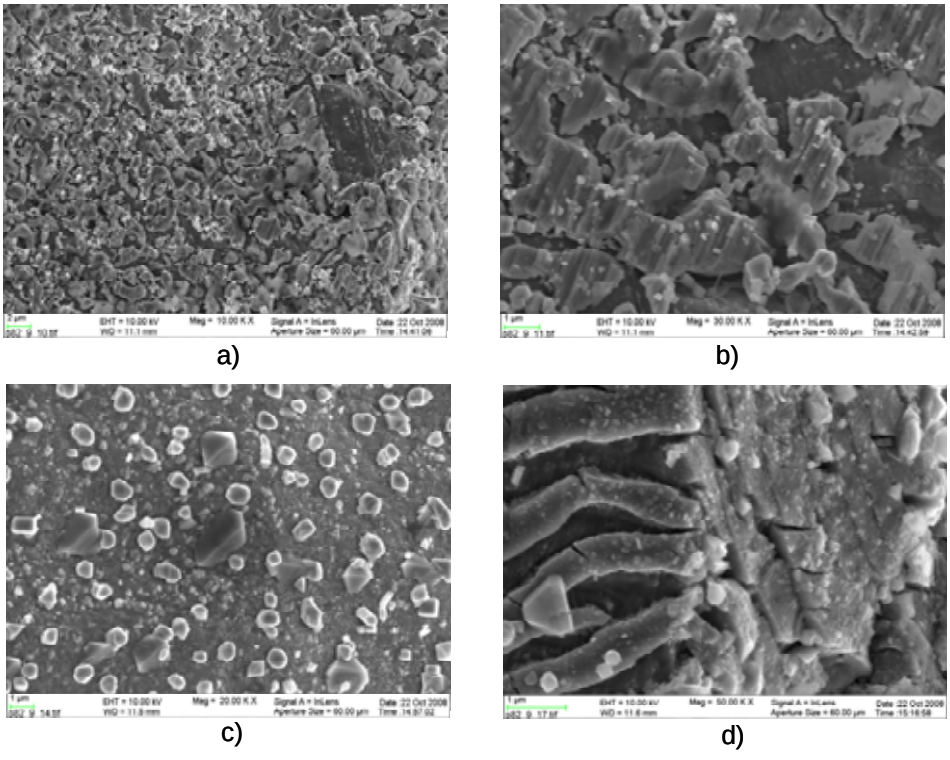

Figure 5. Pure Alloy 82 (specimen No. 9) fracture surface after 240 h exposure time. (a and b) Metallic Ni deposit layer close to the crack mouth. (c) NiO and Fe-rich spinel oxide particles on the fracture surface close to the crack tip. (d) Cracked Cr-rich oxide film due to bending the crack open at the crack tip.

Metallic Ni-deposits are also forming in the fine scale inside the Cr-rich oxide films on the outer surface of the specimens, see Figure 6. Additionally, on the outer surface larger metallic Ni deposit particles are present. Inside the Cr-rich oxide film metallic Ni deposits form spike like structures in areas of deeper penetration of the oxide film into the metal matrix.

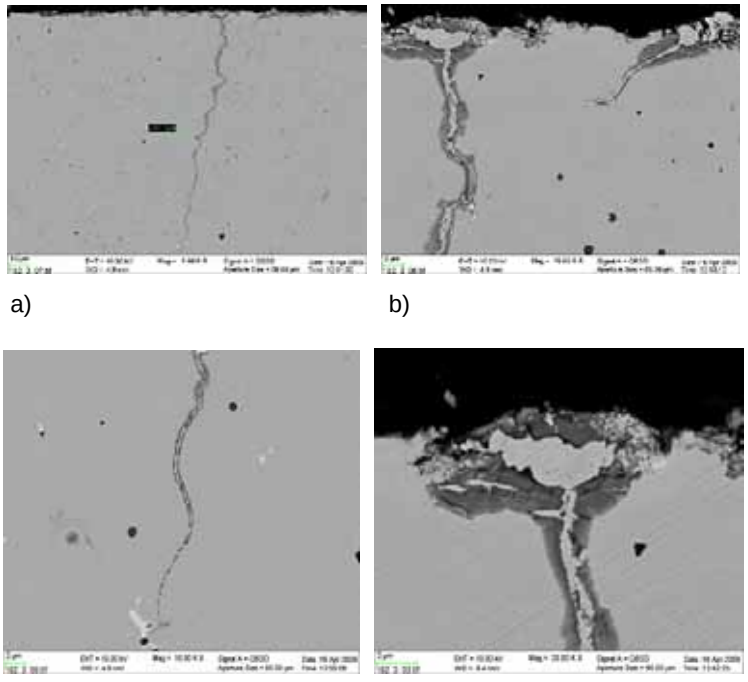

a) b)

c) d)

Figure 6. Cross-section of a crack in Alloy 182 pure weld metal specimen No. 3. Note the formation of metallic Ni deposit layer in the middle of the crack surrounded by Cr-rich oxide layers on both sides. The metallic Ni deposit layer extends almost up to the crack tip in (d).

3.2 Varestraint test results

Figure 7 presents the surface (Alloy 182 weld, augmented strain 4%) of the test piece with hot cracks after Varestraint testing. Optical micrograph of a hot crack (dark areas) in the cross-section of the weld and scanning electron micrographs (FEG-SEM) of hot crack tips show details of the irregularly shaped white phase connected to hot cracks of this alloy. The compositions of the white phase areas were examined by energy dispersive spectroscopy (EDS) analysis. SEM image and EDS analyses of the white phase, presented in Figure 8, show marked Si, Nb, Mn and P enrichment, which is compensated by depletion of Cr, Fe and Ni. Based on the high magnification backscattered electron (BSE) images and the EDS analyses the observed white phase consists of two phases, white and grey, with varying Nb, Si, Mn and Ti contents. Inside and along the dendrite/grain boundaries white Nb-rich particles, Nb(C, N), are present.

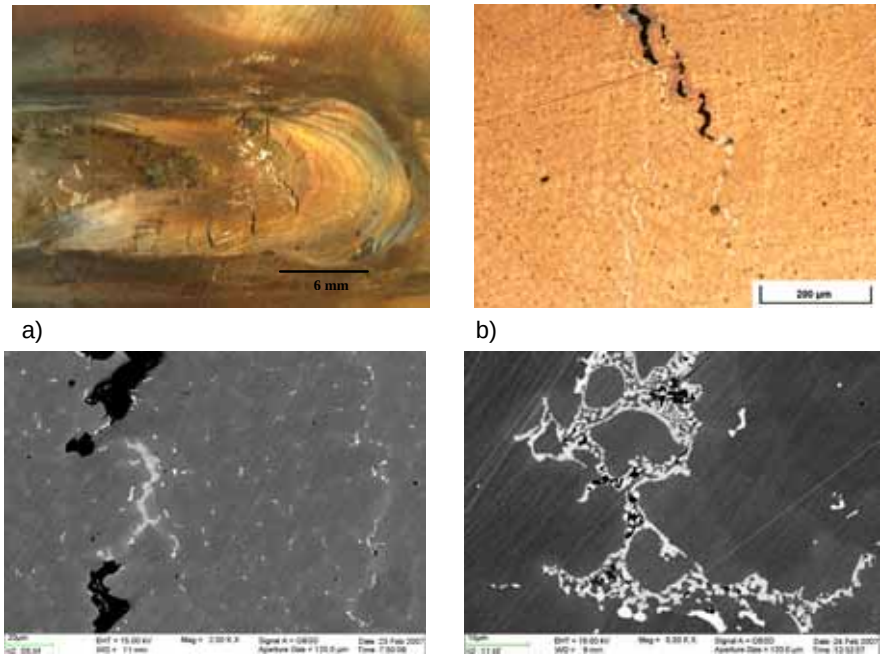

Figure 7. a) Surface (Alloy 182 weld, augmented strain 4%) of a test piece with hot cracks after Varestraint test. b) Optical micrograph of the hot cracks (dark areas) in a cross-section of the weld (note the white phase ahead of the hot crack tip). c), and d) SEM micrographs of weld hot crack tips showing details of the irregularly shaped white phase on the dendrite boundaries.

Study of the fracture surfaces of Alloy 182 test weld hot cracks revealed marked segregation of the same elements of Nb, Si, Mn, and P on fracture surfaces as seen in the white phase in the cross-sections of the hot cracks. On the fracture surface Nb-rich particles, Nb(C, N), and the lamellar white phase are present intermixed in the final microstructure.

Pure Alloy 82 weld metal hot cracking required a higher heat input (Q = 9.4 kJ/cm). The formed hot cracks were markedly oxidized, probably because of the high heat input and also because of segregation to the final melt. SEM image and X-ray element maps of cross-sections of hot cracks exhibited a strong Nb segregation and less marked Si, P and Ti segregation to the dendrite boundaries at the hot crack tip. Nb- and Ti-rich (Ti content of Alloy 82 is 0.34 wt.-%) particles, Nb, Ti(C, N), were also clearly visible. Alloy 152 weld metal shows similar hot cracking tendency as compared to Alloy 182. The Nb-rich white phase is connected to the hot cracks and the phase can be easily found in the

cross-sections of the hot cracks as well as on the fracture surfaces (local coverage can be as high as 30%). The dendrite boundaries containing the white phase show in addition to Nb a marked increase of Si, Mn and P contents both in the white phase, but also in the wider zone along the dendrite boundaries. Simultaneously depletion of Cr, Ni and Fe is observed in these zones. In addition to the white phase both in the cross-section as well as on the fracture surfaces plenty of small particles, Nb, Ti(C, N), are present. Filler metal Alloy 52 contains Ti (0,51 wt.-%), but does not contain Nb as Alloys 182, 82 and 152 and, thus, hot cracks form along the dendrite boundaries without the presence of the Nb-rich white phase.

Figure 9 a) and b) present SEM images of pure weld metal (Alloy 152, augmented strain 4%) hot cracks after Varestraint test and secondary EAC cracks (Alloy 182) after doped steam test. Fracture surface in hot crack contains features of segregation and second phases play role in cracking. These features are not found to enhance EAC in doped steam tests.

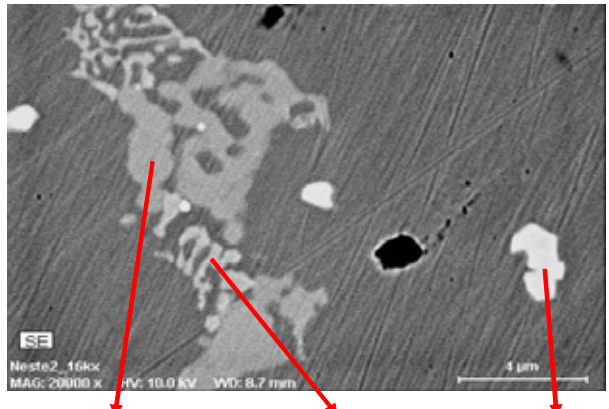

Element	Filler metal wt.%	Grey area wt.%	Enrichment vs. filer metal	Light white area wt.%	Enrichment vs. filer metal	White area wt.%	Enrichment vs. filer metal
Si	0.8	3.4	4.3	6.5	8.1	0	0
P	0.01	1.3	130	1.3	130	0.2	20
Ti	0.1	0.04	0.4	0.7	7	2.8	28
Cr	15.7	5.4	0.3	4.9	0.3	1.4	0.1
Mn	6.5	17.7	2.7	11.8	1.8	1.1	0.2
Fe	6.7	4.7	0.7	4.9	0.7	1.5	0.2
Ni	68	51.4	0.8	49.4	0.7	0	0
Nb	1.8	15.2	8.4	20.6	11.4	89.6	49.8

Figure 8. SEM image and EDS analyses of the white and grey phase showing Nb, Si, Mn and P enrichment and Nb rich particles, Nb(C, N). The spot size in EDS analysis has an interaction diameter about 1 µm, and therefore the surrounding matrix affects also the result.

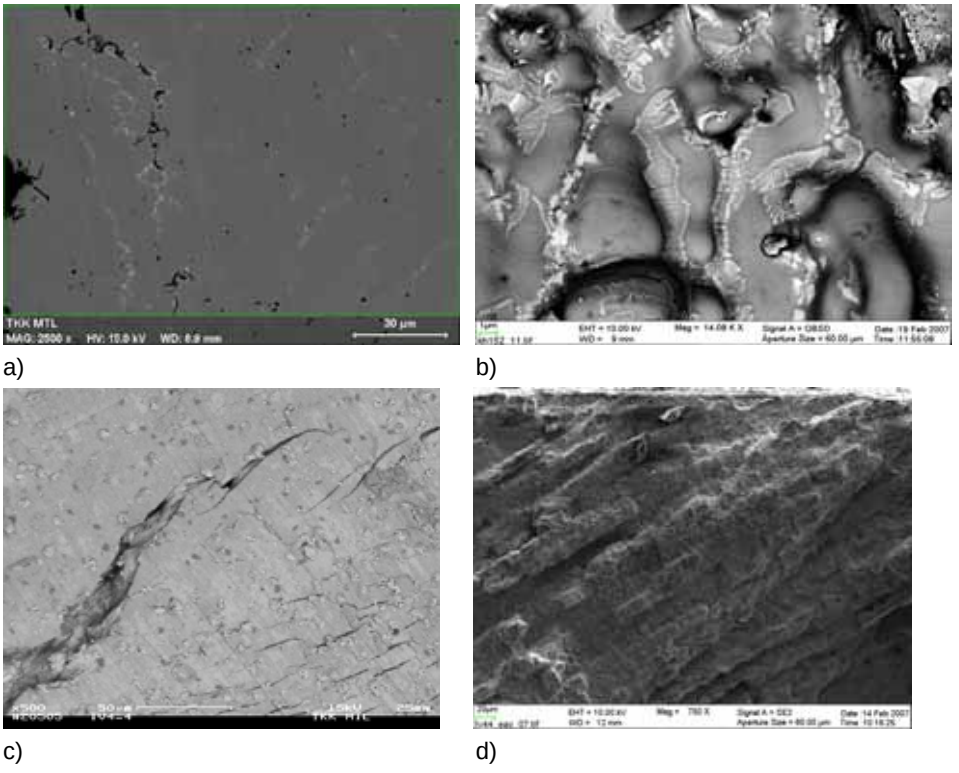

Figure 9. a) and b) SEM image of a cross-section and a fracture surface of hot cracks in Alloy 152 weld metal exhibits the connection of the white phase to hot cracks. c) and d) SEM photograph showing the EAC cracking in Alloy 182 and the interdendritic nature of the fracture surface in weld metal.

4. Discussion

In the doped steam conditions the Ni-base weld metal mock-up specimens showed indications but much less fracture than the pure weld metal specimens of Alloy 182 and 82, which cracked quickly [6, 7]. In mock-up tests Alloy 182 was apparently the most susceptible of the studied mock-up welds. However, in the pure weld metals of Alloy 182 and 82 seem to be equally susceptible. Aging at 420°C for 2 000 h did not seem to affect the cracking susceptibility in these test conditions. Specimens containing hot cracks did not show any crack extension either in pure weld metal samples or in mock-up samples. This may indicate that the local microchemistry and microstructures on the dendrite boundaries ahead of the hot crack tips are not inherently susceptible to EAC. Typical for Nb-

containing alloys is that Nb-rich phases are present in the hot cracks and the adjacent austenite is heavily segregated of Nb (up to 10%) but in Alloy 52 where no Nb alloying is present TiN phase is associated with hot cracking. Additionally, dendrite boundaries exhibit high dislocation densities (residual strain) together with segregation and second phase particles. [6,7]

Fractography of Alloy 182 and 82 pure weld metal specimens showed that the outer surface and fracture surface after EAC testing in doped steam environment are covered with a Cr-rich oxide layer. Metallic Ni deposit forms on the top of the oxide layer and covers the fracture surface close to the outer surface. Metallic Ni deposits form also on the outer surface of the specimens and in a finer scale inside the outer surface oxide film. Close to the crack tip also NiO and Fe-rich spinel oxide particles were observed and the fracture surface is covered by a thin Cr-rich oxide layer up to the crack tip. Thus, in the doped steam test the oxides formed on the crack walls and outer surface of the specimens are similar to those forming in normal reactor conditions.[9,10] In doped steam test, however, the phases are larger and thicker and more clearly separated allowing them to be studied much more easily. The intergranular / interdendritic nature of the EAC fracture is evident (Figure 9d) and its morphology is quite different from the interdendritic morphology of the hot crack fracture surface (Figure 9b). [6, 7]

Selective oxidation leading to separation of Cr-rich oxide and metallic Ni is occurring in the initiation and propagation of IGSCC in doped steam test. Cr-rich oxide layer forms on crack walls and extends to the crack tip. Precipitation of metallic Ni layer and islands behind the crack tip on top of the Cr-rich oxide layer occurs inside the cracks and on outer surface. Whether the entire alloy is oxidizing and the elements undergo hydrolysis except Ni, which is transferred through the oxide layer and re-plated or if the other elements dissolve selectively and a porous Ni-rich sponge is left close to interface or if both mechanisms operate at the same time will be clarified in the future. The details of metallic Ni layer, multilayer Cr-/Nb-rich oxide corrosion product and possible corrosion sponge at Cr-depleted/Ni-enriched base material interface as well as possible vacancy clusters (voids) in the base material are studied by ATEM. The role of hydrogen in cracking may be related to enhancement of oxidation and stabilization of vacancies rather than to hydrogen embrittlement at 400 °C.

Ni stability region is close to the $H_2 – H_2O$ equilibrium line in high temperature water while the stability regions of Fe and Cr are below the line. [9] The critical H_2 fugacity varies with temperature and increasing the H_2 fugacity causes

corrosion potential to decrease into Ni stability region. The hydrolysis reaction of metal ions (Cr, Fe, etc.) produces additional H^+ /H_2. Inside the cracks the increased H_2 fugacity lowers Ni^{2+} and NiO stability and metallic Ni is deposited.

The mechanism of cracking of Ni-base alloys in doped steam test can be explained by the Selective Dissolution – Vacancy Creep (SDVC) model for SCC. [11] Cracking takes place by a selective oxidation mechanism where Cr and Fe are hydrolyzed and Ni is transferred through the oxide film and deposited on the film in metallic form. Vacancy injection into the base material is expected to take place and to enhance the creep rate at the crack tip.

5. Conclusions

The following conclusions can be drawn based on the results of this study:

- Dissimilar metal weld joints of Ni-base weld metals show in their microstructure marked segregation especially of Nb to the dendrite boundaries. In the Nb-bearing alloys eutectic Laves and Nb(C, N) phases form along the dendrite boundaries and in Ti-alloyed Alloy 52 TiN(C) phase forms, respectively. These segregated structures and second phases play important role in hot cracking, but were not found to enhance EAC in doped steam test.
- The differences in the EAC susceptibility between different weld geometries and weld metals can be distinguished by the doped steam test method. Pure weld metals of Alloy 182 and 82 were clearly more susceptible to EAC than pure weld metals of Alloy 152 and 52, which did not show any crack initiation. The mock-up welds with diluted microstructures were less susceptible than the pure weld metals of Alloy 182 and 82.
- Accelerated doped steam test for Ni-base alloys results in a high acceleration factor for cracking and because of high temperature the test conditions lead to enhanced growth of oxide layer structures and clear separation of different phases.
- Metallic Ni forms a continuous layer in the middle of the cracks surrounded by the Cr-rich oxide layer (locally also Nb-rich oxide may be present) in contact with the base material. On the outer surface islands of deposited Ni are also present.

- Cracking takes place by a selective oxidation mechanism where vacancy injection into the base material is expected to enhance the creep rate at the crack tip. The mechanistic processes in steam and high temperature water are thought to be the same, at least for pure water.
- The role of hydrogen in cracking may be related to enhancement of oxidation and stabilization of vacancies rather than to hydrogen embrittlement at 400°C.

Acknowledgments

This report is part of the Performance of the Dissimilar Metal Welds project funded by Tekes, TVO, Fortum Nuclear Service, Vattenfall, OKG, Metso Materials Tech. Oy, Posiva, Neste Oil Corporation, which are gratefully acknowledged.

References

1. Staehle, R. W. & Gorman, J. A. Quantitative assessment of submodes of stress corrosion cracking on the secondary side of steam generator tubing in pressurized water reactors: Part 2. Corrosion, 2004. Vol. 60, No. 1, pp. 5–63.

2. Hood, B. & Lin, W. Weldability testing of Inconel filler materials. Seventh International Symposium on Environmental Degradation of Materials in Nuclear Power Systems – Water Reactors. Breckenridge, Colorado, USA, 7–10 August, 1995, pp. 69–79.

3. Wu, W. & Tsai, C. Hot cracking susceptibility of fillers 52 and 82 in Alloy 690. Met. Mat. Trans., 1999. Vol. 30A, pp. 417–426.

4. Nissley, N., Collins, M., Guaytima, G. & Lippold, J. Development of the strain to fracture test for evaluating ductility dip cracking in austenitic stainless steels and Ni-base alloys. Welding in the World, 2002. Vol. 46, Iss. 7/8, pp. 32–40.

5. Collins, M. & Lippold, J. An investigation of ductility dip cracking in nickel-based filler materials – Parts I-III. Welding Research, 2003, pp. 288–295.

6. Hänninen, H., Toivonen, A., Brederholm, A., Saukkonen, T., Ehrnstén, U. & Aaltonen, P. Environment-assisted cracking and hot cracking of Ni-base alloy dissimilar metal welds. Proceedings of the 13th International Conference on Environmental Degradation of Materials in Nuclear Systems – Water Reactors. Whistler, B.C., Canadian Nuclear Society, 2007. CD-ROM.

7. Hänninen, H., Brederholm, A., Saukkonen, T., Gripenberg, H., Toivonen, A., Ehrnstén, U. & Aaltonen, P. Hot cracking and environment-assisted cracking susceptibility of dissimilar metal welds. Espoo: VTT Technical Research Centre of Finland, 2007. VTT Research Notes 2399. 177 p.

8. CEN ISO/TR 17641-3, “Destructive tests on welds in metallic materials. Hot cracking tests for weldments. Arc welding processes. Part 3: Externally loaded test”, 2005. 17 p.

9. Scott, P. M. An overview of internal oxidation as a possible explanation of intergranular stress corrosion cracking of Alloy 600 in PWRs. Proceedings of the 9th International Symposium on Environmental Degradation of Materials in Nuclear Systems – Water Reactors. Newport Beach, CA, USA, 1–5 August, 1999. Pp. 3–14.

10. Scenini, F., Newman, R. C., Cottis, R. A. & Jacko, R. J. Effect of surface preparation on intergranular stress corrosion cracking of Alloy 600 in hydrogenated steam. Corrosion, 2008. Vol. 64, No. 11, pp. 824–835

11. Aaltonen, P., Saario, T., Karjalainen-Roikonen, P., Piippo, J., Tähtinen, S. Itäaho, M. & Hänninen, H. Vacancy-creep model for EAC of metallic materials in high temperature water. Corrosion 96, NACE. Colorado, Denver, USA, 25–28 March, 1996. Paper 81. 12 p.

Series title, number and report code of publication

VTT Symposium 264
VTT-SYMP-264

Author(s)
Pertti Auerkari & Juha Veivo (eds.)

Title

Baltica VIII
Life Management and Maintenance for Power Plants. Vol. 1

Abstract

BALTICA VIII. International Conference on Life Management and Maintenance for Power Plants, Helsinki–Stockholm–Helsinki, May 18–20, 2010.

This is one of the two volumes of the proceedings of the BALTICA VIII Conference. The Conference aims to review recent experience, new technology and views on future development for supporting successful, safe and productive operation of power plants.

The triannual BALTICA Conference offers an updated state-of-the-art review on the life management and maintenance of thermal power plants. The themes in BALTICA VIII include e.g. consequences of nuclear revival with issues of the life cycle, new insights into tools and methods for life management and improvements in managing the assets under constraints such as aging, cycling, new fuels and increasing fraction of low to zero emission systems, and recent experience on example cases from new and ageing plants.

ISBN
978-951-38-7591-6 (soft back ed.)
978-951-38-7592-3 (URL: http://www.vtt.fi/publications/index.jsp)

Series title and ISSN	Project number
VTT Symposium 0357-9387 (soft back ed.) 1455-0873 (URL: http://www.vtt.fi/publications/index.jsp)	71111

Date	Language	Pages
May 2010	English	400 p.

Name of project	Commissioned by
Baltica VIII	

Keywords
thermal power plant, nuclear plant, boiler, turbine, condition, life, fuel, maintenance, inspection, monitoring, risk, reliability, material, damage, corrosion, fatigue, creep, degradation

Publisher
VTT Technical Research Centre of Finland
P.O. Box 1000, FI-02044 VTT, Finland
Phone internat. +358 20 722 4520
Fax +358 20 722 4374

BALTICA VIII. International Conference on Life Management and Maintenance for Power Plants, Helsinki–Stockholm–Helsinki, May 18–20, 2010.

This is one of the two volumes of the proceedings of the BALTICA VIII Conference. The Conference aims to review recent experience, new technology and views on future developments for supporting successful, safe and productive operation of power plants.

The BALTICA events:

BALTICA I. International Symposium on Materials Aspects in Life Extension of Power Plants, Helsinki–Stockholm–Helsinki, September 19–22, 1988.

BALTICA II. International Conference on Plant Life Management & Extension, Helsinki–Stockholm–Helsinki, October 5–6, together with the International Symposium on Life and Performance of High Temperature Materials and Structures, Tallinn, Estonia, October 7–8, 1992.

BALTICA III. International Conference on Plant Condition & Life Management, Helsinki–Stockholm–Helsinki, June 6–8, 1995.

BALTICA IV. International Conference on Plant Maintenance for Managing Life & Performance, Helsinki–Stockholm–Helsinki, September 7–9, 1998.

BALTICA V. International Conference on Condition and Life Management for Power Plants, Porvoo, Finland, June 6–8, 2001.

BALTICA VI. International Conference on Life Management and Maintenance for Power Plants, Helsinki–Stockholm–Helsinki, June 8–10, 2004.

BALTICA VII International Conference on Life Management and Maintenance for Power Plants, Helsinki–Stockholm–Helsinki, June 12–14, 2007.

BALTICA VIII. International Conference on Life Management and Maintenance for Power Plants, Helsinki–Stockholm–Helsinki, May 18–20, 2010.

ISBN 978-951-38-77591-6 (soft back ed.)
ISSN 0357-9387 (soft back ed.)
ISBN 978-951-38-7592-3 (URL: http://www.vtt.fi/publications/index.jsp)
ISSN 1455-0873 (URL: http://www.vtt.fi/publications/index.jsp)